THE UNIVERSITY OF CHICAGO

ELECTROCHEMICAL AND TRANSPORT PROPERTIES IN REDOX-ACTIVE POLYMERS FOR ENERGY STORAGE AND CONVERSION

A DISSERTATION SUBMITTED TO
THE FACULTY OF THE PRITZKER SCHOOL OF MOLECULAR ENGINEERING
IN CANDIDACY FOR THE DEGREE OF
DOCTOR OF PHILOSOPHY

BY
GARRETT L. GROCKE

CHICAGO, ILLINOIS
AUGUST 2022

Table of Contents

LIST OF FIGURES……………………………………………………………………………….v

LIST OF TABLES……………………………………………………………………………...x

ACKNOWLEDGEMENTS……………………………………………………………………xi

ABSTRACT……………………………………………………………………………..…...xiii

CHAPTER 1: INTRODUCTION……………………………………………………………1
1.1 Redox-Active Polymers and the Use of Insoluble Materials for Energy Storage…………..……3
1.2 Ionic Charge Transport in Polymeric Electrochemical Systems………………………….……7
1.3 Electronic Charge Transport in Polymeric Electrochemical Systems……………………..…...9
1.4 Leveraging Mixed Charge Transport in Polymeric Electrochemical Systems……………..……15
1.5 Disulfides as Redox Centers and Responsive Covalent Chemistries…………….………..17
1.6 References……………………………………………………………………………………18

CHAPTER 2: EXPERIMENTAL TECHNIQUES FOR ELECTROCHEMISTRY…………....23
2.1 Cyclic voltammetry of small molecule solutions and substrate-confined polymeric solids….23
2.2 Electrochemical Impedance Spectroscopy……………………………..………………29
2.3 Galvanostatic cycling with potential limitation………………………………………………34
2.4 Assembling coin cells with lithium foil anodes for battery testing of cathode materials…...…37
2.5 References……………………………………………………………………………………39

CHAPTER 3: DESIGN OF NOVEL EQUIPMENT AND INSTRUMENTATION…………..…40
3.1 Custom heating stages for low signal impedance measurements…………………………..…40
3.2 Vapor doping apparatus for polymer thin films with in-situ conductivity measurement…...…42
3.3 Stage for functional gradient in conjugated polymer via thermal microstructure control…......47
3.4 Cell for in-situ electrochemical doping and characterization of conjugated polymers………..49
3.5 Apparatus for graded heating and through-plane measurement of films and coin cells………52

CHAPTER 4: STRUCTURE-TRANSPORT PROPERTIES GOVERNING THE INTERPLAY IN HUMIDITY-DEPENDENT MIXED IONIC AND ELECTRONIC CONDUCTION OF CONJUGATED POLYELECTROLYTES…………..……………………………………….54
4.1 Introduction……………………………………………………………….……………….55
4.2 Results and Discussion…………………………………………………………….……59
4.3 Conclusions and Outlook……………………………………………………..………73
4.4 Materials and Methods……………………………………………………………….…74
4.5 Appendix………………………………………………………………………….……….80
4.6 Acknowledgements………………………………………………………………….…..96
4.7 References…………………………………………………………………………………97

CHAPTER 5: SYNTHESIS AND CHARACTERIZATION OF REDOX-RESPONSIVE DISULFIDE-CROSSLINKED POLYMER PARTICLES FOR ENERGY STORAGE APPLICATIONS……………………………………………………..……………..…….101

5.1 Introduction……101
5.2 Results and Discussion……103
5.3 Conclusions and Outlook……112
5.4 Materials and Methods……112
5.5 Appendix……119
5.6 Acknowledgements……131
5.7 References……131

CHAPTER 6: ENHANCING PERFORMANCE OF REDOX-RESPONSIVE DISULFIDE-CROSSLINKED POLYMER PARTICLES VIA SYNTHETIC TUNING AND ELECTRODE PREPARATION……135
6.1 Introduction……136
6.2 Results and Discussion……139
6.3 Conclusions and Outlook……151
6.4 Materials and Methods……152
6.5 Appendix……155
6.6 Acknowledgements……156
6.7 References……156

CHAPTER 7: ENHANCING PERFORMANCE OF PEDOT-DMCT HYBRID CHEMISTRY FOR USE IN LI-ION BATTERY CATHODES THROUGH SYNTHESIS OF A NANOPARTICLE MORPHOLOGY……157
7.1 Introduction……158
7.2 Results and Discussion……160
7.3 Conclusions and Outlook……170
7.4 Materials and Methods……171
7.5 Acknowledgements……173
7.6 References……173

CHAPTER 8: STIMULUS-TRIGGERED RELEASE OF SURFACE-BOUND PARTICLES USING REVERSIBLE DYNAMIC CHEMISTRIES……175
8.1 Introduction……176
8.2 Results and Discussion……182
8.3 Conclusions and Outlook……194
8.4 Materials and Methods……196
8.5 Appendix……200
8.6 Acknowledgements……205
8.7 References……206

CHAPTER 9: SUMMARY AND OUTLOOK……209

List of Figures

1.1. Schematic demonstrating the size exclusion principle for rejection of high molecular weight polymeric redox-active materials across a semi-permeable membrane separator………………...4

1.2. Solvation schemes for ionic conduction in polymers…………………………………….....8

1.3. Scheme for electronic charge transport in a nonconjugated polymer………………………..10

1.4. Schema for electronically-conductive conjugated polymers……………………………...11

1.5. Molecular doping of P3HT with F4TCNQ…………………...…………………………...13

1.6. Examples of polymer systems capable of mixed ionic-electronic conduction………………16

2.1. Evolution of concentration profiles for a redox-active small molecule at an electrode during cyclic voltammetry as it pertains to various points on the voltammogram………………………..25

2.2. Electrochemical cells for CV analysis…………………………………………………….28

2.3. Current response of a pseudo-linear system to sinusoidal excitation potential……………….30

2.4. Nyquist plot of a Randles circuit…………………………………………………………..33

2.5. Galvanostatic battery cycling curve including rest (relaxation) periods……………………..35

2.6. Assembly of a full coin cell battery with lithium foil anode………………………………….39

3.1. Design of a heating stage for measurement of polymer thin film samples……………………41

3.2. Renders describing assembly of apparatus for vapor doping with in-situ conductivity measurement…………………...…………...……………………………...……………43

3.3. Schematic for mounting sample to in-situ doping apparatus using retention ring…………..45

3.4. Placement of doping apparatus for in-situ conductivity measurement………………………46

3.5. Schematic and demonstration for thermal gradient annealing stage…………………………49

3.6. Design of cell for electrochemical doping and characterization of conjugated polymers……51

3.7. Assembly and operation of through-plane apparatus……………………………………...53

4.1. Chemical structure for the P3K*n*T polymer family……………………………………………..59

4.2. UV-Vis of P3K*n*T solutions and thin films as-cast and after heating…………………..……60

4.3. Continuous wave (CW) X-band EPR spectra for as-cast, dried, and re-humidified P3K*n*T films cast on quartz substrates……………………………………………………………………………62

4.4. Responses of P3K*n*T to water sorption at increasing RH……………………………………64

4.5. GIWAXS analysis of "dry" P3K*n*T thin films………………………………………………66

4.6. In-situ RH-dependent GIWAXS of P3K*n*T thin films…………...…………………….……67

4.7. EIS analysis of P3K*n*T thin films on interdigitated electrodes………………………………69

4.8. Schematic for influence of absorbed water on P3K*n*T thin film morphology and conductivity………………………………………………………………………………………71

4.9. Spano model fitting of UV-Vis spectra for P3K*n*T thin films and solution………………….80

4.10. Characterization of EPR spectra of P3K*n*T films equilibrated at different RH…………..…81

4.11. Calculated hydration level (λ) for P3K*n*T powder samples via DVS………………………82

4.12. Schematic of environmental chamber for in-situ humidified GIWAXS……………….......82

4.13. In-situ GIWAXS analysis of P3K*n*T thin films……………………………………………..83

4.14. Relative degree of crystallinity (rDoC) determination for P3K*n*T thin films………………86

4.15. DC I-V curves for dried P3K*n*T polymer thin films on IDEs under argon gas…………….87

4.16. Nyquist plots for P3K*n*T thin films on IDE with increasing RH……………………………88

4.17. Material characterization (DSC and TGA) of P3K*n*T polymers……………………………92

4.18. P3K*n*T ^{1}H NMR (400 MHz, D_2O/ACN-d3)..93

4.19. Gel permeation chromatography (GPC) of P3K4T and P3K5T solutions………………….95

4.20. Atomic force microscopy (AFM) images of P3K*n*T thin films on Si wafer………………...96

5.1. Design of disulfide-crosslinked particles…………………………………………………...104

5.2. Densification of disulfide crosslinks…………………………………………………………..106

5.3. DS-RAP CV data with inset schemes…………………………………………………………108

5.4. Galvanostatic cycling (GC) of DS-RAP (ca. 1000 nm) at a C-rate of 0.10 and 0.25C……..110

5.5. Raman and FT-IR spectra of P1, 1-SS-1, P2-SS, and DS-RAP……………………………119

5.6. FT-IR Voight curve model fitting of P1 and P2-SS epoxide group and carbonyl group……120

5.7. Quantification of 1-SS-1 small molecule released during UV annealing…………………...123

5.8. Reaction scheme for epoxy ring-opening in P2-SS particles using *N*-methylbutylamine to produce DS-RAP…………………………………………………………………………………..123

5.9. Cyclic voltammetry (CV) data for electrode selection and electrochemical reactivity……..124

5.10. UV-Vis absorbance spectra for covalently-bound x-SS-x in DS-RAP dispersion………..126

5.11. Galvanostatic cycling (GC) of DS-RAP using different cell preparations at a C-rate of 0.25C……………………………………………………………………………………………128

5.12. Particle size change characterization and scanning electron microscopy (SEM) imaging for smaller DS-RAP………………………………………………………………………….…..129

5.13. SEM images of smaller DS-RAP blended with carbon black before and after charge/discharge cycling…………………………………………………………………………..130

6.1. Typical makeup and calendaring for dense inorganic battery electrode composites………136

6.2. Impact of PGMA-ATDDS epoxide passivation…………………………………………140

6.3. Synthetic scheme for and SEM images of monodispersed nano-sized PGMA particles..…141

6.4. Impact of solvent selection on particle behavior…………………………………………143

6.5. SEM images of "CO2" particle electrodes with 75:20:5 active material/carbon black/PVDF mass ratios…………………………………………………………………………………144

6.6. Impact of epoxide passivation chemistry on discharge capacity in Li metal full cell using DS-RAP cathode active material……………………………………………………..…………..146

6.7. Galvanostatic cycling of "MBA" and "CO_2" particles with and without hot pressing……..147

6.8. SEM images of DS-RAP particle electrodes cast from NMP before and after hot pressing…………………………………………………………………………………………149

6.9. Galvanostatic cycling of differently sized "CO_2" particles with different blend ratios……..150

6.10. FTIR of PGMA-ATDDS particles with different epoxy passivation chemistries…………155

6.11. Representative charge-discharge curves for cathodes containing DS-RAP-MBA and DS-RAP-CO_2 active materials……………..…………………………………………….……………155

7.1. Synthesis of PEDOT-DMcT nanoparticles……………………………………………....161

7.2. TGA analysis of PEDOT-OTs and PEDOT-DMcT particle powders………………………162

7.3. Cyclic voltammetry of PEDOT-DMcT particles cast on carbon paper electrode…………..163

7.4. Cyclic voltammetry of PEDOT particles cast on carbon paper electrode…………………..164

7.5. UV-Vis spectra for PEDOT-OTs and PEDOT-DMcT suspensions………………………...165

7.6. Galvanostatic cycling of Li metal cell with PEDOT-DMcT particle cathode………………166

7.7. Modified Peukert plot of electrodes containing DS-RAP, DS-RAP-CO_2, or PEDOT-DMcT as the active material……………………………………………………………….………...168

7.8. Discharge capacity of Li metal cell with hot-pressed PEDOT-DMcT cathodes……………169

8.1. Concept schematic for stimulus-triggered defouling of redox flow battery electrodes……..181

8.2. Scheme for particles bearing stimulus-responsive disulfide crosslinkers…………………..183

8.3. Process flow for quantitative determination of particle removal……………………………185

8.4. Particle removal from 2D substrates via controlled stimulus under sheer flow conditions….187

8.5. Approach for electrochemically reducing disulfides to thiolates and tagging with brominated compounds…………………………………………………………………………………...191
8.6. Confocal microscopy of P2-SS particles tagged with BrMePyr…………………………….192
8.7. Examining the impact of fouling and defouling on electrode accessibility……………….....194
8.8. Methodology for selection of cleavable disulfide crosslinker……………………………....200
8.9. FT-IR spectra of PGMA and P2-SS…………………………………………………….....201
8.10. UV-Vis absorbance spectra for covalently-bound 1-SS-1 in P2-SS DMSO dispersion…..202
8.11. Design of modular half flow cell defouling apparatus…………………………………….203
8.12. Geometry for flow through channel in defouling flow cell……………………………….204
8.13. Synthetic scheme for PVBC-Fc particles for electrode regeneration experiment…………205

List of Tables

2.1. Common circuit elements used in EIS equivalent circuit model fitting…………...………….32

4.1. Results from Spano model fitting of P3K*n*T thin film UV-vis spectra………………....……..81

5.1. Peak area integration data for P1 and P2-SS FT-IR Voight curve model fitting…………….121

5.2. Viscosity values of electrolyte solvents for DLS measurement parameters……………..…122

5.3. Particle diameters from DLS measurements for P1, P2, P2-SS, and DS-RAP in different solvents and electrolytes……………………………………………………………...…....122

5.4. Qualitative observations for screening of non-selected electrolyte solvents………………..127

5.5. Summary DS-RAP specific discharge capacity (SDC) and Coulombic efficiency (CE) results under different conditions (0.25C C-rate)……………………………………………………….129

8.1. Flow calculations for narrow channel flow field…………………………...…………….204

Acknowledgements

I start by thanking my advisor, Shrayesh Patel. As your first student, we embarked together on what became a rare, meaningful, and successful journey. I am grateful for your guidance, not only teaching me more than I ever expected to gain from one individual, but for also pushing me to go beyond and chase that which intrigued and inspired me. Thank you for trusting me and allowing me to exercise my creativity in both my own projects, and in growing our lab. I feel privileged in being able to have such a large and positive impact on those around me, and it would not have been possible without your blessing and encouragement. For all this and more, thank you for being a mentor, colleague, and friend.

I would also like to thank Stuart Rowan for his advice and counsel throughout the years of our collaboration. I am deeply grateful for the immediacy with which you treated me as one of your own. Thank you for broadening the breadth of my knowledge, for raising the bar for what it means to think like a scientist, and for bringing much color to my graduate experience.

Next, I would like to thank the members of the Patel Lab, former and present. For so many reasons, a research group is a family unlike any other, and I am grateful for everyone with whom I was able to learn and grow. Thank you to Mark DiTusa and Tengzhou Ma for taking the dive in joining a new group alongside me and for laying the bedrock to an endlessly engaging and enjoyable group dynamic. Thank you to Peter Bennington for your knowledge and insight, elevating the level of discourse and serving as a role model for what you can achieve with focus and dedication. Thank you to Ban Dong and Zhongyang Wang for never hesitating to provide guidance to myself and others. Thank you to Priya Mirmira for your continued collaboration and camaraderie long after leaving the Patel office. And thank you to the current members of the Patel

Lab I leave behind. To Nick, Sam, Andrea, Jie-Hao, and Mincheol, thank you for making our time together well-spent, and for giving me confidence that I leave everything in good hands.

I would like to give special and heart-felt thanks to my project partner, Hongyi Zhang. I cannot state how much I appreciate being able to work with you these last several years. I owe so much to your incomparable ethic, your endless generosity, and your loyal friendship. I am grateful for having been able to both teach and learn from you. Thank you for being both a sounding board and a sanity check, and for making the long hours genuinely enjoyable. I will miss getting to share a bench with you, and I am proud to call you my friend.

I would not be where I am today without my family. Words simply cannot describe my gratitude for you. Dad, thank you for always nurturing my curiosity for the world around me, and for motivating me in my lifelong pursuit of knowledge. I cherish each one of our long, winding conversations more than you may ever know. Mom, thank you for your tireless, unfaltering support at every turn in my life. You are the vital constant that has granted me confidence and means, and anything I do in return will never be enough. Drew and Gillian, thank you for trusting in me to be your big brother, for letting me teach you, and help you when you needed it. I am grateful for the impenetrable and irreplaceable friendship we share. A loving and nurturing family is something to never be taken for granted, and I know I am truly blessed to have that and so much more. Thank you for being the ones to give that to me. I love you all so much.

Lastly, to my wife, Ariel, for whom my appreciation and admiration is beyond measure. You support me in body and spirit. You challenge me to be a better person. You endlessly impress me each and every day. I am proud to share my life with you and aspire to be more because of you. You are my confidante, my coach, my anchor, and my best friend. I am incomprehensibly lucky to have found you and love you more than you will ever know. Thank you.

Abstract

In the goal of designing polymer systems for electrochemical devices with effective mixed conduction of ions and electrons, it is necessary to understand the requirements for effective transport of both ionic and electronic charge carrier species and to design materials and systems capable of accommodating them. In this dissertation, approaches to probing charge transport in redox active polymeric systems are detailed, and several investigations are highlighted showcasing the characterization and varied application of these systems. In Chapter 2, attention is drawn to several fundamental techniques for probing redox activity and charge transport in electrochemical systems. In Chapter 3, the design and construction of several custom-fabricated instruments for the fabrication and characterization of conductive polymer systems is discussed, allowing those who follow to a means to use, reproduce, and improve upon their design in the future. Chapter 4 highlights an in-depth study of evolving mixed conduction in a conjugated polyelectrolyte, poly[3-(potassium-n-alkanoate) thiophene-2,5-diyl] (P3K*n*T), in response to an environmental stimulus, ambient humidity. Spectroscopic and morphological analyses reveal the presence of water results in a self-doping phenomenon, but also disturbs molecular packing, resulting in a non-monotonic electronic conductivity profile. This behavior occurs alongside increasing ionic conductivity with a similar overall magnitude. The identification and characterization of a MIEC with mixed conductivity values approaching parity presents an exciting material for electrochemical devices, but also an important model material for studying the tuning of mixed conductivity in such systems. Chapters 5, 6, and 7 discuss the design, synthesis, and implementation of disulfide-bearing insoluble polymer particles for use as rechargeable battery cathodes. Throughout the investigations, the materials are regularly compared and contrasted to existing cathode materials, highlighting key differences in preparation and the impact on cycling performance. Chapter 5

highlights the design of poly(glycidyl methacrylate) (PGMA) particles densely crosslinked with bis(5-amino-l,3,4-thiadiazol-2-yl) disulfide, resulting in redox-active particles with improved electrochemical kinetics when compared to solutions of analogous small molecule disulfides. Implementation of these particles in cathodes reveals stable cycling, but ultimately poor discharge capacity. Chapter 6 showcases a multi-directional approach to improving this performance, modifying particle size, secondary pendant chemistry, and electrode preparation, ultimately showing a dramatically improved cathode capacity without modification of the disulfide redox center. Finally, Chapter 7 highlights preliminary work in designing a disulfide particle system with enhanced intraparticle kinetics, taking advantage of an electrocatalytic effect observed between poly(3,4-ethylenedioxythiophene) (PEDOT), a conductive conjugated polymer, and 2,5-dimercapto-1,3,4-thiadiazole (DMcT), another thiadiazole-derived organosulfur molecule. Initial investigation reveals PEDOT-DMcT particles retain more discharge capacity at faster charge rates than similarly-sized PGMA counterparts, owed to the electrocatalytic effect combined with improved electronic charge transport from PEDOT's conjugated backbone. Chapter 8 demonstrates an alternative use for the disulfide-crosslinked polymer particles in the context of improving performance lifetime for redox flow batteries based on insoluble polymer electrolyte suspensions. Through either electrochemical reduction or UV photoexcitation, particle disulfide crosslinks are cleaved. It is shown that when these particles are adhered to an electrode surface, this controlled de-crosslinking allows the particles to be washed away from the electrode, increasing its access to the fluid electrolyte and improving flow battery performance without need for disassembly, offering a potential method of in-line regeneration for fouled polymer-based redox flow batteries. A conclusion chapter summarizes the results of these studies and discusses the outlook of polymeric materials for use in energy conversion and storage applications.

Chapter 1

Introduction

The demand for accessible energy is not only increasing annually but accelerating as densely populated regions continue to industrialize while contending with the existing energy demands of an electricity-dependent global infrastructure. Intrinsically coupled to this increasing demand is the existential need to relieve dependency on limited and ecologically detrimental fossil fuel energy sources. The promise of renewable and sustainable energy can be found in many sources demonstrated throughout the years. Geological energy sources such as geothermal or hydroelectric currently account for a large percentage of total global electricity generation, but while technically ubiquitous in their availability, are practically limited by available energy density, such as regions of high geothermal activity, or where large volumes of running water exist either naturally or by man-made means. Nuclear power presents another high-availability supply of energy relative to fossil fuels, but poor public education and policy making following accidents involving nuclear power plants has resulted in a current climate of fear surrounding the energy source, making it difficult to start new projects and as well as maintain existing plants. Non-combustion-based renewable energy sources, such as wind and solar, continue to gain more utilization every year, but by their very nature contain one inherent flaw- they are only intermittently available. As a result, a means of balancing the availability of energy generated by these sources across a continuous timeframe is necessary to meet the circadian rhythm of electricity demands. In bridging this gap between temporal supply and demand, numerous energy storage schema exist, but the most relevant means for today is electrochemical energy storage, namely batteries.

This, of course, is not the limit to the importance of battery advancement. As every aspect of daily life becomes electrified, the need for safe and long-lasting batteries is greater now than ever before. Thus, reliable batteries technologies need to fit applications on a multitude of scales, ranging from the grid level down to miniature personal electronic devices. However, across all scales, one important consideration is constant. Much like energy generation itself, the increasing demand for batteries requires that they can be produced through sustainable means. While the current research vogue relies on alkali and alkaline earth metals as the redox-active ionic charge carrier, which are not without their own challenges, the electrodes required to make these systems viable commonly feature a variety of transition metals. Not only do these materials pose toxicity-related safety risks to the end user, but their extraction from minerals is difficult and deeply harmful to the surrounding environment, in addition to putting a cap on long-term material availability.[1] For these reasons, organic redox-active compounds are an attractive future direction for electrode materials. The raw materials of organic synthesis are extremely abundant in nature, and the degree to which organic molecules can be tailored presents immense opportunity to tune chemistries to meet the needs of batteries for numerous scales and applications.[2,3]

The same reasoning can be applied to the devices into which batteries integrate. In recent decades, a great deal of attention has been drawn to the need for electronic devices beyond the capabilities of inorganic conducting and semiconducting materials. Most broadly, being able to generate effective electronic components from organic sources reduces the need for materials sourced from mining, including metalloids such as silicon and germanium, as well as expensive metals such as copper and gold. In addition to the potential opportunity to reduce the cost of production, moving away from materials sourced from minerals can ease the demand for manpower and reduce carbon emissions. Additionally, the use of organic materials affords properties not previously possible. Organic materials allow for the construction of highly flexible and conformable semiconductors for use in applications such as bending solar cells and displays.[4] The soft material properties of organic chemistries also make them much more compatible with biological systems, allowing for the creation of small and highly-sensitive bioelectronic devices with long lifetime and reduced immune response.[5] All things considered, the need for organic chemistries for use in efficient energy conversion and storage seems inevitable.

1.1 Redox-Active Polymers and the Use of Insoluble Materials for Energy Storage

A subset of organic materials particularly suited for use in energy storage and conversion application are redox-active polymers, macromolecules capable of charge transport and/or storage resulting from a change in oxidation state.[6] Redox active polymers may be achieved by covalently attaching a unit of redox active chemistry, or redox center, as a pendant group to the polymer backbone, or integrating it into the backbone directly. The result is a high molecular weight species with many redox-active sites. The ability to define a polymer's architecture results in precise morphological control of the material, dictating how the material integrates into and behaves within electrochemical devices in a much more manageable way than small molecules. This is especially important in the field of energy storage, where generation and maintenance of charge gradients is critical.

A perfect example of an energy storage technology that stands to benefit from polymeric redox active materials is the redox flow battery. Intended to meet large-scale energy requirements, a redox flow battery uses liquid electrolytes as charge storage medium, allowing for decoupling of battery power and energy by storing the electrolyte away from the battery cell in large-volume satellite tanks. Energy density in these systems is therefore tied to the concentration of the redox active species in the electrolyte solution. Traditional redox flow battery research has focused on using transition metal ions as the redox active species. Achieving a high concentration of these species in the electrolyte presents a substantial challenge, requiring extreme pH values or high temperature.[7] The use of organic solvents and redox active species allows for much higher electrolyte concentrations at ambient and neutral conditions, but it is not without its own challenges. Organic solutes readily diffuse across most of the commercially-available membranes used as separators in energy storage applications. Even expensive ion exchange membranes ultimately fail to meet the long-term needs of an organic redox flow battery for commercial use. One approach to addressing this challenge is the use of high molecular weight materials, namely polymers, coupled with membranes that operate purely on a size-exclusion principle.[8] A schematic for visualization of this principle can be seen below in **Figure 1.1.**

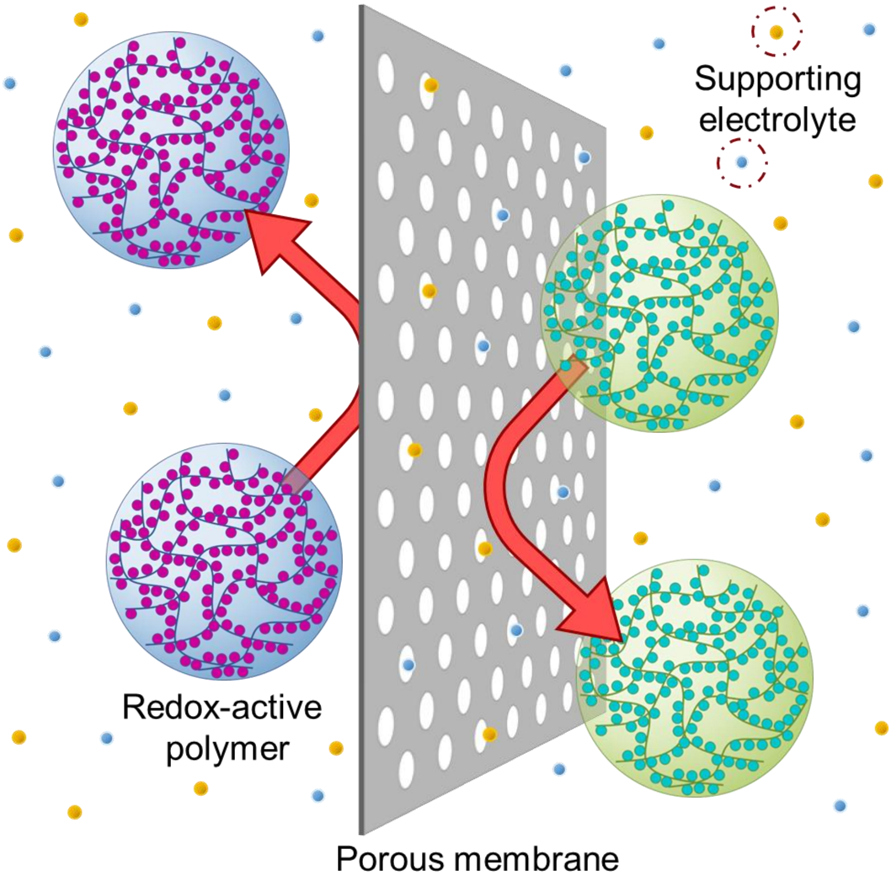

Figure 1.1. Schematic demonstrating the size exclusion principle for rejection of high molecular weight polymeric redox-active materials across a semi-permeable membrane separator.

The increased molecular size results in the solvated polymers being unable to cross the small pores of the membrane, confining them to one half of the battery. At the same time, using a porous membrane instead of an ion exchange membrane means small molecules, including the supporting electrolyte, can achieve higher flux, increasing overall battery performance, while also reducing capital cost by eliminating the need for an ion exchange membrane. Montoto et al. fabricated redox flow battery with polymers as both the catholyte and anolyte, separated by a porous membrane. Their polymer-based system exhibited excellent performance, with an energy efficiency of 90%, Coulombic efficiency of 98%, and voltage efficiency of 92%. In comparison, the performance of a system with equivalent monomer electrolytes resulted in an energy efficiency, Coulombic efficiency, and voltage efficiency of 65%, 72%, and 90%, respectively. Additionally, the polymer-based system was able to access significantly more of its theoretical capacity and suffered far less capacity fade with extending cycling.[9]

The benefits gained by using polymeric active species are only improved upon by utilizing higher order polymer structures. Crosslinked polymer particles swell in solvent but remain insoluble. These materials can be made large relative to the membrane pore size, and result in nearly complete membrane rejection. In another study by the same research groups, stable and insoluble polymer particles were synthesized using the same polymer electrolyte chemistry, this time achieving nearly 99% theoretical capacity and Coulombic efficiency, with complete rejection of the particle across the separator.[10] This approach has been demonstrated in several other studies to similar effect.[11,12] As an added benefit, the use of an insoluble active material leads to reduced electrolyte viscosity, an important consideration in both charge transport and capital concerns, decreasing pumping load and improving equipment lifetime.[12] Coupling this with high separator porosity, allowing increased performance at a lower cost, insoluble high molecular weight materials give direction to practical viability to organic redox flow batteries.

Transitioning back to static systems, redox-active polymers insoluble in electrolyte also make attractive potential materials for secondary battery electrodes. Contemporary technology for Li-ion batteries relies on electrodes composed of an inorganic active material, some conductive additive, typically carbon, and a non-participating polymeric binder to keep the material confined to the half-cell current collector. Relying on this system of composites has several drawbacks. Firstly, the overall specific capacity of the electrode (the capacity per unit of electrode mass) is reduced. Additionally, even with the use of a binder, the arrangement and packing of the active material and conductive additive can become disturbed via mechanical forces resulting from external shock as well as the inherent volumetric changes associated with charge and discharge. Being able to replace one or more of these existing components with redox-active polymers incapable of diffusing across the separator layer stands to improve the entire system. In addition to the considerations of sustainability regarding the active material, a polymeric material is more resilient to stresses originating from inside and outside the cell. Replacing the conductive carbon additive and inert binder with conductive polymers stands to improve battery performance while reducing the weight fraction of these components.[13,14] With proper engineering, a hypothetical polymer capable of both efficient ionic and electronic charge transport could enable a single-species organic electrode with significantly-reduced construction complexity.

All but one of the studies presented in this work focus on the use of polymer particles. Particulates afford many advantages over films cast from linear polymer. Purely from the perspective of charge transport, the geometry of a particle allows for greater accessibility of diffusive species into the material. While an effectively planar film dictates diffusion occur primarily perpendicular to the film surface, a particle allows for more radial diffusion from all exposed surfaces. Small voids in particle packing result in significantly increased available surface area for a surrounding fluid as compared to a wetted film.[15] In the case of applications such as battery electrodes, the increased ion flux in the battery electrolyte allows for overall higher performance.[16,17] The same logic applies to electronically-conductive coatings or additives. In addition to charge transport, particulates drive added simplicity in synthesis and processing. Being able to separate particles mechanically greatly reduces complexity- and time-driven costs in synthesis, chemical modification, and washing. Using insoluble materials in formulations for device fabrication also decreases the selection demands on processing solvents, allowing choice to be dictated by other requirements, such as rheology, boiling point, or chemical compatibility with other species, such as appropriate solvents for battery electrode binders.

1.2 Ionic Charge Transport in Polymeric Electrochemical Systems

Ionic conduction in both dry and solvated polymer systems has been studied thoroughly over the years, and it has been demonstrated that ionic mobility is highest in less dense, more disordered polymer morphologies.[18] Compared to electronic charge carriers, ions are extremely large, occupying appreciable volume within the polymer matrix. More diffuse, easily-distorted polymer structures allow for increased ion mobility in an environment where polymer chain motion presents an activation barrier to ion movement.[19] Additionally, the polymer environment must promote solvation of the selected electrolyte to its ionic species. Dissociation of the ion of interest from any counterion must be thermodynamically preferential for effective ionic conduction. Large, relatively immobile counterions are typically favorable, allowing for decreased Coulombic attraction with the active species.[20] Examples of this include the hexafluorophosphate ($PF6^-$) and bis(trifluoromethanesulfonyl)imide ($TFSI^-$) anions for use in Li-ion electrolytes.

Coupled with this, the local environment must promote coordination of the target ion to prevent reassociation with the counterion. This may be accomplished via covalently-bound permanent charges on the polymer, or by chemistries with preferential electronegativity, such as the coordination of Li^+ to the electron lone pairs on ether oxygens comprising poly(ethylene oxide) (PEO), a commonly-studied polymer for solid electrolytes in Li-ion batteries. Alternatively, the presence of a supporting electrolyte or polar solvent can lead to preferential ionic interactions, screening either the bulky counterion or the relatively immobile polymer, dramatically increasing ion mobility (**Figure 1.2**).[21]

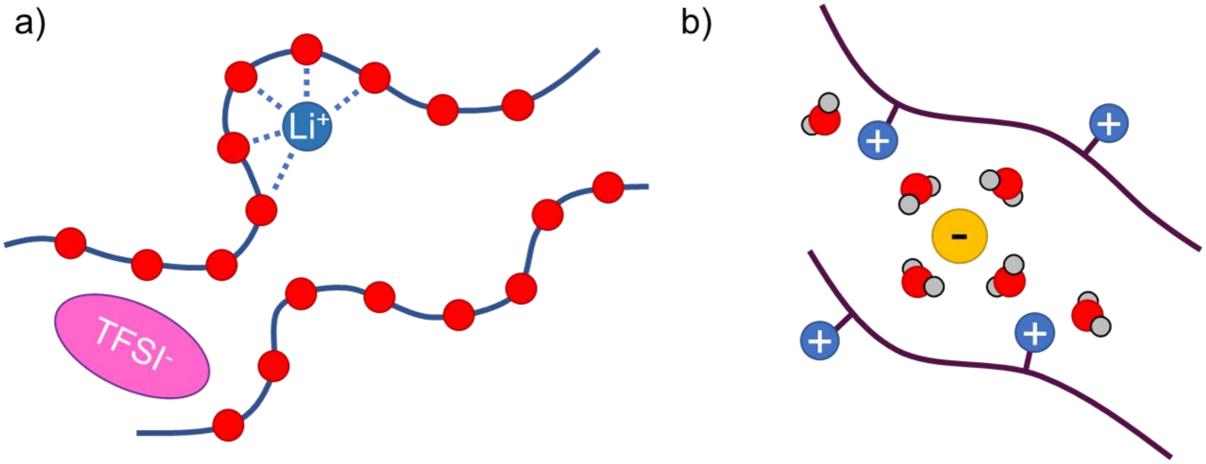

Figure 1.2. Solvation schemes for ionic conduction in polymers. a) Li-ion solvation by ether oxygens in PEO solid electrolyte (red spheres indicate PEO oxygen atoms). b) Water-mediated solvation of a polyelectrolyte counterion (only one counterion of multiple local is shown).

Regardless of the scheme, to achieve effective ion transport, these regions of preferential ion solvation must be present throughout the polymer matrix, and must interconnect with one another, ensuring continuous favorable transport throughout the entire length of the device. This has been demonstrated a necessity on all relevant length scales. Once again, the conduction of Li using ether oxygen-bearing polymers provides an excellent example. Work done to synthesize polymers with different lengths of molecular spacing between ether oxygens revealed that taking into consideration all other variables, increased distance reduced the "connectivity" of the coordination sites, and as a result, decreased the obtainable conductivity of the polymer.[22] Moving to larger length scales, polymeric systems frequently consist of multiple material domains, whether the differentiable phases consist of different chemistries or different morphologies of the same molecular material. In studying the impact of this phenomenon, the use of block copolymers, where controlled phase separation between ionic and nonionic domains allows for precise probing of the effects of defects in the interconnectivity of ion-conducting domains. Frequently used poly(styrene)-*b*-poly(ethylene oxide), or PS-PEO, leads to microphase separation into conducting and nonconducting domains. Use of these materials has demonstrated the need for connectivity between the conductive phases across all relevant length scales of the polymer body, with any interruptions in this percolation leading to diminished performance.[23]

1.3 Electronic Charge Transport in Polymeric Electrochemical Systems

For both organic and inorganic chemistries, redox active materials for energy storage are typically electronically insulating. For polymeric materials, this problem is of special concern. With small molecules, redox centers can diffuse freely in the presence of a supporting electrolyte. With polymers, the redox centers are fixed to a specific position on the polymer chain. Within a polymer bulk, charge hopping from one redox center to another is limited by the spatially-confined Brownian motion of neighboring pendant groups alongside the segmental motion of the polymer chain itself, resulting in much slower electron transfer compared to heterogeneous charge transfer at the electrode surface (**Figure 1.3**).[24] As the characteristic length of an electrode material increases, this slow process becomes increasingly prohibitive to charge migration.

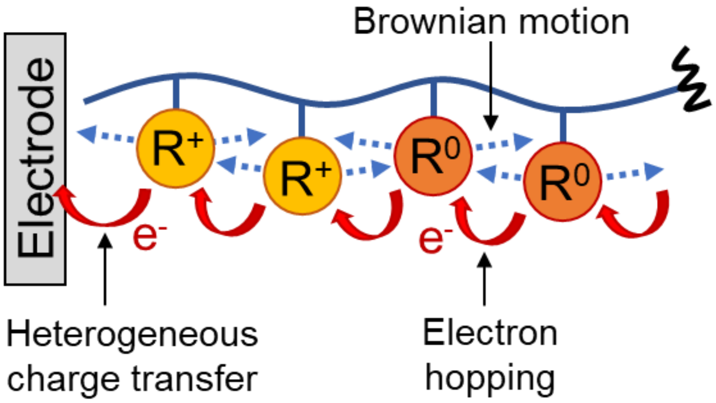

Figure 1.3. Scheme for electronic charge transport in a nonconjugated polymer. Charge transport occurs as electron hopping between redox centers (homogeneous charge transfer), and to the electrode surface (heterogeneous charge transfer. Adapted from Ref 24.

An immense amount of research has gone into identifying means of circumventing the electronically-insulating nature typically associated with polymeric materials. Numerous approaches have been shown that careful molecular design can yield materials capable of efficient electronic conduction. Work in the last several years has demonstrated the use of radical polymers to obtain high electronic conductivity. Through proper annealing of poly(4-glycidyloxy-2,2,6,6-tetramethylpiperidine-1-oxyl) (PTEO), a polymer consisting of radical-bearing pendant groups on an epoxide-based ring-opened backbone, a reorganized structure results in effective percolation of an electronically-connected network of open-shell sites owed to the (2,2,6,6-tetramethylpiperidin-1-yl)oxyl (TEMPO) radicals.[25] Radical redox centers such as these exhibit very fast homogeneous charge transfer constants, making them exciting materials for a growing focus in electronically-conductive polymer systems.[26]

Another class of organic macromolecules capable of electronic conduction are conjugated polymers (**Figure 1.4**). Under appropriate conditions, polymers with backbones containing alternating single and double bonds can conduct electronic charge carriers via overlapping πorbitals. In addition to being capable of effective electronic conduction, these materials are known to be highly stable, showing good resilience to attack by chemicals and solvents. These conjugated systems show promise for use in organic electronics such as flexible solar cells and transistors,[27,28] as well as in place of traditional binder polymers for battery applications, allowing for enhanced electronic connectivity with the different components of the electrode composite[29], as well as within the redox-active material itself, enhancing the overall amount of material available for energy storage.[30,31]

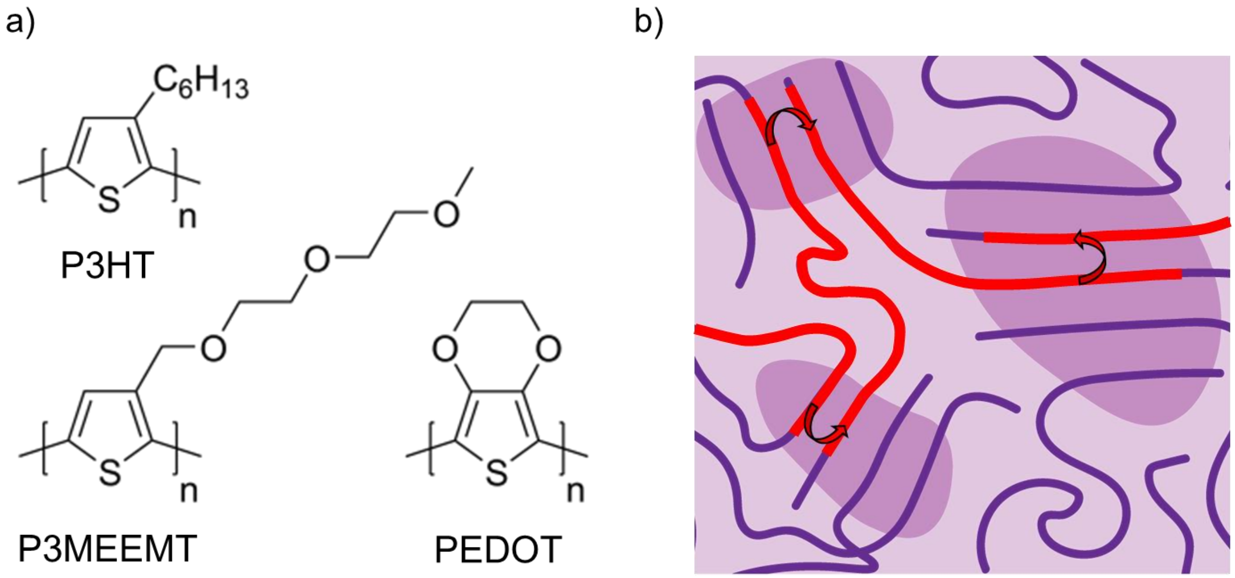

Figure 1.4. Schema for electronically-conductive conjugated polymers. a) Examples of commonly-studied conjugated polymers. b) Electronic charge transport in conjugated polymers, both along the backbone (intrachain) and hopping between adjacent backbones (interchain).

Effective electronic charge transfer in conjugated polymer systems is influenced by two key factors- the number of electronic charge carriers in the system and their mobility. Charge carrier mobility is influenced by several factors, but largely impacted by polymer morphology. Studies coupling computational and experimental approaches have shown how conjugated polymer microstructure influences electronic charge carrier mobility across multiple length scales.

At the smallest scale, planarity of the conjugated backbone drives high mobility, and polymers designed with highly rigid backbone chemistries, such as those with fused monomers, tend to allow for higher π-orbital conjugation lengths, improving intra-polymer charge transfer.[32] Zooming out, regularity in conjugated polymer ordered or crystalline domains is key for the correlation of high intra- and inter-chain charge transfer. Planar alignment of neighboring conjugated polymer backbones, referred to as π-π stacking, increases the likelihood of charge carrier hopping across neighboring chains, with decreased stacking distances resulting in higher mobility. As such, a high degree of crystallinity is desirable for these electronically-conductive systems.[33] However, as conjugated polymer bodies exist in a semicrystalline state, additional mechanisms of transport between ordered domains are necessary. Single or few-stranded polymer "tie chains" bridge nearby ordered domains, allowing for charge transfer between the regions.[34] Conjugated polymers with higher molecular weights potentially allow for a larger number of tie chains within a polymer body, and as such are favored for high mobility on the meso- and greater scales, allowing for higher conductivity devices (**Figure 1.4b**).[35]

The process of raising a semiconducting material's conductivity by increasing its charge carrier concentration is known as doping. With inorganic semiconductors, this is typically accomplished by introducing atomic impurities with a dissimilar number of electrons to the host material, resulting in a concentration of charge within the material lattice. With organic polymer semiconductors, doping can be accomplished via several different means, potentially used in conjunction. The overwhelming majority of organic doping techniques leverage redox chemistry. An electron is donated or extracted from a repeat unit in the polymer backbone, rather than by means of a chemical substitution. This means that the process is ultimately reversible, making polymer doping much more freely modified by comparison to inorganic.

A large amount of research has focused on the use of small molecule molecular dopants.[36] If a small molecule is introduced to a polymer with a sufficiently close energy level, an electron transfer may occur. A dopant with a relatively high HOMO level may donate an electron to the polymer, resulting in a negative charge carrier, or a relatively low LUMO may accept an electron from the polymer, resulting in a positive charge carrier (the more common scenario for commonly-studied polymers). This event results in two charged materials, the polymer and the neighboring dopant, an example of which is shown in **Figure 1.5**.

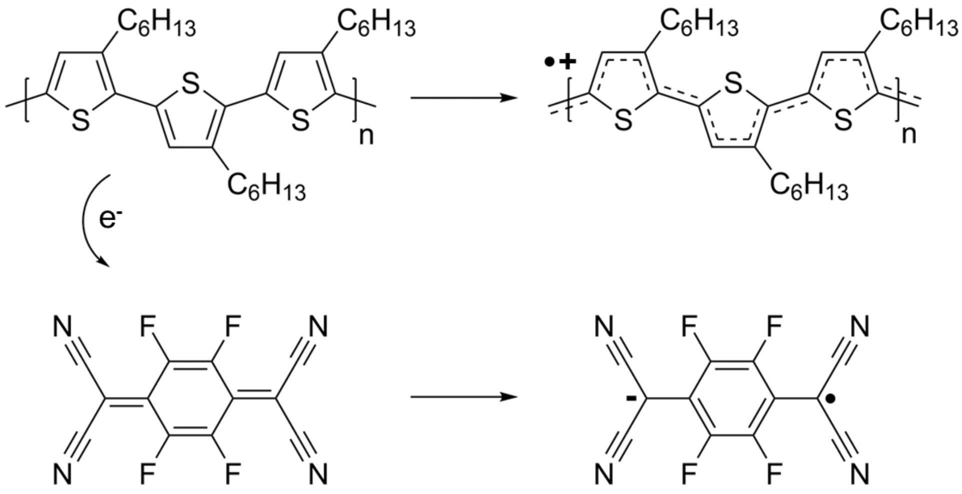

Figure 1.5. Molecular doping of poly(3-hexylthiophene-2,5-diyl) (P3HT) with 2,3,5,6-tetrafluoro-7,7,8,8-tetracyanoquinodimethane (F4TCNQ). Electron transfer occurs from P3HT to F4TCNQ, resulting in a positive electronic charge carrier on P3HT (polaron).

The opposing charged states result in a Coulombic attraction between the two materials, potentially limiting the mobility of the charge carrier. For this reason, a great deal of work has gone into designing extremely bulky dopant molecules, increasing the space between the opposing charges to weaken the Coulombic attraction, and sterically hindering the movement of the dopant molecule as the polymer charge carrier is allowed to freely move.[37] This approach, however, is not without drawbacks. The large size of the dopant molecule can result in a great deal of disruption to the molecular packing of the host polymer as more and more dopant is introduced, negatively impacting charge carrier mobility within the polymer body. As a result, an upper limit to dopant concentration in semiconducting polymer systems must be considering, directly impacting the useful charge carrier concentration generated by this approach.

Electronic charge carriers in a semiconducting polymer can also be generated by electrochemical stimulus.[38] By applying an electrochemical potential to a semiconducting polymer in contact with an electrode, electrons can be directly injected or extracted to the conjugated backbone. Using an electrochemical potential offers some distinct advantages over molecular dopants. By very nature of the mechanism, electrochemical doping is highly controllable. The amount of charge carriers introduced to a material can be highly controlled and monitored by counting the total charge delivered over time. The fact that charge is directly added to the polymer also makes electrochemical doping a more efficient and effective process than molecular doping. Limited only by their ability to traverse the material, the large majority of charge transferred to or from the polymer results in a charge carrier.[39] By comparison, every molecule of dopant delivered to a polymer does not result in a charge carrier, and a portion of those that do may result in lower-mobility charge transfer complexes rather than integer charge transfer, and even then, the products of integer charge transfer may not be freely mobile.[40] Additionally, electrochemical doping is much less likely to negatively impact the morphology of the polymer as compared to molecular doping, where large strain and deformation is nearly unavoidable at high dopant concentrations. Lastly, the process is also much more reversible than molecular doping. By performing the opposite charge transfer process required for doping, a semiconducting polymer can be de-doped with relative ease compared to molecular doping, which requires the physical removal of the small molecule dopant through washing or sublimation via heat and/or vacuum. Despite all this, electrochemical doping is not without its limitations. To efficiently dope a polymer body, it must be in good contact with the supplying electrode. Poor contact with the electrode surface from fabrication or mechanical disruptions may lead to inhomogeneity in the doping process. Additionally, electrochemical doping is known to fade over time. Undesirable redox reactions with other chemical species present in the system or charge trapping due to counterion migration can reduce the number of available charge carriers in an electrochemically-doped device.[41]

Self-doped semiconducting polymers have been the focus of recent attention. Under appropriate environmental conditions, these materials may undergo a redox reaction without the need for an additional redox agent or electrochemical stimulus.[42] The predominant example of such materials are water-soluble self-doped conjugated polyelectrolytes. These polymers consist of the conjugated backbone necessary for electronic conduction with covalently-bound side chain pendant groups featuring permanently charged species. If the charged species is sufficiently dissociable in the presence of a solvent, such as a metal sulfonate in water, the unbalanced side chain negative charge can stabilize the formation of a positive charge on the polymer backbone.[43] Implementation of such materials as a binder in cathodes for Li-ion batteries has not only been shown to improve their capacity and cycling performance but provides a means of facile and environmentally-friendly electrode preparation using water in place of harsh organic solvents.[14]

1.4 Leveraging Mixed Charge Transport in Polymeric Electrochemical Systems

When considering what steps can be taken to improve either ionic or electronic conductivity in energy storage systems, it must be remembered that all electrochemical systems are inherently electronically and ionically conductive on some scale. With this knowledge, care must be taken to not overly limit the conductivity of one charge carrier in favor of another. The need for mixed conduction presents a challenge to organic electrochemical systems in that ionic and electronic conduction in polymeric systems rely on very different pathways and polymer morphologies.[44] While electronic conduction relies on tightly packed structures, as described previously, ions typically demand the opposite. Thankfully, the synthetic flexibility and high processibility of polymeric materials allow for numerous approaches to addressing this challenge. Past research has focused on design of multiphasic polymer blends, such as PEDOT:PSS, or block copolymers like P3HT-*b*-PEO, coupled with solvent or thermal annealing to promote microphase separation within the polymer bulk, providing percolating pathways for both types of charge carrier.

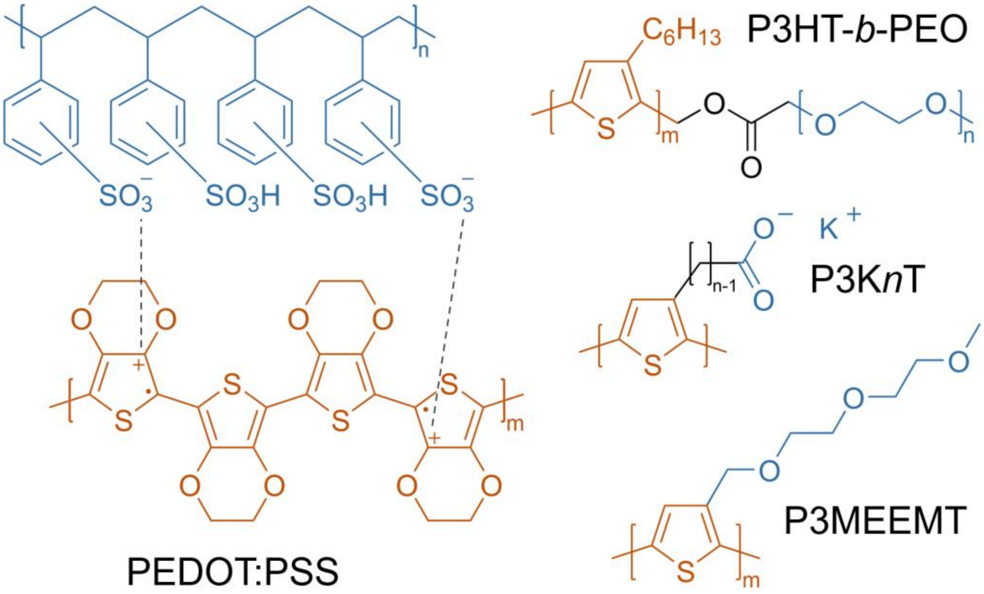

Figure 1.6. Examples of polymer systems capable of mixed ionic-electronic conduction. Structures colored in blue contribute to ionic conduction, while structures in orange contribute to electronic conduction.

Additional work has focused on the creation of homopolymer systems, in which moieties capable of electronic and ionic conduction are present on the same monomer subunit. Such examples include conjugated polymers bearing polyether side chains, such as the increasingly popular poly(3-{[2-(2-methoxyethoxy)ethoxy]methyl}thiophene-2,5-diyl) (P3MEEMT), capable of both electronic and Li-ion conduction.[45,46] As a non-exhaustive final example, previously-mentioned conjugated polyelectrolytes are homopolymers that incorporate the ionic components directly into the monomer chemistry, resulting a material capable of generating mixed charge carriers without the need for small molecule additives such as salt or dopants, such as poly[3-(potassium-*n*-alkanoate) thiophene-2,5-diyl] (P3K*n*T), which couples a polythiophene backbone to negatively-charged pendant groups with a dissociable potassium counterion.[47] As the demand for effective organic optoelectronics, transistors, and energy storage materials increases, focus on the design of efficient mixed conductor polymers will follow.

1.5 Disulfides as Redox Centers and Responsive Covalent Chemistries

In this body of work, one molecular motif of particular interest is the disulfide, a class of molecules centering around a sulfur-sulfur bond. The concept of sulfur as a cathode material for Li-ion batteries is well-established.[48,49] Sulfur is an inexpensive, readily-available material, produced in vast quantities as the byproduct of petroleum and natural gas refinement. In addition, the theoretical capacity of sulfur as a cathode for Li-ion batteries exceeds 1600 mAh/g, a full order of magnitude higher than contemporary oxide cathodes. However, the system is not without its drawbacks. As sulfur is reduced and coordinates with Li ions, it transforms from stable and insoluble cyclic S_8 to increasingly smaller and more soluble linear Li_2S_x chemistries. As the battery is charged, these accumulated species begin to diffuse across the separator membrane in a process known as polysulfide shuttling. This process severely impacts the practical lifetime of LiS batteries. Many different methodologies have been researched to confine the active material to the cathode surface, typically by physically encapsulating it, or hindering diffusion through tortuous pathways, but the problem is only reduced, not resolved. A different approach to this challenge is to instead target organosulfur compounds of the form RSSR, where the -R group can be selected from any number of different chemistries in order to tune the properties of the material.[50] One such immediate advantage is the ability to covalently link the organosulfur moieties to a polymer backbone. Doing so prevents diffusion of the reduced moieties away from the cathode, promoting greatly enhanced stability and lifetime. While challenges still exist in the design of these materials, such as the relatively sluggish nature of the disulfide redox reactions, the immense abundance of raw materials for synthesizing disulfide chemistries, coupled to their energy-dense multi-electron redox reactions, generate continued interest for their use in battery applications.

In addition to energy storage applications, disulfides have been used in diverse applications as stimulus-responsive structural chemistries. The disulfide bond is capable of responding readily to numerous stimuli in a controlled fashion, including electrochemistry, chemical redox, and enzymatic processes to undergo reversible cleavage, or heat or photoexcitation to form radicals and trigger dynamic disulfide exchange (metathesis). This property has made them a popular choice for designing programmed behaviors in functional materials, such as programmed degradation for drug delivery vehicles,[51] and self-healing in polymer coatings.[52] As implementation of polymers in electronic devices increases in complexity, opportunities may arise where programmed responses such as these play a critical role in device functionality and lifetime.

1.6 References

(1) Azadi, M.; Lèbre, É.; Ali, S. H.; Steen, J.; Wall, F. Future of Battery Metals Supply. *Resour. Conserv. Recycl.* 2022, *182*, 106283.

(2) Larcher, D.; Tarascon, J. M. Towards Greener and More Sustainable Batteries for Electrical Energy Storage. *Nat. Chem. 2014 71* **2014**, *7* (1), 19–29.

(3) Gannett, C. N.; Melecio-Zambrano, L.; Theibault, M. J.; Peterson, B. M.; Fors, B. P.; Abruña, H. D. Organic Electrode Materials for Fast-Rate, High-Power Battery Applications. *Mater. Reports Energy* **2021**, *1* (1), 100008.

(4) Wong, W. S.; Salleo, A. *Flexible Electronics: Materials and Applications*, Springer New York, New York, USA, 2009.

(5) Inal, S.; Rivnay, J.; Suiu, A. O.; Malliaras, G. G.; McCulloch, I. Conjugated Polymers in Bioelectronics. *Acc. Chem. Res.* **2018**, *51* (6), 1368–1376.

(6) Kim, J.; Kim, J. H.; Ariga, K. Redox-Active Polymers for Energy Storage Nanoarchitectonics. *Joule* **2017**, *1* (4), 739–768.

(7) Winsberg, J.; Hagemann, T.; Janoschka, T.; Hager, M. D.; Schubert, U. S. Redox-Flow Batteries: From Metals to Organic Redox-Active Materials. *Angew. Chemie - Int. Ed.* **2017**, *56* (3), 686–711.

(8) Nagarjuna, G.; Hui, J.; Cheng, K. J.; Lichtenstein, T.; Shen, M.; Moore, J. S.; Rodríguez-López, J. Impact of Redox-Active Polymer Molecular Weight on the Electrochemical Properties and Transport across Porous Separators in Nonaqueous Solvents. *J. Am. Chem. Soc.* **2014**, *136* (46), 16309–16316.

(9) Montoto, E. C.; Nagarjuna, G.; Moore, J. S.; Rodríguez-López, J. Redox Active Polymers for Non-Aqueous Redox Flow Batteries: Validation of the Size-Exclusion Approach. *J. Electrochem. Soc.* **2017**, *164* (7), A1688–A1694.

(10) Montoto, E. C.; Nagarjuna, G.; Hui, J.; Burgess, M.; Sekerak, N. M.; Hernández-Burgos, K.; Wei, T. S.; Kneer, M.; Grolman, J.; Cheng, K. J.; et al. Redox Active Colloids as Discrete Energy Storage Carriers. *J. Am. Chem. Soc.* **2016**, *138* (40), 13230–13237.

(11) Wu, S.; Zhao, Y.; Li, D.; Xia, Y.; Si, S. An Asymmetric Zn//Ag Doped Polyaniline Microparticle Suspension Flow Battery with High Discharge Capacity. *J. Power Sources* **2015**, *275*, 305–311.

(12) Yan, W.; Wang, C.; Tian, J.; Zhu, G.; Ma, L.; Wang, Y.; Chen, R.; Hu, Y.; Wang, L.; Chen, T.; et al. All-Polymer Particulate Slurry Batteries. *Nat. Commun.* **2019**, *10* (1), 1–11.

(13) Liu, G.; Xun, S.; Vukmirovic, N.; Song, X.; Olalde-Velasco, P.; Zheng, H.; Battaglia, V. S.; Wang, L.; Yang, W. Polymers with Tailored Electronic Structure for High Capacity Lithium Battery Electrodes. *Adv. Mater.* **2011**, *23* (40), 4679–4683.

(14) Li, X.; An, H.; Strzalka, J.; Lutkenhaus, J.; Verduzco, R. Self-Doped Conjugated Polymeric Binders Improve the Capacity and Mechanical Properties of V2O5 Cathodes. *Polymers (Basel).* **2019**, *11* (4).

(15) Chung, D.-W.; Shearing, P. R.; Brandon, N. P.; Harris, S. J.; García, R. E. Particle Size Polydispersity in Li-Ion Batteries. *J. Electrochem. Soc.* **2014**, *161* (3), A422–A430.

(16) Wang, Y.; Ding, Y.; Pan, L.; Shi, Y.; Yue, Z.; Shi, Y.; Yu, G. Understanding the Size-Dependent Sodium Storage Properties of Na2C6O6-Based Organic Electrodes for Sodium-Ion Batteries. *Nano Lett.* **2016**, *16* (5), 3329–3334.

(17) Zhang, J.; Qiao, J.; Sun, K.; Wang, Z. Balancing Particle Properties for Practical Lithium-Ion Batteries. *Particuology* **2022**, *61*, 18–29.

(18) Padma Kumar, P.; Yashonath, S. Ionic Conduction in the Solid State. *J. Chem. Sci.* **2006**, *118* (1), 135–154.

(19) Shah, D. B.; Olson, K. R.; Karny, A.; Mecham, S. J.; DeSimone, J. M.; Balsara, N. P. Effect of Anion Size on Conductivity and Transference Number of Perfluoroether Electrolytes with Lithium Salts. *J. Electrochem. Soc.* **2017**, *164* (14), A3511–A3517.

(20) Agrawal, R. C.; Pandey, G. P. Solid Polymer Electrolytes: Materials Designing and All-Solid-State Battery Applications: An Overview. *J. Phys. D. Appl. Phys.* **2008**, *41* (22), 223001.

(21) Chu, W.; Webb, M. A.; Deng, C.; Colón, Y. J.; Kambe, Y.; Krishnan, S.; Nealey, P. F.; De Pablo, J. J. Understanding Ion Mobility in P2VP/NMP+I- Polymer Electrolytes: A Combined Simulation and Experimental Study. *Macromolecules* **2020**.

(22) Pesko, D. M.; Webb, M. A.; Jung, Y.; Zheng, Q.; Miller, T. F.; Coates, G. W.; Balsara, N. P. Universal Relationship between Conductivity and Solvation-Site Connectivity in Ether-Based Polymer Electrolytes. *Macromolecules* **2016**, *49* (14), 5244–5255.

(23) Arges, C. G.; Kambe, Y.; Dolejsi, M.; Wu, G. P.; Segal-Pertz, T.; Ren, J.; Cao, C.; Craig, G. S. W.; Nealey, P. F. Interconnected Ionic Domains Enhance Conductivity in Microphase Separated Block Copolymer Electrolytes. *J. Mater. Chem. A* **2017**, *5* (11), 5619–5629.

(24) Sato, K.; Ichinoi, R.; Mizukami, R.; Serikawa, T.; Sasaki, Y.; Lutkenhaus, J.; Nishide, H.; Oyaizu, K. Diffusion-Cooperative Model for Charge Transport by Redox-Active Nonconjugated Polymers. *J. Am. Chem. Soc.* **2018**, *140* (3), 1049–1056.

(25) Joo, Y.; Agarkar, V.; Sung, S. H.; Savoie, B. M.; Boudouris, B. W. A Nonconjugated Radical Polymer Glass with High Electrical Conductivity. *Science.* **2018**, *359* (6382), 1391–1395.

(26) Zhang, S.; Pink, M.; Junghoefer, T.; Zhao, W.; Hsu, S. N.; Rajca, S.; Calzolari, A.; Boudouris, B. W.; Casu, M. B.; Rajca, A. High-Spin (S = 1) Blatter-Based Diradical with Robust Stability and Electrical Conductivity. *J. Am. Chem. Soc.* **2022**, *144* (13), 6059–6070.

(27) Rivnay, J.; Inal, S.; Salleo, A.; Owens, R. M.; Berggren, M.; Malliaras, G. G. Organic Electrochemical Transistors. *Nat. Rev. Mater.* **2018**, *3* (2), 1–14.

(28) Li, Z.; Chueh, C. C.; Jen, A. K. Y. Recent Advances in Molecular Design of Functional Conjugated Polymers for High-Performance Polymer Solar Cells. *Prog. Polym. Sci.* **2019**, *99*, 101175.

(29) Elizalde-Segovia, R.; Das, P.; Zayat, B.; Irshad, A.; Thompson, B. C.; Narayanan, S. R. Understanding the Role of π-Conjugated Polymers as Binders in Enabling Designs for High-Energy/High-Rate Lithium Metal Batteries. *J. Electrochem. Soc.* **2021**, *168* (11), 110541.

(30) Rodríguez-Calero, G. G.; Conte, S.; Lowe, M. A.; Gao, J.; Kiya, Y.; Henderson, J. C.; Abruña, H. D. Synthesis and Characterization of Poly-3,4-Ethylenedioxythiophene/2,5-Dimercapto-1,3,4-Thiadiazole (PEDOT-DMcT) Hybrids. *Electrochim. Acta* **2015**, *167*, 55–60.

(31) Liang, Y.; Chen, Z.; Jing, Y.; Rong, Y.; Facchetti, A.; Yao, Y. Heavily N-Dopable π-Conjugated Redox Polymers with Ultrafast Energy Storage Capability. *J. Am. Chem. Soc.* **2015**, *137* (15), 4956–4959.

(32) Prodhan, S.; Qiu, J.; Ricci, M.; Roscioni, O. M.; Wang, L.; Beljonne, D. Design Rules to Maximize Charge-Carrier Mobility along Conjugated Polymer Chains. *J. Phys. Chem. Lett.* **2020**, *11* (16), 6519–6525.

(33) Noriega, R.; Rivnay, J.; Vandewal, K.; Koch, F. P. V.; Stingelin, N.; Smith, P.; Toney, M. F.; Salleo, A. A General Relationship between Disorder, Aggregation and Charge Transport in Conjugated Polymers. *Nat. Mater.* **2013**, *12* (11), 1038–1044.

(34) Noriega, R. Efficient Charge Transport in Disordered Conjugated Polymer Microstructures. *Macromol. Rapid Commun.* **2018**, *39* (14), 1800096.

(35) Gu, K.; Snyder, C. R.; Onorato, J.; Luscombe, C. K.; Bosse, A. W.; Loo, Y. L. Assessing the Huang-Brown Description of Tie Chains for Charge Transport in Conjugated Polymers. *ACS Macro Lett.* **2018**, *7* (11), 1333–1338.

(36) Salzmann, I.; Heimel, G. Toward a Comprehensive Understanding of Molecular Doping Organic Semiconductors (Review). *J. Electron Spectros. Relat. Phenomena* **2015**, *204*, 208–222.

(37) Jacobs, I. E.; Moulé, A. J. Controlling Molecular Doping in Organic Semiconductors. *Adv. Mater.* **2017**, *29* (42), 1703063.

(38) Ofer, D.; Crooks, R. M.; Wrighton, M. S. Potential Dependence of the Conductivity of Highly Oxidized Poly Thiophenes, Polypyrroles, and Poly Aniline: Finite Windows of High Conductivity. *J. Am. Chem. Soc.* **1990**, *112* (22), 7869–7879.

(39) Bargigia, I.; Savagian, L. R.; Österholm, A. M.; Reynolds, J. R.; Silva, C. Charge-Transfer Intermediates in the Electrochemical Doping Mechanism of Conjugated Polymers. *J. Am. Chem. Soc.* **2021**, *143* (1), 294–308.

(40) Pingel, P.; Neher, D. Comprehensive Picture of P-Type Doping of P3HT with the Molecular Acceptor F4TCNQ. *Phys. Rev. B - Condens. Matter Mater. Phys.* **2013**, *87* (11), 115209.

(41) Tang, S.; Irgum, K.; Edman, L. Chemical Stabilization of Doping in Conjugated Polymers. *Org. Electron.* **2010**, *11* (6), 1079–1087.

(42) Patil, A. O.; Ikenoue, Y.; Basescu, N.; Colaneri, N.; Chen, J.; Wudl, F.; Heeger, A. J. Self-Doped Conducting Polymers. *Synth. Met.* **1987**, *20* (2), 151–159.

(43) Mai, C. K.; Zhou, H.; Zhang, Y.; Henson, Z. B.; Nguyen, T. Q.; Heeger, A. J.; Bazan, G. C. Facile Doping of Anionic Narrow-Band-Gap Conjugated Polyelectrolytes during Dialysis. *Angew. Chemie - Int. Ed.* **2013**, *52* (49), 12874–12878.

(44) Onorato, J. W.; Luscombe, C. K. Morphological Effects on Polymeric Mixed Ionic/Electronic Conductors. *Molecular Systems Design and Engineering*. Royal Society of Chemistry April 1, 2019, pp 310–324.

(45) Flagg, L. Q.; Bischak, C. G.; Onorato, J. W.; Rashid, R. B.; Luscombe, C. K.; Ginger, D. S. Polymer Crystallinity Controls Water Uptake in Glycol Side-Chain Polymer Organic Electrochemical Transistors. *J. Am. Chem. Soc.* **2019**, *141* (10), 4345–4354.

(46) Dong, B. X.; Nowak, C.; Onorato, J. W.; Strzalka, J.; Escobedo, F. A.; Luscombe, C. K.; Nealey, P. F.; Patel, S. N. Influence of Side-Chain Chemistry on Structure and Ionic Conduction Characteristics of Polythiophene Derivatives: A Computational and Experimental Study. *Chem. Mater.* **2019**, *31* (4), 1418–1429.

(47) Grocke, G. L.; Dong, B. X.; Taggart, A. D.; Martinson, A. B. F.; Niklas, J.; Poluektov, O. G.; Strzalka, J. W.; Patel, S. N. Structure–Transport Properties Governing the Interplay in Humidity-Dependent Mixed Ionic and Electronic Conduction of Conjugated Polyelectrolytes. *ACS Polym. Au* **2022**, acspolymersau.2c00005.

(48) Manthiram, A.; Fu, Y.; Chung, S. H.; Zu, C.; Su, Y. S. Rechargeable Lithium-Sulfur Batteries. *Chem. Rev.* **2014**, *114* (23), 11751–11787.

(49) Li, T.; Bai, X.; Gulzar, U.; Bai, Y. J.; Capiglia, C.; Deng, W.; Zhou, X.; Liu, Z.; Feng, Z.; Proietti Zaccaria, R. A Comprehensive Understanding of Lithium–Sulfur Battery Technology. *Adv. Funct. Mater.* **2019**, *29* (32), 1901730.

(50) Shadike, Z.; Tan, S.; Wang, Q. C.; Lin, R.; Hu, E.; Qu, D.; Yang, X. Q. Review on Organosulfur Materials for Rechargeable Lithium Batteries. *Mater. Horizons* **2021**, *8* (2), 471–500.

(51) Beaupre, D. M.; Weiss, R. G. Thiol-and Disulfide-Based Stimulus-Responsive Soft Materials and Self-Assembling Systems. *Molecules* **2021**, *26* (11), 3332.

(52) Yoon, J. A.; Kamada, J.; Koynov, K.; Mohin, J.; Nicolaÿ, R.; Zhang, Y.; Balazs, A. C.; Kowalewski, T.; Matyjaszewski, K. Self-Healing Polymer Films Based on Thiol-Disulfide Exchange Reactions and Self-Healing Kinetics Measured Using Atomic Force Microscopy. *Macromolecules* **2012**, *45* (1), 142–149.

Chapter 2

Experimental Techniques for Electrochemistry

2.1 Cyclic voltammetry of small molecule solutions and substrate-confined polymeric solids

Cyclic voltammetry is perhaps the most heavily relied-upon technique for investigative electrochemical characterization. It uniquely powerful for demonstrating the electrochemical potential of a molecule's charge transfer process. In addition, careful application can allow the user to determine the specific charge transfer mechanism, the rates of multiple kinetic components of the system, as well as the influence of the environment surrounding the redox-active species. This section will highlight the use of cyclic voltammetry for investigating small molecules in solution, examining thin films of semiconducting polymers, and employing targeted strategies for characterizing the activity of insoluble polymer particles.

Cyclic voltammetry (herein "CV") involves applying a controlled electrochemical potential to a sample material using a closed circuit. This circuit consists of two electrodes referenced against a potential third. The controlled electrochemical process occurs at the working electrode (WE). A counter electrode (CE) is used to complete the circuit through the sample volume. The working electrode potential is varied at a steady rate across a defined range in both "forward" and "reverse" directions. If the sample material exhibits a charge transfer process within the defined potential range, an evolution in circuit current can be observed and measured. The potential at which this occurs can be compared to a reference point, either via a third reference electrode (RE) containing a chemical with a well-defined redox potential, or a molecule added directly to the sample itself that can be observed with the working electrode. Comparison against these known values provides a frame of reference for which different molecules can be compared and experiments repeated.

The classically-accepted “ideal” electrochemical system is one in which the charge transfer process is kinetically fast and highly “reversible”, meaning the forward and reverse processes are equally unimpeded, and as a result occurred tightly around the same electrochemical potential. Exhibiting these characteristics produces a distinct pattern in CV resulting from the change in species concentration over time and changing electrode potential, which is explained below in **Figure 2.1**. (It is worthy of note, Reference X from which the figure is borrowed is an excellent open access primer on CV and is an excellent starting point for experimentalists new to the technique).[1] This shape, lovingly referred to as a “duck”, can be seen below in the bottom left of **Figure 2.1**, and is the result of different rate-limiting steps in electron transfer between the system’s redox-active species and the working electrode. To understand this evolution over time, one should look to the Nernst equation (**Equation 2.1**), which relates the concentration equilibrium of a redox-active species’ different redox states to an observed potential (*E*). In an electrochemical cell, this is the overpotential, the difference between the thermodynamically-derived potential of the redox reaction (E^0, or “standard potential”) and the effective potential at the working electrode.

$$\boldsymbol{E = E^0 + \frac{RT}{nF} ln \frac{[Ox]}{[Red]}} \qquad \boldsymbol{(Eq. 2.1)}$$

In this equation, the observed potential changes as a function the relative difference in the concentration of the oxidized and reduced form of the redox-active species, [*Ox*] and [*Red*], respectively. The remaining variables are the gas constant, *R*, the system temperature, *T*, the number of electrons transferred in the process, *n*, and Faraday’s constant, *F*. (It is important to note that the equation is most properly applied when using relative “activities” of the different oxidation states, which are defined as the effective concentrations under non-ideal conditions. In reality, interactions between individual molecules cause deviations from the theoretical concentration. In most cases, keeping working concentrations of the active species low drives the system towards ideality).

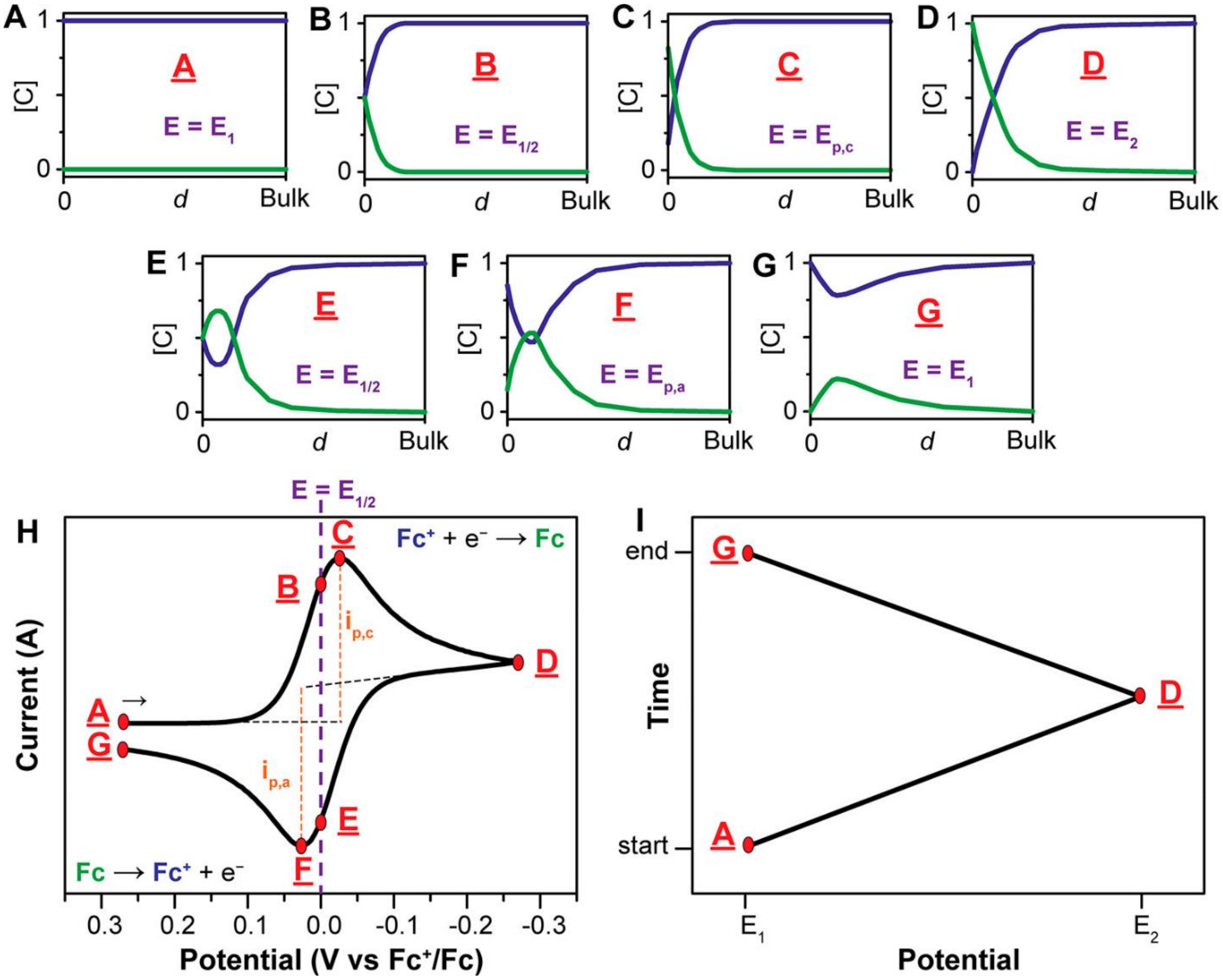

Figure 2.1. Evolution of concentration profiles for a redox-active small molecule at an electrode during cyclic voltammetry as it pertains to various points on the voltammogram. Subfigure **I** shows the profile of the applied potential excitation as a function of time. Adapted from Ref 1.

As the relative concentrations of the different oxidation states shifts, the observed potential also changes in response. The inverse is true as well. Applying an overpotential to a system containing redox-active species causes a change in the relative concentrations of the oxidation states. Referring to Figure X, point A represents the system at a potential sufficiently positive vs the standard potential of the redox-active species, Ferrocene (Fc). Accordingly, the Nernst equation dictates the equilibrium state favors the oxidized form, Fc^+. As the working electrode potential is decreased from point **A** to point **B**, the concentration of the Fc^+ begins to decrease and Fc increases. Points **B** and **E** represent the potential at which the concentrations of Fc and Fc^+ are equal at the electrode surface. Point **C** is the point of peak reductive current, indicated in the figure as $i_{p,c}$ ("peak cathodic current"). Beyond this point, a decrease in reductive current is observed. Fc in its reduced state accumulates near the electrode surface as it is generated. As a result, diffusion of Fc^+ to the electrode surface becomes limited as the potential continues to increase. Ultimately, beyond point **D** a steady-state current is achieved in which the reduction of Fc^+ is entirely dictated by the rate at which it can travel through this "diffusion layer". This mass transport-limited regime continues out so long as the system is electrochemically stable. When the potential sweep direction is reversed, the process occurs in reverse, with the Fc near the electrode surface converting back to Fc^+.

A consideration important to the performance of all electrochemical devices is the electrochemical reversibility of the redox-active material. Electrochemical reversibility does not indicate whether the electrochemical reaction can occur reversibly in both directions. It is instead a measure of the rate of electron transfer, where a reversible electrochemical reaction is one in which the rate of charge transfer is higher than the rate of mass transfer to the electrode, an irreversible reaction being the opposite, and a "quasi-reversible" reaction occupying an intermediate ground. While this definition lacks strictly-defined boundaries between the different designations, reversibility can be observed via the shape of a CV profile. In an ideally-reversible system, the CV peak-to-peak spacing is mathematically determined to be 57 mV divided by the number of electrons transferred per molecule. When the peak spacing for the forward and reverse processes exceeds this value, but remain relatively close, with little difference in the peak magnitudes, the process is considered quasi-reversible. With electrochemically-irreversible processes, the peaks are highly separated, with little to no appreciable peak overlap. However, these guidelines are not foolproof. Numerous factors can increase the peak spacing for electrochemically-reversible chemistries, so long as they create an obstruction to fast charge transfer. These may include a fouled electrode limiting the number of molecules that can react at its surface, or an insufficient concentration of supporting electrolyte resulting in higher than desirable solution resistance. These phenomena can result in an electrochemically reversible process appearing to be quasi-reversible. Understanding why a CV appears nonideal must therefore be taken on a case-by-case basis and is critical to understanding the nature of novel electrochemical materials. It is important to note that an electrochemical process may also be chemically irreversible. In this case, the species resulting from the forward electrochemical process is stable enough that a current cannot be extracted from the reverse sweep. When performing a CV on a novel system, it is important to sample a wide potential range to differentiate between an electrochemically and chemically irreversible process.

The systems presented in this work make use of organic solvents for supporting electrolyte. One of the most common reference electrodes for organic systems is the nonaqueous silver electrode. 10 mM silver nitrate ($AgNO_3$) as the active species is dissolved in acetonitrile along with 100 mM tetrabutylammonium hexafluorophosphate ($TBAPF_6$). A silver wire provides the surface for Ag/Ag^+ plating/stripping. The wire is soldered to a rigid post and inserted into a PTFE body. A glass tube ending in a porous separator is filled with the electrolyte solution, and the wire is inserted within the tube and sealed by the PTFE body. The porous separator ensures connectivity of the electrode to the sample solution while minimizing the flux of solute species in and out of the electrode.

Performing CV of insoluble particles can prove challenging, especially if the kinetics of the particle redox-active moieties ("redox centers") are sluggish. Unlike small molecules, which are free to diffuse towards an electrode surface, particles above a certain critical size in a liquid suspension are at the mercy of gravity and will settle over time, especially in the still conditions required for traditional CV analysis. As a result, it is convenient to immobilize the particle on the working electrode (WE) surface, an example of which can be seen in **Figure 2.2**.

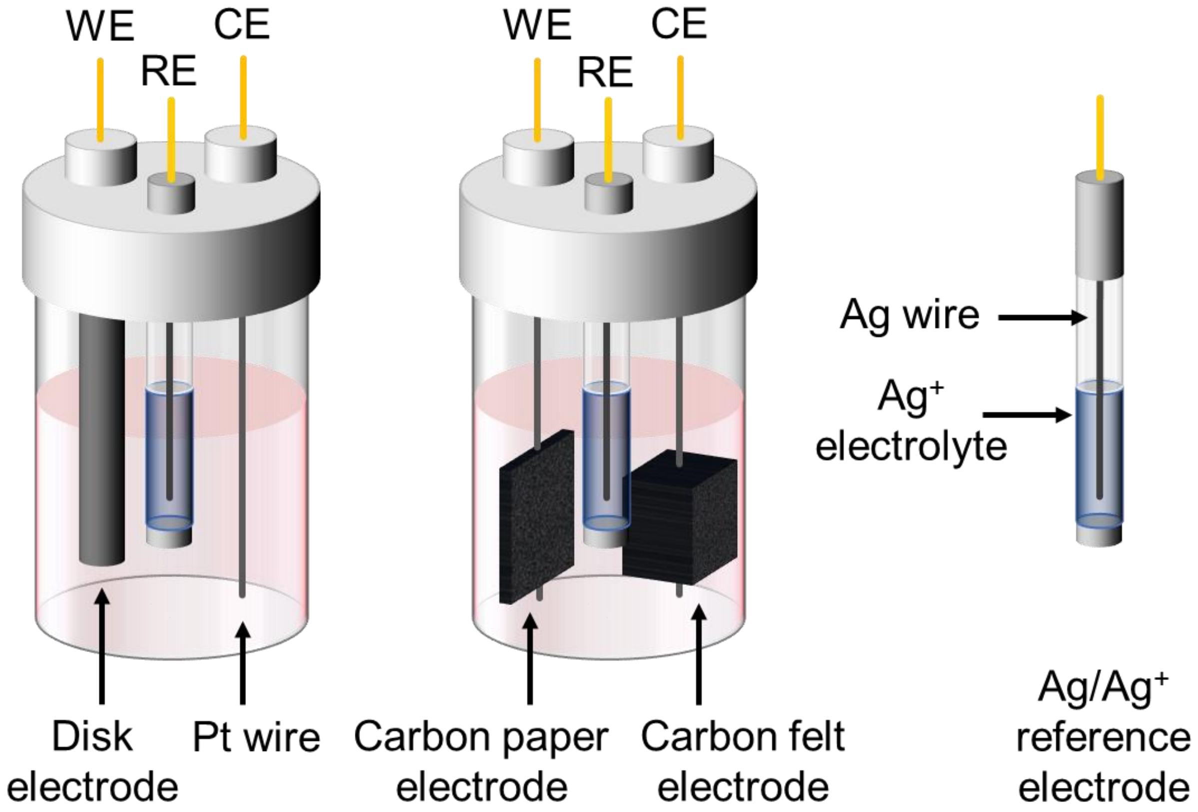

Figure 2.2. Electrochemical cells for CV analysis. Numerous geometries may be used for electrodes depending on the needs of the system. Reference electrodes are constructed so that diffusion between the reference electrolyte and the work electrolyte is minimized. The Ag/Ag$^+$ reference electrode shown here is most appropriate for CV analysis in organic electrolytes.

This immobilized-solids electrode configuration is accomplished through simple drop casting and can be supplemented by heating the particle above a melting transition to better adhere it to the electrode surface, providing it does not degrade the particle chemistry. Indium tin oxide, or ITO, is a common substrate for this approach. It is commercially available as a thin layer on glass microscope slides or slipcovers, and is oxidatively stable, but can degrade under reducing conditions. Conversely, carbon substrates, such as glassy carbon or graphitic pyrolysis products are stable under reducing conditions but can oxidize under strongly positive potentials. Porous carbon substrates such as carbon paper or felt are particularly useful for retaining particulate. Simply spearing a platinum wire through the porous material provides an effective scaffold to retain the active material that can still be used as part of a conventional 3-probe cell. Preparation of such an electrode is used throughout the studies presented in this work.

2.2 Electrochemical Impedance Spectroscopy

Electrochemical impedance spectroscopy (EIS) is an extremely robust technique for investigating numerous aspects of electrochemical systems, including, but not limited to, diffusion of charged species, the formation of double layers, or the presence of faradaic reactions. Applications for EIS include investigation of surface kinetics of electrodes, corrosion studies, photovoltaics, batteries, and biological systems. EIS is performed by recording the response of a system to an oscillating electric field across a range of frequencies and fitting the gathered data to an appropriate model circuit based on the anticipated processes occurring within the system. As such, it is critical to understand the nature of the studied system and how to correlate it to an equivalent circuit model to properly extract the parameter values. EIS is particularly useful to study charge transport in mixed conductor systems, allowing for determination of both ionic and electronic conductivity from one measurement, as it is applied in Chapter 4.

EIS can be performed through the application of either an alternating potential or current and measuring the reciprocal value. In the case of utilizing a direct current (DC) measurement to observe an ideal resistor, electrical resistance (*R*) is determined by the relation $R = E/I$, otherwise known as Ohm's Law, where *E* is electrical potential, and *I* is the current passing through the system. However, in the case of real systems as measured by alternating current (AC), it is more appropriate to describe the system's ability to resist alternating current by *Z*, otherwise known as the impedance of the system, as described by **Equation 2.2**.

$$\boldsymbol{Z = \frac{E}{I} \quad (Eq. 2.2)}$$

Figure 2.3 depicts expected behavior of a pseudo-linear system in response to an AC potential. The concept of pseudo-linearity is important to successful application of the EIS technique.

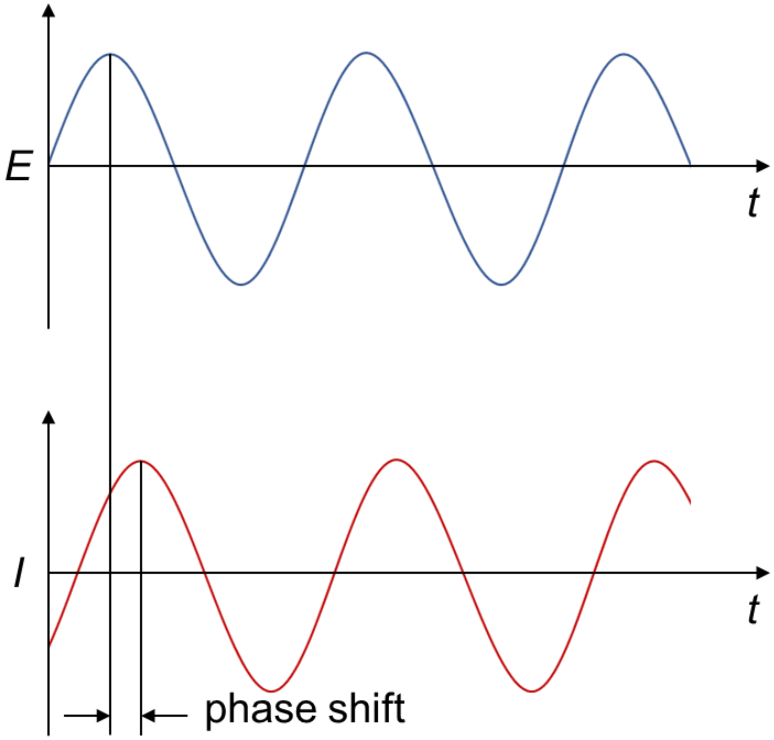

Figure 2.3. Current response of a pseudo-linear system to sinusoidal excitation potential.

In order to correctly interpret EIS data, the system is assumed to be stable and pseudo-linear in response. In order for this to be true, it is important to use as small an excitation as possible to avoid pushing the system out of steady state. This value is typically below 100 mV from open circuit and can be determined by sampling different excitation intensities until the output data begins to deviate. The sinusoidal excitation is expressed as a function of time by **Equation 2.3**,

$$\boldsymbol{E(t) = E_o \sin(\omega t) \quad (Eq. 2.3)}$$

where E_o is the amplitude of the excitation, and ω is the angular frequency, defined by the equation $\omega = 2\pi f$, where f is the frequency in Hz. Assuming the system is stable and pseudo-linear, the current response to the excitation can be expressed in the form

$$\boldsymbol{I(t) = I_o \sin(\omega t + \phi) \quad (Eq. 2.4)}$$

where I_o is the amplitude of the response current, and ϕ is the phase shift as seen in **Figure 2.3**. From this, the impedance of the system can be calculated as a function of a magnitude and the phase shift, as seen in **Equation 2.5**,

$$\boldsymbol{Z(t) = \frac{E(t)}{I(t)} = \frac{E_o \sin(\omega t)}{I_o \sin(\omega t + \phi)} = Z_o \frac{\sin(\omega t)}{\sin(\omega t + \phi)} \quad (Eq. 2.5)}$$

where Z_o is the magnitude of the impedance. Through application of Euler’s formula, impedance can be expressed as a complex number, circumventing the need to interpret angular velocity, and making it convenient to represent the response graphically. This form is seen in **Equation 2.6**.

$$\boldsymbol{Z(\omega) = Z_o(\cos\phi + j \sin\phi) \quad (Eq. 2.6)}$$

where j is the imaginary number, $\sqrt{-1}$.

EIS data is most commonly analyzed by fitting to an equivalent circuit model, where individual circuit elements correspond to phenomena at different points in the system. Table 2.1 describes several of the common elements used in analysis of conductive polymer systems.

Table 2.1. Common circuit elements used in EIS equivalent circuit model fitting.

Element	**Resistor**	**Capacitor**	**Constant phase element**	**Warburg element**
Equation	$Z = R$	$Z = \frac{1}{j\omega C}$	$Z = \frac{1}{(j\omega)^{a} Q}$	$Z = \frac{1}{(j\omega)^{0.5} Q}$

As with electrical circuits, these elements combine based on their physical arrangement. Elements in series combine additively ($Z = Z_1 + Z_2 + Z_3$), while elements in parallel combine in the form $Z^{-1} = Z_1^{-1} + Z_2^{-1} + Z_3^{-1}$. Understanding how these elements correlate to physical phenomena in the electrochemical system is key to proper fitting. While not discussed here in detail, it is important to note that a thorough interpretation of EIS data is not possible without a conceptual understanding of how charge carriers move through materials and across interfaces within a system. Ions moving through an electrolyte in phase with the oscillating potential can be modeled as a resistor, while the formation of an electrical double layer at an electrode surface can be represented by a capacitor. An example of modeling a complete system can be found in reflecting upon the electrochemical cell from Section 2.1. When the working electrode of the electrochemical cell is polarized, it attracts oppositely-charged ionic species to its surface, leading to an accumulation of charges unable to pass through the electrode. This phenomenon, known as the electrochemical double layer, can be modeled as a capacitor, C_{dl}. Also at the electrode surface, the redox-active species in solution will undergo an electronic charge transfer process with the electrode. The impedance to this process can be modeled as a resistor, R_{ct}. As these processes are occurring as alternative modes of charge transfer within the same region, they can be modeled as parallel processes. Lastly, the solution resistance, R_s, between the working and counter electrode must be considered. As the species in this system are impacted by this portion of the circuit regardless of their interaction with the working electrode, it is modeled as an element in series. This system, referred to as the Randles circuit, can be modeled with the **Equation 2.7**,

$$\boldsymbol{Z = R_s + \frac{R_{ct}}{1 + R_{ct}C_{dl}(j\omega)}} \quad (\boldsymbol{Eq. 2.7})$$

following mathematical rearrangement and simplification from the combination of individual elements as described previously.

There exist several means to graphically represent the data from EIS. A Nyquist plot is a popular and powerful method of showing EIS data in which the x- and y-axis show the “real” and “imaginary” impedance, respectively, resulting from the use of a complex number system as described earlier. These values are Nyquist plots are valued for the amount of useful data capable of being extracted by simple inspection. Specific shapes in Nyquist plot data are indicative of specific phenomena in an electrochemical system, and values, such as resistances, can be extracted without complex fitting. A typical Nyquist plot of a Randles circuit can be seen in **Figure 2.4**.

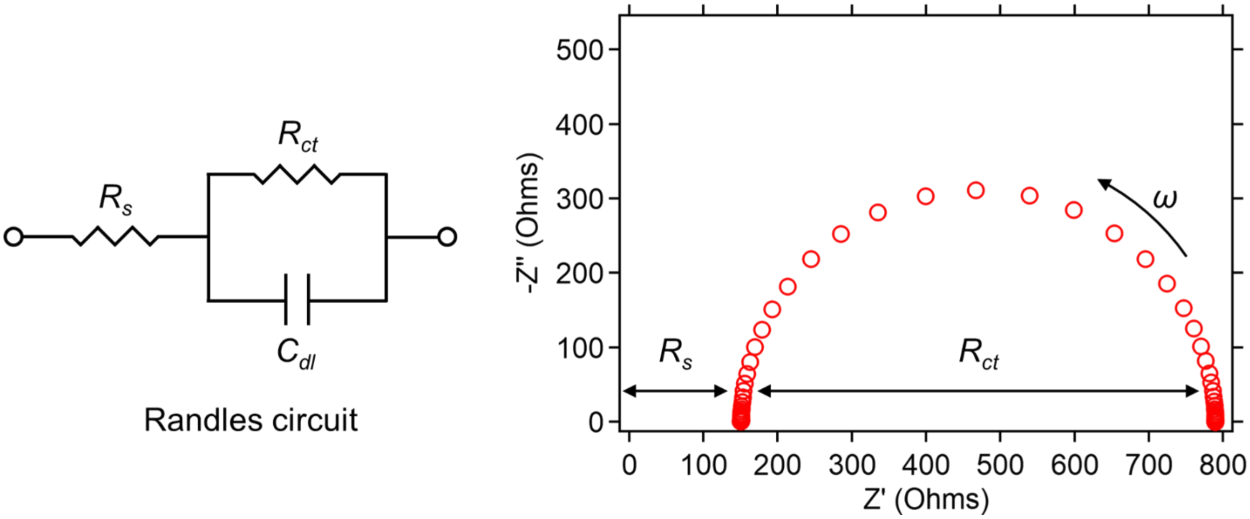

Figure 2.4. Nyquist plot of a Randles circuit. Impedance contributions for solution and charge transfer resistance are labeled on the plot, as well as the direction of increasing frequency.

From this plot, R_s and R_{ct} can be extracted simply by examining the points at which the imaginary impedance (Z'') is minimal, and C_{dl} can be subsequently determined from **Equation 2.7**. While ω is not shown directly in the Nyquist plot, values at individual points are recorded during the measurement. When inspecting a Nyquist plot, it is important to remember that frequency is typically lower on the right side of the plot (high Z') and increases towards the left (low Z').

In addition to the Nyquist plot, another common graphical representation of EIS data is the Bode plot, which consists of two separate plots, in which the magnitude and phase shift of the measured impedance are plotted against frequency. The Bode plot allows direct observation of transitions between frequency-dependent regimes in the impedance response. While useful in specific situations, the Bode plot will not be used for any studies included in this work.

2.3 Galvanostatic cycling with potential limitation

The ultimate test of a candidate battery material is, of course, repeated charge and discharge cycling demonstrating favorable capacity, efficiency, and stability. The traditional battery cycling experiment involves delivering a controlled direct current over time and observing the evolution in cell potential with charging and discharging. The potential limits to which the cell is allowed to charge and discharge in terms of an upper and lower potential are dictated by the stability of the individual chemical components of the cell at high potentials and the lowest point at which the majority of the “useful” energy of the cell has been discharged, respectively. An example charge and discharge profile of a hypothetical electrode material under application of a single current value for both charge and discharge steps can be seen in **Figure 2.5**.

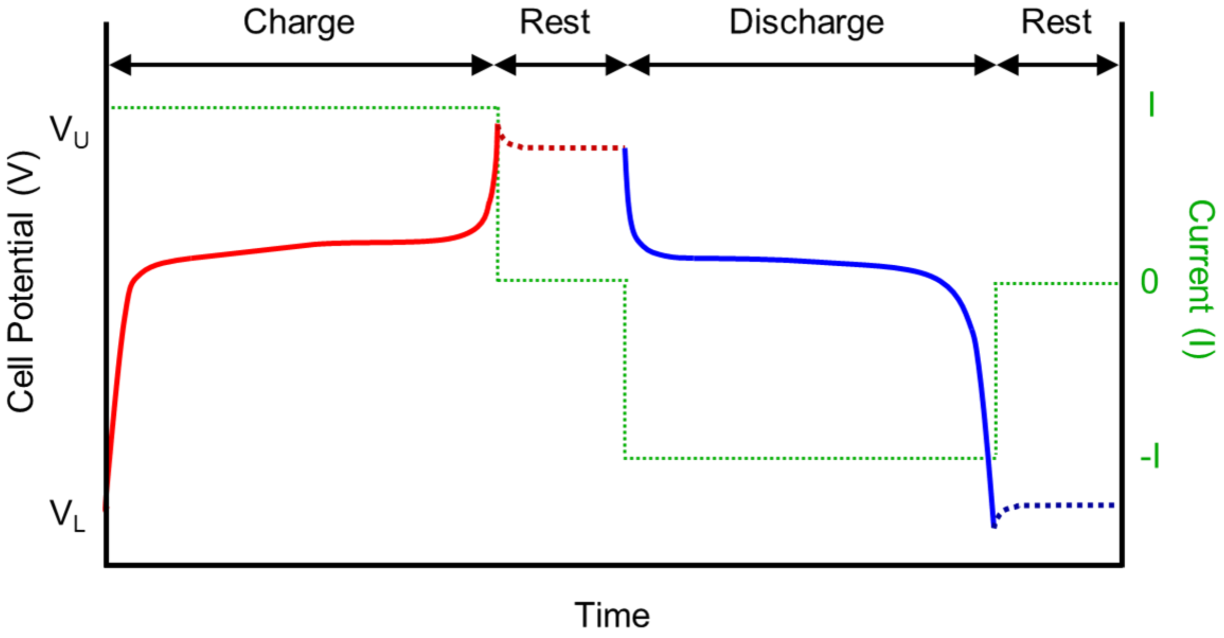

Figure 2.5. Galvanostatic battery cycling curve including rest (relaxation) periods. The x-axis may also be represented in terms of capacity by integrating the step current over time.

An initial rapid rise in cell voltage is the result of charge accumulation at the electrode surfaces without appreciable charge transfer to the active material. This process continues until the redox potential of the electrode active material is achieved, after which the slope rapidly flattens. The broad, flat middle region of the profile corresponds to faradaic charging of the redox-active material. This will proceed until all the accessible active material has undergone reaction. Once the faradaic process has saturated, another rapid rise is observed. This is the result of charge accumulation at the electrode surfaces, as charge can no longer transfer to the active material. An upper cutoff voltage (V_U) is designated to prevent cell potentials becoming too high, after which degradative electrochemical processes can occur. The discharge profile curve shows all the same processes but inverted. As mentioned earlier, the lower limit cutoff (V_L) for discharge is usually dictated by the depletion of “useful” energy, where the potential becomes prohibitively low for practical applications. Discharging beyond this point is typically not irreversibly harmful to the cell, unlike high potentials, but can also require a longer subsequent charging step to recover the previous cycle's discharge capacity.

An important consideration for evaluating battery materials is the impact of charge/discharge rate on capacity. The depth of charge capable in a battery is dependent on the kinetics of the active material. If the rate of charge delivery (current) exceeds the kinetic limits of the material, a charge carrier concentration gradient will develop causing a higher potential closer to the electrode and resulting in the battery reaching the potential limit before charge has had time to diffuse into the less accessible active material. If the battery is given time to equilibrate before discharge, the potential will lower as the charge distribution homogenizes. This can be seen in the "rest" step of **Figure 2.5**. The same phenomenon is true for discharging. Discharging at a rate higher than capable by the active material results in a region of charge carrier depletion nearest the electrode surface, resulting in a rapid decrease in measured potential. If the cell is allowed to relax, the voltage will increase as equilibration occurs. This process is commonly referred to as the recovery effect.

There exist multiple ways of describing battery capacity and charge rate. Capacity can be described most directly using the number of electrons capable of being discharged across a load. The SI unit of charge is the Coulomb, *C*, which equates to approximately $6.242*10^{18}$ charges. This means of measurement is typically considered cumbersome. An alternative approach is to describe it in terms of current over time. The SI unit of current is the Ampere (*A*) and is defined as $1\ A = 1\ C/s$. Integrating the current during battery discharge over the time of discharge yields units of total charge carried, and thus a more commonly accepted means of describing capacity of a battery is this product of current and time, with the units of *Ah* (Amp hours). The specific capacity of an electrode material would then be described in capacity per unit mass, most commonly *mAh/g*.

However, as the capacity of a particular battery cell is not intrinsic, battery charge rate is typically described in terms of raw current, but rather in a normalized sense relative to capacity. This is known as the C-rate and is defined as the current required to fully charge the battery over the course of 1 hour. Higher and lower C rates are inverse to the required time (2C charges in 30 min, C/2 charges in 2 hours, etc.). This convention may seem confusing at first, but better serves to describe charging rates across all arbitrarily-sized batteries.

2.4 Assembling coin cells with lithium foil anodes for battery testing of cathode materials

Coin cells provide a cheap, fast, and reliable means of reproducibly testing materials for battery electrodes and electrolytes. Each coin cell requires a very small amount of active material (on the order of milligrams), and a well-prepared coin cell can cycle stably in a variety of environments for the entirety of the material's natural lifetime without exposing it to air or moisture. A full coin cell contains all the parts of a conventional battery (**Figure 2.6a**). Two electrodes make up the battery half-cells. They are backed by current collectors and kept apart by a permeable separator layer. Liquid electrolytes are typically added in aliquots between layers, but coin cells can also be used in studies for solid electrolytes. Finally, a corrosion-resistant metal casing with an impermeable gasket creates an air-tight seal and increases the mechanical robustness of the assembly. Assembly of a standard 2032 can be seen below in **Figure 2.6b**. Layers are stacked in the negative case of the cell, assuring proper alignment. A spring is placed first to help maintain a tight interface between the layers when the cell is assembled. A stainless-steel current collector disc is placed on top of the spring. Lithium foil provides a material excess on the anode, ensuring any limiting species is the result of the electrolyte or cathode material. Rounds of Li foil are prepared based on techniques from the previous section and punched to appropriate size. Li adheres readily to many surfaces, and will stick to the current collector disc. The foil is pressed down firmly to ensure good contact. Next, the first aliquot of liquid electrolyte is dispensed directly onto the Li round. Next, the separator is placed directly onto the wetted Li. The separator should be slightly bigger than the current collector, ensuring a short does not occur between the two half cells. Another electrolyte aliquot is then dispensed on top of the separator. The cathode material is then added. If the cathode is highly porous, a final aliquot of electrolyte may be added. A final current collector may be placed on top of the cathode, if necessary (depending on sample thickness and robustness), and the positive case is carefully fit over the entire assembly. Coin cell crimping, the act of closing and sealing the assembly, is performed with a dedicated instrument (**Figure 2.6c**). A hydraulic press provides the necessary force to crimp the metal casing, and spring-loaded dies ensure the crimp shape is properly formed. Once the cell is fully crimped, any excess electrolyte should be wiped away, and the cell can be tested for integrity using standard EIS analysis. The user should examine for unexpectedly small or large resistances, providing evidence of an electronic short or poor interlayer contact, respectively. Poor contact may be the result of misalignment of the layers or not enough liquid electrolyte. It is good practice to allow coin cells sufficient time to equilibrate before testing. This allows electrolyte to permeate all the necessary layers, and for the formation of any solid electrolyte interphase (SEI) layers.

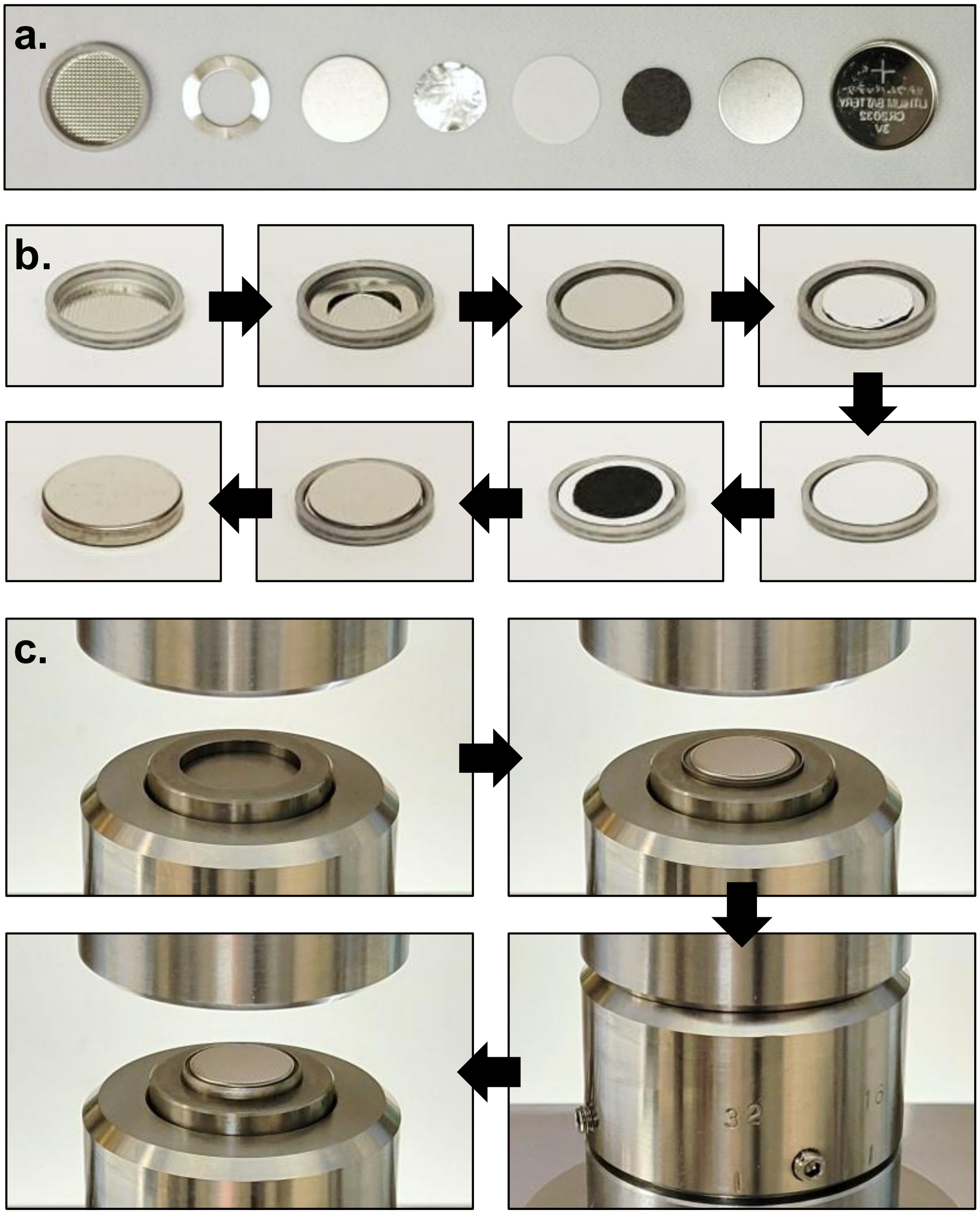

Figure 2.6. Assembly of a full coin cell battery with lithium foil anode. i) Necessary solid components for full cell assembly and ii) step-wise assembly of solid components (liquid electrolyte not shown). iii) Visual guide for proper placement and crimping of assembled coin cell.

2.5 References

(1) Elgrishi, N.; Rountree, K. J.; McCarthy, B. D.; Rountree, E. S.; Eisenhart, T. T.; Dempsey, J. L. A Practical Beginner's Guide to Cyclic Voltammetry. *J. Chem. Educ.* 2018, *95* (2), 197–206.

Chapter 3

Design of novel equipment and instrumentation

3.1 Custom heating stages for low signal impedance measurements

Performing sensitive electrochemical measurements such as EIS at elevated temperatures relies on the ability to deliver steady temperature profiles while avoiding generation of any electromagnetic interference, which can create background noise in high frequency regimes. As such, all the instruments presented in this section rely on heaters with direct current (DC) control coupled with appropriate thermal management. Resistive heating elements inserted into a larger thermal mass can provide power in steady state or pulsed configurations, and the surrounding material slows heat dissipation, resulting in a more linear temperature profile over time, avoiding oscillatory fluctuations on time scales that can impact experimental results. Adequately insulating surfaces of metal or other thermally conductive materials improves this effect even further. Another means of highly controllable heat delivery is the use of Peltier modules, which can provide precisely maintained temperatures above or below ambient. However, Peltier modules are limited in the range of achievable temperatures, both in maximum achievable temperatures, and in the temperature differential versus ambient. Heating or cooling the opposite side of the module through a secondary device can increase the viable range, but high temperature applications are better suited with resistive element heaters. **Figure 3.1** illustrates a simple and reliable approach for fabrication of such a heating stage. Note- all necessary materials for construction of this stage are available from McMaster Carr, a supplier of hardware, tools, and raw materials, but can also be substituted based on specifications or compatibility with common instrument suppliers (Omega Engineering, Inc., etc.). The body of the heating stage is a single piece of aluminum with the top surface machined to as smooth a surface as possible. Aluminum is an excellent thermal conductor, has good machining properties, and is both cheaper and more chemically and oxidatively stable than the next best alternative, copper. A block thickness of less than 1” is preferable. A minimum stage thickness is desirable to ensure steady high temperatures, maximizing volume to surface area ratios, but too great a thickness impedes the ability to heat or cool when changing temperatures, slowing measurements. Into the side of the stage (parallel to the surface), a series of holes are drilled (**Figure 3.1a**). A hole terminating just below the center of the stage will houses a temperature probe (thermocouple, thermistor, RTD). Care is taken to make the hole as close to the surface as possible without deforming the aluminum, as this allows for fast and accurate readings of the temperature nearest the sample placement location. The temperature sensor hole is flanked by additional holes for heating elements. Placing elements on both sides of the sample location, but with some separation distance (typically ca. 1”) allows for development of an even temperature gradient, with leveled profiles as the elements cycle on and off (**Figure 3.1b**).

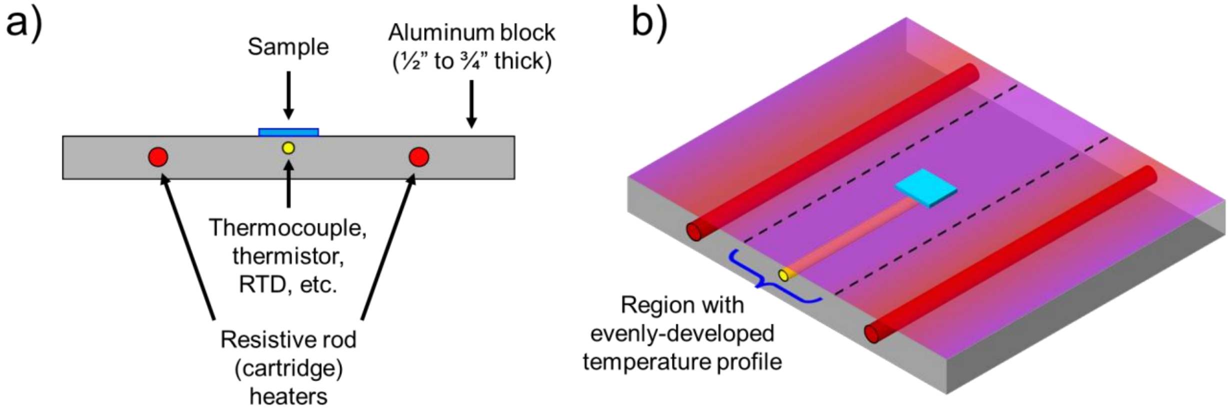

Figure 3.1. Design of a heating stage for measurement of polymer thin film samples. a) Side-view of placement for temperature sensor and heating elements. b) Schematic of temperature gradient development, highlighting stable zone at center used to place samples.

When drilling the holes for the probe and heaters, it is important to make the fit as tight as possible while still being able to insert the elements. Good contact is necessary for both temperature measurement and heat conduction to the stage. The temperature probe should make thorough contact with the stage by means of adding a flowable heat transfer compound to the hole before inserting the probe. Once the probe and heaters are properly inserted, a high-temperature epoxy can be used to secure them in place. After fabrication, care should be taken to thoroughly insulate the heating stage on all surfaces minus the sample placement area. Fiberglass fabric provide an easy-to-shape material for this application, allowing for cutting, bending, and taping in place. Control of the heating stage is best accomplished with a dedicated heater controller. The controller uses a traditional PID approach to measure the stage temperature using the installed probe and respond with pulsed on/off power delivery to the heaters. After installing and connecting the heating stage to the heater controller, it is important to perform a controller tuning operation. This allows the controller to adjust the PID control values to ensure steady, level heating profiles at the desired measurement temperatures. The tuning should only be performed once the stage is installed in its permanent location and the insulation is properly attached.

3.2 Vapor doping apparatus for polymer thin films with in-situ conductivity measurement

The goal of the in-situ vapor doping apparatus was to allow for conductivity measurements of a conjugated polymer thin film previously spin coated onto an IDE while simultaneously doping it with a sublimated vapor dopant under controlled conditions. This allows the user to observe the evolution of conductivity in the sample over time with increasing dopant content while fixing the temperature of the dopant source and the polymer thin film independently. To accomplish this, the apparatus was designed in three major sections (**Figure 3.2**).

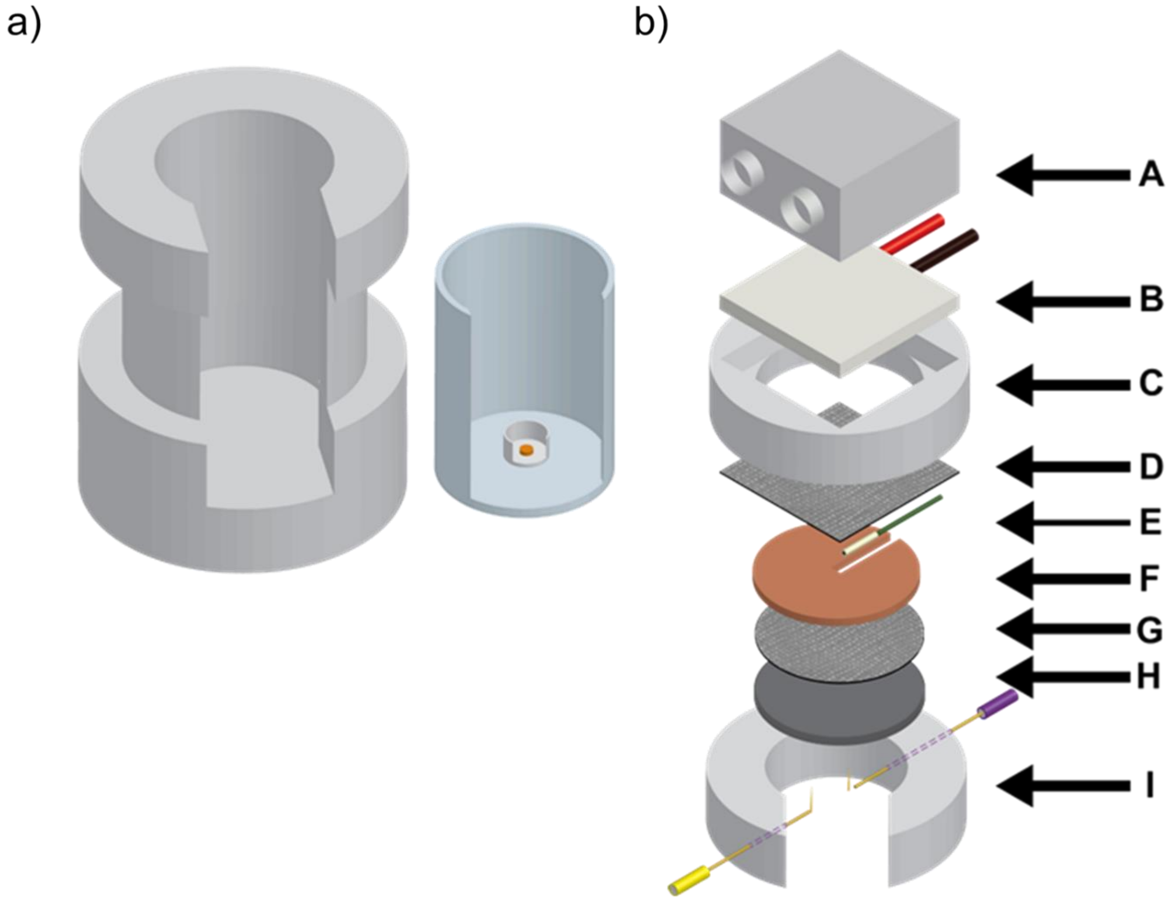

Figure 3.2. Renders describing assembly of apparatus for vapor doping with in-situ conductivity measurement. a) Doping chamber, showing metal jacket, quartz insert, and alumina crucible containing dopant pellet. b) Exploded view of doping apparatus head (A-H) and retention ring (I).

The first is the dopant chamber (**Figure 3.2a**). The purpose of the doping chamber is to provide an enclosed volume with a relatively constant temperature in which the dopant can sublimate upwards without recondensing, reacting with a surface, or escaping to the surrounding environment. The outside of the doping chamber is a stainless-steel jacket consisting of a 2” long flanged pipe attached to a blank ConFlat flange (DN40CF, MDC Precision, LLC). A 1/16” hole is drilled into the side of the blank flange to its radial center and a thermocouple is inserted for recording the temperature of the chamber directly, allowing for interchangeable use of any heating source (hot plate, etc.). Inside the metal jacket resides a custom-fabricated quartz glass insert

(Chemglass Life Sciences, LLC, part # UC-1707-241LP). Quartz is unreactive to the dopant vapor and allows for easy removal of the dopant from the chamber. The dopant source is a compressed pellet, made by loading dopant into a homemade pellet press, followed by placing the pressed pellet into an alumina crucible. The crucible prevents the pellet from moving around inside the doping chamber and can be cleaned using solvents and/or high heat. The crucible is lowered into the center of the quartz insert using tweezers. Different sets of insert and crucible are used for each different dopant species to prevent cross-contamination. The second component of the in-situ doping apparatus is the temperature control apparatus for the sample, hereon in referred to as the “head” (**Figure 3.2a, A-H**). A Peltier cooler thermoelectric module (Custom Thermoelectric, LLC, 03111-5L31-06CG) is used to control the temperature of the sample (**B**). The sample itself rests on a silicon wafer (**H**) (University Wafer, 1” diameter, 500 µm thickness). This wafer is attached to a copper heat spreader disc (**F**) (McMaster Carr, 1” diameter, 0.032” thick) using a thermal conductor (**G**) (Bergquist Gap Pad 1500). The copper disc contains a 1/16” wide cutout from one edge to the disc center. This cutout provides the location for placement of a thermistor probe (**E**) (TE Technology, Inc., MP-2444, 15K ohms) allowing for PID control of the Peltier module. The Peltier module is placed in a PTFE housing and the disc assembly is secured to it using more thermal conductor. On the reverse side of the Peltier, a water block (**A**) (Custom Thermoelectric, LLC, WBA-1.00-0.49-AL-01) is secured using reinforced thermally-conductive adhesive (**D**) (TCDT1, Thorlabs, Inc.). The entire assembly is set within a PTFE ring with a square inset for alignment (**C**) and retained via screw mounts on the water block. Chilled water is used to regulate the back side of the Peltier while the module is being used in cooling configuration. Flexible silicone tubing is used to provide water to the water block via feedthroughs to the water chiller, while the thermistor and Peltier module leads are soldiered to BNC terminals, which are then attached to an electrical feedthrough. Control of the Peltier module is done using a controller (TE Technology, Inc., TC-720) with a LabVIEW-based standalone software package. The final component of the apparatus is a ring serving as both the sample retainer as well as electrical leads for sample measurement (**Figures 3.2b and 3.3a, I**).

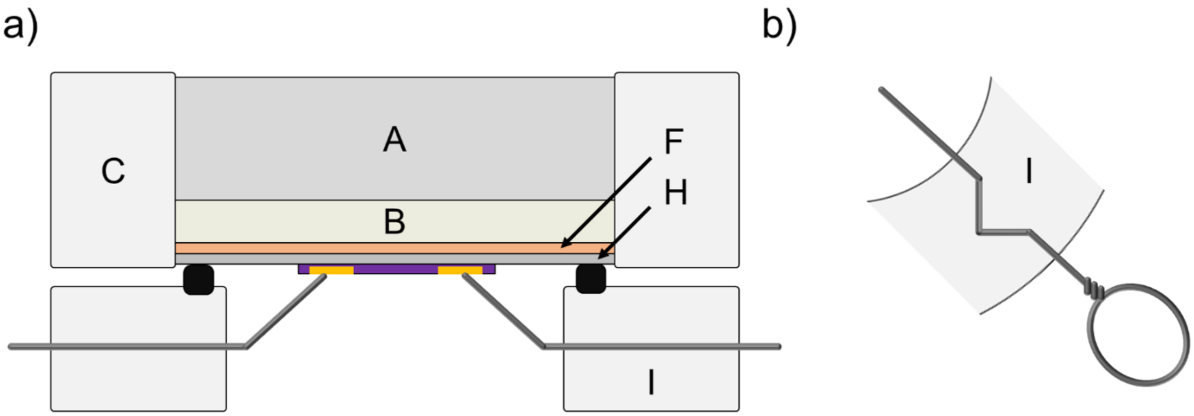

Figure 3.3. Schematic for mounting sample to in-situ doping apparatus using retention ring. a) Cross-section of apparatus "head" with sample in place. b) Top-down view showing final shape of stainless-steel wires after bending.

A PTFE ring was lathed to the same outer diameter as the Peltier module housing with an internal diameter of SIZE. A recess was then cut on one face of the ring to allow for mounting of a rubber gasket. Into the same face, two 1/4"-deep "elbow" pattern grooves consisting of 90-degree bends extending inward were cut into opposing ends of the ring. A stainless-steel wire (McMaster Carr) was then bent to match the elbows and inserted into each of these grooves and epoxied in place. Once the epoxy was cured, the exposed ends of the wire were twisted into a loop, and the inside ends of the wire were bent in such a way that when the ring is mated to the apparatus head, the ends of the wire press onto the contact pads of the sample IDE, holding it in place while providing points of electrical contact. The "elbow" patterns in the ring prevent the wire from twisting when force is applied. The retention ring is currently held in place on the head using a silicone strap, which is wrapped around the back of the head (water block side) and secured on opposing ends of the retention ring. Operation of the in-situ vapor doping apparatus is simple. A sample is placed on the apparatus head and held in place by the retention ring as described. After the appropriate doping chamber temperature has been reached, a crucible with dopant pellet is placed in the chamber. Electrical leads are connected to the retention ring loops (usually in the form of alligator clips) and the apparatus head is placed sample-down atop the doping chamber. A double-blank flange is place on top the resting apparatus head as a weight to ensure good contact with the chamber throughout the doping procedure (**Figure 3.4**). Conductivity values in the form of current under applied potential are collected in real time using a potentiostat or meter of choice.

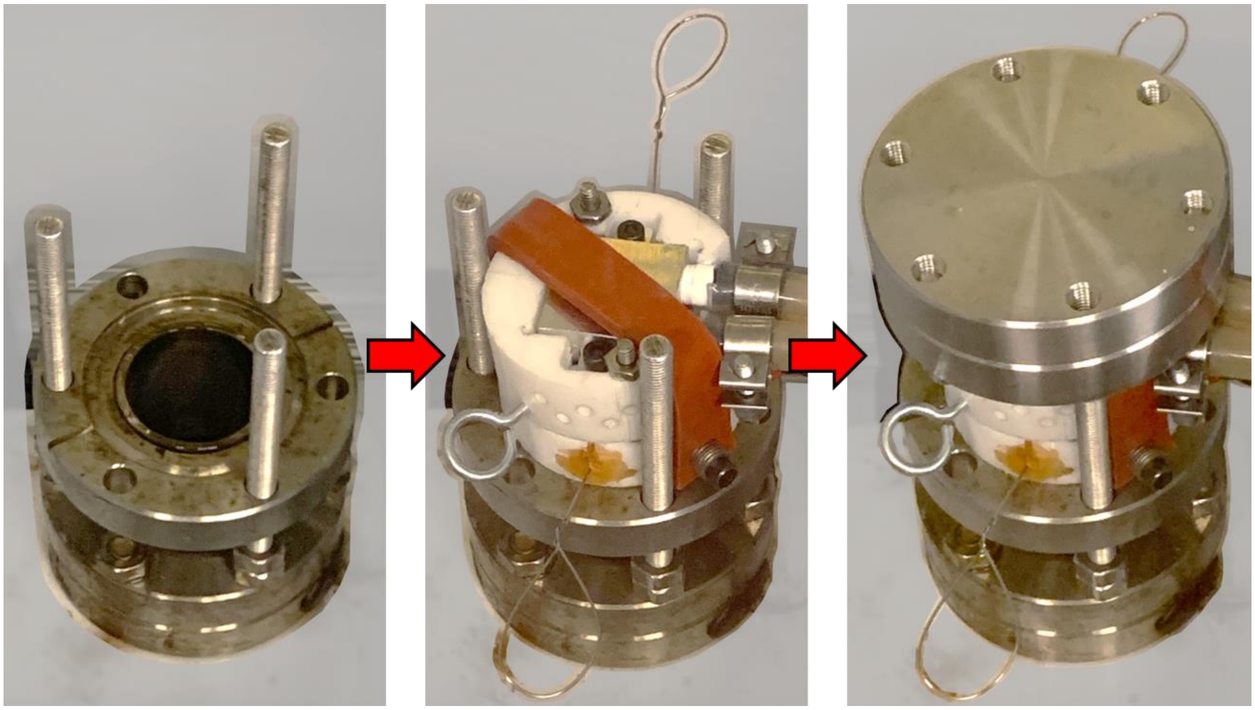

Figure 3.4. Placement of doping apparatus for in-situ conductivity measurement. The assembled doping chamber "head" is placed on the doping chamber, and the weighted flange is place on top.

3.3 Stage for functional gradient in conjugated polymer via thermal microstructure control

The goal of this device is to allow for formation of a functional gradient in conductivity and Seebeck coefficient in a conjugated polymer thin film by heterogeneously annealing it using an approximately linear one-dimensional temperature gradient across the plane of the film. This process is accomplished by using a two-part annealing stage with an air gap between the two halves (**Figure 3.5a**). One side is heated to a temperature above one or more of the sample material's thermal transitions, and the other is kept at a specified temperature below the transition. The opposing ends of the sample substrate heat to the temperature of the stage halves, and a gradient develops across the air gap. The result is a gradient morphology in the polymer thin film deposited on the substrate, and a resultant enhancement in thermoelectric performance relative to a homogeneous sample of the same material. The annealing stage functions in three major sections- a high temperature stage, a low temperature stage, and an IR camera (**Figure 3.5a**). The high temperature stage consists of an aluminum block containing holes drilled for rod cartridge heaters (McMaster Carr, sizing and wattage variable based on required temperature range) and a thermocouple or RTD probe. The heaters are DC-powered and controlled via feedback from the temperature probe using a benchtop controller (OMEGA Platinum Series Universal High Accuracy Digital Benchtop PID). The aluminum block is mounted to an optical breadboard using posts tapped for 1/4-20 thread bolts. The block itself is slotted to provide linear travel of approximately 1", allowing the user to adjust the length of the air gap and as a result the overall gradient distance (**Figure 3.5b**). The slots are positioned on the opposite edge of the block from the sample location and extend from the main body of the block, minimizing thermal loses through the posts and creating a more stable steady state temperature profile. Additionally, the flat surfaces of the stage, minus the area on which the sample rests, are wrapped in fiberglass felt to provide insulation. The second half of the annealing stage is controlled to a lower temperature range using a Peltier module, allowing it to be set to temperatures above or below ambient. The body of the stage is made of an aluminum block with the same dimensions as the high-temperature side, but with a recess cut into it to allow for positioning of the Peltier. The recess is cut deep enough that the top of the Peltier "stack" is flush to the top of the high temperature stage, allowing the sample to sit flush across the air gap. The Peltier stack consists of several layers, each held in place using adhesive thermal conductor (Bergquist Gap Pad 1500). The bottom layer consists of the Peltier module (Custom Thermoelectric, LLC, MAKE AND MODEL). Above that, two copper plates (McMaster Carr, DIMENSIONS, 0.032" thick) are positioned with a gap between them, allowing for placement of a thermistor temperature probe (TE Technology, Inc., MP-2444, 15K ohms). The top layer is an appropriately-cut silicon wafer, providing a flat surface to place the sample.

The Peltier stack is positioned to provide the inside edge of the stage and is adjustable, same as the high-temperature stage. Peltier module leads are soldiered to BNC terminals, which are then attached to an electrical feedthrough. Control of the Peltier module is done using a controller (TE Technology, Inc., TC-720) with a LabVIEW-based standalone software package. A FLIR ETS320 IR camera is used to measure the thermal gradient across the sample. Using the provided software, a linear temperature profile can be plotted, or multiple specific points can be measured simultaneously. An example image of a one-dimensional temperature gradient across a sample substrate and the resultant temperature profile can be seen in **Figures 3.5c** and **3.5d**.

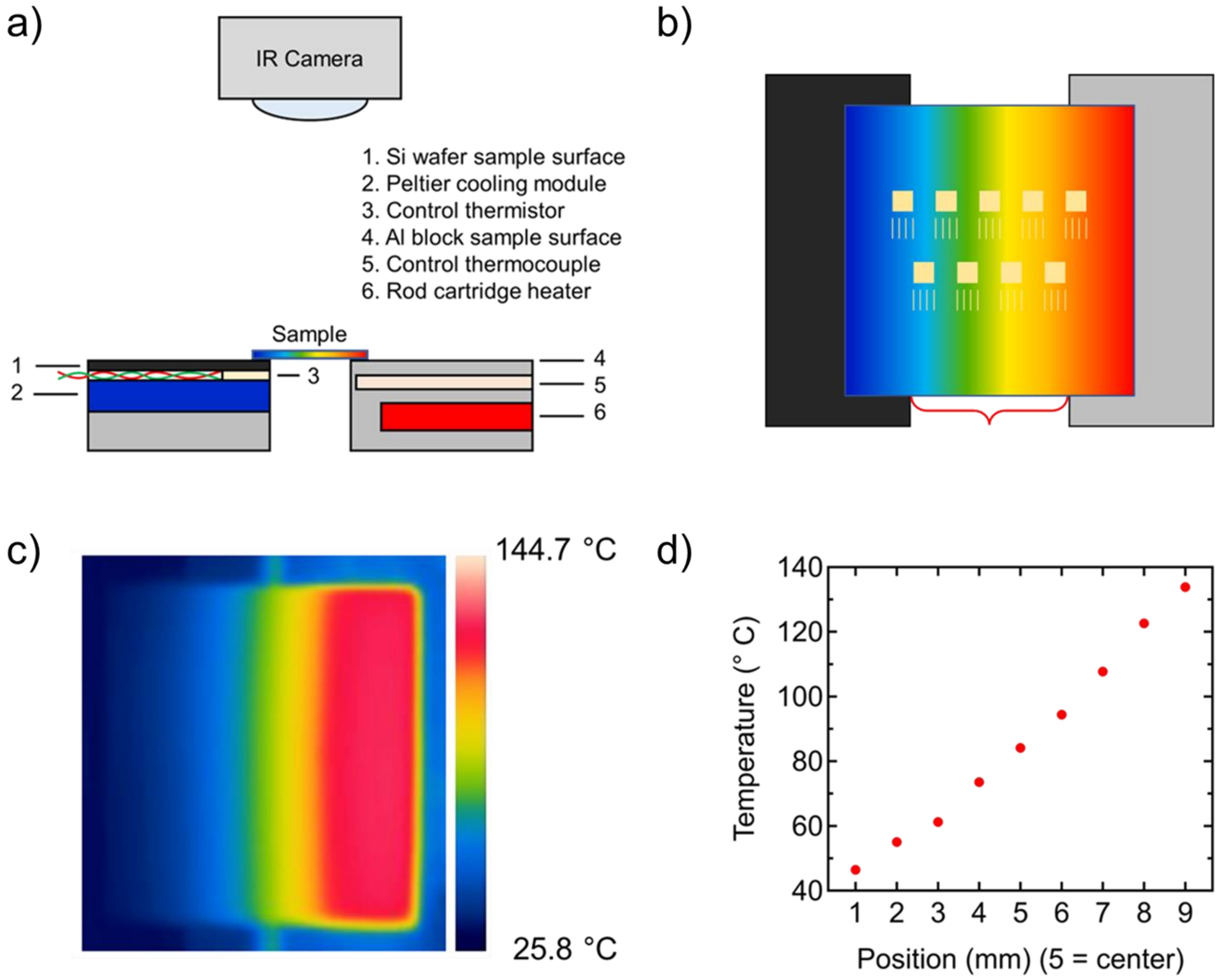

Figure 3.5. Schematic and demonstration for thermal gradient annealing stage. a) Cross-sectional view of components for fully assembled annealing stage. b) Top-down view of sample positioning between halves of annealing stage with one possible configuration for sample contact pattern. c) Image obtained from IR camera of fully developed thermal gradient through quartz substrate placed across annealing stage. d) Measured temperature gradient for 9 positions across quartz substrate placed on annealing stage. First point is taken 0.5 mm from edge of air gap between stage halves, visually represented by the center of the leftmost square contact in **b**.

3.4 Cell for in-situ electrochemical doping and characterization of conjugated polymers

The goal of this arrangement is to provide a means of measuring dual conduction of a single conjugated polymer thin film sample before and after exposing it to an electrochemical potential. Depending on the potential, the polymer can become doped or undoped, modulating its electronic conductivity, as well as the ionic conductivity as a result of flux of electrolyte associated with a change in polymer redox state. The methodology for this apparatus was adopted from Zayat et al and modified to allow use of rapidly interchangeable IDEs. Custom IDE geometries were created to make use of a standard USB interface. The interdigitated array occupies one end of the rectangular device, while each of the two leads extends to the other end. Each of these leads communicates with the outer two pins when inserted into a female USB port. A thin PTFE spacer is inserted behind the device to maintain good contact. A picture of an example device can be seen in **Figure 3.6a**. The USB port is integrated into an in-house fabricated PTFE electrochemical cell cap. The cap was designed to secure to the top of a standard 20 mL beaker. This arrangement allows for sufficient space between the supporting electrolyte and the USB interface to prevent wetting the interface and creating a short circuit. Traditional counter and fritted reference electrodes may be used, or they may be substituted for strips of Li foil. All three electrode are immersed in the supporting electrolyte of choice (**Figure 3.6b**). The cell can be used in two configurations. The first is a two-probe configuration for measuring conductivity across the IDE. The working electrode is connected to one wire of the IDE interface, and the counter and reference are shorted and connected to the other. EIS is used to measure across the thin film sample, and both electronic and ionic conduction can be perceived. The second configuration is that of a traditional three-probe electrochemical cell. The two ends of the IDE interface are shorted and connected to the working electrode, while the counter and reference electrodes are attached respectively to their own leads. In this configuration, EIS of the entire cell can be measured, allowing for determination of ionic conductivity solely (**Figure 3.6c**).

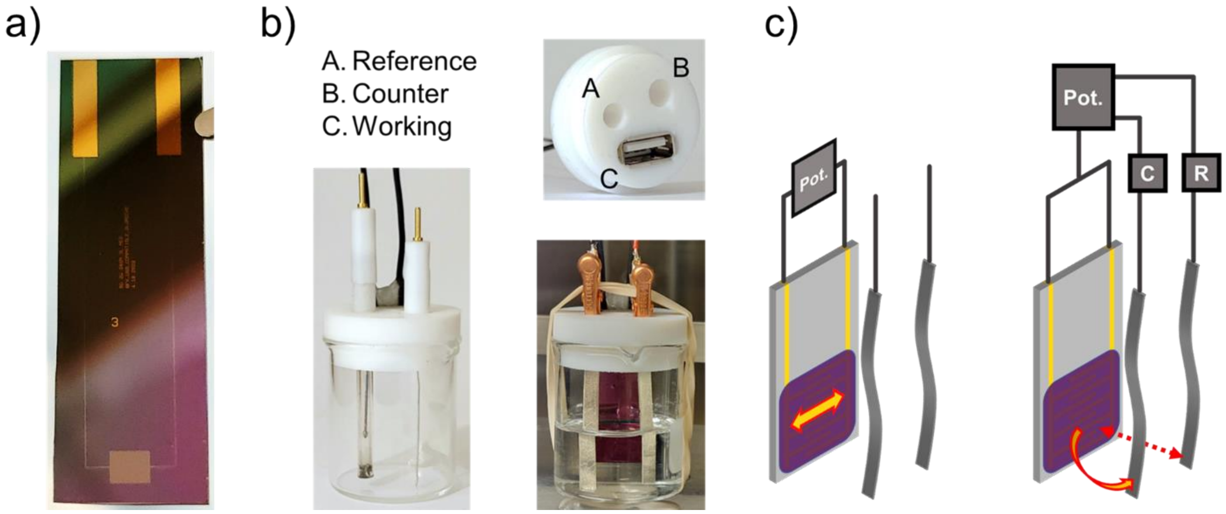

Figure 3.6. Design of cell for electrochemical doping and characterization of conjugated polymers. a) Example IDE with USB interface. b) Images of USB working electrode connector and options for traditional or Li foil counter and reference electrodes. c) Schematic of interchangeable 2-probe and 3-probe cell configurations.

In addition, cyclic voltammetry can be performed on the working electrode. Lastly, a constant potential can be applied to the working electrode vs the reference, allowing for the doping of the conjugated polymer film. In order to perform the in-situ electrochemical doping characterization, all of these techniques are used in conjunction. Cyclic voltammetry allows the user to determine the expected potentials for oxidation and reduction. In the case of conventional p-type conjugated polymers, the onset of electrochemical doping can be observed as an increase in current during the positive voltage sweep. Using this information, a potential may be applied to the working electrode, doping the polymer film. After doping, full-cell EIS may be performed. At this point, the configuration of the leads is swapped, and two probe EIS is performed, revealing any change in electronic conductivity as a function of doping.

3.5 Apparatus for graded heating and through-plane measurement of films and coin cells

The goal of this apparatus was to allow for in-situ through-plane conductivity measurements of polymer thin films, material stacks, and assembled coin cells under the application of graded heating. This is accomplished using Peltier heating elements in a similar configuration to the apparatus in **Sections 3.2** and **3.3**. The apparatus consists of two Peltier module assemblies (**Figure 3.7a**). One assembly is simply mounted to a base. The other of the two assemblies is fitted with an aluminum plate between the water block and Peltier module layers. This plate has been cut with holes for mounting to the water block, as well as four ½" diameter holes in the corners spaced in a 4 x 4" square pattern. These ½" diameter holes allow the plate-mounted Peltier assembly to slide up and down a set of ½" stainless steel rods (Thorlabs, Inc.) positioned around the lower Peltier assembly on the apparatus base. The plate-mounted assembly is slid onto the rods "upside down", with the working surface facing down towards the working surface of the base-mounted assembly. A second aluminum plate is attached to the top of the rods. In the plate center, a screw clamp is used to apply pressure to the plate-mounted Peltier assembly. With this clamp, variable pressure can be applied to a sample placed between the two assemblies (**Figure 3.7b**). The temperatures of the two Peltier modules are controlled individually using two separate Peltier module controllers (TE Technology, Inc., TC-48-20). To measure conductivity, metal foils are placed on either side of the polymer thin film sample prior to insertion into the apparatus and connected to the appropriate measurement with alligator clips or similar clamps.

Between these two assemblies, an optional PTFE retainer containing a 20 mm hole may be used for measuring coin cell samples. A set of copper discs with attached lead wires are used to create good thermal contact with the Peltier assemblies as well as provide connections for conductivity measurement, or to apply a stimulus to the sample. First, the retainer and bottom disc are positioned onto the bottom Peltier assembly. Next, the coin cell sample is dropped into the retainer, and finally the top disc is placed atop the coin cell, and the top Peltier assembly is lowered to make contact. The retainer is capable of accepting any 20 mm diameter coin cell (CR2032, CR2016, etc.) but is capable of accommodating smaller sizes as well.

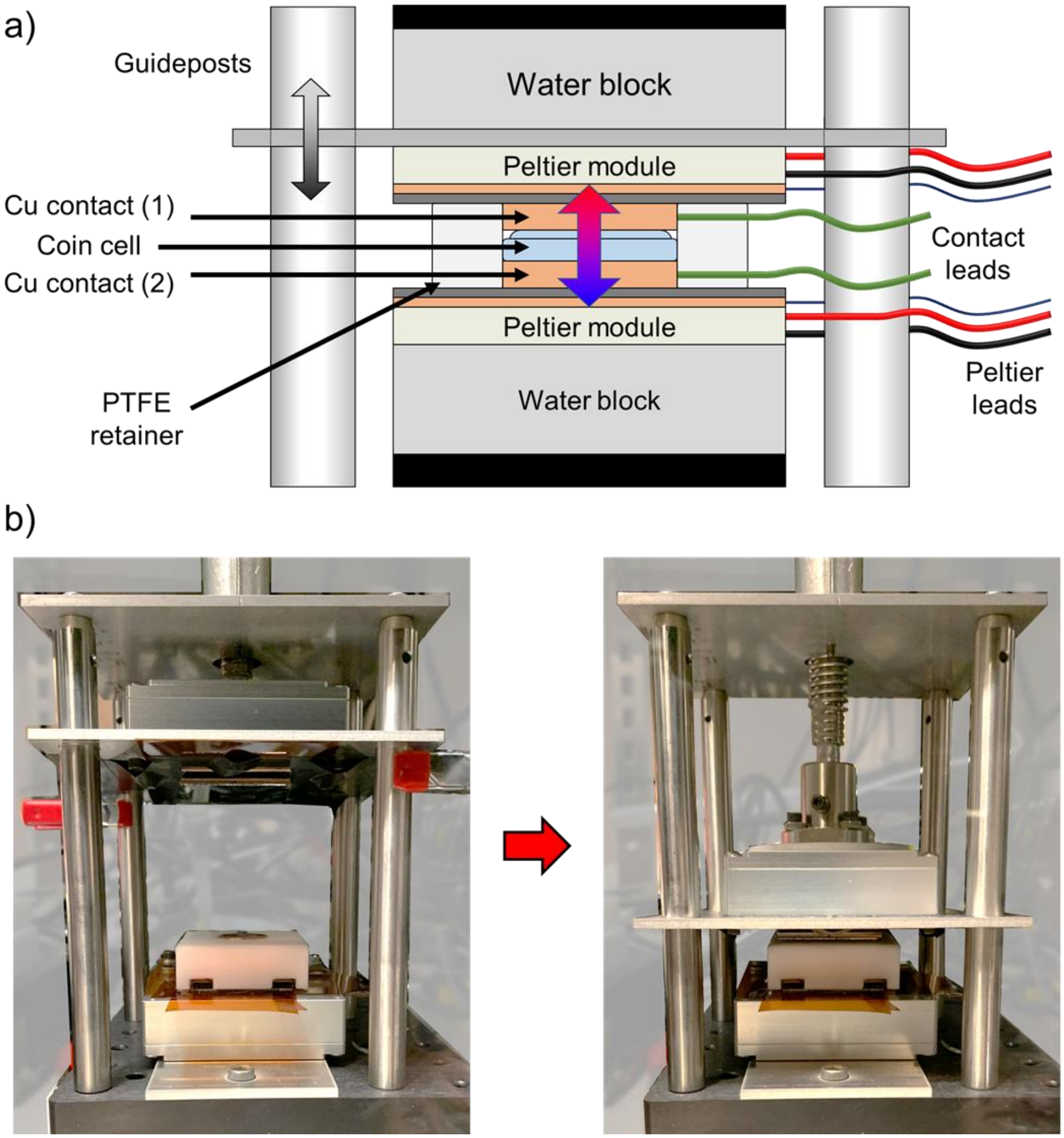

Figure 3.7. Assembly and operation of through-plane apparatus. a) Schematic for assembly of two-Peltier system with optional coin cell retainer. b) Application of pressure via screw clamp.

Chapter 4

Structure-Transport Properties Governing the Interplay in Humidity-Dependent Mixed Ionic and Electronic Conduction of Conjugated Polyelectrolytes

Abstract: Polymeric mixed ionic-electronic conductors (MIECs) are of broad interest in the field of energy storage and conversion, opto-electronics, and bioelectronics. A class of polymeric MIECs are conjugated polyelectrolytes (CPEs), which possess a π-conjugated backbone imparting electronic transport characteristics along with side chains comprised of a pendant ionic group to allow for ionic transport. Here, our study focuses on the humidity-dependent structure-transport properties of poly[3-(potassium-*n*-alkanoate) thiophene-2,5-diyl] (P3K*n*T) CPEs with varied side-chain lengths of n = 4, 5, 6, and 7. UV-Vis spectroscopy along with electronic paramagnetic resonance (EPR) spectros-copy reveal the infiltration of water leads to a hydrated, self-doped state that allows for electronic transport. The resulting humidity-dependent ionic conductivity (σ_i) of the thin films shows a monotonic increase with relative humidity (RH) while electronic conductivity (σ_e) follows a non-monotonic profile. The values of σ_e continue to rise with increasing RH reaching a local maximum after which σ_e begins to decrease. P3K*n*Ts with higher n values demonstrate greater resiliency to increasing RH before suffering decrease in σ_e. This drop in σ_e is attributed to two factors. First, disruption of the locally-ordered π-stacked domains observed through in-situ humidity-dependent grazing incidence wide angle X-ray scattering (GIWAXS) experiments can account for some of the decrease in σ_e. A second and more dominant factor is attributed to the swelling of the amorphous domains where electronic transport pathways connecting ordered domains are impeded. P3K7T is most resilient to swelling (based on ellipsometry and water uptake measurements) where sufficient hydration allows for high σ_i (1.0 × 10-1 S/cm at 95% RH) while not substantially disrupting σ_e (1.7 × 10-2 S/cm at 85% RH and 8.0

× 10-3 S/cm at 95% RH). Overall, our study highlights the complexity of balancing electronic and ionic transport in hydrated CPEs.

4.1 Introduction

Materials capable of conducting both electronic and ionic charge carriers are referred to as mixed ionic-electronic conductors (MIECs), or more simply, mixed conductors. These materials show great promise in a variety of applications, including batteries and supercapacitors, optoelectronics, bioelectronics, and electrochromic devices.[1–4] MIECs come in many forms, in both homogeneous and heterogeneous materials, which include metals, covalent inorganics such as oxides, perovskites, and ceramics, composites, and organic small molecules and polymers. Polymeric MIECs garner particular interest owed to their physical properties and synthetic tunability, enabling use in lighter, more conformable electronics. For example, the ability to transport electronic and ionic charge carriers makes polymeric MIECs valuable multifunctional binder materials in battery electrodes.[5] Polymeric materials have an inherently low thermal conductivity, making polymeric MIECs attractive candidates for electrochemical thermoelectric devices.[6,7] Additionally, their soft, flexible morphology imparts heightened biocompatibility, making them uniquely ideal for bioelectronics, such as organic electrochemical transistors (OECTs) for biosensors and neural interfaces.[8,9]

A subset of polymeric MIECs are conjugated polyelectrolytes (CPEs), polymers containing both ionically-charged functional side chains, capable of associating with free ions of opposing charge, as well as a conjugated backbone capable of conducting electronic charge carriers (electrons or holes).[10–12] Wudl and co-workers synthesized and characterized polythiophenes with anionic (*e.g.*, sulfonate) terminated side chains, now recognized as the first CPEs.[13] Overall, the library of CPEs is diverse, consisting of both *n*- and *p*-type conjugated backbones, as well as cationic, anionic, and zwitterionic functional groups.[10,12,14] More advanced CPEs are a current subject of interest, an example being "donor-acceptor" polymers, in which electron-donating and accepting moieties alternate along the backbone, which provides better control of the electronic and optical band gap and increased electronic conductivity.[15] These CPEs have been designed for interfacial layer materials in optoelectronic devices such as organic light-emitting diodes (OLEDs) and organic photovoltaics (OPV) cells. Additionally, the polar ionic character of CPEs makes them soluble in water and other polar solvents, allowing for increased processing capabilities in environmentally-friendly solvents.[13]

CPEs and conjugated polymers in general are formally semiconductors and thus are electronic insulators in their pristine form. Doping either chemically or electrochemically is the common route of enabling electronic conduction. In the case of chemical *p*-doping, a small molecule dopant anion balances the hole charge carrier (polaron) on the polymer backbone. Foundational work by Wudl and co-workers on CPEs introduced the concept of so-called "self-doping."[16] In this scenario, self-doping is derived from the fact that the anionic side chains fixed along the backbone serve to balance the hole charge carriers. However, it is important to clarify that self-doping does not necessarily mean CPEs are intrinsically conductive simply from the presence of ionized side chains. An external driving force is still needed to generate electronic carriers either electrochemically or chemically. A particularly interesting aspect of these materials, the electronic transport in CPEs can be modulated through the presence of water.[16–18] In self-doped CPEs, liberation of a free cation allows the covalently-bound anion to stabilize the formation of a polaronic hole charge carrier along the polymer backbone. As the free cation's ability to dissociate from the side chain is requisite for this to occur, the presence of water or other sufficiently polar solvent is a critical component of the self-doping mechanism. This phenomenon has been observed in the earliest polythiophene-based CPEs[16] to most recently by Cao et al. in which a pendant sulfonate group was shown to stabilize polaron formation in the poly[2,6-(4,4-bis-potassium butanylsulfonate-4*H*-cyclopenta-[2,1-*b*;3,4-*b′*]-dithiophene)-*alt*-4,7-(2,1,3-benzothiadiazole)] (PCPDTBT-SO_3K) donor-acceptor polymer.[19] The presence of water was demonstrated necessary for the self-doping process, and the material de-doped by removing water via thermal annealing.

It is a well-accepted fact that the morphology of conjugated polymers has a large impact on their charge transfer behavior.[20,21] In general, it is believed that electronic transport is optimized in the presence of sufficient chain aggregation with π-stacking (ordered domains) and sufficient inter-aggregate tie-chains spanning the amorphous domain. In contrast, amorphous polymers are favorable for ionic conduction. A random, more diffuse polymer structure allows for physical passage of ionic species more readily than dense ordered arrangements, a concept well-explored in systems such as Nafion for fuel cells[22], and poly(ethylene oxide) (PEO) for lithium ion batteries[23].

Understanding the complex role of morphology in permitting efficient mixed ionic and electronic transport in conjugated polymers remains a challenging task[24]. Many recent efforts have investigated ion transport in conjugated polymers bearing oligo(ethylene glycol) side chains, examining the impact of specific side-chain chemistry and ion selection, with a large focus on application to OECTs.[25–29] Despite these efforts, the mechanisms by which ion conduction is mediated are still less rigorously studied than their electronic counterparts. In addition, the operation of many mixed conduction-based devices commonly occurs in an aqueous media where water and ions inevitably infiltrate and impact the device performance.[27,29–31]

Recent efforts have demonstrated the impact of hydration on mixed conducting systems via control of local humidity on thin film samples. Wang et al. compared derivatives of PEDOT with varying ionic groups under humidified conditions, revealing RH-dependent mixed conductivity and thermoelectric effect.[32] R. Merkle et al. demonstrated the ability to selectively tune ionic conductivity (σ_i) and electronic conductivity (σ_e) of a polythiophene-based anionic sulfonate CPE by modulating electronic conduction with molecular dopants and ionic conduction by varying RH.[17] More recently, M. Wieland et al. further investigated this phenomenon by coupling a study of water uptake in this system to the changes in conductivity, drawing comparisons to well-characterized PEDOT:PSS-Na dual-conducting and Nafion ion-conducting systems, proposing a commonality in their morphologies, with a separation of hydrophilic and hydrophobic phases, with each conducting electronic and ionic charge carriers, respectively.[33]

While the response of mixed ionic and electronic conduction characteristics of CPEs to local environment (e.g., humidity) has been detailed in studies such as those previously discussed, a more in-depth structure-property analysis of CPEs under these conditions remains the topic of ongoing investigation. In this work we report on the impact of humidity on structure and mixed conductivity for a series of conjugated polyelectrolytes poly[3-(potassium-*n*-alkanoate) thiophene-2,5-diyl] (P3K*n*T) where n = 4, 5, 6, and 7 (**Figure 4.1**). UV-Vis spectroscopy and EPR spectroscopy reveal water infiltration leads to hydrated, self-doped thin films critical to enabling electronic conduction. Additionally, based on humidity-dependent ellipsometry and dynamic vapor sorption (DVS), the extent of the water uptake and swelling as a function of RH varies across the four P3K*n*T derivatives. In-situ RH-dependent grazing incidence wide angle X-ray scattering (GIWAXS) indicate that the locally ordered domains are partially disrupted from the infiltration of water. Based on electrochemical impedance spectroscopy (EIS) measurements, σ_i is found to monotonically increase with RH whereas σ_e follows a non-monotonic profile where σ_e increases until dropping at high RH. In addition to the disruption of locally ordered π-stacked domains, the decrease in σ_e is largely attributed to the swelling of amorphous domains where electronic transport pathways are impeded.

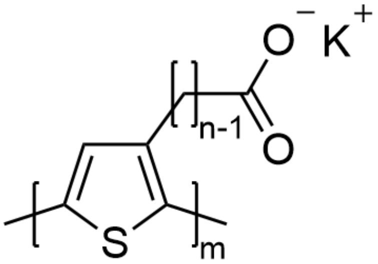

Figure 4.3. Chemical structure for the P3K*n*T polymer family. Polymer lot analysis can be found in the **Materials** section.

4.2 Results and Discussion

4.2.1 UV-Vis Absorption Reveal π-Stacked Aggregation and Electronic Carrier Generation.

UV-Vis spectra of the polymer solutions and thin films reveal absorption features characteristic of both π-stacked aggregates and amorphous bands (**Figure 4.2**). Spectra do not exhibit a dramatic red shift from solution to solid state, indicating a high degree of aggregation already present in solution. A small red shift from solution to solid state is more present in shorter side-chain species, and diminishes with increasing *n*. This trend suggests that longer alkyl side chains contribute to a higher nonpolar character, resulting in a higher degree of aggregation in solution. The use of a Spano model fit identifies individual contributions of the ordered and amorphous domains of the polymers (**Figure 4.9**). The large absorption feature at lower energy peaking at ~2.3 to ~2.4 eV corresponds to the ordered aggregates in the sample, with deconvoluted peaks associated with the 0-0, 0-1, and 0-2 vibronic transitions of π-stacked aggregates shown. The absorption feature peaking at ~2.7-2.8 eV corresponds to disordered (amorphous) fraction of polymer chains. By visual inspection, and through deconvoluting the π-stacking peaks, we observe a low A_{0-0}/A_{0-1} ratio for all P3K*n*T species. This is indicative of the formation of H-aggregates, in which interchain π-π excitonic coupling dominates. These characteristics appear to be largely preserved from solution to solid state, supports the notion that local ordering is largely preserved as π-stacked aggregates in solution coalesce to form a solid film.

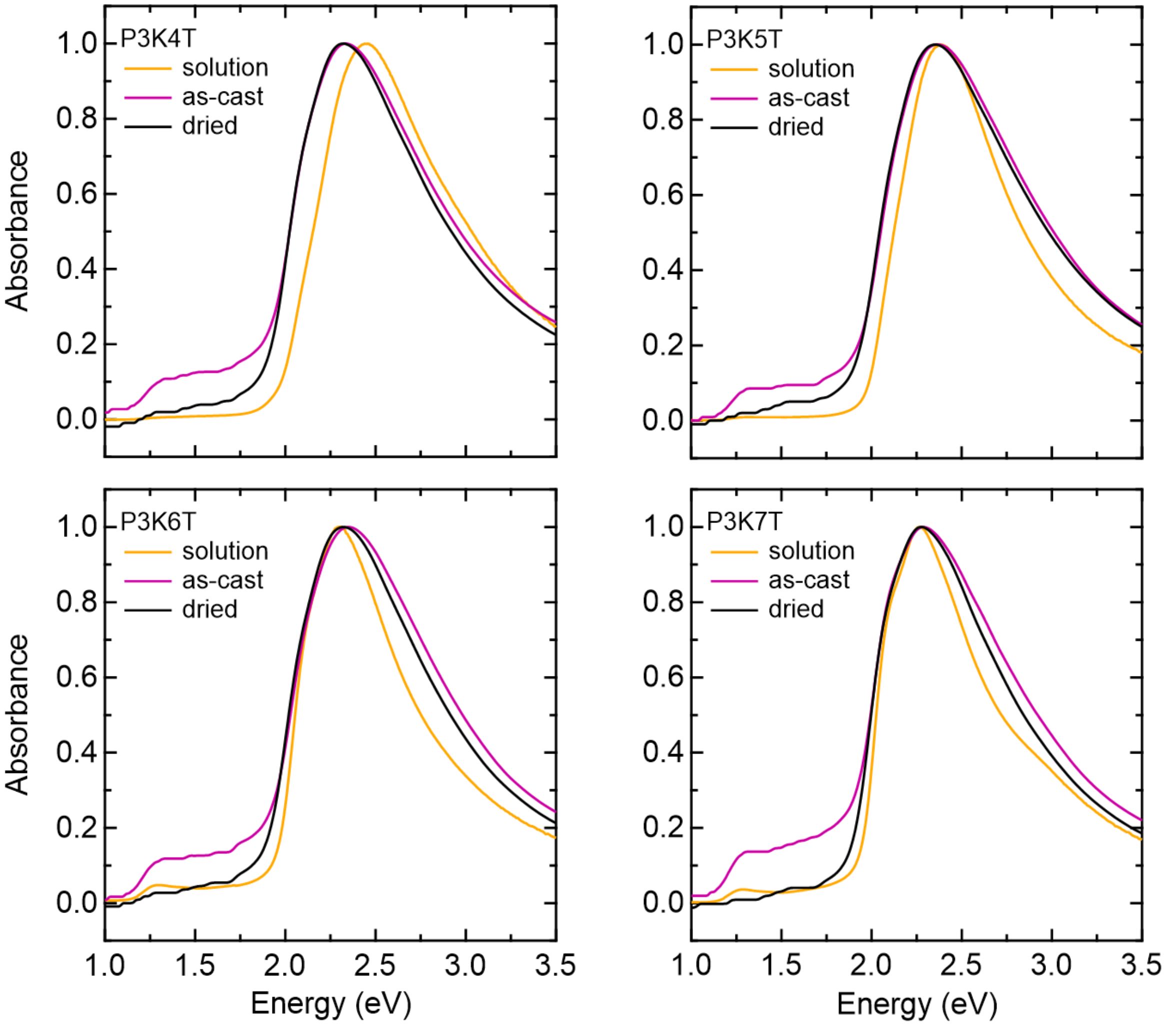

Figure 4.4. UV-Vis of P3K*n*T solutions (4 mg/mL in DI water) and P3K*n*T thin films as-cast and after heating (at 60 °C for 24 h in an argon glovebox). All curves are normalized based on their peak absorbance.

Extracted values from the Spano fit for thin film samples can be found in **Table 4.1**. The polymer aggregate fraction is roughly 9% less in as-cast films compared to sufficiently dried samples, suggesting the presence of water plays a role in disrupting the ordered domains of the polymer thin film.

In the lower energy (1-2 eV) regime, absorption features indicate a sub-band gap transition characteristic of the formation of polarons (hole charge carriers). This feature is most present in the as-cast condition where more residual water remains. After the thin films are heated at 60 °C overnight in argon to remove water, the intensity of the polaronic absorption feature decreases. This feature is also visible in the solution state, being more apparent in species with a longer side chain of greater *n*. The formation of the polaronic hole charge in hydrated thin films arises from the self-doping process of conjugated polyelectrolytes described in the introduction. Here, the self-doping process arises from water molecules dissociating and solvating K^+ ions from the alkanoate side chains, and in turn allowing the negatively charged side chain to stabilize hole charge formation on the backbone brought about by protonation from the water.[19]

4.2.2 EPR Spectroscopy Reveals Spin Concentration Increases with Humidity.

Electron paramagnetic resonance (EPR) spectroscopy experiments were performed to further verify the formation of polaronic charge carriers (unpaired spins) from the presence of water in the thin films. Experiments were performed on thin films (ca. 20 nm) cast on quartz substrates. These thins films were equilibrated under three different conditions, as-cast, dried via heating as defined previously, as well as rehydrated to 35% RH to best simulate approximate ambient conditions resulting from spin-coating. Continuous wave (CW) X-band EPR spectra are shown in **Figure 4.3**. An increase in signal from the dried state to either hydrated state is observed for all four P3K*n*T derivatives. The higher intensity arises from the presence of unpaired electrons from the polaronic charge formed by the presence of water facilitating the self-doping mechanism.

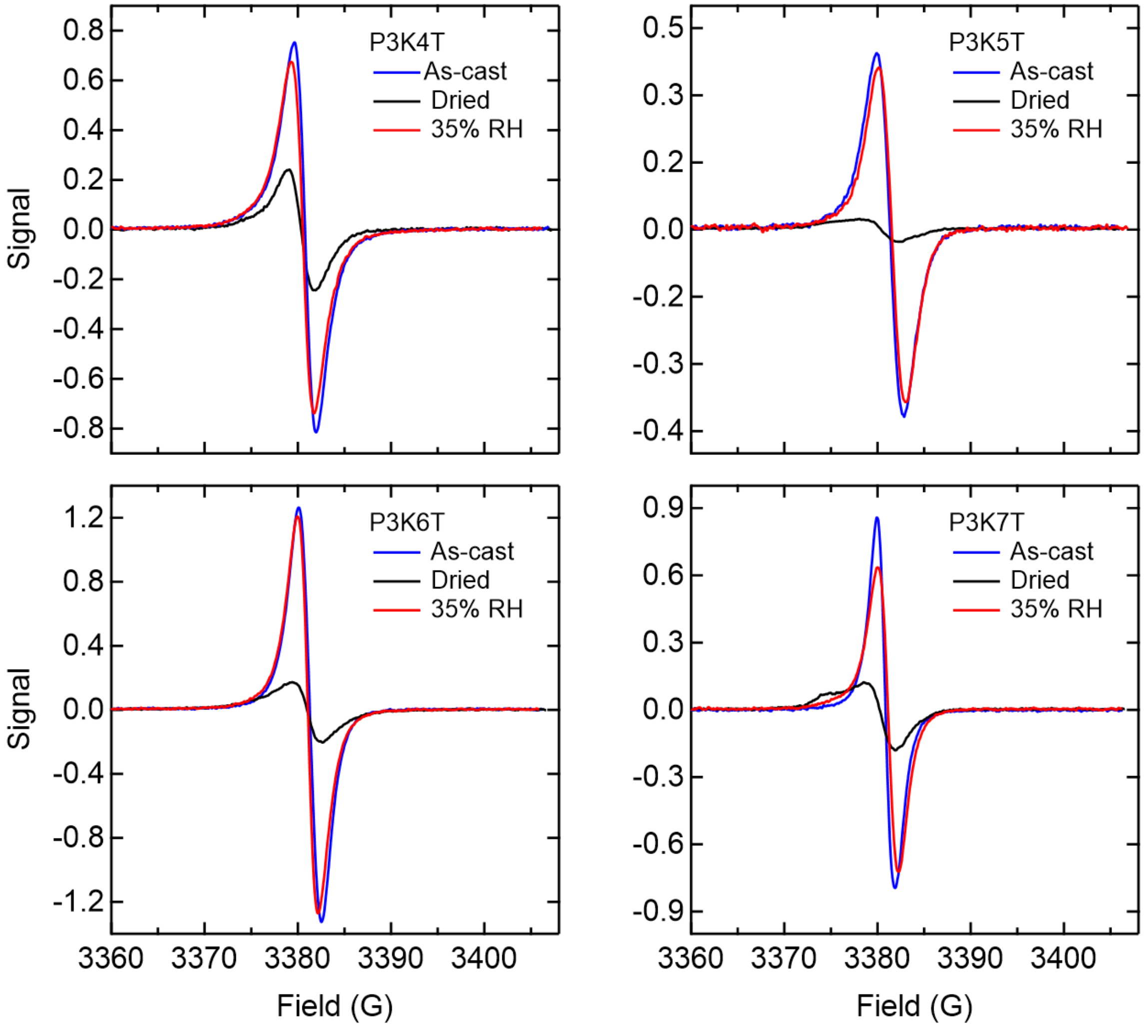

Figure 4.3. Continuous wave (CW) X-band EPR spectra for as-cast, dried, and re-humidified P3K*n*T films cast on quartz substrates.

To approximate the extent of self-doping as a function of RH, a more granular quantification of the spin concentration (N) was performed for two representative derivatives: P3K4T and P3K6T. Here, EPR sample tubes were coated internally with the polymer, dried under vacuum at 60 °C overnight, and then equilibrated over a range of RH from 0 to 95%. For these samples, the EPR signal increases as a function of RH (**Figure 4.10)**. The value of N at each RH was calculated through double integration of the EPR spectrum, normalized by the mass of the polymer. As shown in **Figure 4.10b**, N increases monotonically from ca. 1×10^{18} spins/g at 0% RH to ca. 3×10^{19} spins/g at 95% RH for both polymers. While small variations in N are observed between P3K4T and P3K6T, they share a common trend, wherein N is within a factor of 2. As a frame of reference, common values for N are on the order of $10^{20} – 10^{21}$ spins/g for polythiophene derivatives when extrinsically doped by a strong oxidant.[34] Therefore, the doping level (or polaronic charge carrier concentration) in P3K*n*Ts is in the lower to moderate levels across the RH range.

4.2.3 DVS and Ellipsometry Show Impact of Water Uptake and Swelling with Increasing Humidity.

Dynamic vapor sorption (DVS) was used to measure the water uptake (WU) level in as-received P3K*n*T polymer powders at different RH levels. The WU level increases at a relatively constant rate up to RH = 75% at approximately the same rate for the four P3K*n*T derivatives (**Figure 4.4a**). At RH = 75%, the WU level is between 25-30 wt %. Beyond this point, the WU level increases rapidly and is more substantial for P3K4T and P3K6T compared to P3K5T and P3K7T. At 95% RH, the WU level is 80.8% for P3K4T, 50.9% for P3K5T, 84.1% for P3K6T, and 53.3% for P3K7T. This difference appears to correlate with the size of the polymer chains, where the molecular weight (M_W) of P3K4T and P3K6T are significantly smaller than the other two derivatives (see **Materials** section). The hydration level (λ) is also calculated based on the WU level for each P3K*n*T derivative as a function of RH to provide insight on the number of water molecules per monomer (**Figure 4.11**). At RH = 25 %, λ is about <1 for all four P3K*n*T derivatives. At RH = 95%, λ is about 9 for P3K4T, 6 for P3K5T, 11 for P3K6T, and 7 for P3K7T.

To account for the WU on thin film thickness, humidity-dependent ellipsometry measurements were performed for each P3K*n*T derivative. The calculated change in the thin film thickness is shown in **Figure 4b**.

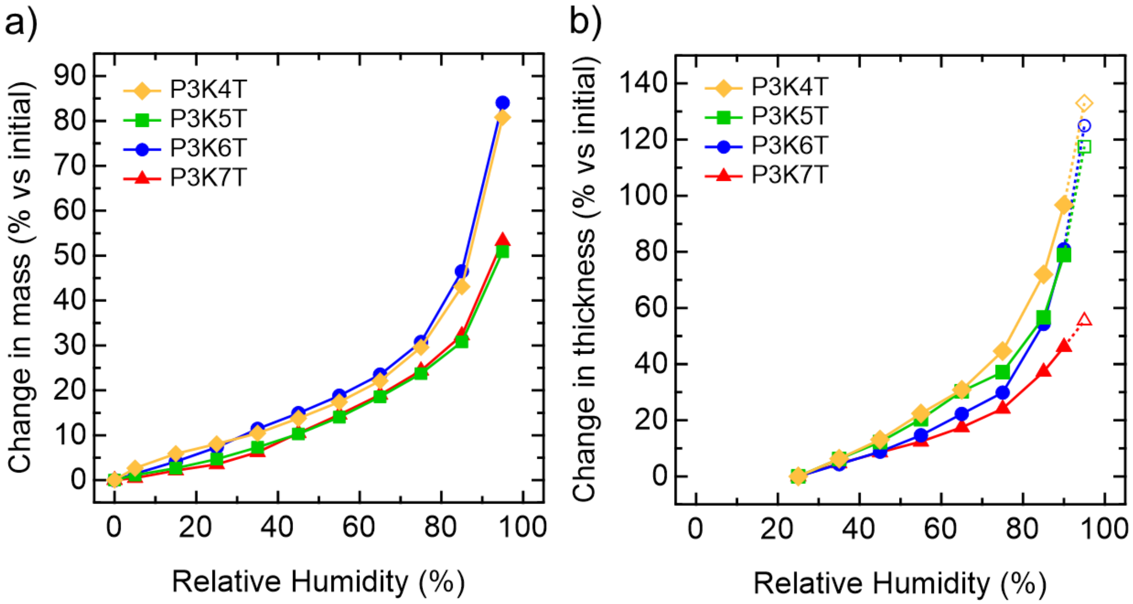

Figure 4.4. Responses of P3K*n*T to water sorption at increasing RH. a) DVS curves for P3K*n*T bulk powders. b) Change in thin film thickness as measured by ellipsometry. Values for change in thickness at 95% RH are extrapolated from best fit curves from 25% to 90% RH.

Overall, the thin film thickness change follows a similar trend to the DVS measurement where a rapid rise beyond some critical point around 75% RH can be observed. In this processed thin film configuration (consistent to subsequent X-ray scattering and conductivity measurements), a new trend can be observed when comparing the different P3K*n*Ts. An increasing *n* value results in a smaller increase thin film thickness at the same RH. At RH = 90%, the change in thin film thickness is 96.7% for P3K4T, 78.9% for P3K5T, 80.9% for P3K6T, and 46.1% for P3K7T. Overall, P3K7T thin films swells substantially less with water compared to the other P3K*n*T derivatives. Processing the polymers into thin films appears to ablate the impact of polymer

M_W on uptake, and enhance the role of polymer microstructure, specifically the impact of polymer side-chain length.

4.2.4 Underlying Local Ordering of Dry and Humidified P3K*n*T Thin Films.

It is well understood that the underlying semicrystalline microstructure comprising of nanoscale crystalline domains interconnected through the amorphous regions controls the extent of electronic charge mobility and conductivity. Here, grazing incidence wide angle X-ray scattering (GIWAXS) was specifically used to characterize the molecular order and packing of the crystalline domains for the thin films under dry and humidified conditions. Representative 2D scattering images of dry thin films are shown in **Figure 4.5a**. Overall, all the P3K*n*T thin films exhibit similar scattering patterns that are indicative of a packing arrangement comprising π-stacked polymer backbones and interpolymer spacing along the side-chain direction. Such a molecular packing arrangement has been seen in CPEs based on donor/acceptor backbone chemistries.[7] The dehydrated 1D scattering profiles from radial integration of the 2D images are shown in **Figure 4.5b**. The most intense peak at lower q (e.g., 8.54 nm^{-1} for P3K4T) is attributed to interpolymer side-chain spacing whereas the peak at higher q (*e.g.*, 17.78 nm^{-1} for P34KT) corresponds to π-stacking. The lower q feature shows similarities in shape and position to other CPEs bearing side chains with covalently-bound anionic groups.[7] Additionally, the spacing attributed to this side-chain feature (d_{sc}) monotonically increases with side-chain aliphatic carbon number in a linear relation, with d_{sc} increasing from 0.745 nm for $n = 4$ to 1.15 nm for $n = 7$ (**Figure 4.5c**). In comparison, the π-stacking distance ($d_{\pi-\pi}$) monotonically increases similarly to d_{sc}, but to a much lower degree, with $d_{\pi-\pi}$ increasing from 0.353 for $n = 4$ to 0.370 nm for $n = 7$. These values are on the same order as other polythiophenes, including P3HT.

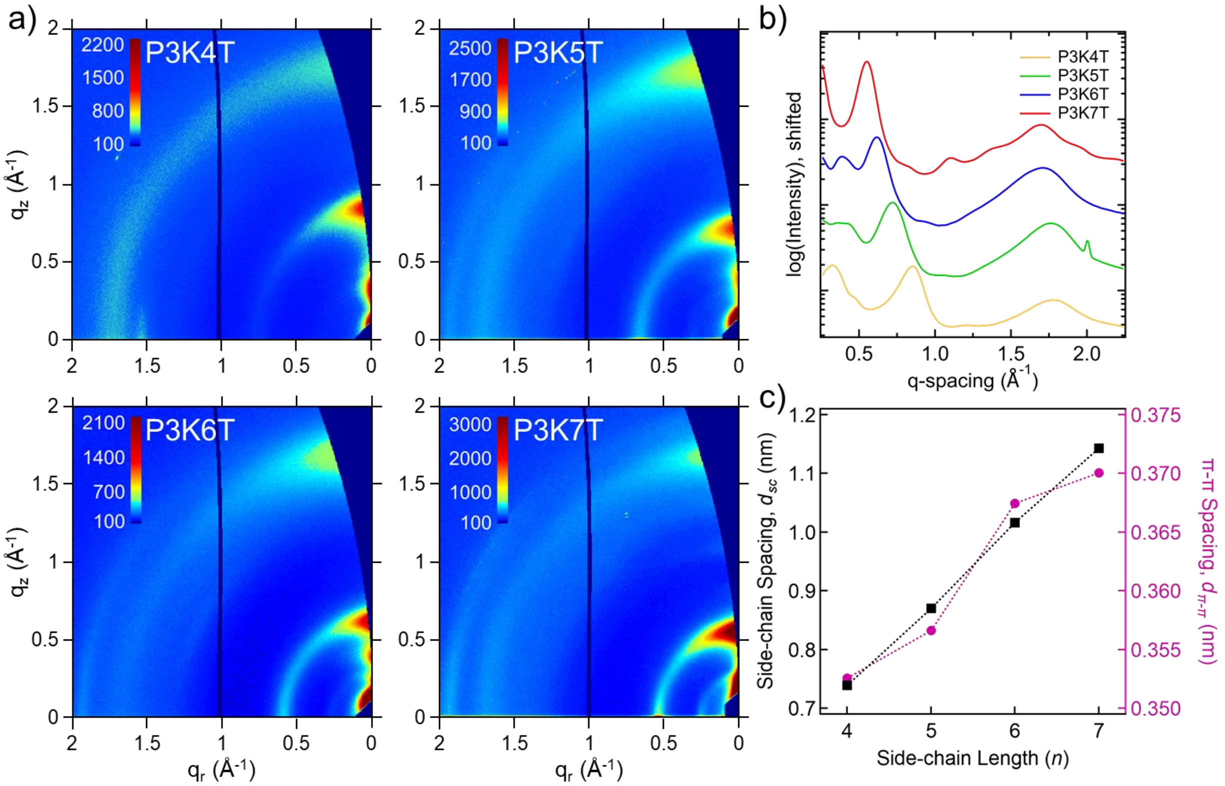

Figure 4.5. GIWAXS analysis of "dry" P3K*n*T thin films. a) Example 2D images for thin films in sufficiently dehydrated condition. b) Integrated 10° linecuts taken 80-90° from horizontal and c) dry feature spacing peak values vs *n*.

4.2.5 Humidity-Dependent GIWAXS.

To study the influence of water on the molecular ordering and packing of P3K*n*Ts, RH-dependent GIWAXS experiments were performed using a custom-built RH GIWAXS chamber as shown on **Figure 4.6a** (more experimental details can be found in the **Materials and Methods** section and a complete schematic can be found in **Figure 4.12**). The constraints of the experimental setup limited the RH range from 20% to 75%. Representative GIWAXS detector images of P3K*n*T films at different RH levels can be found in **Figure 4.13a** and the corresponding radial linecuts in **Figure 4.13b**. For all P3K*n*T thin films, d_{sc} increases with increasing RH (**Figure 4.6b**), with a calculated change in d_{sc} between 15-25% at high RH (**Figure 4.13c**). This expansion in d_{sc}

indicates the ionic end groups of the side chains form hydrophilic regions within the ordered domain that preferentially absorbs water. Additionally, $d_{\pi-\pi}$ spacing is observed to increase 3.5 – 5% at high RH, although the change is relatively smaller compared to that of the side-chain feature expansion (**Figure 4.6c**). We posit the increase in $d_{\pi-\pi}$ arises from distortion of the conjugated backbone driven by the infiltration of the water in the side-chain domains. This distortion effect increasing $d_{\pi-\pi}$ outweighs any contraction in $d_{\pi-\pi}$ that should arise from the formation of polaronic charge along the conjugated backbone.[35] Lastly, a relative degree of crystallization (rDoC) calculation was performed on the side-chain feature of the 2D GIWAXS images (**Figure 4.14**) as function of RH to approximate the impact of water infiltration on crystallinity. Though overall intensity and fluctuations vary from sample to sample, a common trend is observed where a linear decrease in overall rDoC is observed with increasing RH.

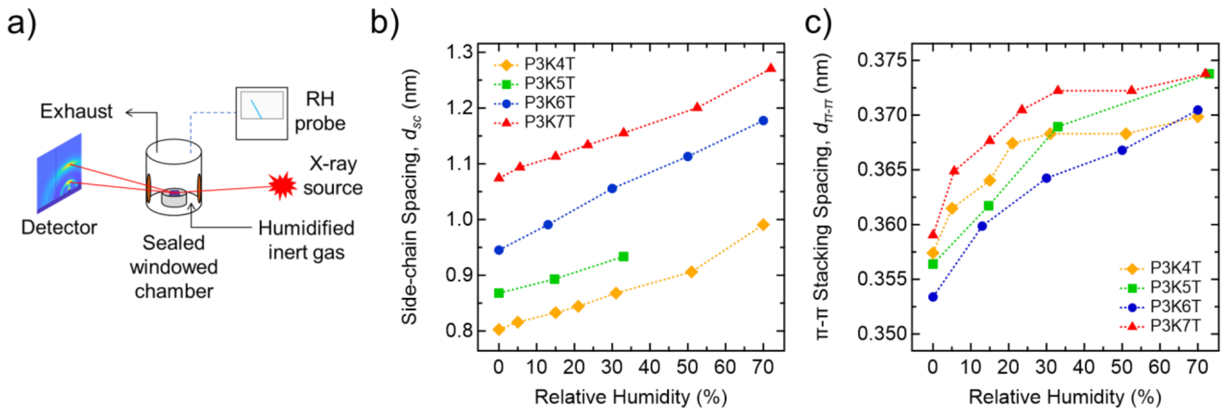

Figure 4.6. In-situ RH-dependent GIWAXS of P3K*n*T thin films. a) Schematic for in-situ RH-dependent GIWAXS setup. b) Spacing for the polymer side-chain GIWAXS feature vs RH and c) spacing for the π-stacking GIWAXS feature vs RH.

4.2.6 Humidity-Dependent Electronic and Ionic Conductivities.

To determine the influence of water on the charge transport characteristics of P3K*n*T thin films, the frequency dependence of electrochemical impedance spectroscopy (EIS) is leveraged to decouple σ_i and σ_e values as a function of RH (25% to 95%). Thin films were deposited on custom-microfabricated interdigitated electrodes (IDEs) to achieve sufficient signal to noise ratio across the wide-ranging impedance of the films. Note that in the dehydrated conditions inside a dry argon-filled glovebox, the P3K*n*T thin films are highly resistive (total conductivity less than 10^{-5} S/cm). Measured conductivity arises from residual water in the film facilitating electronic charge carriers, which is consistent with results of EPR measurements (**Figure 4.15**).

Representative Nyquist plots over three different RH levels of 25%, 45% and 65% of P3K6T thin film are shown in **Figure 4.7**. The summary of all Nyquist plots can be found in **Figure 4.16**. At all RH studied, the Nyquist plots consist of two semicircles, which is a signature of mixed ion and electron conduction.[36,37] To quantify σ_i and σ_e, EIS data were fit to a simplified equivalent circuit describing parallel, simultaneous conduction of electronic and ionic charge carriers in the presence of ion-blocking electrodes, as seen in the inset of **Figure 4.7a**.[38] The radius of the first semicircle on the left reflects the combined contribution of ionic resistance (R_i) and electronic resistance (R_e) whereas the total radius of the two semicircles represent the electronic resistance R_e.[36] It is observed that as RH is increased, the radius of the first semicircle significantly reduces. However, the combined radius of both semicircles (the rightmost point) only reduces to a certain point with increasing RH, after which point it begins to expand. These two trends indicate that the ionic contribution to resistance in the system is decreasing continually with increasing RH, while the electronic resistance is initially decreasing, but then increasing after a certain RH.

Figure 4.7c shows σ_i of each P3K*n*T thin film as a function of RH where σ_i follows a monotonic increase across several orders of magnitude. For all P3K*n*T derivatives, the RH-dependent σ_i trend is qualitatively similar. Overall, P3K7T exhibits the highest σ_i across the full range of RH compared to other P3K*n*T derivatives. At the lowest RH of 25%, σ_i is 7.5×10^{-5}, 5.6

$\times 10^{-5}$, 6.5×10^{-5}, and 1.5×10^{-4} S/cm for P3K4T, P3K5T, P3K6T, and P3K7T, respectively. At highest RH of 95%, σ_i increases by nearly four orders of magnitude, where σ_i is 2.6×10^{-2}, 4.8×10^{-2}, 5.5×10^{-2}, and 1.0×10^{-1} S/cm for P3K4T, P3K5T, P3K6T, and P3K7T, respectively.

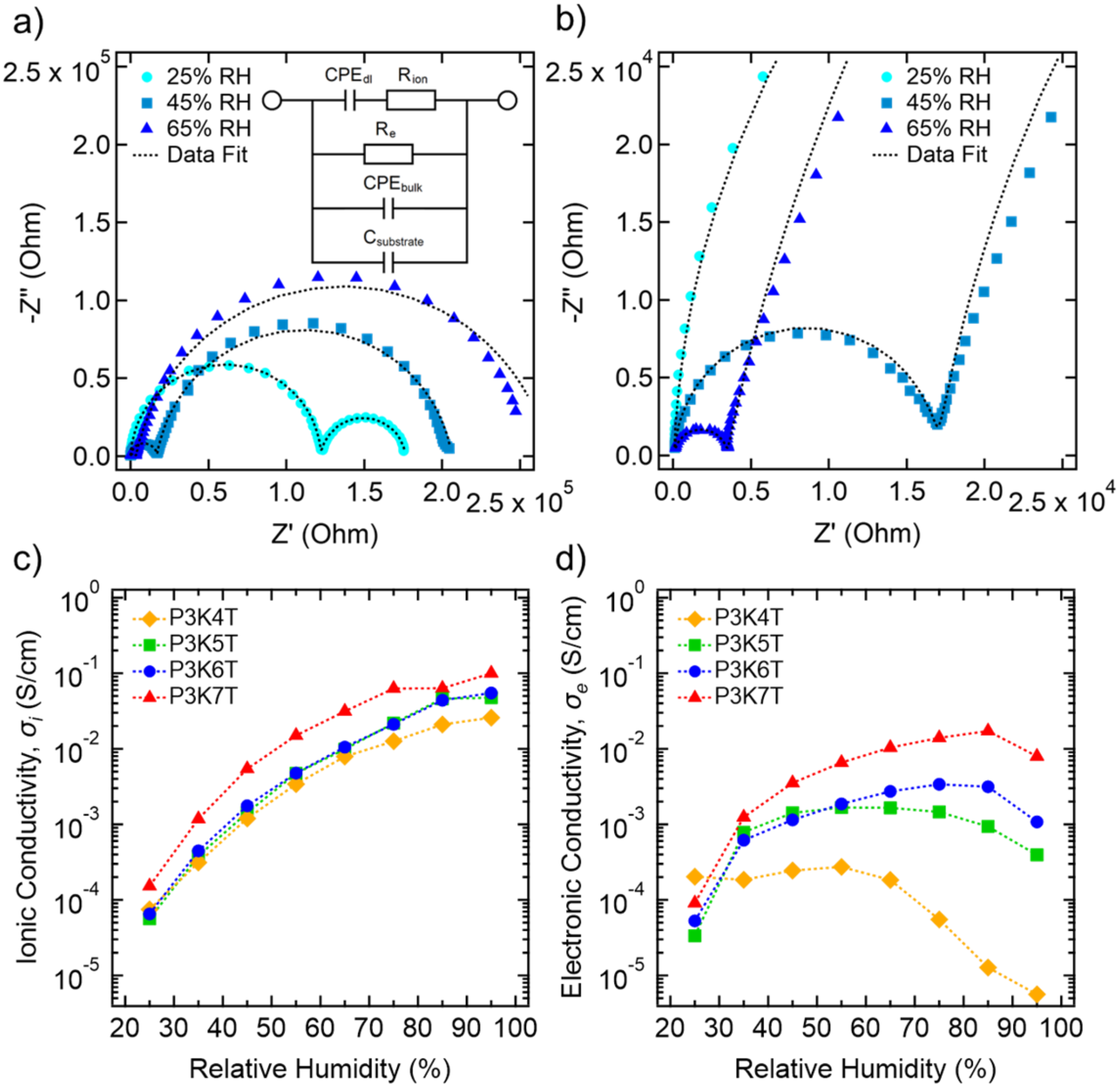

Figure 4.7. EIS analysis of P3K*n*T thin films on interdigitated electrodes. a) Example Nyquist plots of P3K6T thin films on IDEs at three RH conditions with equivalent circuit used to fit EIS data and b) expansion of the high frequency regime. c) σ_i and d) σ_e of P3K*n*T thin films as functions of RH.

These values σ_i are remarkably high, especially for P3K7T. For example, a benchmark material such as Nafion is reported to have a σ_i of ca. 10^{-1} S/cm at RH = 100%.[39] Other polyelectrolytes such as polystyrene sulfonic acid (PSSH) and polystyrene sodium sulfonate (PSSNa) are reported to have σ_i values ca. 1.0×10^{-3} S/cm and ca. 1.0×10^{-2} S/cm at RH = 100%, respectively.[40,41] Overall, the measured σ_i of the P3K*n*Ts are on the higher end of hydrated polyelectrolytes.

In contrast, σ_e shows a more complex behavior as a function of RH where σ_e follows a non-monotonic profile (**Figure 4.7d**). At RH of 25%, the σ_e of all P3K*n*Ts exceeds 10^{-5} S/cm. As RH rises, σ_e increases more than an order of magnitude where σ_e is approaching and exceeding 10^{-3} S/cm for all P3K*n*Ts except for P3K4T. Notably, a decrease in σ_e is seen as RH increases and varies depending on the P3K*n*T derivative. The RH value at which σ_e begins to drop increases and the extent of the drop decreases with increasing *n* value (P3K4T to P3K7T). For P3K4T, σ_e is comparable from RH of 25 % to 55 % but σ_e starts to continuously drop at RH = 65 % and beyond. At RH = 95 %, σ_e for P3K4T has decreased by over an order of magnitude to 5.6×10^{-6} S/cm. In contrast, σ_e for P3K7T continues to increase until reaching $\sigma_\mathrm{e} = 1.7 \times 10^{-2}$ S/cm at RH = 85%, after which σ_e decreases by a factor 2 (8×10^{-3} S/cm) at RH = 95%. Overall, as with σ_i, the values σ_e are comparatively highest for P3K7T.

4.2.7 Factors Influencing the Balance Between Ionic and Electronic Conduction.

The results above provide insight to the structure-transport properties governing the complex interplay between ionic and electronic conduction in P3K*n*T thin films. With respect to ionic conduction, the absorbed water forms solvation shells around the potassium ion enabling dissociation from the pendant anionic side chain to generate mobile ionic carriers (**Figure 4.8a**). As the hydration level increases with RH, more cations dissociate, and the additional water forms percolating channels facilitating ionic mobility of solvated potassium ions across macroscopic length scales. Ionic conduction can occur through both the amorphous and ordered domains.[26]

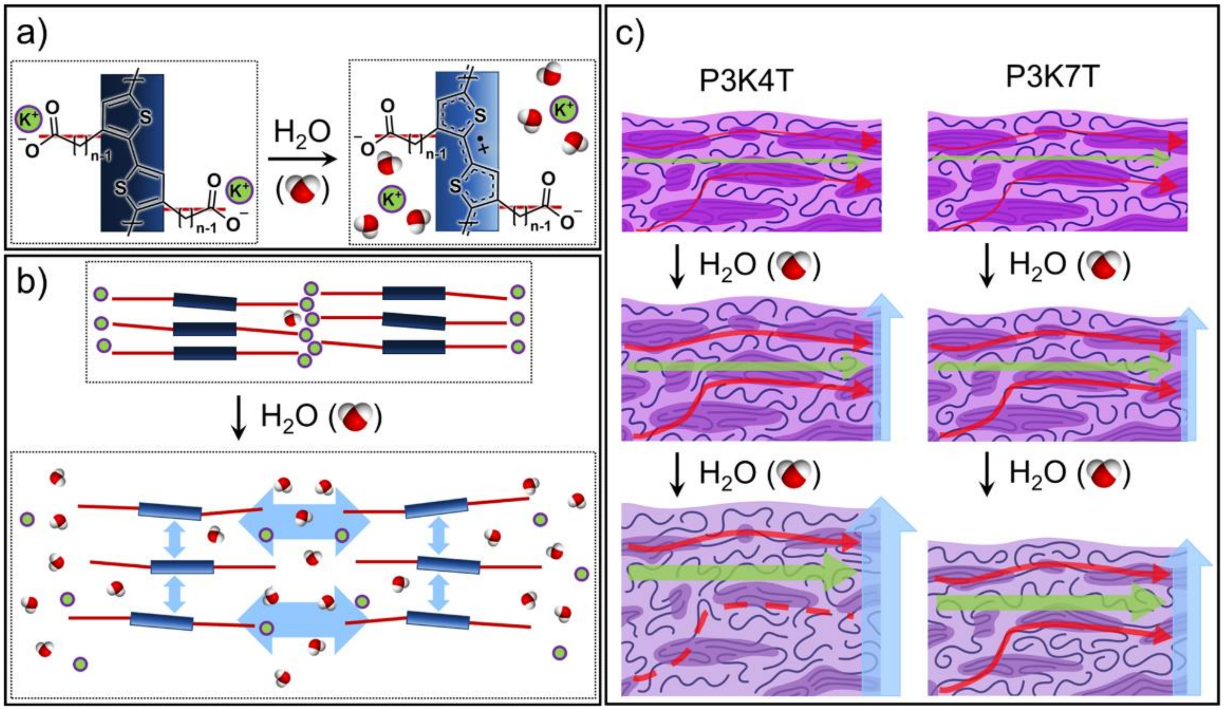

Figure 4.8. Schematic for influence of absorbed water on P3KnT thin film morphology and conductivity. a) Water solvates potassium ions, allowing the side-chain anion to stabilize backbone hole formation. b) Water infiltrates the ordered domains of P3KnT, increasing side-chain and π-stacking spacing. c) P3K7T swells less than P3K4T at similar RH values, and increased polymer M_w allows for greater retention of inter-aggregate tie chains, resulting in a smaller drop in σ_e, while σ_i increases monotonically with increasing water content.

While the relative contribution from each domain is not known, it's reasonable to assume the amorphous domains create the easiest path for ionic conduction. Moreover, the absorbed water will plasticize the polymer to further facilitate ionic conduction. As shown with DVS and humidity-dependent thickness measurements, WU varies with P3KnT derivatives where the swelling is highest for P3K4T and the lowest for P3K7T. Despite their lower swelling, P3K7T exhibits the highest ionic conduction across the full RH range. We posit the longer side chain of P3K7T would exhibit faster positional dependent segmental mobility along the side chain. Here, the pendant charged moiety is farther decoupled from the rigid backbone, which allows for more efficient ion transfer.

With respect to electronic conduction, the infiltration of water controls both electronic carrier concentration (n_e) and the electronic carrier mobility (μ_e), which in total impacts the extent of σ_e as function of RH. As noted earlier, the equilibration of thin films at different RH sets the n_e through the self-doping mechanism (**Figure 4.8a**). At lower RH (<35%), the increase in charge carrier concentration outweighs any disruption in the underlying hierarchical structure that may reduce μ_e. As RH increases, the increased WU starts to disrupt the local and long-range order, which would reduce μ_e. Here, the disruption in μ_e starts to have an outsized role in controlling σ_e compared to the increase in n_e. First, based on the humidity-dependent GIWAXS results, the small expansion in $d_{\pi-\pi}$ and the reduction in crystallinity would contribute to a reduction in $\mu_{e,}$ and thus σ_e (**Figure 4.8b,c**). Second, as the WU level increases in the thin film, the swelling in the amorphous domain diminishes the interconnectivity of the ordered domains, interrupting electronic conduction pathways and thus reducing μ_e. This disruption of the electronic conduction pathways is the dominant factor in reducing σ_e at elevated RH. The sum of these individual factors serves to explain the non-monotonic profile of σ_e as a function of RH.

By comparing P3K4T and P3K7T, one can the see most dramatic difference in WU and thin film thickness increase on σ_e. The higher WU of P3K4T leads to substantial swelling and thus the larger separation between ordered domains (**Figure 4.8c**). Note that P3K4T has the lowest M_W, and as a result would intrinsically exhibit poorer interconnectivity through inter-aggregate tie-chains. In total, the high level of swelling and lower M_W would have the greatest impact in impeding electronic conduction pathways for P3K4T. In contrast, P3K7T has the lowest level of swelling and thus less separation between ordered domains. Additionally, the higher M_W of P3K7T would allow for more intrinsic tie-chain interconnectivity, better preserving electronic conducting pathways across ordered and disordered (amorphous) domains.

4.3 Conclusions and Outlook

In this work, factors governing the extent of simultaneous electronic and ionic conduction as a function of relative humidity (RH) on a series of P3K*n*Ts were investigated through a combination of molecular spectroscopy, water uptake (WU) analysis, X-ray scattering, and electrochemical impedance spectroscopy. UV-Vis spectroscopy along with electronic paramagnetic resonance spectroscopy reveal the infiltration of water leads to hydrated, self-doped materials for all four P3K*n*Ts. This self-doping process in the presence of water is critical to generating electronic charge carriers, which increases as function of RH. Water vapor sorption and thickness measurements *via* humidity-dependent ellipsometry highlight that WU level varies across the four P3K*n*Ts. P3K4T exhibited highest WU whereas P3K7T exhibited the lowest WU throughout the full RH range. Moreover, at 90% RH, the thin film thickness (h) increased by nearly 100% for P3K4T whereas h only increased by 45% for P3K7T. To determine the effect of this WU on the local molecular order, the thin films were characterized through in-situ humidity-dependent grazing incidence wide angle X-ray scattering (GIWAXS). Importantly, all four P3K*n*Ts showed disruption in the local order where a monotonic expansion in the interpolymer side-chain spacing (d_{sc}) and π-stacking distance ($d_{\pi-\pi}$) were seen as a function of RH along with a decrease in crystallinity.

The resulting humidity-dependent ionic conductivity (σ_{i}) and electronic conductivity (σ_{e}) of the P3K*n*T thin films were determined through electrochemical impedance spectroscopy. σ_{i} shows a monotonic increase with RH. Overall, σ_{i} of P3K*n*Ts is quite high. At RH = 95%, P3K7T exhibited the highest σ_{i} of 1×10^{-1} S/cm compared to 2.6×10^{-2} S/cm for P3K4T. In contrast, the values σ_e exhibit a non-monotonic profile with RH where a drop in σ_e is seen at higher RH. For P3K4T, the $\sigma_e = 2.0 \times 10^{-4}$ S/cm at RH = 25% but drops to 5.6×10^{-6} S/cm at RH = 95%. On the other hand, for P3K7T, the $\sigma_e = 9.1 \times 10^{-5}$ S/cm at RH = 25% but continues to increase to 1.7×10^{-2} S/cm at RH = 85% until seeing a decrease to 8×10^{-3} S/cm at RH = 95%. By taking into consideration the WU and GIWAXS results, two factors are likely leading to the drop in σ_e at high RH. First, some of the decrease in σ_e as function of RH can be attributed to the increase in $d_{\pi-\pi}$. More significantly, a second factor lies in the interruption of electronic transport pathways between ordered domains, where water absorption leads to swelling in the amorphous regions of the film and erosion of the ordered domains themselves, especially at higher RH. P3K7T is demonstrated to swell the least, allowing sufficient hydration for very high σ_i while not substantially disrupting the pathways for electronic transport across ordered and disordered (amorphous) domains. In contrast, P3K4T demonstrates the highest WU and exhibits the most substantial drop in σ_e. Overall, our study highlights inherent challenges of balancing electronic and ionic transport in hydrated CPEs. Increasing the distance between the electronically- and ionically-conductive regions of the CPE demonstrates a positive effect on both conduction pathways, and higher polymer molecular weight plays a role in the retention of σ_e at RH values approaching 100%. These observations should be considered in the future synthetic design and materials processing of CPEs for applications in which absorption of water plays a critical role.

4.4 Materials and Methods

Materials. Poly[3-(potassium-n-alkanoate)thiophene-2,5-diyl] polymers were purchased from Rieke Metals, with n = 4 to 7[42]. Polymer lot analysis was obtained from manufacturer. P3K4T: M_w = 17-21K, RR = 89%, Đ = 2.2 (M_n = 7.7-9.5k). P3K5T: M_w = 47-59K, RR = 91%, Đ = 2.4 (M_n = 19.6-24.6k). P3K6T: M_w = 30-36K, RR = 88%, Đ = 1.8 (M_n = 16.7-20k). P3K7T: M_w = 39-53K, RR = 93%, Đ = 2.2 (M_n = 17.7-24.1k). Manufacturer claims full functionalization of alkanoate side-chain groups within analytical error. Milli-Q deionized/filtered water (18.2 MΩ·cm at 25 °C) was obtained in-house from an in-line filtration system. Anhydrous acetonitrile (>99.8%) was obtained from Sigma Aldrich and used as received. DSC traces for dried P3K*n*T powders and TGA traces for P3K*n*T powders equilibrated at ambient conditions can be found in **Figure 4.17**. ^{1}H NMR of all species was performed at 400 MHz in a cosolvent of 2:1 D_2O and acetonitrile-d3 (**Figure 4.18**). GPC analysis of P3K4T and P3K5T was performed in a cosolvent of 2:1 water and THF. The water contained 0.2 M NaNO3 as well as phosphate buffer necessary to achieve pH = 7 (**Figure 4.19**). P3K6T and P3K7T were unable to dissolve in any available cosolvent system to a sufficient degree to obtain acceptable eluent profiles.

Solution Preparation. P3K*n*T polymers were dissolved in Milli-Q water at 60 °C for a minimum of 12 hours. All solutions were prepared to a final concentration of 8 mg/mL. The solubility of different polymers varied based on polymer M_W. P3K4T and P3K6T dissolve readily, with stable solutions in concentrations exceeding 30 mg/mL. P3K5T and P3K7T, alternatively, take additional effort to dissolve, requiring prolonged heated stirring and/or cosolvents. Approximately 25% by volume acetonitrile was required to fully dissolve P3K7T. Acetonitrile was removed by heating the solution to 90 °C until the sample returned to the original mass of vial plus contents prior to acetonitrile addition.

Thin Film Casting. P3K*n*T thin films were produced via spin coating. For thin film UV-Vis measurements, 0.5 mm thick z-cut quartz substrates was purchased from University Wafer. Silicon wafer with native oxide (0.5 mm, University Wafer) was used for GIWAXS measurements. In-house-designed interdigitated electrodes (IDEs) consisted of gold electrode patterned on passivated silicon wafer were used for EIS measurements. The IDE pattern consisted of 160 electrode “teeth” with a length of 1 mm and 8 μm spacing between each tooth. IDEs were fabricated following methodology reported in Sharon et al.[43] All substrates were cleaned using a 3-step sonication procedure, starting with acetone, followed by isopropanol, and finally Milli-Q water, for 10-15 minutes each. Prior to spin coating, clean substrates were exposed to air plasma under partial vacuum for 10 minutes in order to increase surface hydroxylation and improve wettability. A two-step spin-coating procedure was used, with a first step of 1000 rpm for 30 seconds followed by 3000 rpm for 60 seconds. Samples were dried on a heating block in an argon glovebox at 60 °C overnight to sufficiently dehydrate films. The surface topographies of the thin film samples cast on Si wafers were characterized by a Cypher ES AFM (Asylum Research Oxford) with FS-1500AuD cantilever at room temperature in tapping mode. Images were analyzed using the Gwyddion software package (**Figure 4.20**).

UV-Vis Spectroscopy. UV-Vis measurements were performed using Shimadzu UV-3600 Plus UV-Vis-NIR Dual Beam and Agilent Cary 5000 UV-Vis-NIR spectrophotometers for thin film and solution measurements, respectively. Measurements were taken from a wavelength range of 250 to 3300 nm. Dry inert gas was flowed over the surface of dehydrated thin film samples during UV Vis measurements in order to minimize the absorption of moisture during the scan. 0.1 mm short path length quartz cells (Starna) were used to measure solution samples.

In-Situ Humidity-Thickness Measurements. Ellipsometry was performed using a J. A. Woollam α-SE ellipsometer with a wavelength range of 380 – 900 nm at an angle of 70°. Samples were placed under a J. A. Woollam 500 µL liquid cell with a Viton o-ring to create a seal. The inlet and outlet ports were connected to a Linkam RH95 humidity controller, with the humidity detector downstream of the cell. A Cauchy model was fit using the CompleteEase ellipsometry software package by fitting for the thickness and parameterized optical constants that yield a minimum mean squared error (MSE). Due to the polymer's absorption around 550 nm, a multi-wavelength fitting range from 650-900 nm was used for the transparent region of the visible spectrum. Humidity was stepped from 25-90% RH. Spectra were continuously collected at each humidity step until the thickness changes became minimal (typically 5-10 minutes). Once reaching a steady-state, the final spectrum was used to calculate the thickness of the film.

Electron Paramagnetic Resonance (EPR) Spectroscopy. EPR measurements were performed at the Advanced EPR Facility at Argonne National Laboratory. CW X-band (9–10 GHz) EPR experiments were carried out with a Bruker ELEXSYS II E500 EPR spectrometer (Bruker Biospin, Rheinstetten, Germany), equipped with a TE_{102} rectangular EPR resonator (Bruker ER 4102ST). Note, that the CW EPR technique uses field modulation with lock-in detection which leads to first derivative-type spectra. Measurements were performed at room temperature (T = 295 K). Data processing was done using Xepr software (Bruker BioSpin, Rheinstetten). For "as-cast/dry/35%RH" measurements, samples cast onto quartz substrates of approximately 2 mm × 15 mm were placed in quartz EPR tubes. For increasing RH samples (**Figure 4.10**), solutions were deposited in the bottom of EPR tubes and dried at 60 °C under vacuum, then equilibrated in an RH chamber before sealing. Spin quantification of a single crystal of $CuSO_4{\cdot}H_2O$ with known spin concentration was used as a reference sample. Spin quantifications were done by comparing double integrals of the experimental and reference EPR. Spin concentration was calculated based on the dry mass of the polymer deposited in the EPR tube.

Dynamic Vapor Sorption (DVS). DVS measurements were performed using a Surface Measurement Systems DVS Intrinsic Plus system. Approximately 20 mg samples of P3K*n*T powders were used as-received. All experiments were performed at a fixed temperature of 25 °C.

Conductivity Measurements. Electrochemical impedance spectroscopy was performed using a Gamry Reference 600 potentiostat with a frequency sweep from 1 MHz to 0.1 Hz at 100 mV vs OCP. RH was controlled using an Espec temperature and humidity chamber. Spin-coated IDEs were placed inside the chamber and connected to the potentiostat via isolated alligator clips. Samples were equilibrated with respect to absorbed moisture for extended times (greater than 1 hour) prior to measurements. All samples for this work were measured at a constant temperature of 25°C. Nyquist plots were fit to a model represented by the diagram in **Figure 4.7a**. A detailed description of IDE geometry and Nyquist plot interpretation can be found accompanying **Figure 4.16**. DC conductivity measurements of dried samples were performed in an argon glove box on a temperature-controlled stage using a Gamry Reference 600 potentiostat to perform an I-V sweep followed by linear regression of the profile to determine R_e (**Figure 4.15**).

Dry Grazing Incidence Wide-Angle X-ray Scattering (GIWAXS). GIWAXS was used to characterize the morphology of P3K*n*T thin films. Films were spin-coated onto native oxide silicon using the previously described method. GIWAXS experiments were performed at sector 8-ID-E of the Advanced Photon Source at Argonne National Laboratory.[44] Samples were measured using an attenuated 10.86 keV beam with 10 second measurements repeated three times at different locations and then summed to improve signal-to-noise ratio. Measurements were taken at an incidence angle of 0.15°. Images were captured using a Pilatus 1MF pixel array detector (pixel size = 172 μm). Samples were measured from two different positions in order to gap-fill rows of inactive pixels between individual modules within the detector. Samples were measured over a 1-D q-range of 0 to 2 $Å^{-1}$. Dried films were measured under vacuum (10^{-3} mbar) in order to reduce air scattering and to minimize beam radiation damage. Acquired 2D intensity map images were processed using the GIXSGUI MATLAB toolbox.[45]

In-Situ Humidity-Dependent GIWAXS. These experiments were performed using a custom solvent annealing chamber designed at 8-ID-E (**Figure 4.12**). Due to time constraints, % RH levels were taken at "close enough" stable values across samples (e.g., 14.7% and 15% RH). Inert gas (nitrogen or argon) was flowed into two mass flow controllers (MFC 1 and MFC 2) at empirically determined ratios, controlled via a custom software package. Gas flowed through MFC 1 then entered a sealed bubbler containing filtered deionized water before entering a mixer with gas from MFC 2. An RH probe was used to determine relative humidity of gas entering the sample chamber, and MFC ratios were adjusted manually. Pressure inside the sample chamber was approximately ambient. An aluminum frame was covered with Kapton polyimide windows to allow transmission of the x-ray beam through chamber. Substantial background scattering was present due to the relatively large volume of humidified N_2 gas in the solvent annealing chamber. A straight-line background correction was used to account for this during image analysis of humidity-dependent measurements.

Relative degree of "crystallinity" (rDoC) determination was performed using the side-chain feature with wedge cuts taken every 2° along a χ arc to account for the total sum of this feature in all orientations from fully out-of-plane (vertical) to in-plane (horizontal). A $\sin(\chi)$ correction was applied to account for the Ewald sphere intensity distortion, where $\chi = 0$ for the out-of-plane (vertical) direction, and $\chi = 90$ for the in-plane (horizontal) direction. Each wedge cut was fit to an empirical baseline function to subtract the substantial background intensity. The background-subtracted wedge cut was then fit to a Voigt function to extract the peak position and the FWHM of the side-chain feature reflection. The resultant intensity distributions vs orientation were then integrated to get an overall intensity for the side-chain feature in each sample. The relative change in intensity was then evaluated as a function of RH for each species.

4.5 Appendix

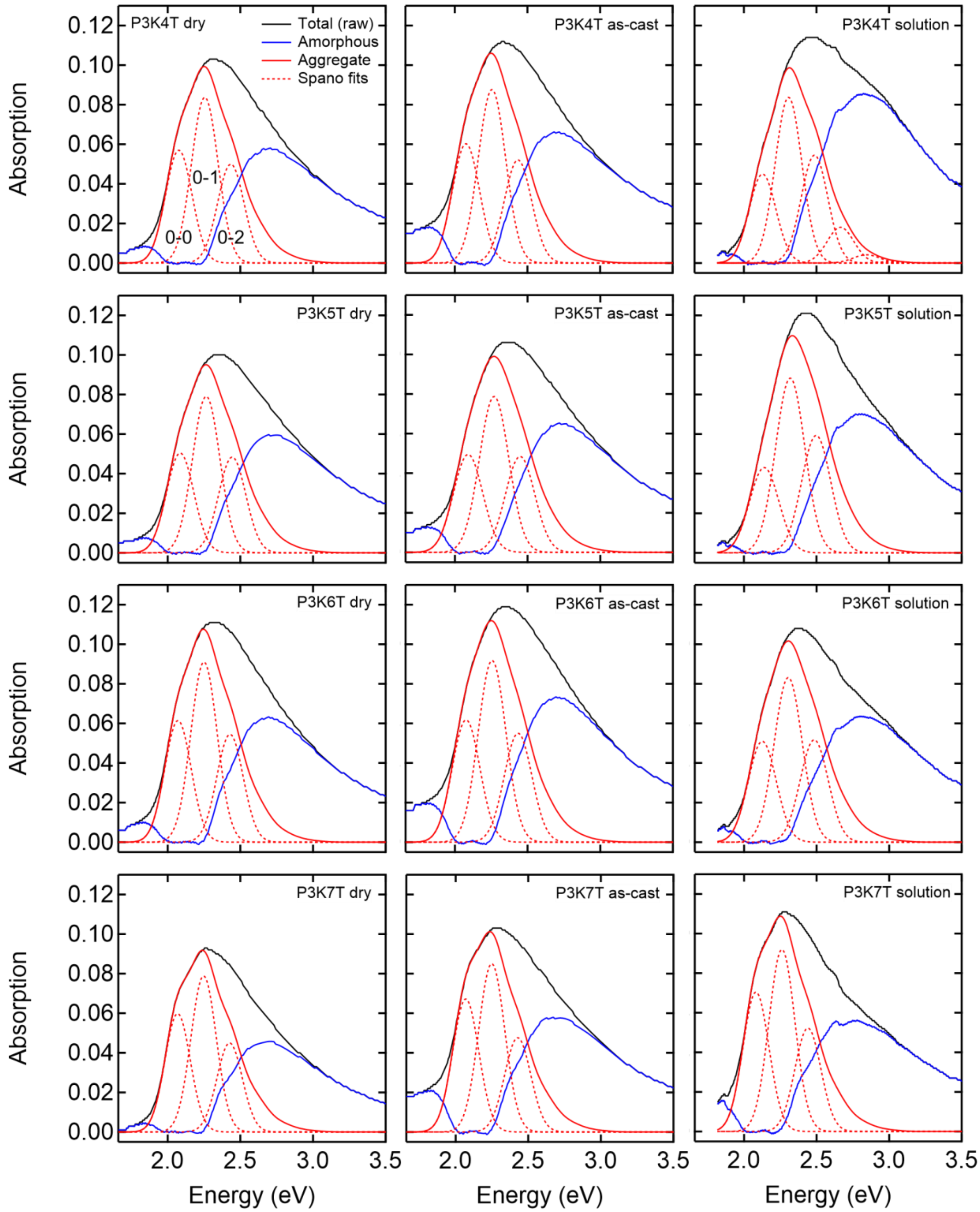

Figure 4.9. Spano model fitting of UV-Vis spectra for P3K*n*T thin films and solution. Fitting was performed using a MATLAB toolbox for polythiophene materials. Toolbox was written in-house using methodologies from references 46 and 47.

Table 4.1. Results from Spano model fitting of P3K*n*T thin film UV-vis spectra.

Sample	**Sigma**	**W**	**E_0**	**A_0**	**Aggregate**	**A_{00}**	**A_{01}**	**A_{00}/A_{01}**	**Amorphous**
n = 4, dry	91.149	103.240	2.057	0.077	0.4069	0.057	0.084	0.68100	0.124
4, as-cast	93.912	100.778	2.058	0.081	0.3740	0.060	0.088	0.68721	0.139
5, dry	93.829	119.670	2.064	0.072	0.3902	0.050	0.079	0.63797	0.119
5, as-cast	100.832	123.447	2.068	0.071	0.3789	0.049	0.079	0.62770	0.135
6, dry	90.708	105.468	2.051	0.084	0.4059	0.061	0.091	0.67473	0.121
6, as-cast	95.366	106.207	2.057	0.084	0.3693	0.062	0.092	0.67211	0.152
7, dry	87.267	75.232	2.054	0.074	0.4572	0.060	0.079	0.75888	0.092
7, as-cast	89.882	64.5426	2.057	0.081	0.3856	0.067	0.085	0.79059	0.127

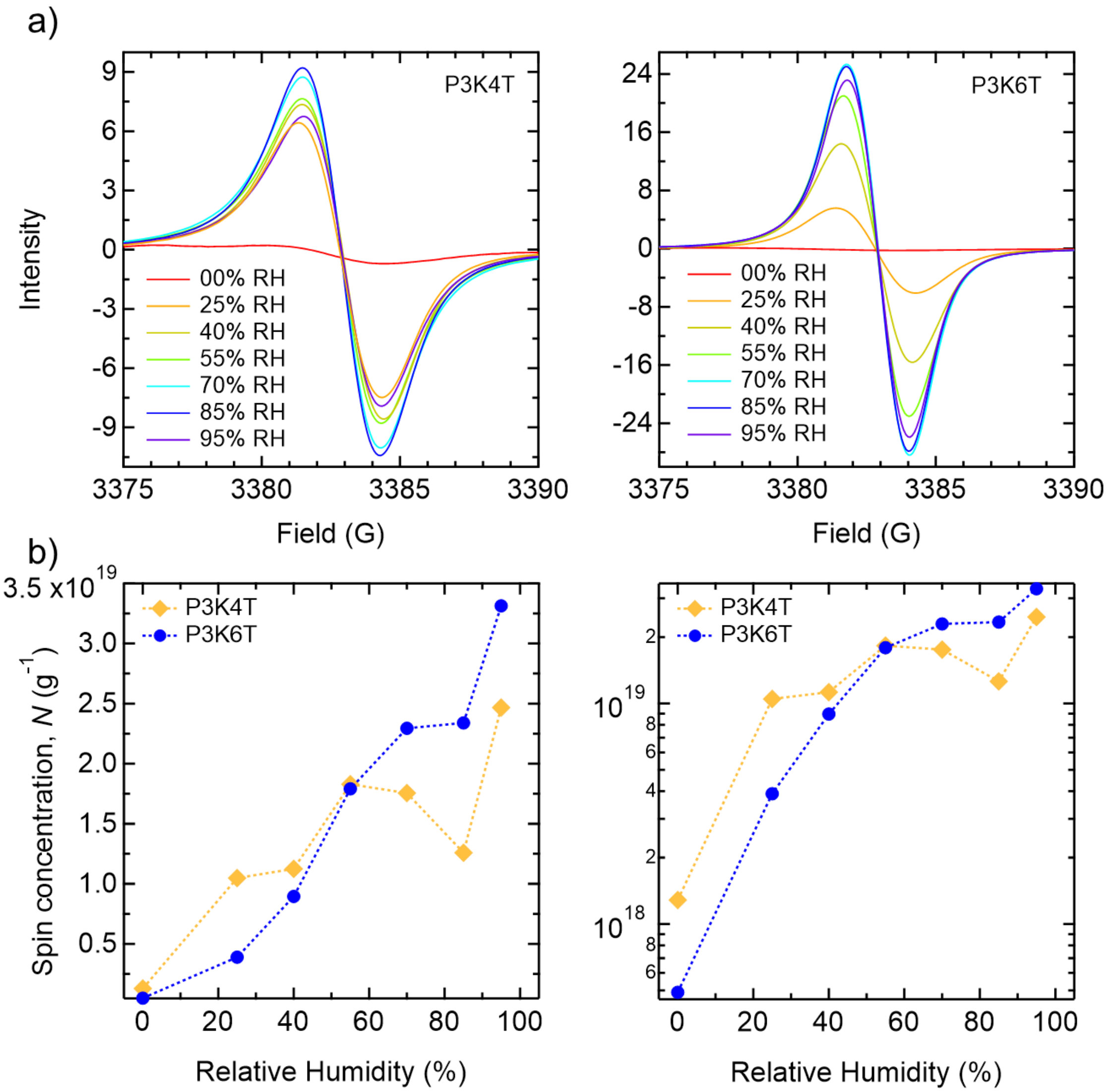

Figure 4.10. Characterization of a) Continuous wave (CW) X-band EPR spectra of P3K*n*T films equilibrated at different RH. Raw spectra are not adjusted for sample mass. b) Calculated spin concentration vs RH, presented with linear and log y-axis.

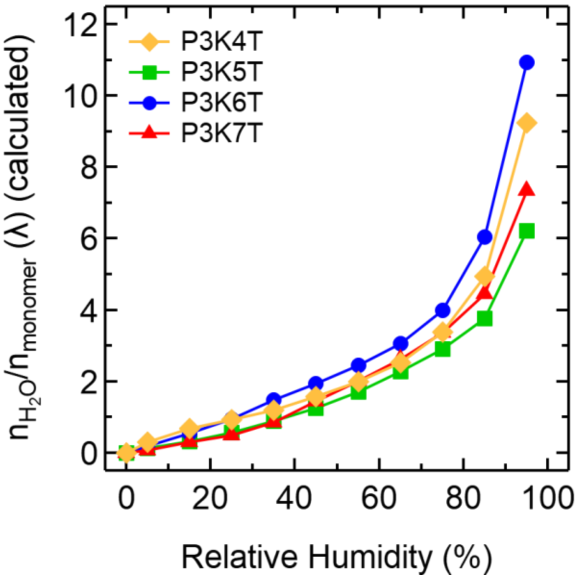

Figure 4.11. Calculated hydration level (λ) for P3K*n*T powder samples via DVS. Molecular weights of each monomer were calculated as 206.3 g/mol for P3K4T, 220.33 g/mol for P3K5T, 234.36 g/mol for P3K6T, and 248.38 g/mol for P3K7T.

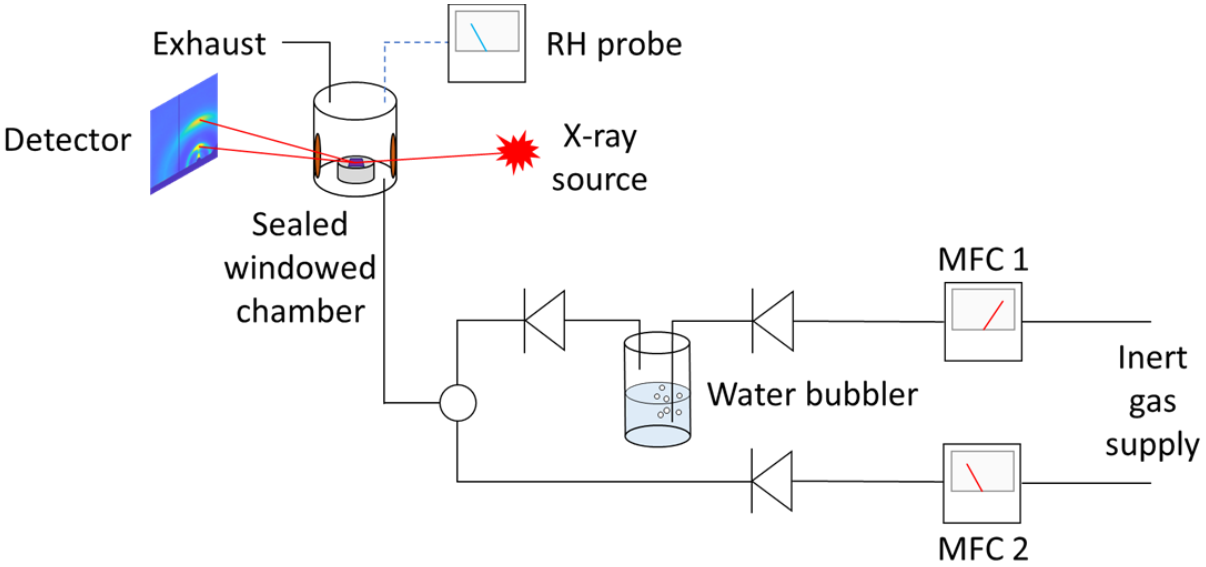

Figure 4.12. Schematic of environmental chamber for in-situ humidified GIWAXS.

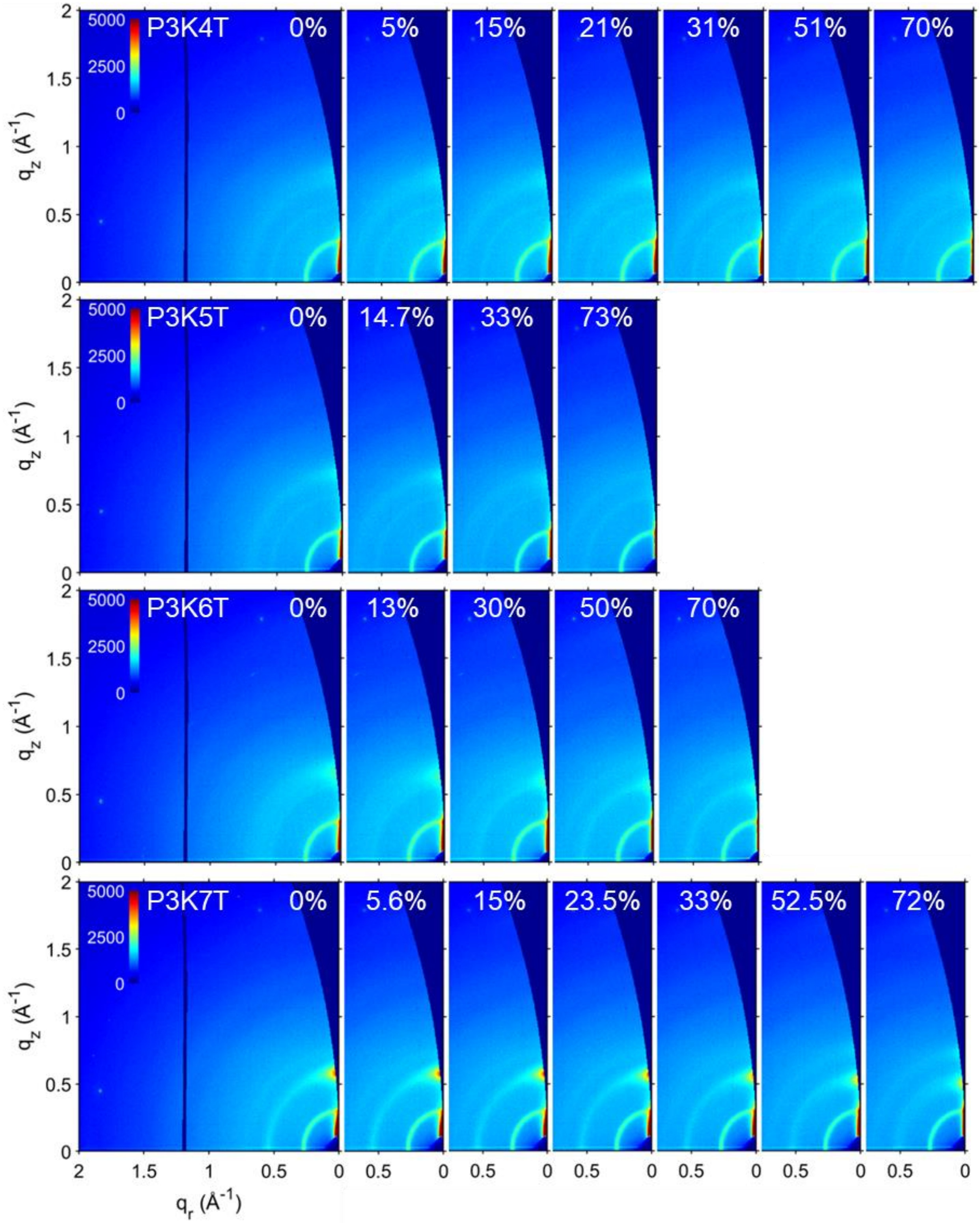

Figure 4.13a. Images for 2D in-situ humidified GIWAXS of P3K*n*T thin films. Images for RH > 0% are truncated to 0.75 Å^{-1} on the horizontal axis to aid the eye in observing the feature trends with increasing humidity.

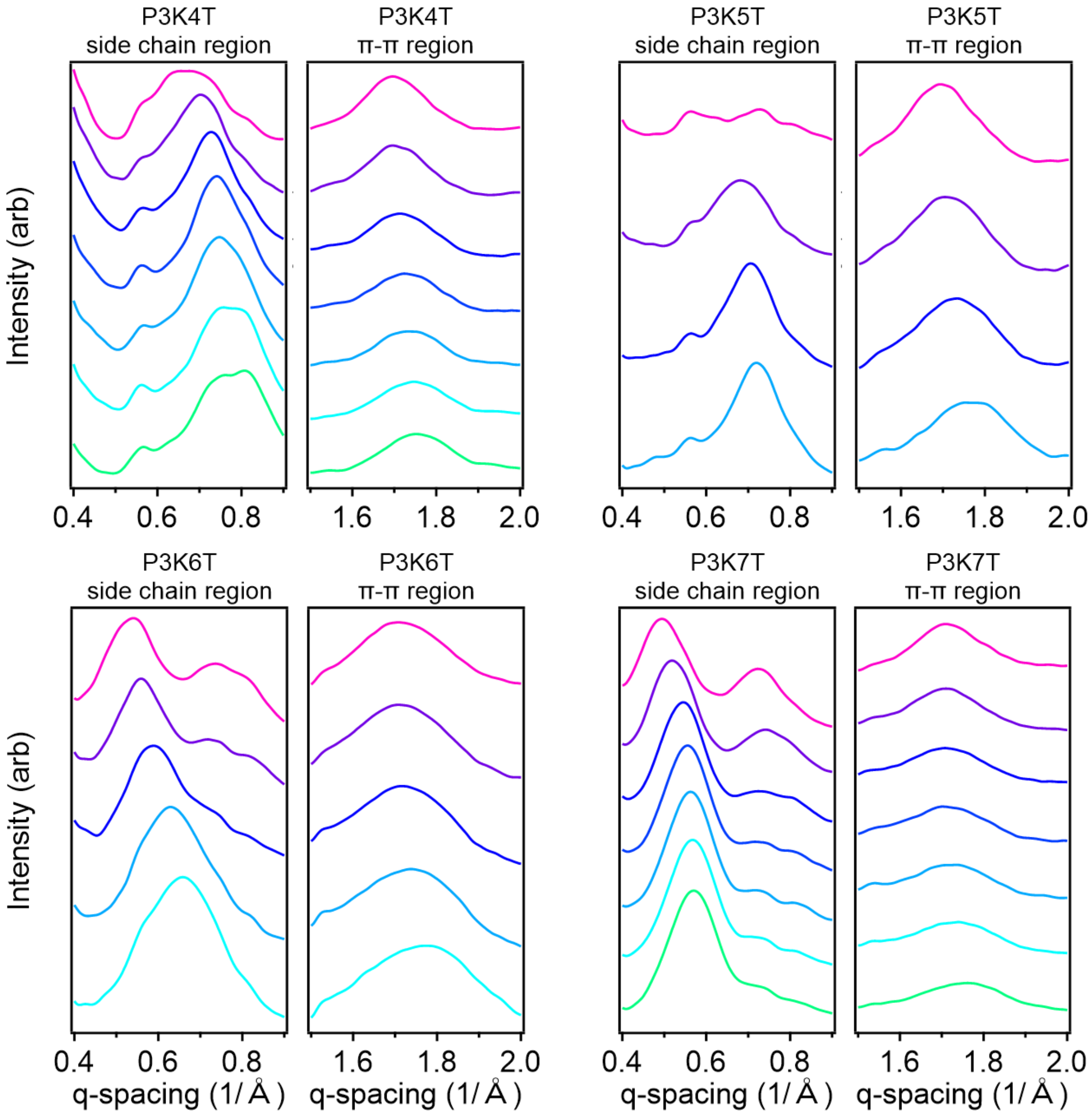

Figure 4.13b. Radially-integrated line cuts from 2D in-situ humified GIWAXS images of P3K*n*T thin films. Ascending linecuts (green/blue to pink) correlate to increasing RH values as seen in Figure S5a.

Calculated changes in feature spacing with increasing RH according to **Equation 4.1** can be seen below, corresponding to feature size trends seen in **Figure 4.13c**.

$$\% \, \boldsymbol{change} = \frac{\boldsymbol{d_i - d_o}}{\boldsymbol{d_o}} \quad (\boldsymbol{Eq. 4.1})$$

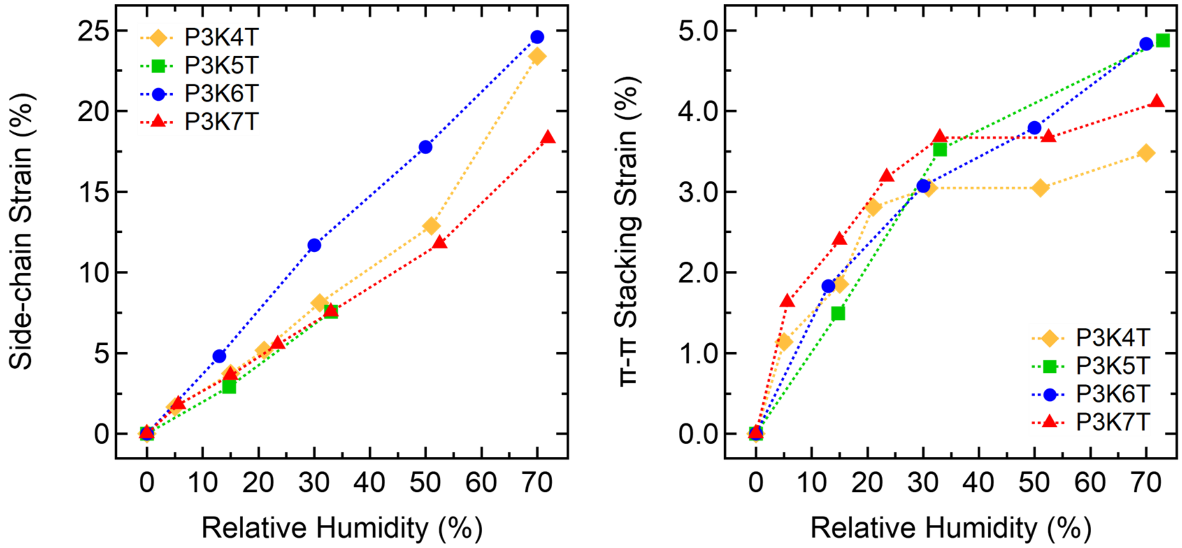

Figure 4.13c. Size change (strain) of side chain and π-π features spacing with increasing RH determined from 2D in-situ humidified GIWAXS of P3K*n*T thin films.

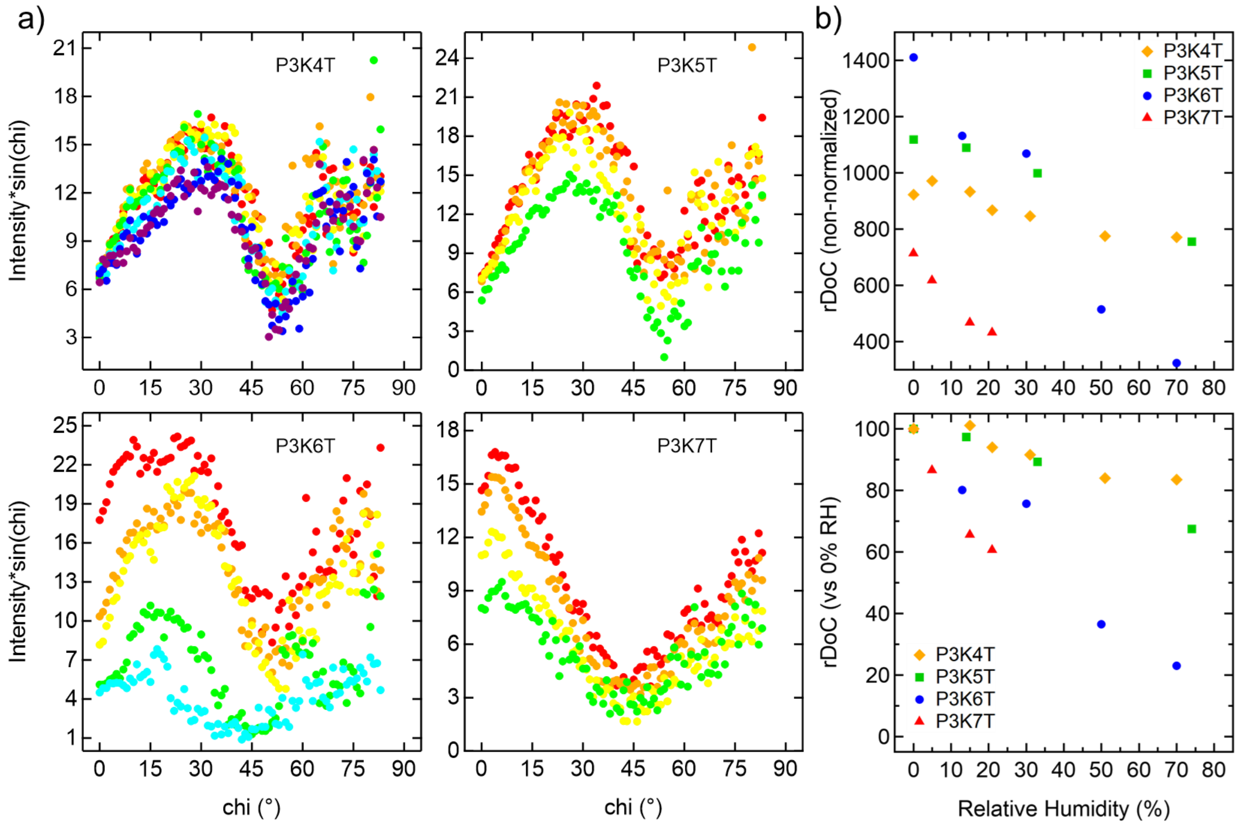

Figure 4.14. Relative degree of crystallinity (rDoC) determination for P3K*n*T thin films. a) Sin(chi)-corrected pole figures for P3K*n*T thin films from out of plane (90°) to in-plane (180°) orientation along the χ-direction with increasing RH constructed for the side-chain feature reflection. b) rDoC of P3K*n*T thin films with increasing RH, both as raw data, non-normalized and as normalized vs the dry film state. rDoC data is not normalized for film thickness. 0° indicates the vertical (edge-on) orientation while 90° indicates the horizontal in-plane (face-on) orientation. Data for rDoC is presented as non-normalized due to the high of background scattering creating difficulty in establishing a basis for normalization.

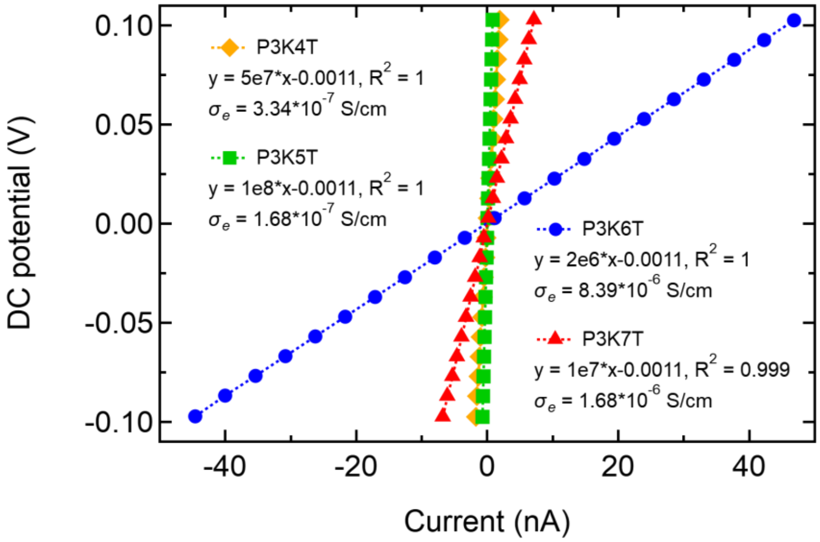

Figure 4.15. DC I-V curves for dried P3K*n*T polymer thin films on IDEs under argon gas.

Nyquist plots of P3K*n*T films under increasing relative humidity. Nyquist plots were fit to a model represented by the diagram in **Figure 4.7a**. Conductivity was determined based on resistances from this model fit applied to **Equations 4.2** and **4.3** below, where R1 is the point where the intersection between the two semicircles of the Nyquist plot approaches Z" = 0, and R2 is the rightmost point of the Nyquist plot approaching Z" = 0, and where R_e is the electronic resistance and R_i is the ionic resistance. Knowing R_e and R_i, conductivity values σ_e and σ_i are calculated via **Equation 4.4** where *l* is the length of one electrode tooth (1 mm), *d* is the distance between teeth (8 μm), *N* is the number of electrodes teeth (160), *h* is the thickness of thin film samples, and *R* the film resistance extracted from the fit of EIS data to the equivalent circuit.[48]

$$\boldsymbol{R2 = Re} \quad (\boldsymbol{Eq\ 4.2})$$

$$\boldsymbol{R1} = \frac{\mathbf{1}}{\left(\frac{\mathbf{1}}{\boldsymbol{Re}}\right) + \left(\frac{\mathbf{1}}{\boldsymbol{Ri}}\right)} \quad (\boldsymbol{Eq.4.3})$$

$$\boldsymbol{\sigma} = \frac{\mathbf{1}}{\boldsymbol{R}}\frac{\boldsymbol{d}}{\boldsymbol{l(N-1)h}} \quad (\boldsymbol{Eq.4.4})$$

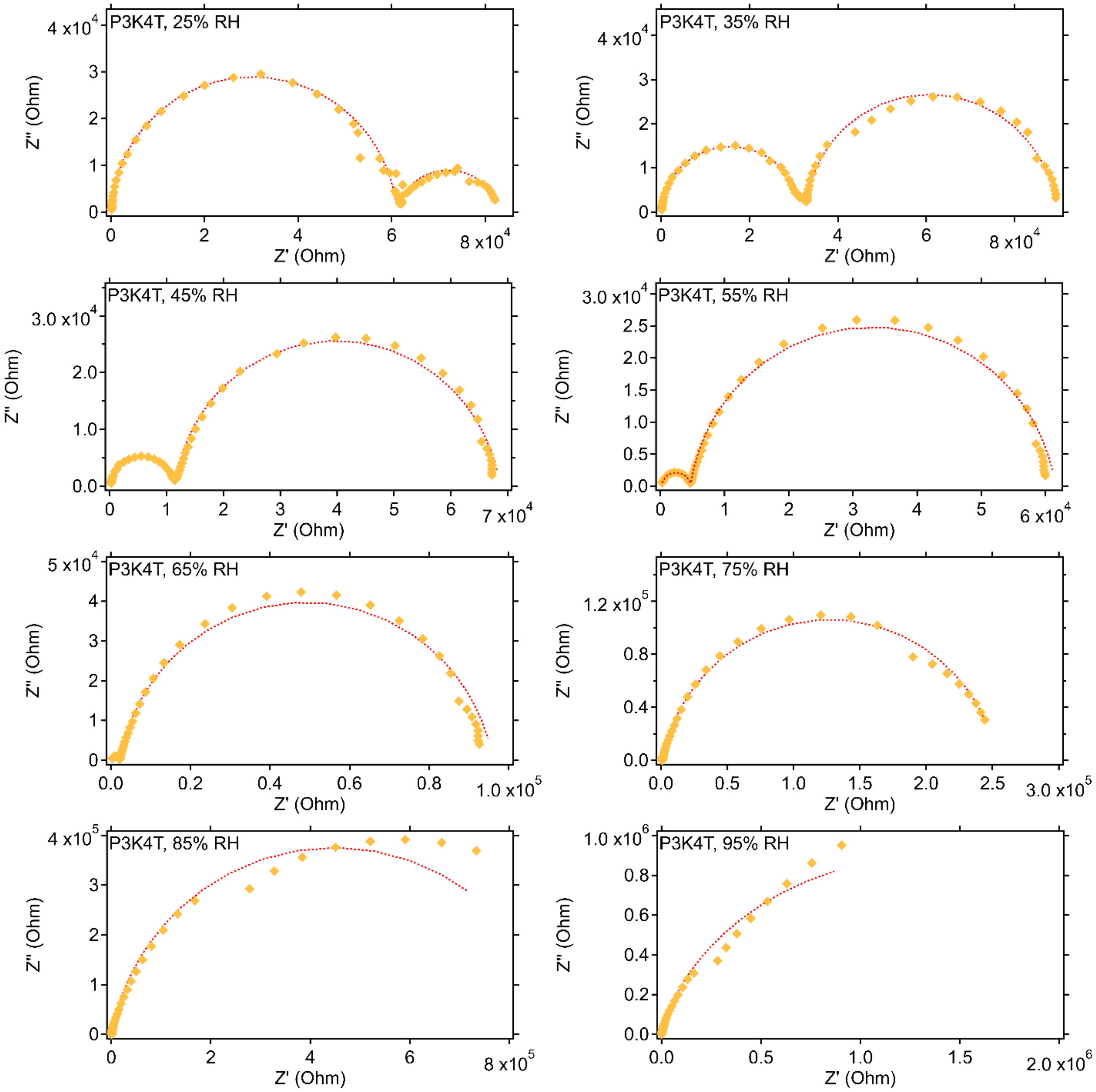

Figure 4.16a. Nyquist plots for P3K4T thin films on IDE with increasing RH.

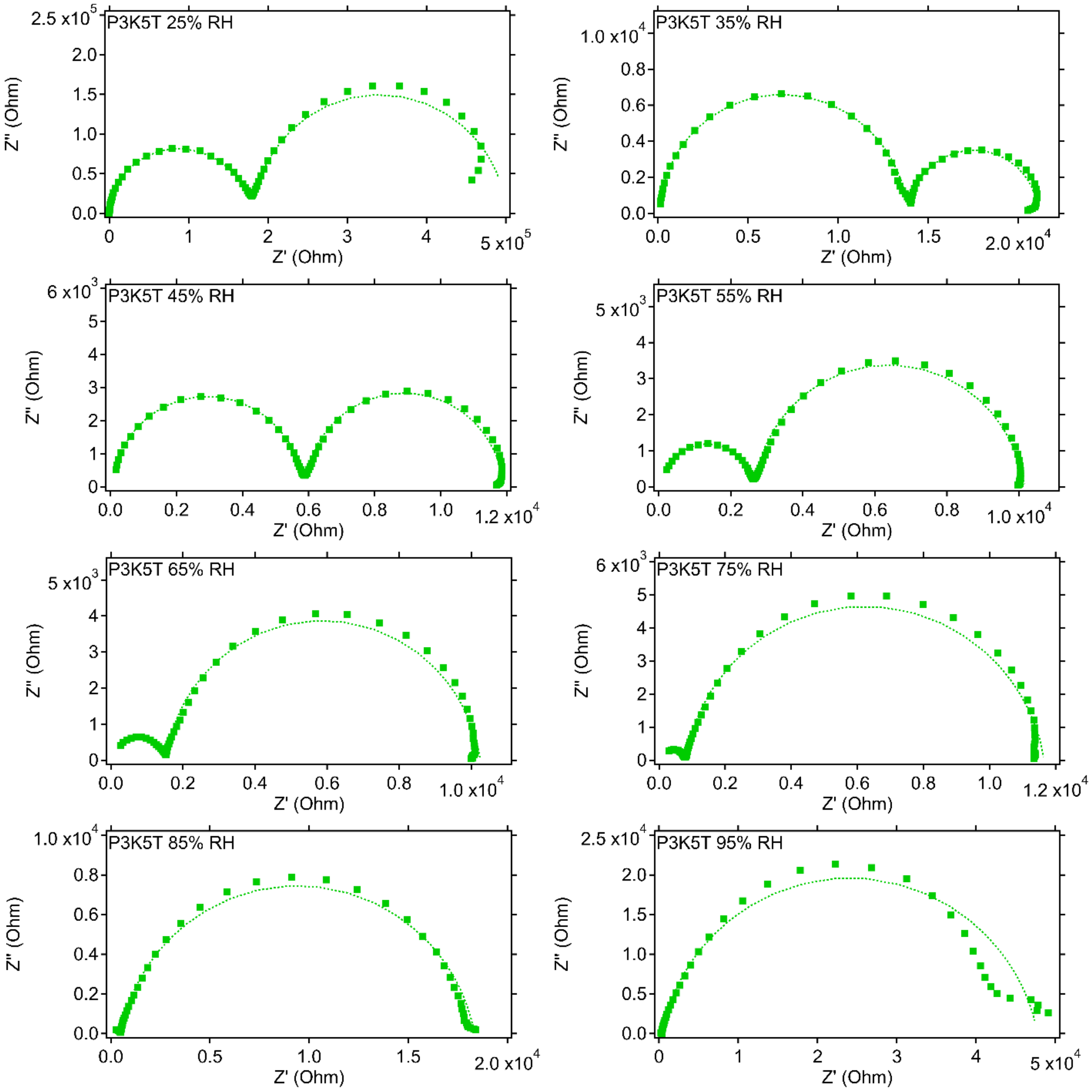

Figure 4.16b. Nyquist plots for P3K5T thin films on IDE with increasing RH.

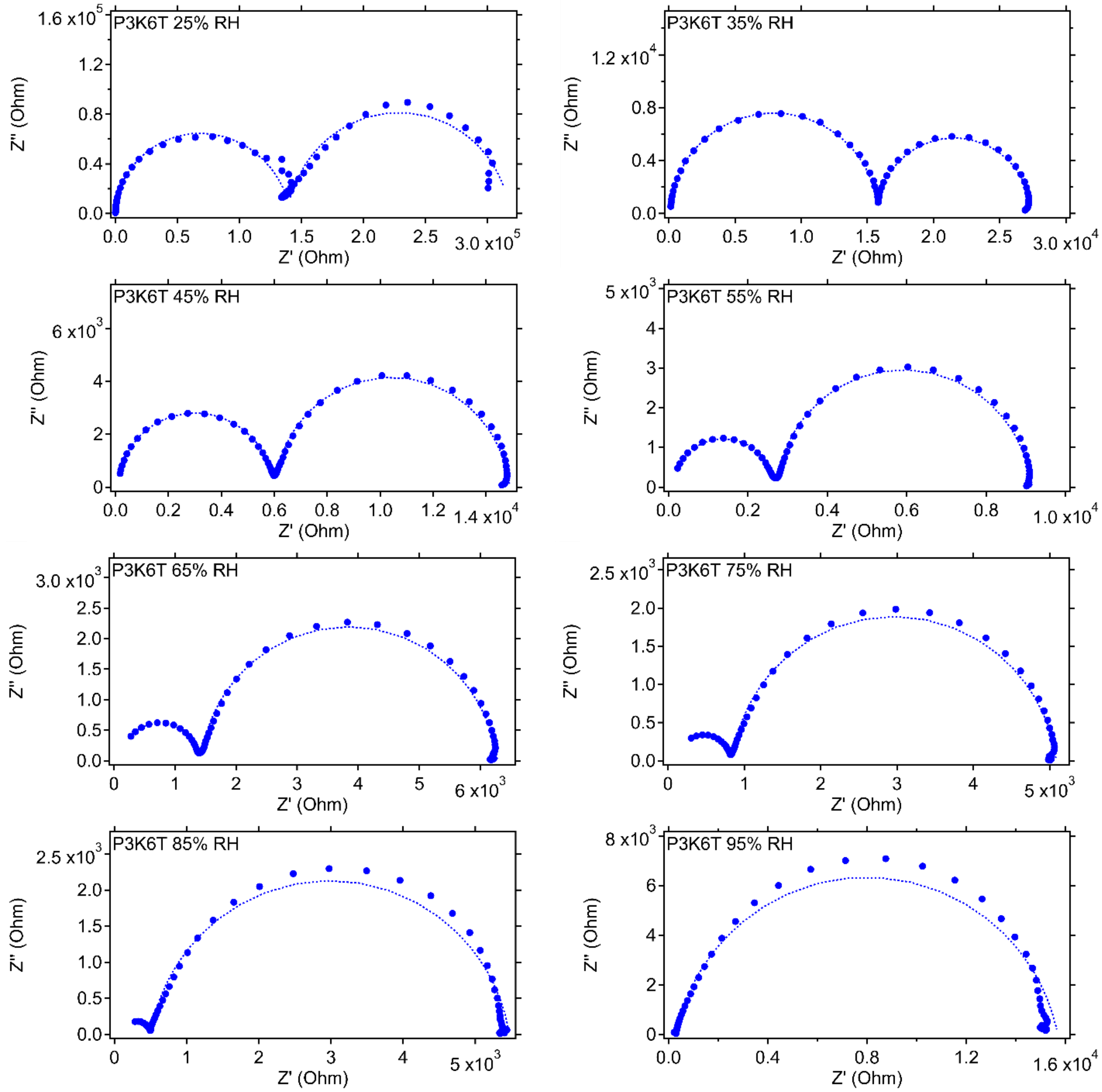

Figure 4.16c. Nyquist plots for P3K6T thin films on IDE with increasing RH.

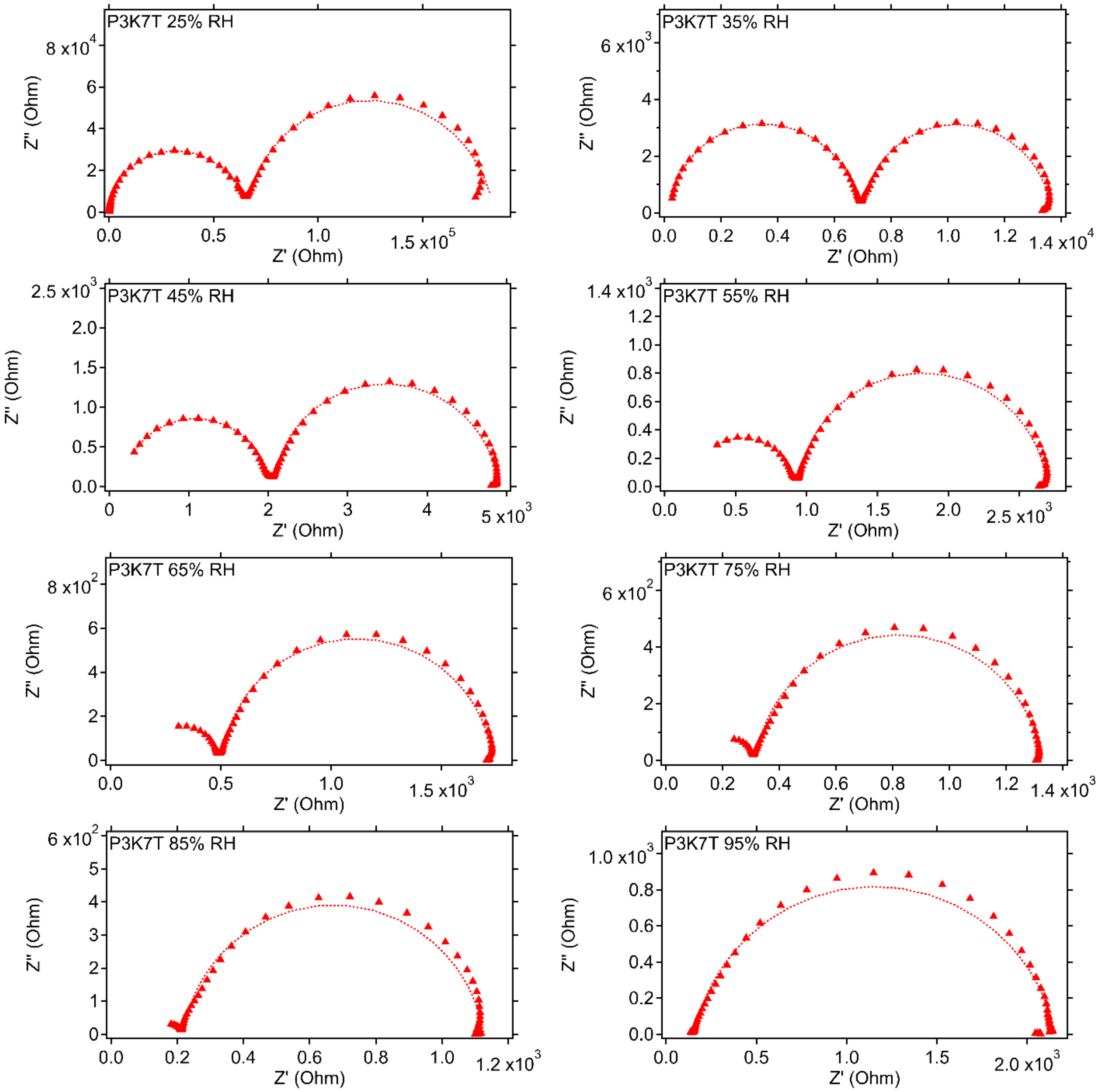

Figure 4.16d. Nyquist plots for P3K7T thin films on IDE with increasing RH.

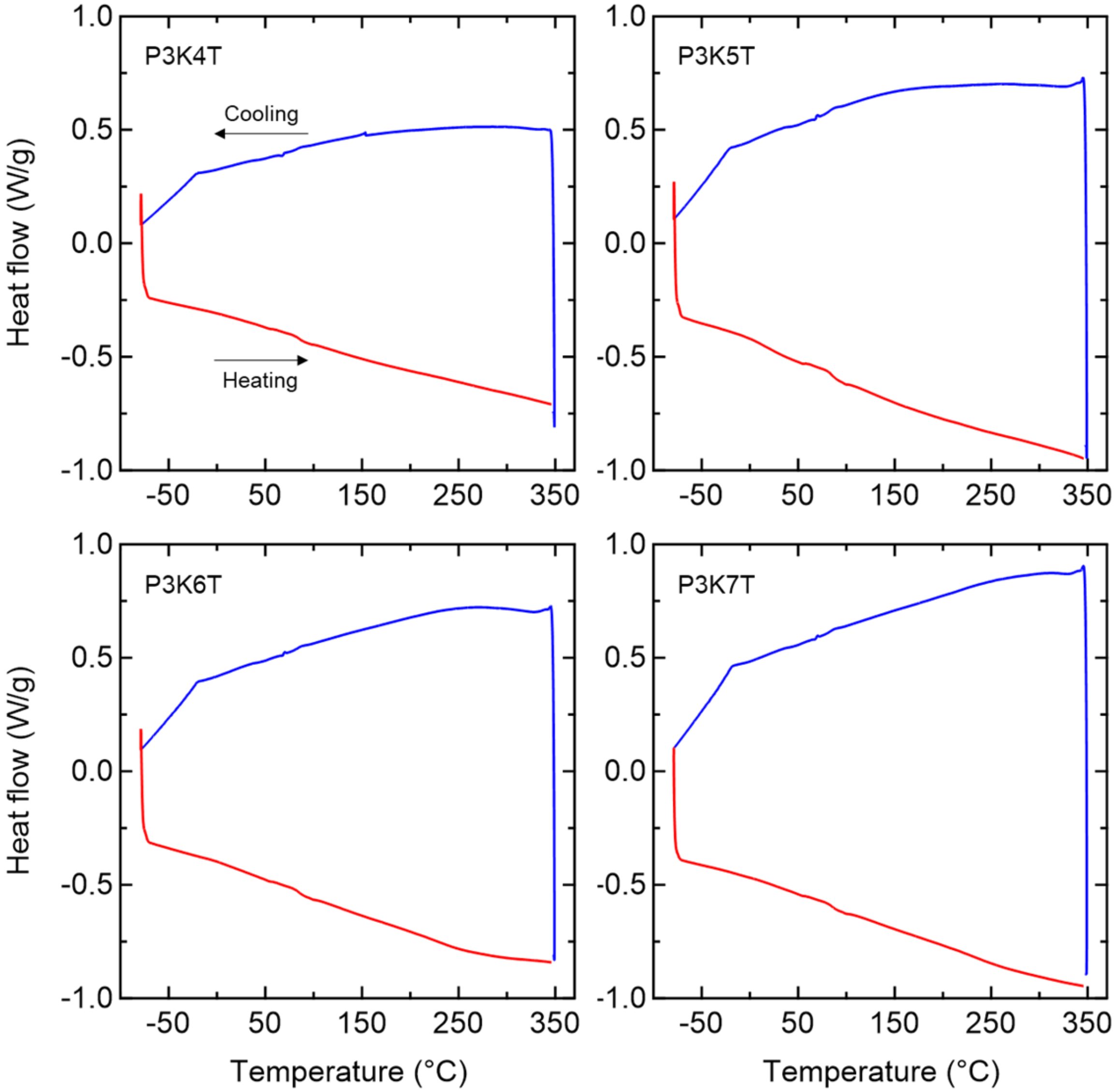

Figure 4.17a. DSC for P3K*n*T powders, 20 °C/min scan rate. First cooling and second heating scans shown.

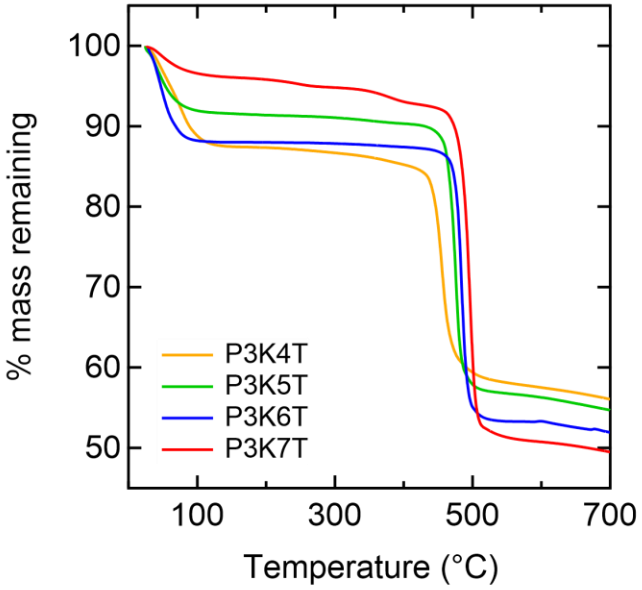

Figure 4.17b. TGA for P3K*n*T powders, 20 °C/min ramp rate.

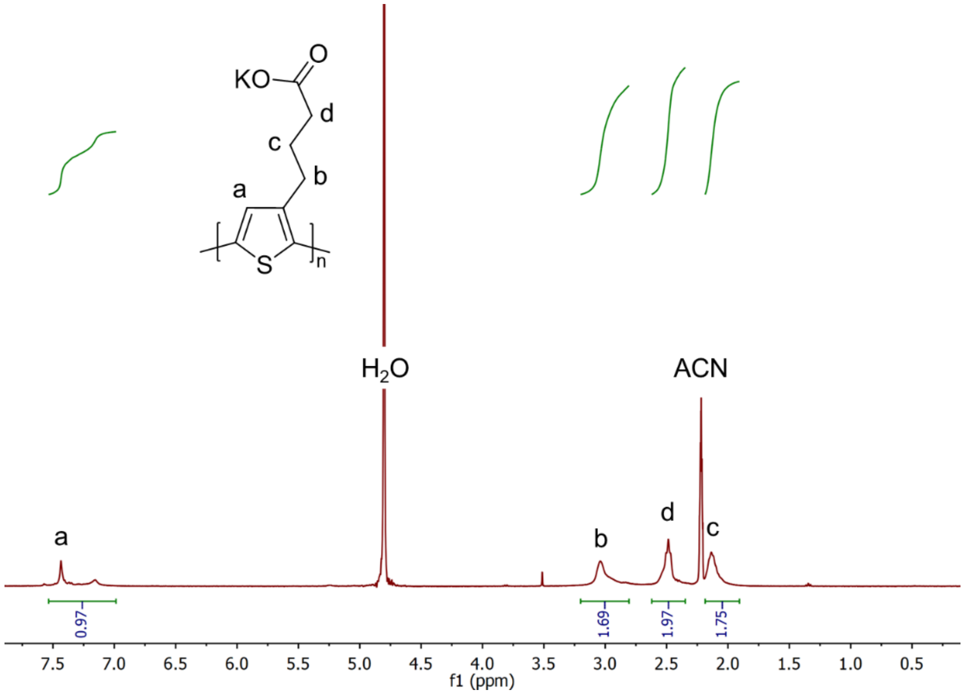

Figure 4.18a. P3K4T ^{1}H NMR (400 MHz, D_2O/ACN-d3) δ 2.13 (m, 2H), 2.49-2.51(m, 2H), 3.04 (m, 2H), 7.16-7.37 (s, 1H).

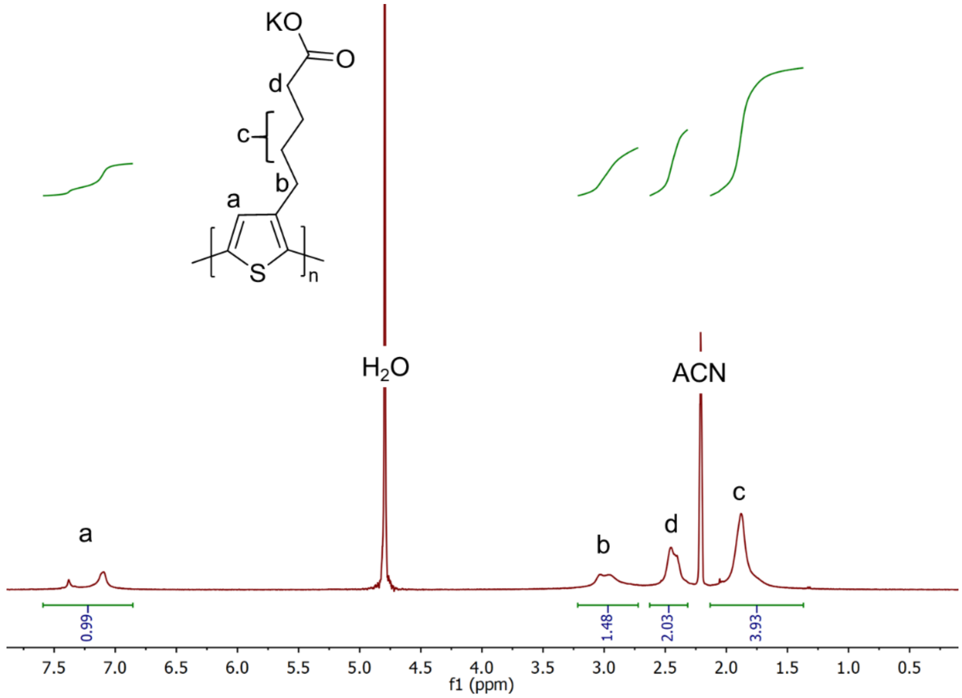

Figure 4.18b. P3K5T ^{1}H NMR (400 MHz, D_2O/ACN-d3) δ 1.89 (m, 4H), 2.41-2.46(m, 2H), 2.96-3.03 (m, 2H), 7.10-7.38 (s, 1H).

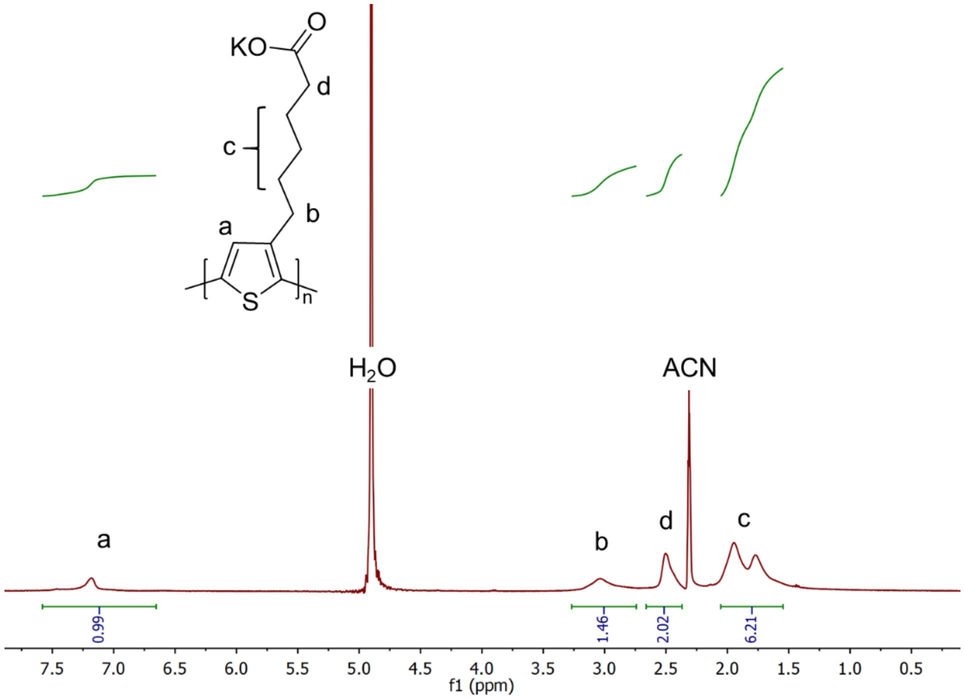

Figure 4.18c. P3K6T ^{1}H NMR (400 MHz, D_2O/ACN-d3) δ 1.66-1.85 (m, 6H), 2.40 (m, 2H), 2.93 (m, 2H), 7.08 (s, 1H).

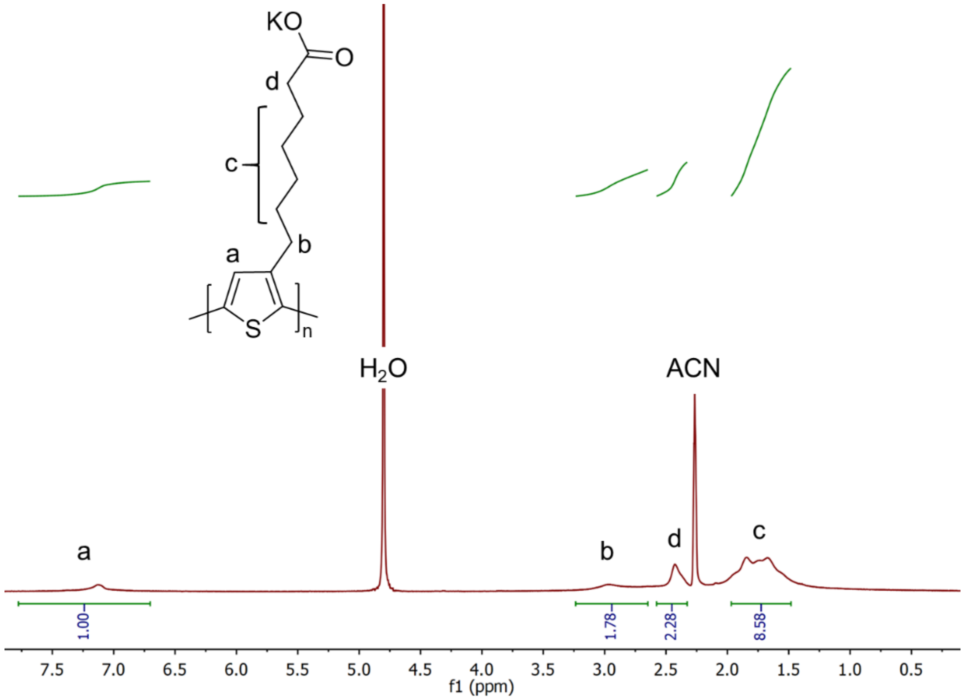

Figure 4.18d. P3K7T ^{1}H NMR (400 MHz, D_2O/ACN-d3) δ 1.66-1.84 (m, 8H), 2.43(m, 2H), 2.96 (m, 2H), 7.13 (s, 1H).

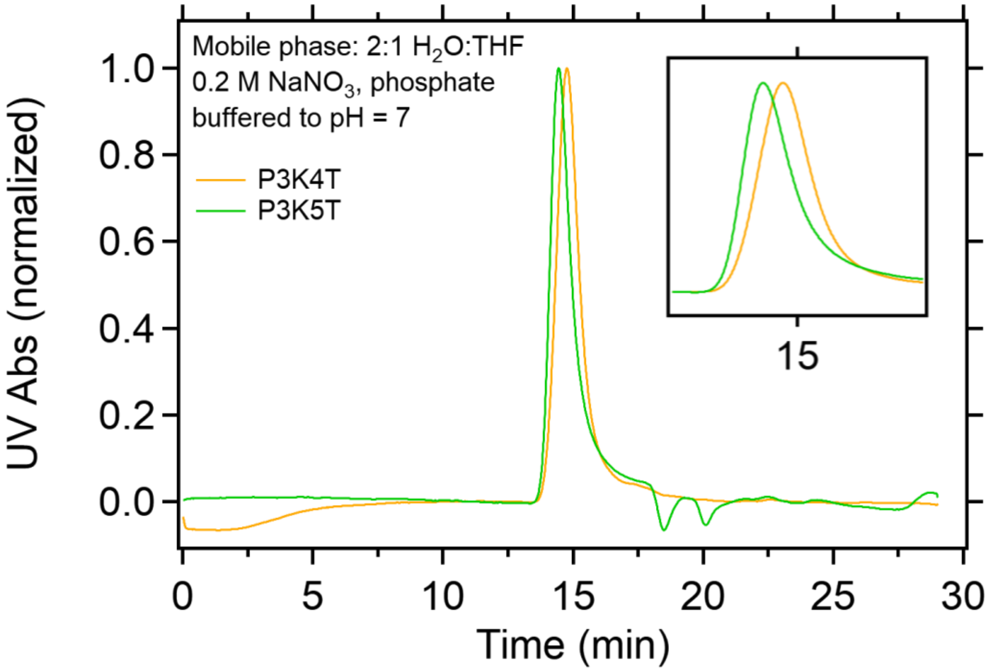

Figure 4.19. Gel permeation chromatography (GPC) of P3K4T and P3K5T solutions.

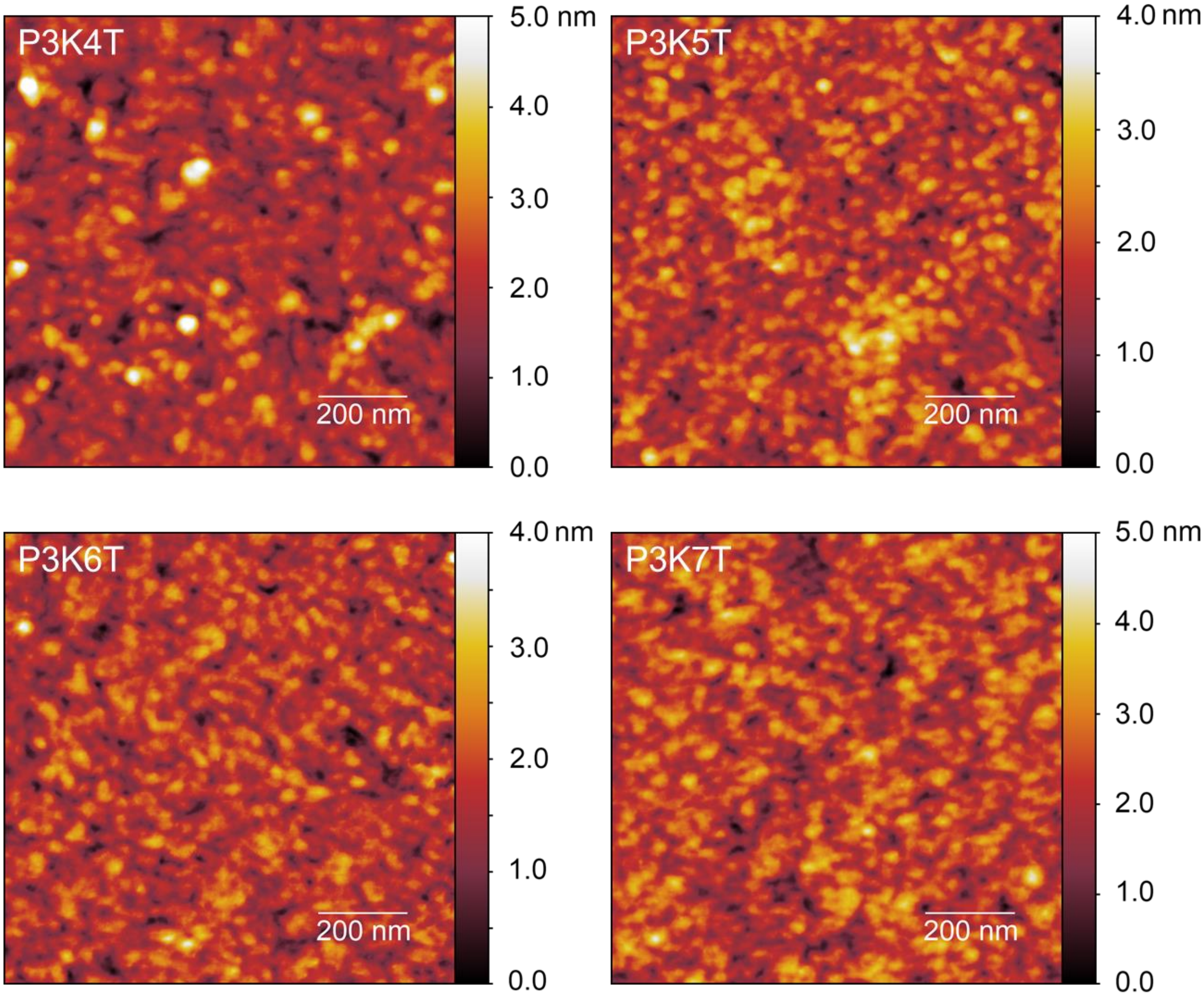

Figure 4.20. Atomic force microscopy (AFM) images of P3K*n*T thin films on Si wafer.

4.6 Acknowledgements

This work made use of the shared facilities at the University of Chicago Materials Research Science and Engineering Center, supported by National Science Foundation under award number DMR-2011854. Parts of this work were carried out at the Soft Matter Characterization Facility of the University of Chicago. The authors gratefully thank Dr. Xiaoying Liu for her assistance in performing DVS measurements, Dr. Zhongyang Wang for assistance in obtaining AFM images, Hongyi Zhang for guidance in NMR interpretation, and Dr. Philip Griffin for his diverse assistance throughout this study. This work made use of the Pritzker Nanofabrication Facility, which receives partial support from the SHyNE Resource, a node of the National Science Foundation's National Nanotechnology Coordinated Infrastructure (NSF ECCS-2025633). The in-situ humidity-thickness measurements were supported as part of the Advanced Materials for Energy-Water Systems (AMEWS) Center, an Energy Frontier Research Center funded by the U.S. Department of Energy, Office of Science, Basic Energy Sciences. This research used resources of the Advanced Photon Source, an Office of Science User Facility operated for the U.S. Department of Energy (DOE) by Argonne National Laboratory under Contract No. DE-AC-02-06CH11357. The EPR work at Argonne National Laboratory was supported by the U.S. Department of Energy (DOE), Office of Basic Energy Sciences, Division of Chemical Sciences, Geosciences, and Biosciences, under Contract no. DE-AC-02-06CH11357.

4.7 References

(1) Riess, I. Mixed Ionic–Electronic Conductors—Material Properties and Applications. Solid State Ionics 2003, 157 (1–4), 1–17.

(2) West, A. R. Solid Electrolytes and Mixed Ionic–Electronic Conductors: An Applications Overview. J. Mater. Chem. 1991, 1 (2), 157–162.

(3) Paulsen, B. D.; Tybrandt, K.; Stavrinidou, E.; Rivnay, J. Organic Mixed Ionic–Electronic Conductors. Nat. Mater. 2020, 19 (1), 13–26.

(4) Rivnay, J.; Inal, S.; Collins, B. A.; Sessolo, M.; Stavrinidou, E.; Strakosas, X.; Tassone, C.; Delongchamp, D. M.; Malliaras, G. G. Structural Control of Mixed Ionic and Electronic Transport in Conducting Polymers. Nat. Commun. 2016, 7 (1), 11287.

(5) Nguyen, V. A.; Kuss, C. Review—Conducting Polymer-Based Binders for Lithium-Ion Batteries and Beyond. J. Electrochem. Soc. 2020, 167 (6), 065501.

(6) Russ, B.; Glaudell, A.; Urban, J. J.; Chabinyc, M. L.; Segalman, R. A. Organic Thermoelectric Materials for Energy Harvesting and Temperature Control. Nat. Rev. Mater. 2016, 1 (10), 16050.

(7) Mai, C. K.; Schlitz, R. A.; Su, G. M.; Spitzer, D.; Wang, X.; Fronk, S. L.; Cahill, D. G.; Chabinyc, M. L.; Bazan, G. C. Side-Chain Effects on the Conductivity, Morphology, and Thermoelectric Properties of Self-Doped Narrow-Band-Gap Conjugated Polyelectrolytes. J. Am. Chem. Soc. 2014, 136 (39), 13478–13481.

(8) Zeglio, E. Self-Doped Conjugated Polyelectrolytes for Bioelectronics Applications. Ph.D. Disseration, Linköping University, Linköping, Sweden, 2016. Linköping University Electronic Press.

(9) Rivnay, J.; Inal, S.; Salleo, A.; Owens, R. M.; Berggren, M.; Malliaras, G. G. Organic Electrochemical Transistors. Nat. Rev. Mater. 2018, 3 (2), 17086.

(10) Jiang, H.; Taranekar, P.; Reynolds, J. R.; Schanze, K. S. Conjugated Polyelectrolytes: Synthesis, Photophysics, and Applications. Angew. Chemie Int. Ed. 2009, 48 (24), 4300–4316.

(11) Hoven, C. V.; Garcia, A.; Bazan, G. C.; Nguyen, T.-Q. Recent Applications of Conjugated Polyelectrolytes in Optoelectronic Devices. Adv. Mater. 2008, 20 (20), 3793–3810.

(12) Lee, W.; Seo, J. H.; Woo, H. Y. Conjugated Polyelectrolytes: A New Class of Semiconducting Material for Organic Electronic Devices. Polym. (United Kingdom) 2013, 54 (19), 5104–5121.

(13) Patil, A. O.; Ikenoue, Y.; Wudl, F.; Heeger, A. J. Water-Soluble Conducting Polymers. J. Am. Chem. Soc. 1987, 109 (6), 1858–1859.

(14) Bazan, G. C.; Henson, Z. Conjugated Polyelectrolytes. In Encyclopedia of Polymeric Nanomaterials; Springer Berlin Heidelberg: Berlin, Heidelberg, 2015; pp 427–433.

(15) Müllen, K.; Pisula, W. Donor–Acceptor Polymers. J. Am. Chem. Soc. 2015, 137 (30), 9503–9505.

(16) Patil, A. O.; Ikenoue, Y.; Basescu, N.; Colaneri, N.; Chen, J.; Wudl, F.; Heeger, A. J. Self-Doped Conducting Polymers. Synth. Met. 1987, 20 (2), 151–159.

(17) Merkle, R.; Gutbrod, P.; Reinold, P.; Katzmaier, M.; Tkachov, R.; Maier, J.; Ludwigs, S. Mixed Conductivity of Polythiophene-Based Ionic Polymers under Controlled Conditions. Polymer (Guildf). 2017, 132, 216–226.

(18) Heinze, J.; Frontana-Uribe, B. A.; Ludwigs, S. Electrochemistry of Conducting Polymers—Persistent Models and New Concepts. Chem. Rev. 2010, 110 (8), 4724–4771.

(19) Cao, D. X.; Leifert, D.; Brus, V. V.; Wong, M. S.; Phan, H.; Yurash, B.; Koch, N.; Bazan, G. C.; Nguyen, T. Q. The Importance of Sulfonate to the Self-Doping Mechanism of the Water-Soluble Conjugated Polyelectrolyte PCPDTBT-SO3K. Mater. Chem. Front. 2020, 4 (12), 3556–3566.

(20) Wang, H.; Xu, Y.; Yu, X.; Xing, R.; Liu, J.; Han, Y. Structure and Morphology Control in Thin Films of Conjugated Polymers for an Improved Charge Transport. Polymers. 2013, 5, 1272-1324.

(21) Noriega, R.; Rivnay, J.; Vandewal, K.; Koch, F. P. V.; Stingelin, N.; Smith, P.; Toney, M. F.; Salleo, A. A General Relationship between Disorder, Aggregation and Charge Transport in Conjugated Polymers. Nat. Mater. 2013, 12 (11), 1038–1044.

(22) Ludvigsson, M.; Lindgren, J.; Tegenfeldt, J. Crystallinity in Cast Nafion. J. Electrochem. Soc. 2000, 147 (4), 1303.

(23) Xue, Z.; He, D.; Xie, X. Poly(Ethylene Oxide)-Based Electrolytes for Lithium-Ion Batteries. J. Mater. Chem. A 2015, 3 (38), 19218–19253.

(24) Onorato, J. W.; Luscombe, C. K. Morphological Effects on Polymeric Mixed Ionic/Electronic Conductors. Molecular Systems Design and Engineering. Royal Society of Chemistry April 1, 2019, pp 310–324.

(25) Cendra, C.; Giovannitti, A.; Savva, A.; Venkatraman, V.; McCulloch, I.; Salleo, A.; Inal, S.; Rivnay, J. Role of the Anion on the Transport and Structure of Organic Mixed Conductors. Adv. Funct. Mater. 2019, 29 (5), 1807034.

(26) Dong, B. X.; Nowak, C.; Onorato, J. W.; Strzalka, J.; Escobedo, F. A.; Luscombe, C. K.; Nealey, P. F.; Patel, S. N. Influence of Side-Chain Chemistry on Structure and Ionic Conduction Characteristics of Polythiophene Derivatives: A Computational and Experimental Study. Chem. Mater. 2019, 31 (4), 1418–1429.

(27) Flagg, L. Q.; Bischak, C. G.; Onorato, J. W.; Rashid, R. B.; Luscombe, C. K.; Ginger, D. S. Polymer Crystallinity Controls Water Uptake in Glycol Side-Chain Polymer Organic Electrochemical Transistors. J. Am. Chem. Soc. 2019, 141 (10), 4345–4354.

(28) Schmode, P.; Savva, A.; Kahl, R.; Ohayon, D.; Meichsner, F.; Dolynchuk, O.; Thurn-Albrecht, T.; Inal, S.; Thelakkat, M. The Key Role of Side Chain Linkage in Structure Formation and Mixed Conduction of Ethylene Glycol Substituted Polythiophenes. ACS Appl. Mater. Interfaces 2020, 12 (11), 13029–13039.

(29) Savva, A.; Cendra, C.; Giugni, A.; Torre, B.; Surgailis, J.; Ohayon, D.; Giovannitti, A.; McCulloch, I.; Di Fabrizio, E.; Salleo, A.; et al. Influence of Water on the Performance of Organic Electrochemical Transistors. Chem. Mater. 2019, 31 (3), 927–937.

(30) Zhang, S.; Kumar, P.; Nouas, A. S.; Fontaine, L.; Tang, H.; Cicoira, F. Solvent-Induced Changes in PEDOT:PSS Films for Organic Electrochemical Transistors. APL Mater. 2014, 3 (1), 014911.

(31) Kim, S. M.; Kim, C. H.; Kim, Y.; Kim, N.; Lee, W. J.; Lee, E. H.; Kim, D.; Park, S.; Lee, K.; Rivnay, J.; et al. Influence of PEDOT:PSS Crystallinity and Composition on Electrochemical Transistor Performance and Long-Term Stability. Nat. Commun. 2018 91 2018, 9 (1), 1–9.

(32) Wang, H.; Ail, U.; Gabrielsson, R.; Berggren, M.; Crispin, X. Ionic Seebeck Effect in Conducting Polymers. Adv. Energy Mater. 2015, 5 (11), 1–6.

(33) Wieland, M.; Dingler, C.; Merkle, R.; Maier, J.; Ludwigs, S. Humidity-Controlled Water Uptake and Conductivities in Ion and Electron Mixed Conducting Polythiophene Films. ACS Appl. Mater. Interfaces 2020, 12 (5), 6742–6751.

(34) Kang, K.; Schott, S.; Venkateshvaran, D.; Broch, K.; Schweicher, G.; Harkin, D.; Jellett, C.; Nielsen, C. B.; McCulloch, I.; Sirringhaus, H. Investigation of the Thermoelectric Response in Conducting Polymers Doped by Solid-State Diffusion. Mater. Today Phys. 2019, 8, 112–122.

(35) Liu, W.; Müller, L.; Ma, S.; Barlow, S.; Marder, S. R.; Kowalsky, W.; Köhn, A.; Lovrincic, R. Origin of the π-π Spacing Change upon Doping of Semiconducting Polymers. J. Phys. Chem. C 2018, 122 (49), 27983–27990.

(36) Patel, S. N.; Javier, A. E.; Stone, G. M.; Mullin, S. A.; Balsara, N. P. Simultaneous Conduction of Electronic Charge and Lithium Ions in Block Copolymers. ACS Nano 2012, 6 (2), 1589–1600.

(37) Dong, B. X.; Liu, Z.; Misra, M.; Strzalka, J.; Niklas, J.; Poluektov, O. G.; Escobedo, F. A.; Ober, C. K.; Nealey, P. F.; Patel, S. N. Structure Control of a π-Conjugated Oligothiophene-Based Liquid Crystal for Enhanced Mixed Ion/Electron Transport Characteristics. ACS Nano 2019, 13 (7), 7665–7675.

(38) Huggins, R. A. Simple Method to Determine Electronic and Ionic Components of the Conductivity in Mixed Conductors a Review. Ionics (Kiel). 2002, 8 (3–4), 300–313.

(39) Sone, Y. Proton Conductivity of Nafion 117 as Measured by a Four-Electrode AC Impedance Method. J. Electrochem. Soc. 1996, 143 (4), 1254.

(40) Wee, G.; Larsson, O.; Srinivasan, M.; Berggren, M.; Crispin, X.; Mhaisalkar, S. Effect of the Ionic Conductivity on the Performance of Polyelectrolyte- Based Supercapacitors. Adv. Funct. Mater. 2010, 20 (24), 4344–4350.

(41) Malti, A.; Edberg, J.; Granberg, H.; Khan, Z. U.; Andreasen, J. W.; Liu, X.; Zhao, D.; Zhang, H.; Yao, Y.; Brill, J. W.; et al. An Organic Mixed Ion-Electron Conductor for Power Electronics. Adv. Sci. 2015, 3 (2), 1500305.

(42) Kim, S. H.; Kim, J. G. Preparation of Water Soluble Polythiophenes Mediated by Highly Active Zinc. Bull. Korean Chem. Soc. 2009, 30 (10), 2283–2286.

(43) Sharon, D.; Bennington, P.; Liu, C.; Kambe, Y.; Dong, B. X.; Burnett, V. F.; Dolejsi, M.; Grocke, G.; Patel, S. N.; Nealey, P. F. Interrogation of Electrochemical Properties of Polymer Electrolyte Thin Films with Interdigitated Electrodes. J. Electrochem. Soc. 2018, 165 (16), H1028–H1039.

(44) Jiang, Z.; Li, X.; Strzalka, J.; Sprung, M.; Sun, T.; Sandy, A. R.; Narayanan, S.; Lee, D. R.; Wang, J. The Dedicated High-Resolution Grazing-Incidence X-Ray Scattering Beamline 8-ID-E at the Advanced Photon Source. J. Synchrotron Radiat. 2012, 19 (4), 627–636.

(45) Jiang, Z. GIXSGUI: A MATLAB Toolbox for Grazing-Incidence X-Ray Scattering Data Visualization and Reduction, and Indexing of Buried Three-Dimensional Periodic Nanostructured Films. J. Appl. Crystallogr. 2015, 48 (3), 917–926.

(46) Spano, F. C. Modeling Disorder in Polymer Aggregates: The Optical Spectroscopy of Regioregular Poly(3-Hexylthiophene) Thin Films. J. Chem. Phys. 2005, 122 (23), 234701.

(47) Spano, F. C. Absorption in Regio-Regular Poly(3-Hexyl)Thiophene Thin Films: Fermi Resonances, Interband Coupling and Disorder. Chem. Phys. 2006, 325 (1), 22–35.

(48) Dong, B. X.; Liu, Z.; Misra, M.; Strzalka, J.; Niklas, J.; Poluektov, O. G.; Escobedo, F. A.; Ober, C. K.; Nealey, P. F.; Patel, S. N. Structure Control of a π-Conjugated Oligothiophene-Based Liquid Crystal for Enhanced Mixed Ion/Electron Transport Characteristics. ACS Nano. 2019, 13 (7), 7665–7675.

Chapter 5

Synthesis and characterization of redox-responsive disulfide-crosslinked polymer particles for energy storage applications

Abstract: Crosslinking poly(glycidyl methacrylate) microparticles with redox-responsive bis(5-amino-l,3,4-thiadiazol-2-yl) disulfide moieties yields redox active particles (RAPs) capable of electrochemical energy storage via a reversible 2-electron reduction of the disulfide bond. The resulting RAPs show improved electrochemical reversibility compared to a small molecule disulfide analogue in solution, attributed to spatial confinement of the polymer-grafted disulfides in the particle. Galvanostatic cycling was used to investigate the impact of electrolyte selection on stability and specific capacity. A dimethyl sulfoxide/magnesium triflate electrolyte was ultimately selected for its favorable electrochemical reversibility and specific capacity. Additionally, the specific capacity showed a strong dependence on particle size where smaller particles yielded higher specific capacity. Overall, these experiments offer a promising direction in designing synthetically facile and electrochemically stable materials for organosulfur-based multi-electron energy storage coupled with beyond Li-ion systems such as Mg.

5.1 Introduction

The development and use of organic materials that can be employed in the next generation of batteries has seen an increase in interest over the last decade or so. Such interest has been spurred by a number of factors,[1] such as the design/development of many redox-active organic molecules that offer competitive if not higher theoretical specific capacities than current inorganic electrode offerings.[2] Furthermore, the ability to systematically tune the structure of organic materials allows fine tuning of their electrochemical behavior/stability and the raw materials for organic systems are generally more abundant compared to many of the key metal oxides employed in inorganic systems, offering an advantage when considering renewable/sustainable technologies.

Disulfides are one class of redox active organic compounds that have been explored as possible alternatives to metal oxide cathode materials for lithium-ion batteries. The disulfide bond undergoes a reversible 2-electron reduction process (**Figure 5.1a**), making it an attractive candidate for energy-dense cathode materials.[3] Furthermore, the electrochemical properties of disulfides can be tuned via the selection of neighboring electron-withdrawing or -donating groups. As such a multitude of disulfide compounds have been investigated with an eye toward battery applications, including soluble dimers and oligomers, linear polymers, and networks.[4] Through such studies, 2,5-dimercapto-1,3,4-thiadiazole (DMcT) and its analogues have garnered particular interest as organosulfur compounds for cathode active materials.[5–9] Numerous studies over the years have demonstrated DMcT as an attractive candidate for lithium battery cathodes, switching between Li-S and disulfide states with high energy density and excellent cyclability. However, DMcT alone suffers from diffusion of the soluble active species away from the electrode, which degrades battery performance.[10–12]

Polymer-bound organosulfur compounds may offer a solution to this challenge. Covalently securing the organosulfur moiety to a scaffold material, such as a non-reactive polymer backbone, results in isolation of the electrode material to the cathode half-cell. This approach has been investigated in films of DMcT functionalized poly(3,4-ethylenedioxythiophene) (PEDOT).[9] However, it was found that the conductivity of PEDOT proved insufficient to adequately charge the entire thickness of the film.[13] A possible solution to this problem rests in the synthetic flexibility of polymer systems. The use of particulate morphologies for electrode active materials results in dramatically increased surface area to volume ratios relative to films and other monolith morphologies, and allows for simple blending with conductive additives, such as carbon black, to enhance electrical connectivity with the electrode substrate. This technique is utilized in current Li^+ ion battery metal oxide electrodes, and has been demonstrated with organic materials, for example, suspensions of polyaniline particles have been shown to charge more thoroughly than polyaniline films.[14] While inorganic electrode materials must be milled to reduce their size, an energetically-intensive process, colloidal polymerization techniques allow for facile synthesis of polymer particles with controlled size. Using particulate morphologies for polymeric redox-active materials has been successfully demonstrated in solid electrode batteries as well as in the emerging field of organic flow batteries.[15–22] This particulate-based modality presents a potential route for simple, modular synthesis of effective electrodes with disulfide active chemistries.

5.2 Results and Discussion

5.2.1 Synthesis of disulfide-crosslinked PGMA particles

Thus, the goal of this work is to explore the synthesis and redox behavior of disulfide containing colloids with an eye toward their use in energy storage applications. Poly(glycidyl methacrylate) (PGMA) was selected as the matrix polymer for this study as it is possible to access narrow dispersed colloidal particles using different polymerization techniques[23] and the epoxide group provides a functional handle for modular epoxy-amine “click” chemistry, allowing for a wide range of functional modifications to the polymer scaffold.[24] Dispersion polymerization was used to produce particles with two targeted sizes (ca. 710 and 1670 nm diameter, measured via scanning electron microscopy, SEM).[23] Hexamethylene diamine (HMDA) (1 wt%) was reacted with these particles to produce crosslinked polymer microspheres (P1).[25] Bis(5-amino-l,3,4-thiadiazol-2-yl) disulfide (1-SS-1) and bis(5-ethylamino-l,3,4-thiadiazol-2-yl) disulfide (2-SS-2) were selected as the disulfide-containing crosslinker and small molecule analogue for this study, and synthesized according to known procedures.[26] Functionalization of P1 with an excess of 1-SS-1 (5 equivalents 1-SS-1 per epoxy moiety) was carried out using a THF/DMSO co-solvent (tetrahydrofuran (THF) is a good solvent for PGMA and dimethyl sulfoxide (DMSO) provides solubility for 1-SS-1)[27] to yield P2 **(Figure 5.1b)**. Successful synthesis of P2 was determined by both Raman and FTIR. Raman of P2 confirmed the presence of disulfide in the system (**Figure 5.5a**), while FTIR monitored the ring-opening of the epoxides (**Figure 5.5b**).[28] Based on this analysis, it was determined that roughly 88% of the available epoxide groups in P1 reacted with 1-SS-1 to produce P2 (**Figure 5.6, Table 5.1**).

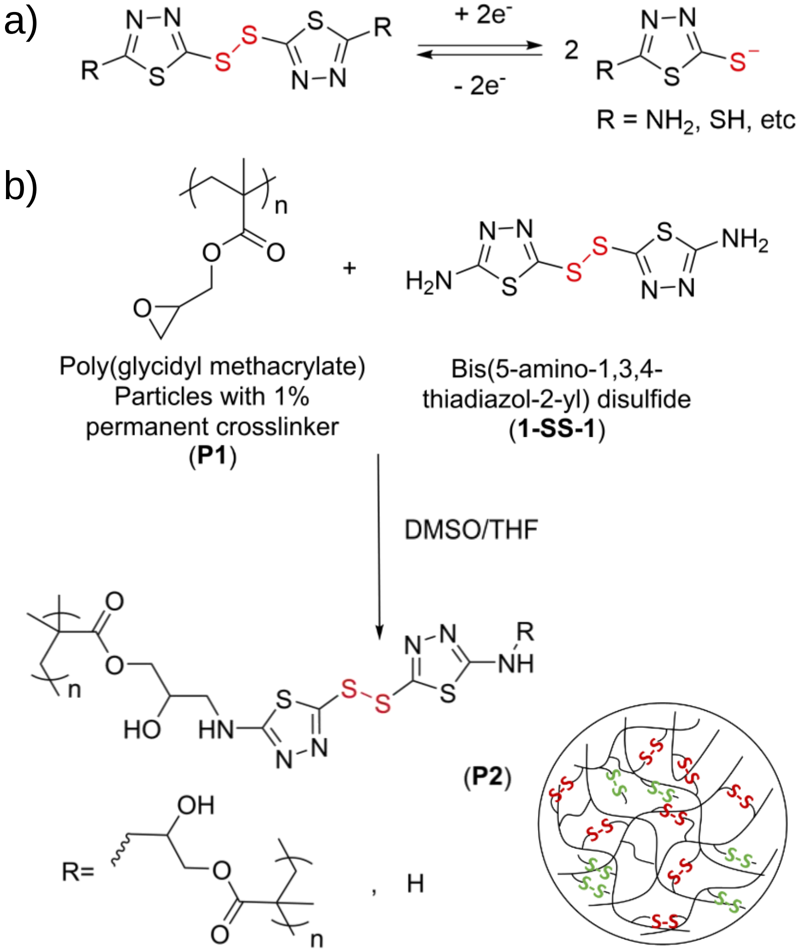

Figure 5.1. Design of disulfide-crosslinked particles. a) Reversible electrochemical reaction of thiadiazole-based disulfides. b) Reaction scheme for the synthesis of 1-SS-1-functionalized PGMA particles (P2) from PGMA particles with 1 wt. % HMDA permanent crosslinker (P1).

Given the relatively low reactivity of the aromatic amine and the large excess of 1-SS-1 used in the reaction, it can be expected that a significant percentage of the reacted 1-SS-1 would only be monofunctionalized to the polymer (x-SS-1) and thus not act as a crosslinker (**Figure 5.1b**, in green). In fact, dynamic light scattering of P1 and P2 showed that there is little-to-no change in the hydrodynamic diameter of the particles upon reaction with 1-SS-1 consistent with this expectation (**Table 5.3**). Removal of these x-SS-1 "loose ends" is critical to accessing electrochemically reversible redox particles, as cleavage of these groups would result in diffusion of the unbound redox-active molecules out of the particle.

5.2.2 DS-RAP crosslink densification by UV photoexcitation-induced dynamic exchange

It is known that disulfide bonds can undergo dynamic exchange with UV light.[29,30] As such it was hypothesized that removal of the x-SS-1 could be achieved by irradiation of the particles to induce disulfide exchange and result in the formation of additional disulfide crosslinks x-SS-x and free 1-SS-1, which can diffuse into the solvent (**Figure 5.2a**). Exposing the particles to UV light (350 mW/cm^2) in DMSO (which both swells the particles and is a good solvent for 1-SS-1) results in the liberation of 1-SS-1 into the solution. To monitor the removal of 1-SS-1, two UV annealing cycles were performed sequentially, and the supernatant was analyzed via UV-Vis at 322 nm to determine the concentration of released 1-SS-1 (**Figure 5.7**). Following each UV irradiation cycle, the particle suspensions were centrifuged, the supernatant was poured off before being replaced by fresh DMSO, and the next irradiation cycle performed. Results showed that no additional 1-SS-1 was detected in the solution during a second UV annealing process, consistent with the removal of x-SS-1 from P2 and the formation of the more densely crosslinked P2-SS containing only disulfide crosslinkers x-SS-x. This is further supported by dynamic light scattering (DLS) of P2-SS, which showed a decrease in diameter to 1731 ± 109 nm in acetonitrile (ACN), which is ca.

21% smaller compared to P2 (**Figure 5.2b**). In addition, the diameter of P2-SS was more consistent across different solvents (ACN, DMSO, and DMSO with salt) than P1 or P2, consistent with a denser crosslinking and demonstrating the effectiveness of the UV annealing technique (**Table 5.3**).

Following functionalization with 1-SS-1, approximately 12% of the PGMA epoxy groups remain unreacted within P2-SS based on FTIR integration data (**Figure 5.6)**. Epoxides are highly reactive electrophiles, and therefore it is desirable to passivate any residual groups. To this end, *N*-methylbutylamine was added to the particle and heated (**Figure 5.8**), where the removal of residual epoxides was confirmed by FTIR (**Figure 5.5**),[31] resulting in stabilized disulfide-functionalized redox-active particles (DS-RAP) as shown in **Figure 5.2c**. DLS data showed DS-RAPs swelled more in the organic solvents tested, presumably resulting from the addition of the aliphatic side groups (**Table 5.3**).

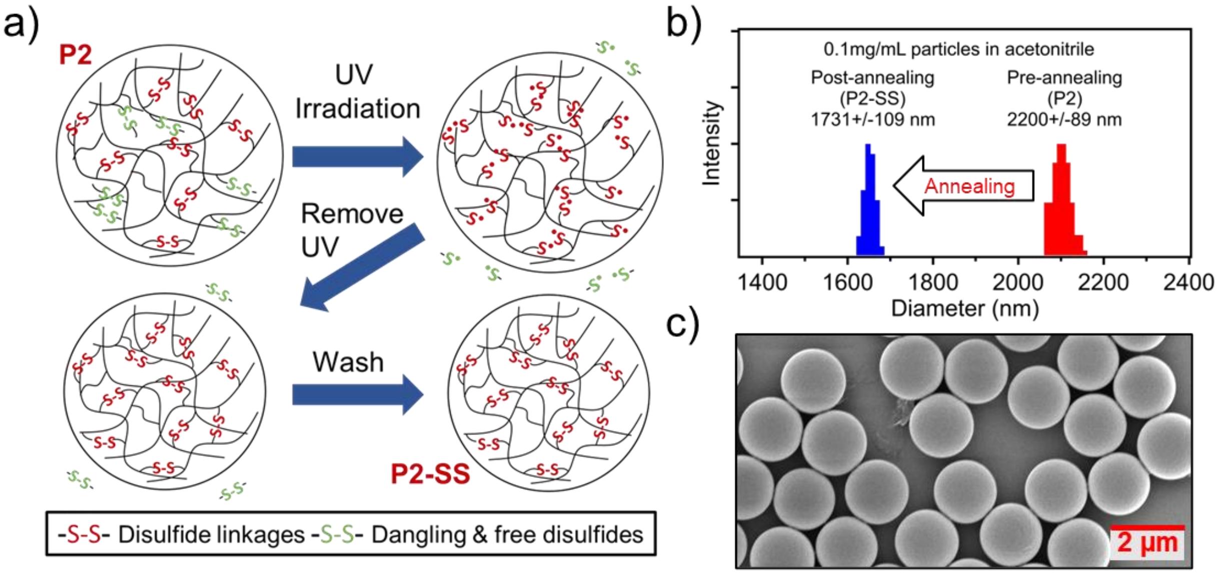

Figure 5.2. Densification of disulfide crosslinks. a) Scheme for UV annealing of P2 particles to remove dangling monofunctionalized x-SS-1. b) Particle size reduction after UV annealing as measured by dynamic light scattering (DLS) in acetonitrile (ACN). c) SEM image of DS-RAP.

5.2.3 Electrochemical Characterization of DS-RAP by CV Analysis

Cyclic voltammetry (CV) and galvanostatic cycling (GC) techniques were used to investigate the electrochemical properties of DS-RAP and compared to the soluble small molecule analog, bis(5-ethylamino-l,3,4-thiadiazol-2-yl) disulfide (2-SS-2). Carbon paper (CP) was selected as the working electrode as it allowed for the best electrochemical reversibility in CV experiments (**Figure 5.9a**). Specifically, solution CV of 2-SS-2 in ACN shows a reduction peak potential ($E_{p,r}$) at -0.79 V vs. Ag/Ag^{+} and an oxidation peak potential ($E_{p,o}$) at -0.39 V vs. Ag/Ag^{+}. Samples for the CV of DS-RAP were obtained by drop-casting from an ethanol suspension onto CP electrodes resulting in 0.2 mg/cm^{2} active material. DS-RAP exhibited an $E_{p,r}$ at -0.69 V vs. Ag/Ag^{+} and an $E_{p,o}$ at -0.41 V vs. Ag/Ag^{+} (**Figure 5.3a**) demonstrating a marked drop in peak to peak spacing (DE_{p}) of 0.28 V relative to the DE_{p} of 0.40 V for 2-SS-2. While the onset of the reduction process for both systems occurs at approximately -0.5 V vs. Ag/Ag^{+}, the more positive $E_{p,r}$ position and sharper peak profile quantitively indicate faster electrochemical kinetics for the DS-RAP particles at the electrode surface. These values total to an approximate 30% overall reduction in DE_{p}, suggesting the immobilization of x-SS-x on a polymer backbone as reversible crosslinks leads to a considerable increase in electrochemical reversibility. This conclusion is supported by the far greater difference between reduction peak current density ($i_{p,r}$) and oxidation peak current density ($i_{p,o}$) in the in 2-SS-2 small molecule when compared to RAP-SS. This can be rationalized by the fact that the reductively-cleaved small molecules are free to diffuse away from the electrode surface, preventing oxidation back to the disulfide during the return sweep (**Figure 5.3a, inset i**). In contrast, the disulfide moieties bound to the polymer are held in a relatively fixed position, keeping them in closer proximity to its cleaved partner (or other thiolates) and the electrode surface (**Figure 5.3a, inset ii**).

A second reductive process is observed in the particle system starting at approximately -0.8 V vs. Ag/Ag$^+$ and extending out to the maximum scan value of -1.2 V vs. Ag/Ag$^+$. To eliminate the possibility that the second reductive process is the result of irreversible reductive degradation, a series of control CV experiments were performed on a series of differently functionalized particles. P1 particles lacking x-SS-x showed no appreciable signal along the reduction sweep (**Figure 5.9b**). Additionally, a batch of P1 was reacted with excess HMDA crosslinker to ring-open the epoxide, resulting in densely crosslinked particles with redox-inert crosslinkers. These particles showed no electrochemical reactivity in the potential window of interest. As such, these control experiments suggest that both reductive processes in the DS-RAP particles are a consequence of the reductive cleavage of x-SS-x.

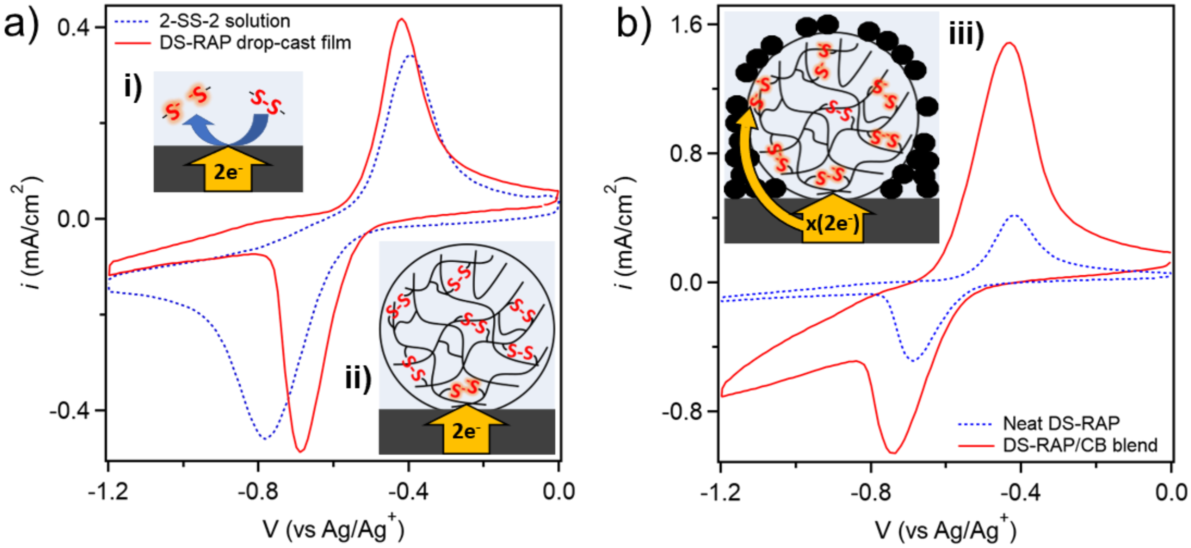

Figure 5.3. DS-RAP CV data with inset schemes. 100 mM tetrabutylammonium hexafluorophosphate ($TBAPF_6$)/ACN electrolyte, 20 mV/s scan rate. Potentials are relative to Ag/Ag$^+$ nonaqueous reference electrode. a) 2-SS-2 solution and drop-cast DS-RAP. b) Enhanced electrochemical response of DS-RAP by 1:1 by weight blending of Super P carbon black (CB).

The DS-RAP particles investigated in this study are electronically insulating. Thus, to increase electronic access, the DS-RAPs were blended with Super P carbon black (CB) particles

(1:1 by weight). For these blended samples, $i_{p,r}$ increased by an approximate factor of two, while the reduction current density increased more than five times across the potential range of -0.8 to -1.2 V vs. Ag/Ag$^+$. The value of $i_{p,o}$ was shown to increase much more than $i_{p,r}$, providing evidence that the reductive process at lower potentials is the result of continued disulfide reduction into the depth of the particle (**Figure 5.3b**). Overall, these CV results show that the DS-RAP particles blended with CB particles in the electrode are more readily accessed electrochemically.

5.2.4 Galvanostatic cycling of DS-RAP cathode composites

Galvanostatic cycling (GC) experiments were performed to test the feasibility of DS-RAPs as an energy storage material. Electrodes were prepared by casting 0.4 mg of 1:1 DS-RAP:CB from ethanol onto 1 cm^2 CP. All GC experiments were performed at a C-rate of 0.25 C (3.95 μA/cm^2) with potentials limits of -1.2 V to 0 V vs Ag/Ag$^+$ (ca. 2.4 V to 3.6 V vs Li/Li$^+$) using a 3-electrode electrochemical cell. **Figure 5.4a** shows a representative charge/discharge profile, while **Figure 5.4b** shows capacity and efficiency over multiple cycles. The DS-RAP synthesized in this study contains an estimated 39% x-SS-x by mass (compared to a theoretical maximum of 48%, assuming two epoxides per x-SS-x) (**Figure 5.10**), leading to a theoretical specific capacity of 79 mAh/g$_{\text{particle}}$, assuming a two-electron reduction process (**Equation 5.1, 5.2**). DS-RAP were initially tested using 1 M TBAPF$_6$ in ACN as the electrolyte. The initial cycle yielded a specific discharge capacity (SDC) of 4.81 mAh/g and Coulombic efficiency (CE) of 88.4 %. However, this system demonstrated a sharp initial decrease in capacity, along with further decrease over progressive cycles, resulting in an SDC of 2.97 mAh/g$_{\text{particle}}$ and CE of 83.7 % at cycle 50 (**Figure 5.11**).

Alternative solvents were explored for the electrolyte as a strategy to improve cycling stability. Of the multiple solvents investigated (**Table 5.4**), DMSO yielded stable cycling across the full 50 cycle range. The initial cycle yielded an SDC of 1.65 mAh/g and CE of 86.1 %. At cycle 50, the SDC remained stable at 1.65 mAh/g along with improvement in CE to 92.7 % **(Figure 5.11b)**. Comparison of the GC results between ACN and DMSO indicate that ACN is likely promoting an irreversible electrochemical reaction that leads to the capacity fade, while contributing to a portion of the specific charging capacity. While the cycling stability is improved in DMSO, the resulting SDC remains below that obtained in ACN. In order to address the low specific capacity of DS-RAP, the effect of particle size and supporting electrolyte salt selection were examined next.

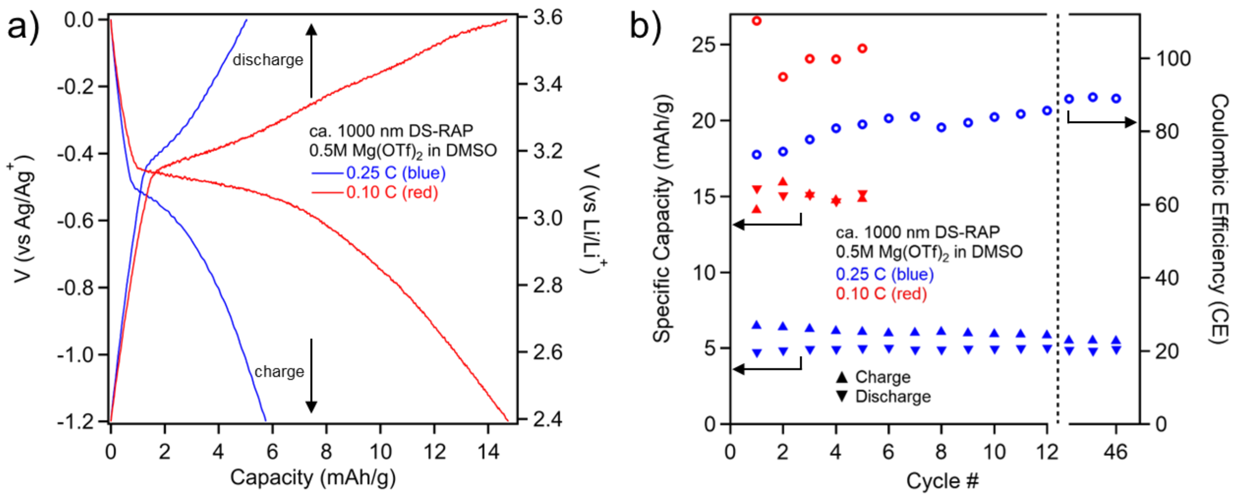

Figure 5.4. Galvanostatic cycling (GC) of DS-RAP (ca. 1000 nm) at a C-rate of 0.10 and 0.25C. a) Charge/discharge curves (cycle 3 for 0.10 C and cycle 46 for 0.25 C). Potential (V) vs Li/Li$^+$ is converted from Ag/Ag$^+$. b) Charge/discharge cycling stability and Coulombic efficiency (CE) data. The reported GC experiments were performed using DMSO with 0.5 M Mg(OTf)$_2$. Additional GC results can be found in **Figure 5.11** and **Table 5.5**.

As a route to further increase the specific capacity, DS-RAPs with a smaller diameter of ca. 711 nm (dry diameter via SEM) were synthesized (**Figure 5.12**) and cycled using TBAPF$_6$/DMSO electrolyte. This particle size approaches the lower limit that DS-RAP can be synthesized using the employed dispersion polymerization method. The new DS-RAP swelled to

1034 ± 57 nm in diameter in $TBAPF_6$/DMSO, compared to 1867 ± 46 nm for the larger particle. Notably, the GC results indicate that the SDC and CE are 3.32 mAh/g and 89.5 % at cycle 50, respectively. The 44.6% smaller DS-RAP exhibited double the SDC of the larger DS-RAP in the presence of $TBAPF_6$/DMSO, while maintaining similar CE at cycle 50 (**Figure 5.11d**). Moreover, the smaller DS-RAP maintains stable cycling across the full 50 cycles similar to the larger DS-RAP. The smaller particles reduce the characteristic diffusion length and have larger surface area to volume ratios, resulting in a larger portion of the particle to be electrochemically accessible as indicated by the improved SDC.

The selection of salt cation for the electrolyte was also shown to impact the cycling capacity. While $TBAPF_6$ is stable in electrochemical applications and highly soluble in many organic solvents, the bulky organic cation can limit diffusion into the particle and how it can stabilize the thiolates in the particle. $LiPF_6$ and KPF_6 were investigated but found to exhibit reduced electrochemical reversibility due to the greater positive potential needed to re-oxidize the thiolates (**Figure 5.9c**). Batteries based on divalent cations, such as Mg^{2+}, continue to garner interest on account of higher theoretical energy densities. Interestingly, unlike $LiPF_6$, magnesium triflate ($Mg(OTf)_2$) did not show substantially increased peak spacing relative to $TBAPF_6$ (**Figure 5.9d**). Thus, $Mg(OTf)_2$ was selected as an alternative to $TBAPF_6$. 0.5 M $Mg(OTf)_2$ DMSO solution was used on account of practical solubility limits. By using the $Mg(OTf)_2$/DMSO electrolyte, the GC experiments showed a SDC and CE of 4.94 mAh/g and 89.0 % at cycle 46, respectively (**Figure 5.11f, Table 5.5**). This SDC is a 49.7 % increase compared to the SDC when using $TBAPF_6$/DMSO, which could be explained, at least in part, by the divalent Mg^{2+} cation being able to neutralize two thiolate anions, reducing the number of cations needed to diffuse into the polymer matrix.

Given the relatively slow charge-transfer kinetics of the disulfide redox couple[5], the C-rate was lowered from 0.25 C used in the screening experiments to 0.10 C, resulting in a SDC of 15.21 mAh/g after 5 cycles, increasing capacity by over three times to 19.25% of theoretical. This result is in line with efficiencies from conceptually similar materials from recent works.[9,32]

5.3 Conclusions and Outlook

In summary, this work demonstrates a simple synthetic approach for disulfide-containing redox-active particles. Through epoxy-amine click chemistry, PGMA particles, prepared using dispersion polymerization, were functionalized with bis(5-amino-1,3,4-thiadiazole-2-yl) disulfide in which the disulfide behaves as a reversible crosslinker, resulting in densely-crosslinked particles with a theoretical capacity of 79 mAh/g. Cyclic voltammetry revealed that the incorporation of the of the disulfide into the particle resulted in improved electrochemical reversibility of the redox couple compared it its small molecule equivalent, reducing CV peak spacing by 30%. Moreover, galvanostatic cycling demonstrated potential use of this material as an energy storage material, using a Mg-based electrolyte to achieve high cycling stability, obtaining 15.21 mAh/g at 0.1 C, with high Coulombic efficiency. A specific discharge capacity reaching 19.25% of theoretical appears to be limited largely by particle size, offering direction for future improvement. Overall, this work shows a successful demonstration of a modular RAC platform and provides a tool for the design of organic battery materials, where spatial confinement of the redox-active material is a key consideration.

5.4 Materials and Methods

Materials. Glycidyl methacrylate (GMA) containing inhibitor, 5-amino-1,3,4-thiadiazole-2-thiol, hydrogen peroxide solution (30% w/w) in aqueous solution containing inhibitor;

polyvinylpyrrolidone (PVP) (average mol. wt 40,000), hexamethylenediamine, 4-ethyl-3-thiosemicarbazide, and carbon disulfide were purchased from Sigma-Aldrich. All other reagents were purchased from Fisher Scientific. All reagents were used without further purification unless mentioned.

Synthesis of PGMA particles (P1). Monodisperse PGMA particles (P1) were synthesized via dispersion polymerization. Two sizes were prepared using the following procedures:

Larger particles. Inhibitor was removed from GMA monomer by passing through a basic alumina column. 4 g PVP was dissolved in 102.7 mL of absolute ethanol and 7.42 mL of deionized water in a 250 mL round-bottom flask. The solution was heated to 70 °C and stirred at 165 rpm. The reaction vessel was sealed and purged for 20 min using filtered dry Ar gas. 0.2 g of AIBN was dissolved in 9.5 mL of GMA monomer and charged to the reaction vessel. The vessel was kept purged for an additional 10 minutes to ensure adequate removal of oxygen. The solution was reacted for 12 hours. The resulting particles were centrifuged, decanted, and washed with methanol. The process was repeated 3 times. The particles were then dried under vacuum and 9.04 g of product was obtained (89% yield).

Smaller particles were synthesized using similar procedures, with the following changes. The solvent was replaced by pure ethanol (100 mL), the monomer feed amount was decreased by half (4.75 mL) and the stirring speed was increased (320 rpm). 4.7 g of particles was obtained (92% yield).

Addition of permanent crosslinkers to PGMA particles. 4 g of particles was redispersed in 50 mL of EtOH in a bath sonicator. 1 wt% (40 mg) of hexamethylene diamine (HMDA) (relative to particle mass) was added to the dispersion in the form of 10 mg/mL HMDA ethanol solution and reacted at 50 °C for 24 hours. Particle size was measured by DLS and SEM. The resulting particles were dispersed in EtOH and freeze-dried before further functionalization. Same procedure was used on smaller particles.

Synthesis of disulfides (1-SS-1 and 2-SS-2). 12 g of 5-amino-l,3,4-thiadiazol-2-thiol was dissolved in 1000 mL of methanol while stirring. 90 mL of 30% aqueous hydrogen peroxide was added dropwise over 45 min. A resulting yellow solid was formed after approximately 2 hours, which was collected by filtration and washed extensively with methanol before being dried under vacuum overnight to yield ca. 11 g of bis(5-amino-l,3,4-thiadiazol-2-yl) disulfide (**1-SS-1**) was obtained with 91.6% yield. ^{1}H NMR (400 MHz, DMSO-d6) δ 7.76 (s, 4H). ^{13}C NMR (400 MHz, DMSO-d6) δ 172.68, 149.15.

11.9 g (0.1 mol) of 4-ethyl-3-thiosemicarbazide was added into 130 mL of EtOH with 4 g (0.1 mol) of sodium hydroxide. 7.6 g (0.1 mol) of carbon disulfide was added to the solution and heated to reflux overnight. The solution was dried in vacuum and yellow solid was obtained. The yellow solid was dissolved in 30 mL of water. Concentrated HCl was added dropwise until the pH of solution was below 2. A white precipitated was formed and filtered. The precipitate was washed with water and dried under vacuum. 11.5 g of product was obtained (71% yield). ^{1}H NMR (400 MHz, DMSO-d6) δ 13.27 (s, 1H), 7.54-7.51 (t, 1H), 3.18-3.12 (m, 2H), 1.14-1.10 (t, 3H). ^{13}C NMR (400 MHz, DMSO-d6) δ 180.89, 161.20, 38.78, 14.45.

Bis(5-ethylamino-l,3,4-thiadiazol-2-yl) disulfide (**2-SS-2**) was synthesized from the above product by the same oxidation procedure as 1-SS-1 with 65% yield. ^{1}H NMR (400 MHz, DMSO-d6) δ 8.26-8.23 (t, 2H), 3.36-3.29 (m, 4H), 1.20-1.16 (t, 6H). ^{13}C NMR (400 MHz, DMSO-d6) δ 172.56, 149.02, 40.05, 14.58.

Functionalization of P1 with 1-SS-1 to produce P2. 1 g (7 mmol) of P1 particles were dispersed in 50 mL of THF via bath sonication. 1-SS-1 (9.30 g, 35 mmol) was dissolved in 100 mL of DMSO and charged into a reaction vessel. The reaction was carried out at 66°C at 300 rpm for 6 days. The particles were then washed with fresh 1:1 DMSO/methanol solution and centrifuged at 4000 rpm for 15 min, after which the supernatant decanted and the washing process repeated 6 times until no unreacted 1-SS-1 was released into the decanted supernatant, as measured by UV-Vis at 325 nm, attributed to the 1-SS-1 small molecule in solution.

UV annealing to remove monofunctionalized 1-SS-1 from P2 to produce P2-SS. A calibration curve was constructed by serial dilution of **1-SS-1** solution in DMSO measured via UV-Vis at 325 nm. 500 mg of P2 was added to 50 mL of DMSO to prepare a 10 mg/mL particle dispersion. The P2 dispersion was sonicated with a bath sonicator for greater than 1 hour. The vial was irradiated with a UV source at 350 mw/cm^2 while stirring. 1 mL of dispersion was taken every 20 min and centrifuged at 6000 rpm to pellet particles. 40 μL of decanted supernatant was taken and was passed through a 0.45 μm filter while the particle pellet was redispersed by bath sonicator and recombined into the bulk dispersion with the addition of 40 μL fresh DMSO. The filtered decanted solvent was then diluted 10 times and measured by UV-Vis. By monitoring the peak at 325 nm, the amount of 1-SS-1 small molecule released to the supernatant from UV annealing process could be determined based on the calibration curve. The process was continued until the amount of 1-SS-1 in solution plateaued. After the first annealing process, the particles were washed and centrifuged again with 1:1 methanol and DMSO. The signature peak of 1-SS-1 was not detectable during a second UV annealing process. After washing and centrifugation with methanol and water, the particles (P2-SS) were dried under vacuum before secondary amine functionalization.

N-methylbutylamine functionalization of P2-SS to produce DS-RAP. 500 mg of P2-SS was dispersed in 50 mL of EtOH in a bath sonicator for 40 min until a homogeneous dispersion was obtained. 500 mg (5.7 mmol, 9 eq. relative to the 12% remaining P2-SS residue epoxides calculated by FTIR integration) of N-methylbutylamine was added to the reaction vessel and the reaction was carried at 50 °C for 2 days. The product was centrifuged, washed with methanol, and the supernatant was decanted. Resulting DS-RAP particles were dried under vacuum overnight. The removal of remaining epoxides was confirmed by FT-IR and the preservation of disulfide was confirmed by Raman.

Synthesis of P1-HMDA control particles. 50 mg (~0.35 mmol GMA repeating units) of dry larger PGMA particles without permanent crosslinker were dispersed in 10 mL of ethanol and sonicated for 1 hour. 20 mg (0.175 mmol) of HMDA was added in the form of 10 mg/mL HMDA ethanol solution. The reaction was carried out at 300 rpm and 70 ºC for 1 day. The resulting particle dispersion was centrifuged, decanted, and washed with methanol. The process was repeated 3 times. The particles were then dried under vacuum and 40.6 mg of product was obtained (57% yield).

Dynamic Light Scattering. DLS measurements were performed using a Brookhaven Instruments BI-200SM. The dry particle samples were dispersed in a 1 mg/mL concentration using bath sonication for a minimum of 1 hour and then diluted to 0.1 mg/mL dispersion prior to measurement. The viscosity parameters of electrolyte solution used for DLS was measured by a TA Instruments ARES-G2 shear rheometer using a cup geometry with a shear rate range from 1 to 200 s^{-1}. Applicable viscosity data can be found in **Table 5.2**.

UV-Vis Spectroscopy. A Shimadzu UV-3600 Plus UV-Vis-NIR spectrophotometer was used to measure from 250 nm to 500 nm with a sampling interval of 1 nm. All sample solutions or dispersions were made using DMSO as the supporting solvent. 0.05 mg/mL suspensions of DS-RAP were used for particle characterization.

FT-IR. Shimadzu IRTracer-100 FT-IR with ATR diamond was used to characterize P1, P2-SS, and DS-RAP. A minimum of 10 mg particle powder was placed directly onto the attenuated total reflection (ATR) crystal. The amount of unreacted epoxide group was quantified by integrating peaks 846 cm^{-1} and 905 cm^{-1}, corresponding to symmetric and asymmetric stretching of the epoxide group. The signal was normalized to the amount of PGMA monomer by integrating the peak at 1760 cm^{-1} corresponding to the PGMA carbonyl. Peaks were fit to a Voight model using Igor Pro multi-peak fitting.

Raman Spectroscopy. A Horiba LabRAM HR Evolution confocal Raman microscope was used with 50X LWD objectives, 10% filter, and 532 nm laser for Raman measurements. Sample powders (ca. 10 mg per sample) were pressed into a pellet on standard glass microscope slide.

Scanning Electron Microscopy.

Bare particles. Silicon substrate was cut into 1cm*1cm squares and washed via sonication in acetone followed by methanol. 50 microliters of 1 mg/mL particle dispersions in ethanol were cast onto the silicon substrates and allowed to air dry.

Composite electrodes. 1:1 DS-RAP/CB samples containing a total of 0.2 mg DS-RAP were cast onto carbon paper electrodes. After galvanostatic cycling, electrodes were cleaned by soaking in clean acetonitrile (ACN) twice followed by drying in a convection oven at 60 °C.

A Cressington 208HR Sputter Coater was used to coat 8 nm of Pt/Pd to prevent sample surface charging during imaging. A Carl Zeiss Merlin SEM was used to image the particles samples at 3 kV EHT.

Cyclic Voltammetry (CV). A Biologic SP-200 potentiostat was used for all electrochemical measurements. All tests were performed using a standard 3-electrode electrochemical cell. 1 cm^2 of Sigracet GDL 39 AA carbon paper (CP) was selected as the working electrode from a selection of different porous carbon substrates based on the relative reversibility of the 1-SS-1 redox couple (**Figure 5.9a**). The CP was attached to a Pt wire electrode (CH Instruments CHI115) by threading the wire through two small holes created near opposing edges of the CP sample. The counter electrode was a bare Pt wire. A non-aqueous Ag/Ag^+ reference electrode was used, comprised of a silver wire immersed in 0.01 M $AgNO_3$ and 0.1 M tetrabutylammonium hexafluorophosphate ($TBAPF_6$) in ACN. 20 µL of DS-RAP particles in a 10 mg/mL ethanol suspension (0.2 mg total DS-RAP mass) were drop-cast onto CP electrodes and allowed to dry. For blended samples, Super P carbon black (CB) was mixed with the DS-RAP in ethanol in a 1:1 mass ratio. 40 µL of the 1:1 suspension, containing 5 mg/mL of each DS-RAP and CB, were drop-cast onto CP electrodes, resulting in the same 0.2 mg total DS-RAP mass. All data presented was measured at 20 mV/s. Solvents for electrochemical experiments were degassed by sparging with Ar gas. All salts were used as-received and stored under Ar gas.

Galvanostatic Cycling (GC) Experiments. Samples were prepared in a similar manner to CV experiments. 1:1 DS-RAP/CB samples containing a total of 0.2 mg DS-RAP were cast onto CP electrodes and immersed in selected supporting electrolyte. A bare carbon felt electrode was attached to a Pt wire for use as the counter electrode, and a nonaqueous Ag/Ag^+ reference electrode was used. Samples were equilibrated for 12 hours prior to cycling.

5.5 Appendix

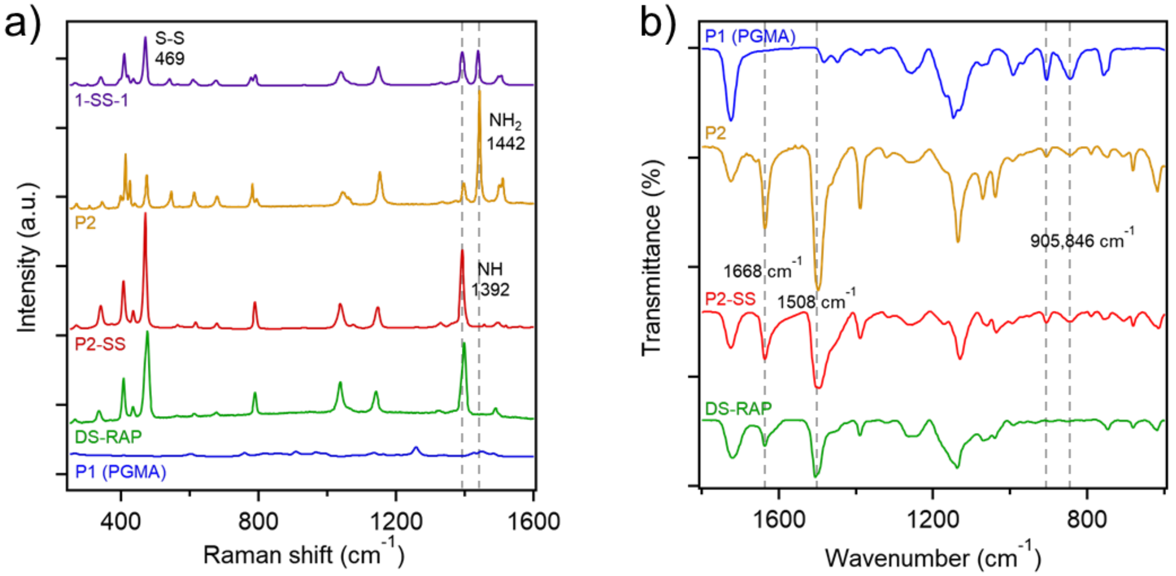

Figure 5.5. Raman and FT-IR spectra of P1, 1-SS-1, P2-SS, and DS-RAP. a) Raman spectra and b) FT-IR spectra with labeled peaks of interest.

Raman of DS-RAP confirms the presence of disulfide bonds via an observed characteristic peak at 469 cm^{-1}, indicating their successful retention in the particle system after UV annealing, and providing evidence for the covalent attachment of 1-SS-1 to the PGMA polymer backbone. The lack of a prominent characteristic NH_2 amine peak at 1442 cm^{-1} and concurrent increase of NH amine peak at 1392 cm^{-1} in DS-RAP provide further confirmation of functionalization of the disulfide moiety onto particles and removal of monofunctionalized 1-SS-1 from P2.

FTIR peaks centered at 846 cm^{-1} and 905 cm^{-1} correspond to the symmetric and asymmetric stretching of the epoxide group, respectively. A characteristic carbonyl peak at 1722 cm^{-1} was observed for particles of all functionalization state. Peaks centered at 1668 cm^{-1} and 1508 cm^{-1} are attributed to N-H bending resulting from amination of epoxide groups.

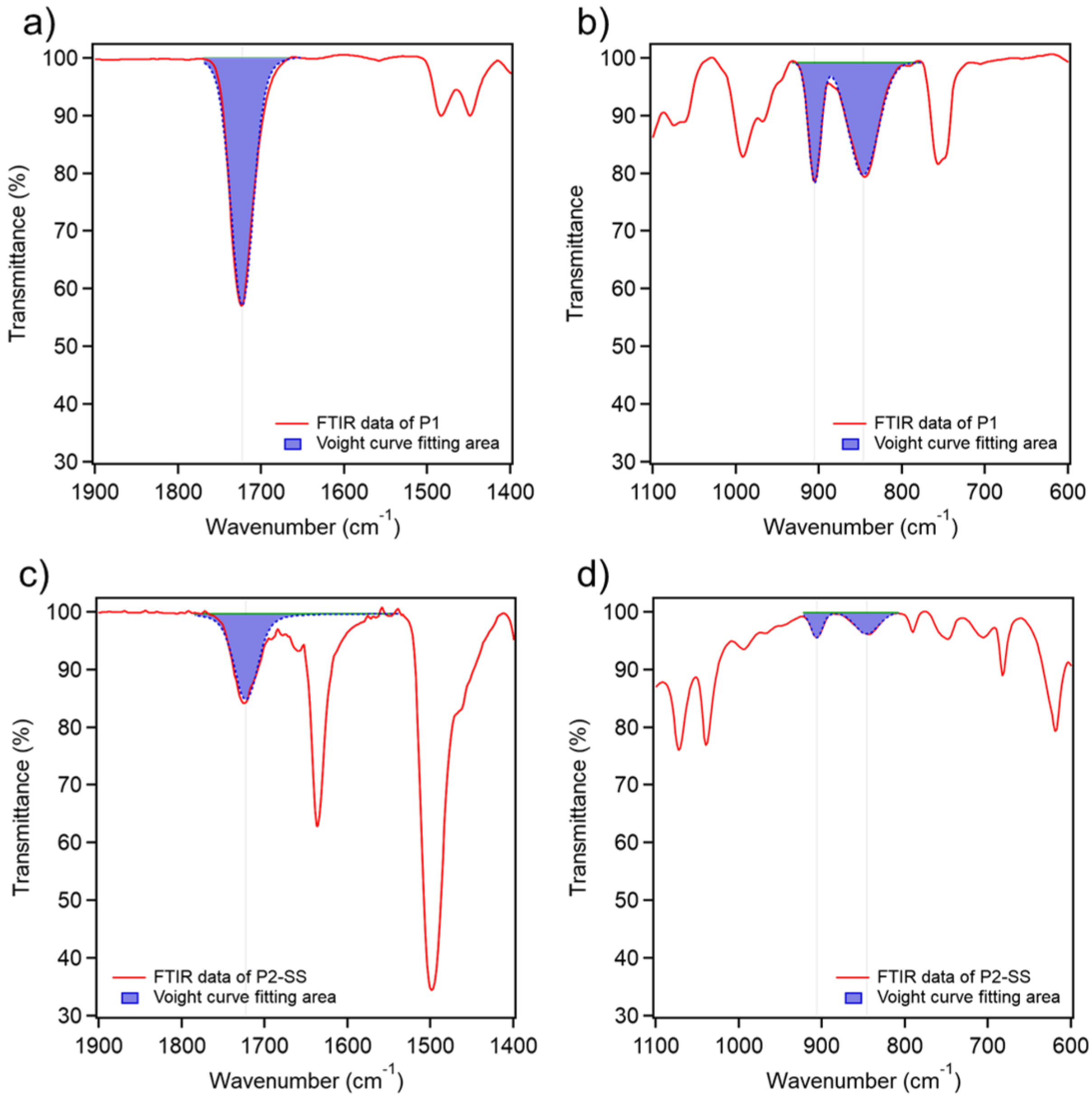

Figure 5.6. FT-IR Voight curve model fitting of a) carbonyl group of P1, b) epoxide group of P1, c) carbonyl group of P2-SS, and d) epoxide group of P2-SS.

Table 5.1. Peak area integration data for P1 and P2-SS FT-IR Voight curve model fitting.

	Area (1722 cm^{-1}) (carbonyl)	**Normalization factor (α)**	**Area (846 cm^{-1}) (symm. epoxide)**	**$j = \alpha$*area (846 cm^{-1})**	**% res. epoxide (j_X/j_{PI})**
P1	972	1	674	674 (j_{P1})	1
P2-SS	1168	1.202	108	89.877 ($j_{PS\text{-}SS}$)	0.133

	〃	〃	**Area (906 cm^{-1}) (asymm. epoxide)**	**α*area(906 cm^{-1})**	**% res. epoxide (j_X/j_{PI})**
P1	〃	〃	267.89	267.89 (j_{P1})	1
P2-SS	〃	〃	36	29.959 ($j_{PS\text{-}SS}$)	0.112

% residual epoxide (estimated from average) = 12.25%

Peak area values for carbonyl stretching (1722 cm^{-1}), epoxide symmetric bending (846 cm^{-1}), and epoxide asymmetric bending (906 cm^{-1}) were obtained from FT-IR profiles. Data was normalized to the carbonyl peak area for P1. The amount of residual epoxide in P2-SS after 1-SS-1 functionalization was determined by the average change in normalized epoxide peak area for the symmetric and asymmetric bending peaks.

The area of the carbonyl stretching peak was used as the basis of normalization for amount of particle present in each measurement, as the amount of carbonyl is directly correlated to the amount of PGMA in sample. The area of each epoxide peak was normalized by this factor, yielding value *j*. The percent remaining epoxide was determined by dividing the normalized epoxide peak area after amination by the normalized value for the pre-amination sample.

Table 5.2. Viscosity values of electrolyte solvents for DLS measurement parameters

Solvent	Viscosity	Reference
ACN	0.334 cP (mPa*s)	33
ACN, 1M $TBAPF_6$	0.799 cP (mPa*s)	Measured for this work
DMSO	1.991 cP (mPa*s)	34
DMSO, 1M $TBAPF_6$	4.490 cP (mPa*s)	Measured for this work
DMSO, 0.5M $Mg(OTf)_2$	5.393 cP (mPa*s)	Measured for this work

Table 5.3. Particle diameters from DLS measurements for P1, P2, P2-SS, and DS-RAP in different solvents and electrolytes.

Larger particle state	P1 (nm)	P2 (nm)	P2-SS (nm)	DS-RAP (nm)
Dry (via SEM)	1672 ± 33	1685 ± 47	1680 ± 21	1723 ± 65
ACN	2198 ± 142	2200 ± 89	1731 ± 109	1894 ± 85
ACN w/ 1M $TBAPF_6$	2086 ± 142	2058 ± 99	1738 ± 69	1956 ± 45
DMSO	2149 ± 138	2364 ± 54	1793 ± 105	1903 ± 130
DMSO w/ 1M $TBAPF_6$	2035 ± 100	2018 ± 117	1736 ± 130	1867 ± 46
DMSO w/ 0.5M $Mg(OTf)_2$	2162 ± 130	2160 ± 229	1734 ± 83	1885 ± 27
Smaller particle state	**P1 (nm)**	**P2 (nm)**	**P2-SS (nm)**	**DS-RAP (nm)**
Dry (via SEM)	711 ± 10	705 ± 20	694 ± 2	796 ± 13
ACN	1316 ± 48	1298 ± 89	716 ± 168	1338 ± 26
ACN w/ 1M $TBAPF_6$	1241 ± 32	1381 ± 86	776 ± 69	1270 ± 113
DMSO	1408 ± 88	1377 ± 63	776 ± 78	1011 ± 73
DMSO w/ 1M $TBAPF_6$	1348 ± 138	1402 ± 56	738 ± 74	1034 ± 57
DMSO w/ 0.5M $Mg(OTf)_2$	1371 ± 60	1416 ± 77	783 ± 61	1013 ± 44

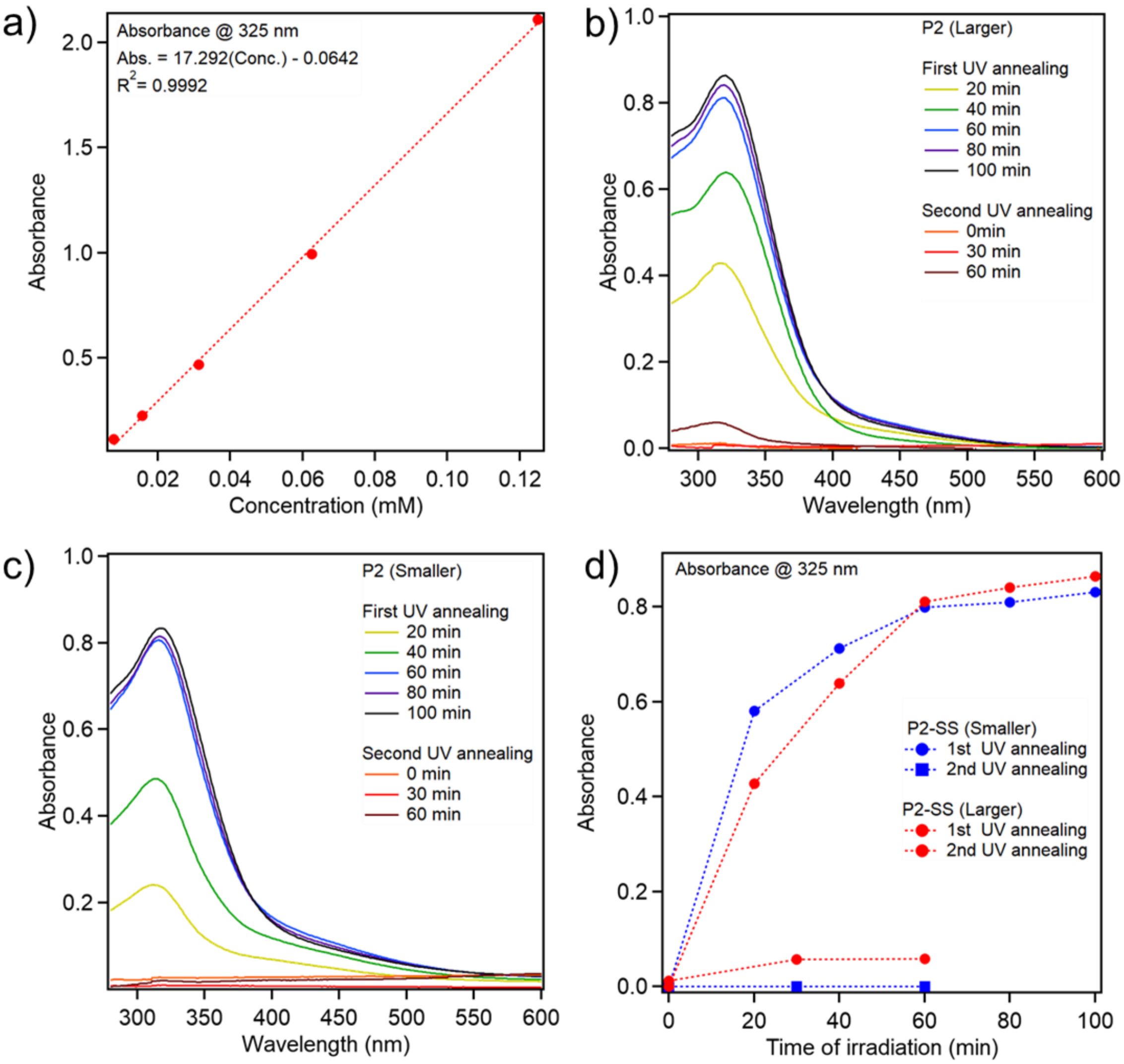

Figure 5.7. Quantification of 1-SS-1 small molecule released during UV annealing. a) UV-Vis calibration curve of 1-SS-1 in DMSO. b) UV-Vis measurements of 1-SS-1 in DMSO supernatant solution taken at various time points during UV annealing on P2-SS (larger) and c) (smaller). d) UV-Vis of supernatant solution to monitor the release of 1-SS-1 small molecule from P2 into solution during UV.

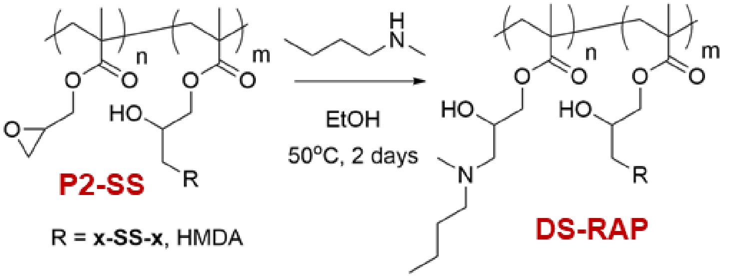

Figure 5.8. Reaction scheme for epoxy ring-opening in P2-SS particles using *N*-methylbutylamine to produce DS-RAP.

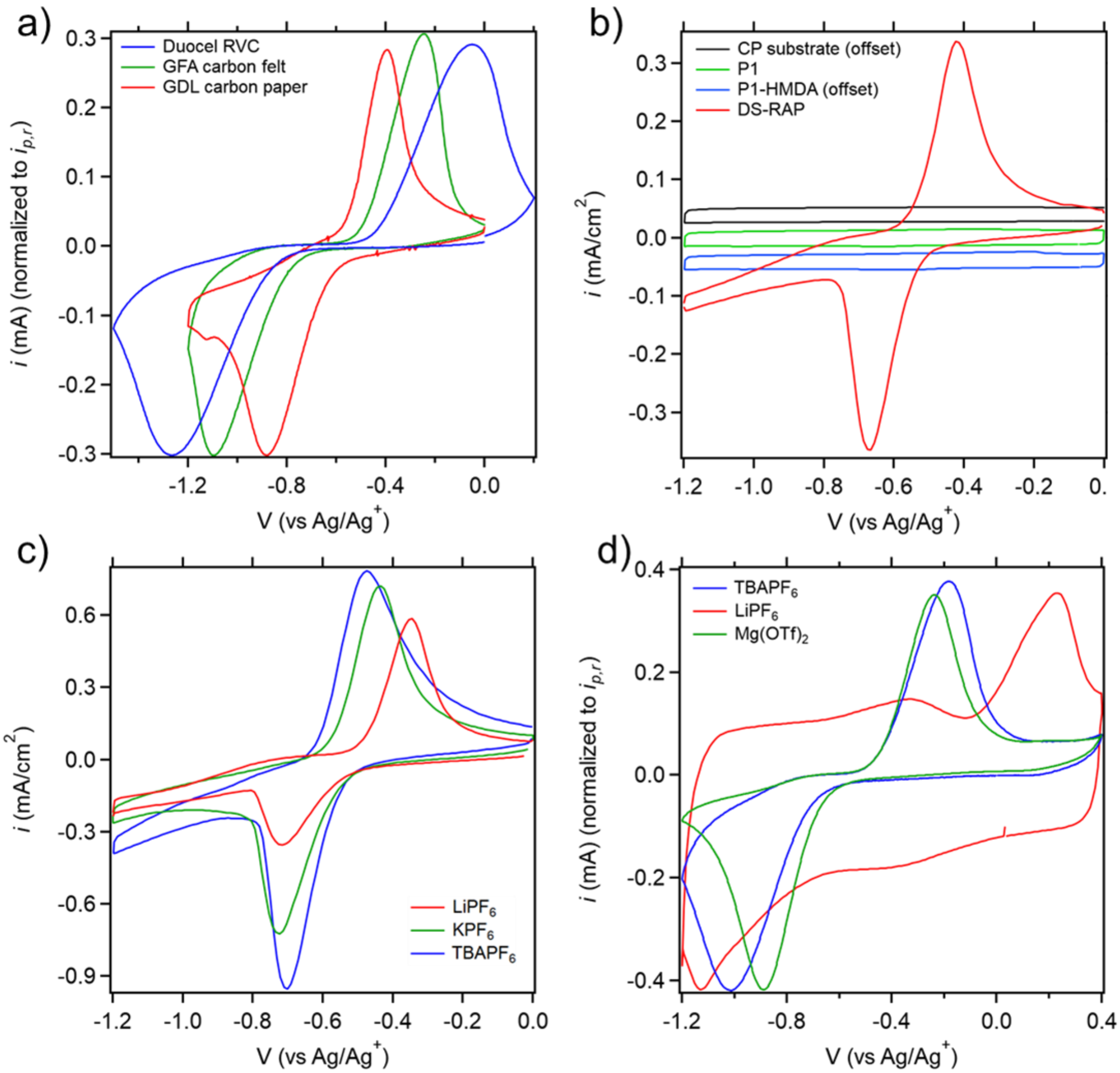

Figure 5.9. Cyclic voltammetry (CV) data for electrode selection and electrochemical reactivity. a) CV data for 2-SS-2 on different carbon electrodes. b) CVs for PGMA particles with or without x-SS-x, in multiple states of functionalization. CV profile for CP substrate and P1-HMDA were offset for clarity. c) CV data for larger DS-RAP using different electrolyte salts at 0.1 M concentration in ACN. d) CV data for larger DS-RAP using TBAPF$_6$, LiPF$_6$, or Mg(OTf)$_2$ at 0.1 M concentration in DMSO. All measurements were performed at 20 mV/s. Single cycle data is shown at cycle > 5 to allow for equilibration.

Electrode Selection. As shown in **Figure 5.9a**, the reactivity of the 1-SS-1 redox couple is electrode material-dependent.[35-37] Taking this into consideration, multiple electrode materials were tested: reticulated vitreous carbon (100 pores per inch, Duocel), carbon felt (Sigracell GFA 6 EA, SGL Carbon), and high temperature treated carbon fiber paper (Sigracet GDL 39 AA, SGL Carbon). Carbon paper (CP) was cut to 1 cm^2 pieces, while RVC and carbon felt electrodes were cut to 1´1´0.5 cm. All electrodes were mounted to Pt wire electrodes. CV traces for **Figure 5.9a** were normalized to peak reduction current density (i_p) to aid visualization of the peak positions. Data is reported for cycle 5, allowing for stabilization of reduction product species concentration.

Electrolyte Selection for CV Measurements. Impact of electrolyte salt cation selection on DS-RAP was investigated using CV with 0.1 M salt in ACN (**Figure 5.9c**). The smaller alkali metal salts ($LiPF_6$, KPF_6) demonstrated reduced electrochemical reversibility as determined by the larger peak spacing compared to $TBAPF_6$. This is attributed to strong association of the metal cation to the reduced state thiolate anion, and resulting additional oxidative potential needed to re-oxidize the thiolate. The larger TBA^+ cation associates less strongly to the thiolate anion, resulting in easier recombination of neighboring thiolate anions to a disulfide during oxidation. A similar study was used for the selection of metallic cation salt in DMSO (**Figure 5.9d**). Using $LiPF_6$ results in large peak spacing compared to the $Mg(OTf)_2$. While reduction onset potentials remain consistent compared to those in ACN (ca. -0.6 V), the positive shift in the oxidation onset potential for $LiPF_6$ is exacerbated by the switch in solvents, also seen in $TBAPF_6$ in DMSO vs ACN (**Figure 5.9c**). CV traces for **Figure 5.9d** were normalized to peak reduction current density (i_p) to aid visualization of the peak positions.

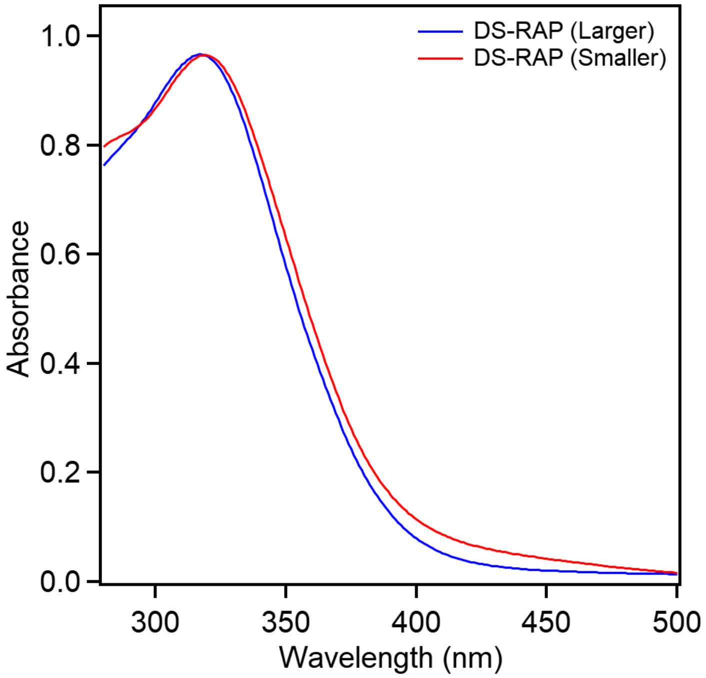

Figure 5.10. UV-Vis absorbance spectra for covalently-bound x-SS-x in DS-RAP dispersion.

Quantifying Level of Disulfide Crosslinker Functionalization. UV-Vis spectra was used to analyze the amount of functionalized disulfide crosslinkers via x-SS-x absorption for DS-RAP dispersions **(Figure 5.10)**. A low concentration of DS-RAP ($C_{particle}$ = 0.05 mg/mL) was required to avoid broadening resulting from scattering caused by large particle sizes.[38] Concentration of x-SS-x in DS-RAP (C_{DS}, mM, as determined by UV-Vis) multiplied by the molecular weight of x-SS-x (Mw = 264.26 g/mol) yields concentration of x-SS-x in dispersion as part of the particle (mg/mL). Dividing the concentration of x-SS-x by the concentration of DS-RAP particles yields the mass% of x-SS-x in DS-RAP (**Equation 5.1**).

$$\boldsymbol{mass\%_{x-SS-x} = \frac{C_{DS} \times 264.26\ g/mol}{C_{particle}}} \qquad (\boldsymbol{Eq. 5.1})$$

The mass% of x-SS-x contained in DS-RAP was calculated to be 38% and 39% for smaller and larger DS-RAP, respectively, compared to a theoretical maximum of 48%. The mole percentage of x-SS-x contained in DS-RAP could be calculated as well. 2 wt% of HMDA is subtracted from the remained mass of PGMA. The mole% of x-SS-x contained in DS-RAP is 25% and 26% for smaller and large DS-RAP, respectively (33% theoretical maximum).

Calculation of Theoretical Specific Capacity. The theoretical capacity of a charge storage material in mAh/g is calculated by **Equation 5.2**.

$$\boldsymbol{Q_{theoretical} = \frac{nF}{3600 \times Mw_{x-SS-x}} \times mass\%_{x-SS-x} \quad (Eq. 5.2)}$$

The theoretical specific capacity of 1-SS-1 is 203 mAh/g. Taking the mass% of x-SS-x contained in DS-RAP as 38 and 39%, the theoretical capacity of DS-RAP is calculated to be 78 mAh/g and 79 mAh/g for smaller and larger DS-RAP, respectively.

Table 5.4. Qualitative observations for screening of non-selected electrolyte solvents.

Solvents screened	**Observations**
Acetonitrile	Relatively low efficiency, GC curve suggests degradation
Propylene carbonate	Very low capacity, reductive degradation (observed in GC curve)
Dimethyl sulfoxide	Relatively low capacity, but high cycling stability and efficiency
Tetrahydrofuran	Very poor efficiency, suggestive of solvent degradation (via GC)
Ethylene carbonate/ dimethyl carbonate	Degradation at oxidative potentials approaching zero (via GC)

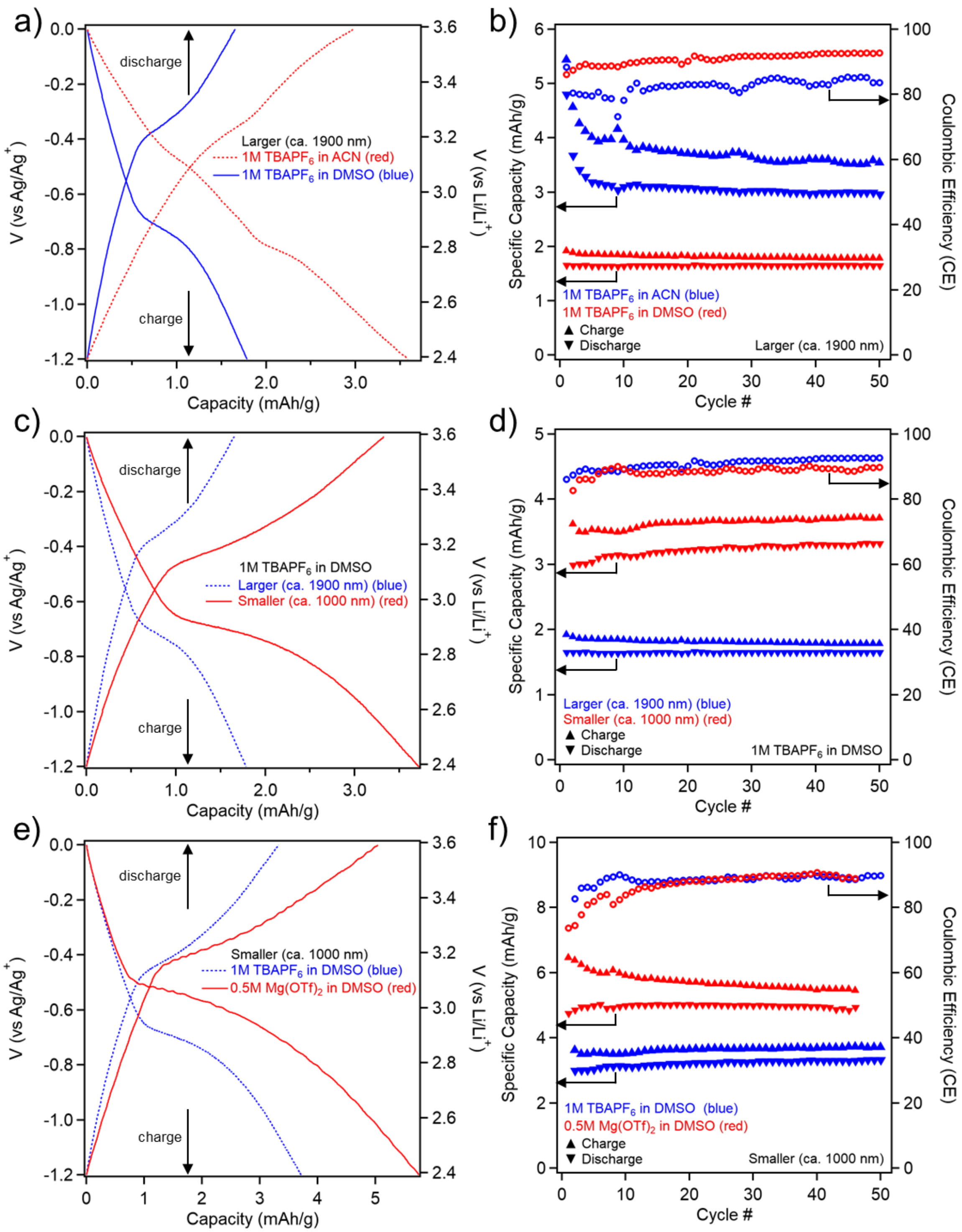

Figure 5.11. Galvanostatic cycling (GC) of DS-RAP using different cell preparations at a C-rate of 0.25C. Potential (V) vs Li/Li$^+$ is converted from Ag/Ag$^+$. a) Charge/discharge curves and b) charge/discharge specific capacity and Coulombic efficiency (CE) data for ca. 1900 nm DS-RAP with 1 M $TBAPF_6$ in ACN or DMSO, c,d) for ca. 1000 nm or ca. 1900 nm DS-RAP with 1 M $TBAPF_6$ in DMSO, and e,f) for ca. 1000 nm DS-RAP with 1 M $TBAPF_6$ or 0.5 M $Mg(OTf)_2$ in DMSO. All particle diameters are from measured values in their respective electrolyte (**Table 5.3**).

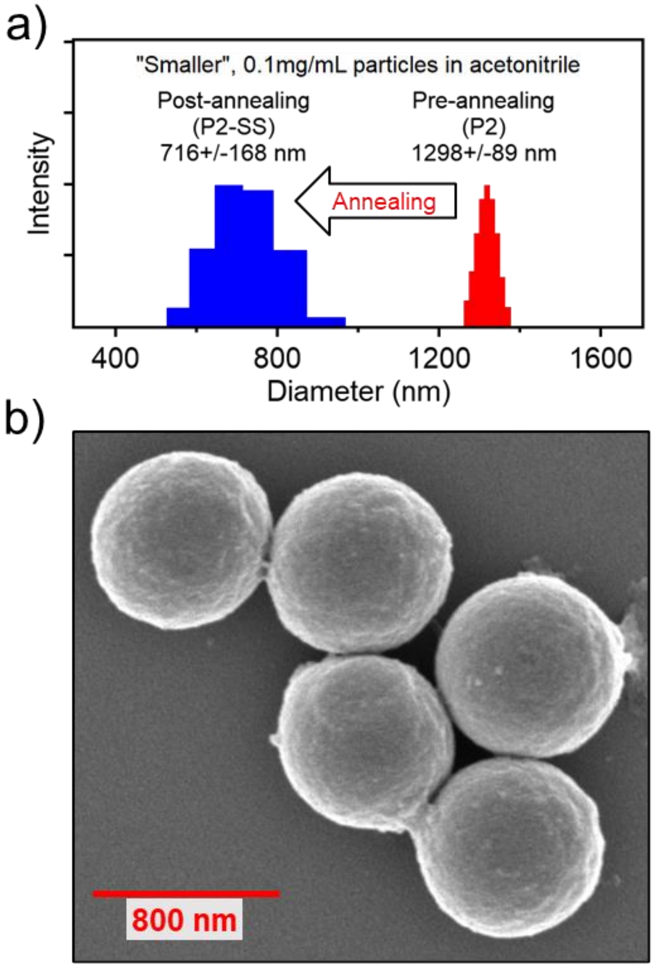

Figure 5.12. Particle size change characterization and scanning electron microscopy (SEM) imaging for smaller DS-RAP. a) Particle size reduction after photo-annealing as measured by dynamic light scattering (DLS) in acetonitrile (ACN) for smaller particles. b) SEM images of smaller DS-RAP particles.

Table 5.5. Summary DS-RAP specific discharge capacity (SDC) and Coulombic efficiency (CE) results under different conditions (0.25C C-rate).

Electrolyte	Diameter (nm)	C-rate	SDC (mAh/g)	Coulombic efficiency (%)
$TBAPF_6$/ ACN	1956 ± 45	0.25	2.97	83.7
$TBAPF_6$/ DMSO	1867 ± 46	0.25	1.65	92.7
$TBAPF_6$/ DMSO	1034 ± 57	0.25	3.32	89.5
$Mg(OTf)_2$/ DMSO	1013 ± 44	0.25	4.94	89.0
$Mg(OTf)_2$/ DMSO	1013 ± 44	0.10	15.21	Not stabilized

a) Before cycling

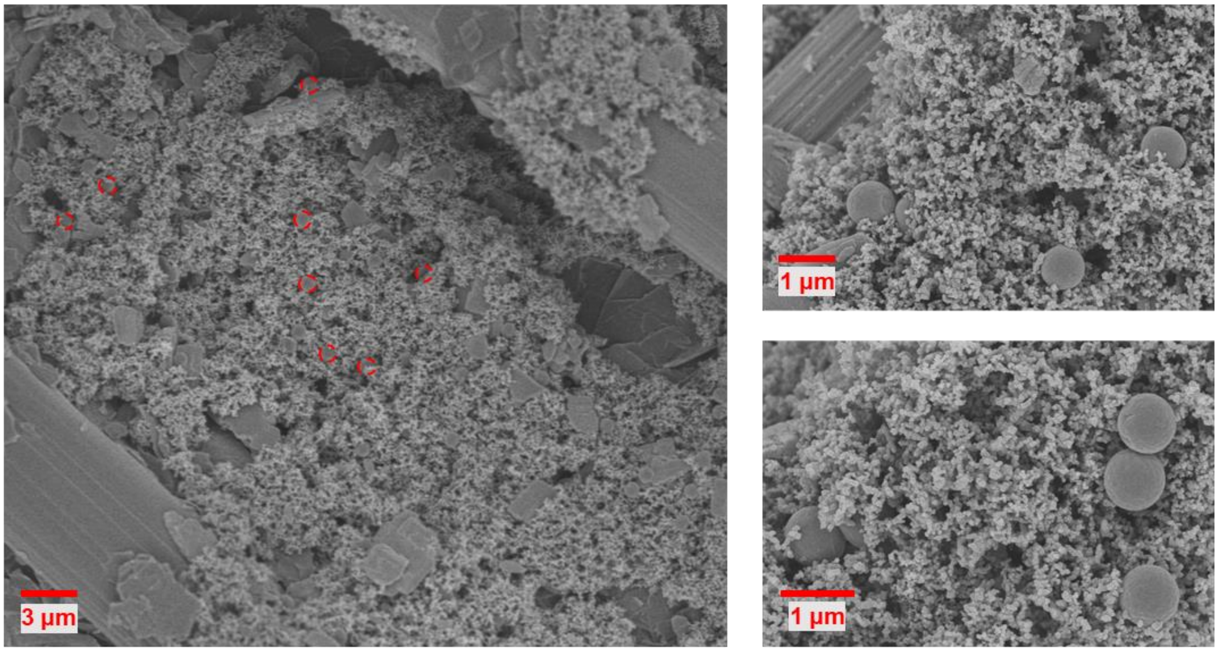

b) After cycling

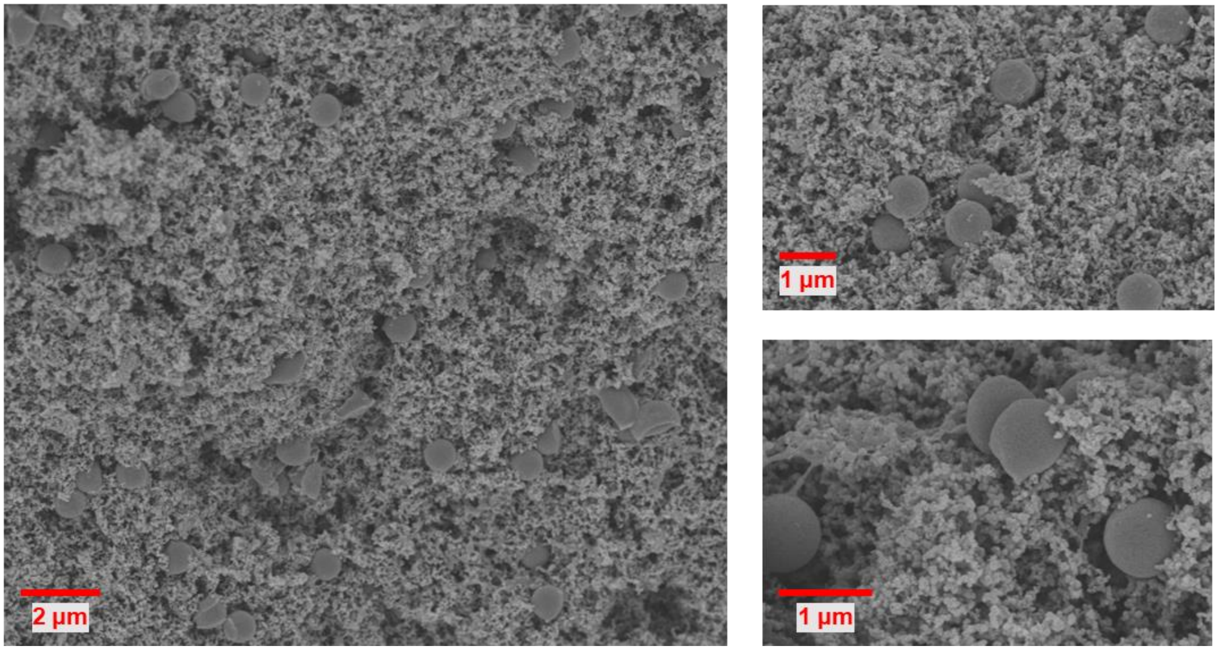

Figure 5.13. SEM images of smaller DS-RAP blended with carbon black before and after charge/discharge cycling. Red circles are added to the first low resolution image to aid in identifying several randomly selected particles. Post-cycling electrode sample was prepared by soaking twice in clean ACN prior to sputter coating. A complete removal of $Mg(OTf)_2$ supporting electrolyte was not validated prior to sputter coating.

5.6 Acknowledgements

The authors gratefully acknowledge financial support from the Joint Center for Energy Storage Research (JCESR), an Energy Innovation Hub funded by the U.S. Department of Energy, Office of Science, Basic Energy Sciences (BES). This work made use of the shared facilities at the University of Chicago Materials Research Science and Engineering Center, supported by National Science Foundation under award number DMR-2011854. Parts of this work were carried out at the Soft Matter Characterization Facility of the University of Chicago. S.S.K. acknowledges support from the National Science Foundation (NSF) Graduate Research Fellowship under Grant No. (DGE-1746045).

5.7 References

(1) Winsberg, J.; Hagemann, T.; Janoschka, T.; Hager, M. D.; Schubert, U. S. Redox-Flow Batteries: From Metals to Organic Redox-Active Materials. Angew. Chemie - Int. Ed. 2017, 56 (3), 686–711.

(2) Lu, Y.; Chen, J. Prospects of Organic Electrode Materials for Practical Lithium Batteries. Nat. Rev. Chem. 2020, 4 (3), 127–142.

(3) Liu, M.; Visco, S. J.; De Jonghe, L. C. Novel Solid Redox Polymerization Electrodes: Electrochemical Properties. J. Electrochem. Soc. 1991, 138 (7), 1896–1901.

(4) Baloch, M.; Ben Youcef, H.; Li, C.; Garcia-Calvo, O.; Rodriguez, L. M.; Shanmukaraj, D.; Rojo, T.; Armand, M. New Redox Polymers That Exhibit Reversible Cleavage of Sulfur Bonds as Cathode Materials. ChemSusChem 2016, 9 (22), 3206–3212.

(5) Oyama, N.; Tatsuma, T.; Sato, T.; Sotomura, T. Dimercaptan–Polyaniline Composite Electrodes for Lithium Batteries with High Energy Density. Nature 1995, 373 (6515), 598–600.

(6) Pope, J. M.; Oyama, N. Organosulfur/Conducting Polymer Composite Cathodes: I. Voltammetric Study of the Polymerization and Depolymerization of 2,5-Dimercapto-1,3,4-thiadiazole in Acetonitrile. J. Electrochem. Soc. 1998, 145 (6), 1893–1901.

(7) Oyama, N.; Kiya, Y.; Hatozaki, O.; Morioka, S.; Abruña, H. D. Dramatic Acceleration of Organosulfur Redox Behavior by Poly(3,4-Ethylenedioxythiophene). Electrochem. Solid-State Lett. 2003, 6 (12), A286.

(8) Kiya, Y.; Henderson, J. C.; Hutchison, G. R.; Abruña, H. D. Synthesis, Computational and Electrochemical Characterization of a Family of Functionalized Dimercaptothiophenes for

Potential Use as High-Energy Cathode Materials for Lithium/Lithium-Ion Batteries. J. Mater. Chem. 2007, 17 (41), 4366–4376.

(9) Rodríguez-Calero, G. G.; Conte, S.; Lowe, M. A.; Gao, J.; Kiya, Y.; Henderson, J. C.; Abruña, H. D. Synthesis and Characterization of Poly-3,4-Ethylenedioxythiophene/2,5-Dimercapto-1,3,4-Thiadiazole (PEDOT-DMcT) Hybrids. Electrochim. Acta 2015, 167, 55–60.

(10) Kiya, Y.; Hutchison, G. R.; Henderson, J. C.; Sarukawa, T.; Hatozaki, O.; Oyama, N.; Abruña, H. D. Elucidation of the Redox Behavior of 2,5-Dimercapto-1,3,4-Thiadiazole (DMcT) at Poly(3,4-Ethylenedioxythiophene) (PEDOT)-Modified Electrodes and Application of the DMcT - PEDOT Composite Cathodes to Lithium/Lithium Ion Batteries. Langmuir 2006, 22 (25), 10554–10563.

(11) Mistry, A. N.; Mukherjee, P. P. “Shuttle” in Polysulfide Shuttle: Friend or Foe? J. Phys. Chem. C 2018, 122 (42), 23845–23851.

(12) Li, J.; Zhan, H.; Zhou, Y. Synthesis and Electrochemical Properties of Polypyrrole-Coated Poly(2,5-Dimercapto-1,3,4-Thiadiazole). Electrochem. commun. 2003, 5 (7), 555–560.

(13) Shi, T.; Tu, Q.; Tian, Y.; Xiao, Y.; Miara, L. J.; Kononova, O.; Ceder, G. High Active Material Loading in All-Solid-State Battery Electrode via Particle Size Optimization. Adv. Energy Mater. 2020, 10 (1), 1902881.

(14) Zhao, Y.; Si, S.; Liao, C. A Single Flow Zinc//Polyaniline Suspension Rechargeable Battery. J. Power Sources 2013, 241, 449–453.

(15) Karami, H.; Mousavi, M. F.; Shamsipur, M. A New Design for Dry Polyaniline Rechargeable Batteries. J. Power Sources 2003, 117 (1–2), 255–259.

(16) Hauffman, G.; Maguin, Q.; Bourgeois, J.-P.; Vlad, A.; Gohy, J.-F. Micellar Cathodes from Self-Assembled Nitroxide-Containing Block Copolymers in Battery Electrolytes. Macromol. Rapid Commun. 2014, 35 (2), 228–233.

(17) Oh, S. H.; Lee, C. W.; Chun, D. H.; Jeon, J. D.; Shim, J.; Shin, K. H.; Yang, J. H. A Metal-Free and All-Organic Redox Flow Battery with Polythiophene as the Electroactive Species. J. Mater. Chem. A 2014, 2 (47), 19994–19998.

(18) Wu, S.; Zhao, Y.; Li, D.; Xia, Y.; Si, S. An Asymmetric Zn//Ag Doped Polyaniline Microparticle Suspension Flow Battery with High Discharge Capacity. J. Power Sources 2015, 275, 305–311.

(19) Montoto, E. C.; Nagarjuna, G.; Hui, J.; Burgess, M.; Sekerak, N. M.; Hernández-Burgos, K.; Wei, T.-S. S.; Kneer, M.; Grolman, J.; Cheng, K. J.; Lewis, J. A.; Moore, J. S.; Rodríguez-López, J. Redox Active Colloids as Discrete Energy Storage Carriers. J. Am. Chem. Soc. 2016, 138 (40), 13230–13237.

(20) Zhuo, S.; Tang, M.; Wu, Y.; Chen, Y.; Zhu, S.; Wang, Q.; Xia, C.; Wang, C. Size Control of Zwitterionic Polymer Micro/Nanospheres and Its Dependence on Sodium Storage. Nanoscale Horizons 2019, 4 (5), 1092–1098.

(21) Wei, Z.; Wang, D.; Liu, Y.; Guo, X.; Zhu, Y.; Meng, Z.; Yu, Z.-Q.; Wong, W.-Y. Ferrocene-Based Hyperbranched Polymers: A Synthetic Strategy for Shape Control and Applications as Electroactive Materials and Precursor-Derived Magnetic Ceramics. J. Mater. Chem. C 2020, 8 (31), 10774–10780.

(22) Lai, Y. Y.; Li, X.; Zhu, Y. Polymeric Active Materials for Redox Flow Battery Application. ACS Appl. Polym. Mater. 2020, 2 (2), 113–128.

(23) Horák, D.; Shapoval, P. Reactive Poly(Glycidyl Methacrylate) Microspheres Prepared by Dispersion Polymerization. J. Polym. Sci. Part A Polym. Chem. 2000, 38 (21), 3855–3863.

(24) Muzammil, E. M.; Khan, A.; Stuparu, M. C. Post-Polymerization Modification Reactions of Poly(Glycidyl Methacrylate)S. RSC Adv. 2017, 7 (88), 55874–55884.

(25) Kocak, G.; Solmaz, G.; Dikmen, Z.; Bütün, V. Preparation of Cross-Linked Micelles from Glycidyl Methacrylate Based Block Copolymers and Their Usages as Nanoreactors in the Preparation of Gold Nanoparticles. J. Polym. Sci. Part A Polym. Chem. 2018, 56 (5), 514–526.

(26) Bartels-Keith, J. R.; Burgess, M. T.; Stevenson, J. M. Carbon-13 Nuclear Magnetic Resonance Studies of Heterocycles Bearing Carbon-Sulfur and Carbon-Selenium Bonds: 1,3,4-Thiadiazole, 1,3,4-Selenadiazole, and Tetrazole Derivatives. J. Org. Chem. 1977, 42 (23), 3725–3731.

(27) McEwan, K. A.; Slavin, S.; Tunnah, E.; Haddleton, D. M. Dual-Functional Materials via CCTP and Selective Orthogonal Thiol-Michael Addition/Epoxide Ring Opening Reactions. Polym. Chem. 2013, 4 (8), 2608–2614.

(28) Jang, J.; Bae, J.; Ko, S. Synthesis and Curing of Poly(Glycidyl Methacrylate) Nanoparticles. J. Polym. Sci. Part A Polym. Chem. 2005, 43 (11), 2258–2265.

(29) Patai, S. The Chemistry of the Thiol Group. Chem. Thiol Gr. 2010, 1–479.

(30) Helmkamp, G. K. Organic Chemistry of Sulfur (Oae, S.); Plenum Press, 1978; Vol. 55.

(31) Gao, H.; Elsabahy, M.; Giger, E. V.; Li, D.; Prud'homme, R. E.; Leroux, J.-C. Aminated Linear and Star-Shape Poly(Glycerol Methacrylate)s: Synthesis and Self-Assembling Properties. Biomacromolecules 2010, 11 (4), 889–895.

(32) Kozhunova, E. Y.; Gvozdik, N. A.; Motyakin, M. V.; Vyshivannaya, O. V.; Stevenson, K. J.; Itkis, D. M.; Chertovich, A. V. Redox-Active Aqueous Microgels for Energy Storage Applications. J. Phys. Chem. Lett. 2020, 11 (24), 1–5.

(33) Viscosity of Acetonitrile – viscosity table and viscosity chart. Anton Paar Wiki. https://wiki.anton-paar.com/en/acetonitrile/

(34) DMSO Physical Properties. Gaylord Chemical. https://www.gaylordchemical.com/literature/dmso-physical-properties

(35) Pope, J. M.; Sato, T.; Shoji, E.; Oyama, N.; White, K. C.; Buttry, D. A. Organosulfur/Conducting Polymer Composite Cathodes. J. Electrochem. Soc. 2002, 149 (7), A939.

(36) Tatsuma, T.; Yokoyama, Y.; Buttry, D. A.; Oyama, N. Electrochemical Polymerization and Depolymerization of 2,5-Dimercapto-1,3,4-Thiadiazole. QCM and Spectroscopic Analysis. J. Phys. Chem. B 1997, 101 (38), 7556–7562.

(37) Pope, J. M.; Oyama, N. Organosulfur/Conducting Polymer Composite Cathodes: I. Voltammetric Study of the Polymerization and Depolymerization of 2,5-Dimercapto-1,3,4-thiadiazole in Acetonitrile. J. Electrochem. Soc. 1998, 145 (6), 1893–1901.

(38) van de Hulst, H. C. Light scattering by small particles. Courier Corporation. 1981.

Chapter 6

Enhancing Performance of Redox-Responsive Disulfide-Crosslinking Polymer Particles via Synthetic Tuning and Electrode Preparation

Abstract: While the identification of stable redox centers is the first hurdle in designing new materials for battery electrode, a thorough understanding of the role their surrounding environment plays is also critical. Transport of electronic charge and balancing ionic species to the redox center is frequently the limiting factor in many electrode assemblies. In this study, the impact of secondary pendant chemistries, particle size, and electrode preparation are investigated for their role in dictating the performance PGMA-ATDDS DS-RAP cathode composites. By changing the DS-RAP epoxide passivation chemistry from a nonpolar aliphatic amine to a polar cyclic carbonate moiety, the ability of the polymer particle to accept charge is increased significantly, improving overall capacity roughly 15%. A reduction in DS-RAP particle size is also shown to improve Coulombic efficiency during galvanostatic cycling, resulting from a dramatic reduction in particle diffusion length (diameter). Lastly, the impact of solvent selection during electrode casting is evaluated, where the more favorable polar solvent NMP results in significantly more particle swelling, leading to better contact with electronically conductive electrode components, increasing overall discharge capacity to 50.5 mAh/g, exceeding 80% of the theoretical capacity for the material used in this study. These results highlight the importance of careful system optimization whenever investigating new redox chemistries for use in energy storage applications and present a path forward to making DS-RAPs a more attractive organic cathode material family.

6.1 Introduction

Electrode preparation for electrochemical energy storage systems (batteries and supercapacitors) is critically important for achieving viable power delivery devices. With inorganic materials, the hard and rigid nature ubiquitously associated with ceramics, oxides, and other crystalline materials has resulted in a fairly generalized approach to electrode preparation, involving reducing the active material to a desired particle size by crushing. The particles are then blended in high mass loading with a conductive additive, such as carbon black, and a polymeric binder, typically polyvinylidene difluoride (PVDF), in a high boiling point solvent (most frequently NMP). This blend, or slurry, is coated onto foil electrodes before drying, resulting in a coating thickness on the order of 100 µm or less. The coated foils are then rolled between heated rollers in a process known as calendaring to compact the film, reducing interstitial space between particles and increasing contact with the conductive additive (**Figure 6.1**). The final result is a highly regular electrode with reduced void volume and good electronic connectivity.[1]

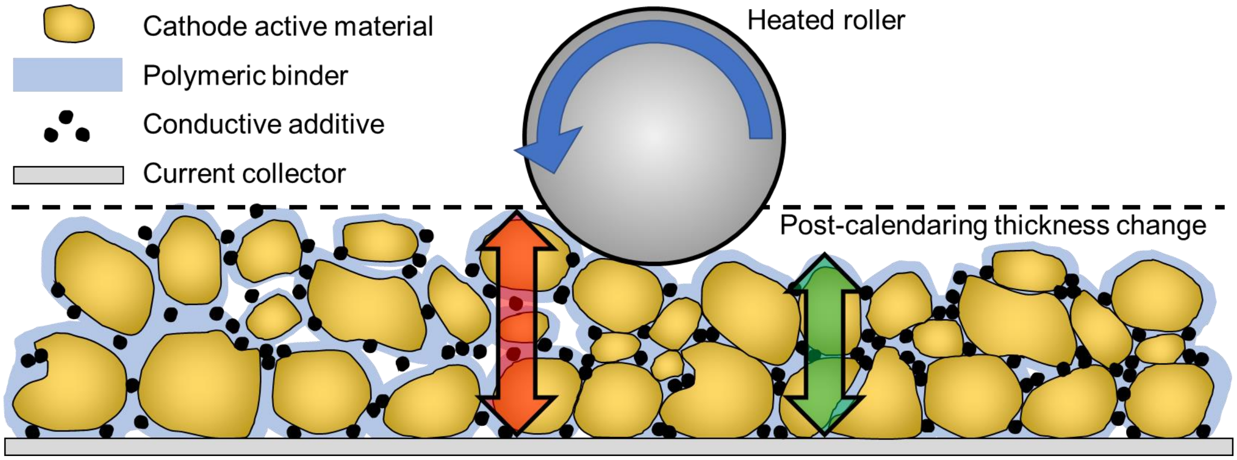

Figure 6.1. Typical makeup and calendaring for dense inorganic battery electrode composites.

Electrode preparation for organic redox active materials, by comparison, is in a state of infancy. A great deal of work is underway in optimizing electrode preparation for different types of organic material chemistry, as well as molecular size and architecture.[2] Compared to inorganic chemistries, organic redox active materials behave wildly different from one another depending on their solubility (or in the case of polymers, swellability) in different preparation solvents, and as such, may require different approaches. In addition, soluble or highly swellable materials are expected to interact differently with inorganic conductive carbon, polymer binder, and any other necessary additives. Rheology of solutions and soft materials is dramatically different than suspensions of hard particles as well, resulting in necessary modifications to electrode coating as well. Finally, in systems utilizing liquid electrolytes, polymeric redox active materials may undergo dramatic swelling, not even considering volumetric changes as a result of ion flux resulting from cycling. In a particularly dramatic case, polymers bearing disulfide redox centers are expected to undergo shifts in architecture resulting from the cleavage and reformation of disulfide bonds associated with charge cycling. The impact of behaviors like this are not yet well-studied, but is necessary to understand if these materials are to ever see commercial application.

In the previous chapter, it was demonstrated how covalently fixating the aromatic disulfide bis(5-ethylamino-l,3,4-thiadiazol-2-yl) disulfide (ATDDS) to a poly(glycidyl methacrylate) (PGMA) polymer backbone improved the electrode-surface electrochemical kinetics compared to a solution of small molecule disulfide.[3] This improvement was attributed to the spatial confinement of the disulfides near the electrode surface, as compared to the solution, where the reduced thiolate reduction products were free to diffuse from the electrode. This polymer system was then applied in the form of micro-scale particles to cathodes for use in metal ion batteries. Despite showing stable cycling performance in both Li and Mg ion half-cells, their discharge capacity remained relatively low compared to the theoretical value. Examining the performance of the system under a multitude of different conditions (solvent, supporting electrolyte, etc.) did, however, provide guidance for future improvements without modifying the core redox active chemistry. Reducing the active material particle diameter by approximately half roughly doubled the specific capacity of the material. Additionally, as the particles were cycled, the Coulombic efficiency of the samples increased without a concurrent reduction in capacity (**Figure 5.4**). SEM analysis showed that after cycling, the particles had changed shape, and were in greater contact with the surrounding conductive carbon additive, providing additional points of electronic contact (**Figure 5.13**).

In order to improve the performance of the DS-RAP system, several factors were taken into consideration. Firstly, seeing an opportunity to improve ionic conductivity of the polymer particles, the residual epoxide groups remaining after disulfide functionalization were reacted using a simple procedure to form carbonate pendants, increasing the polarity of the polymer as a whole. Additionally, based on the results of the previous chapter, further decreasing the particle size was seen as a way to improve electrochemical accessibility. Lastly, techniques were applied from typical electrode preparation methodology for inorganic cathode materials while taking into consideration the differences between these materials and the polymer particles in this study. As a result, a dramatic increase in specific capacity was obtained vs the previous study, highlighting the importance of factors other than redox center when designing materials for battery applications.

6.2 Results and Discussion

6.2.1 Modification of epoxide passivation chemistry allows for improved charge transport

With inorganic and organic materials alike, ionic conductivity of the electrode material is a key point of consideration. As discussed in the previous chapter, functionalizing PGMA particles with ATDDS results in a small amount of unreacted epoxide pendants. In order to avoid parasitic side reactions with any number of species in the assembled battery, these highly reactive groups are passivated with a secondary functionalization. Previously, the selected chemistry to neutralize the residual epoxides was *N*-methylbutylamine herein "MBA" (**Figure 6.2a**). This species was chosen for its relatively inert nature once reacted to a tertiary amine, coupled to its good solubility in the reaction solvent. Particles functionalized with *N*-methylbutylamine also showed increased diameter in organic solvent as compared to particles with only ATDDS functionalization. Despite this, functionalizing the remaining epoxide groups with MBA imparts additional non-polar character to the particle matrix. Decreasing the polarity of the polymer can result in reduced ion motion into the particle matrix, electrochemical activity by preventing counterion association with charged redox centers.[4] Examining particles still bearing epoxide groups with those functionalized with MBA via cyclic voltammetry, a marked decrease in peak intensity is observed with the MBA condition (**Figure 6.2b**). In practical terms, this reduced electrochemical activity in battery application results in reduced capacity, especially at higher charge rates. In order to address this issue, a polar functional group was selected to passivate the residual epoxides while simultaneously offering a potential increase to electrochemical performance. A simple process by which reacting epoxides with CO_2 to yield glycidyl carbonate pendant groups has been previously demonstrated for use in ion-conducting polymers for solid electrolytes.[5] Performing this reaction on PGMA-ATDDS particles resulted in thorough passivation of the residual epoxide groups, confirmed by FTIR (**Figure 6.10**). Particles with this chemistry are herein referred to as "DS-RAP-CO_2", or simply "CO_2" for brevity. CV characterization of these DS-RAP-CO_2 particles resulted in significantly increased peak intensity, indicating increased electrochemical activity.

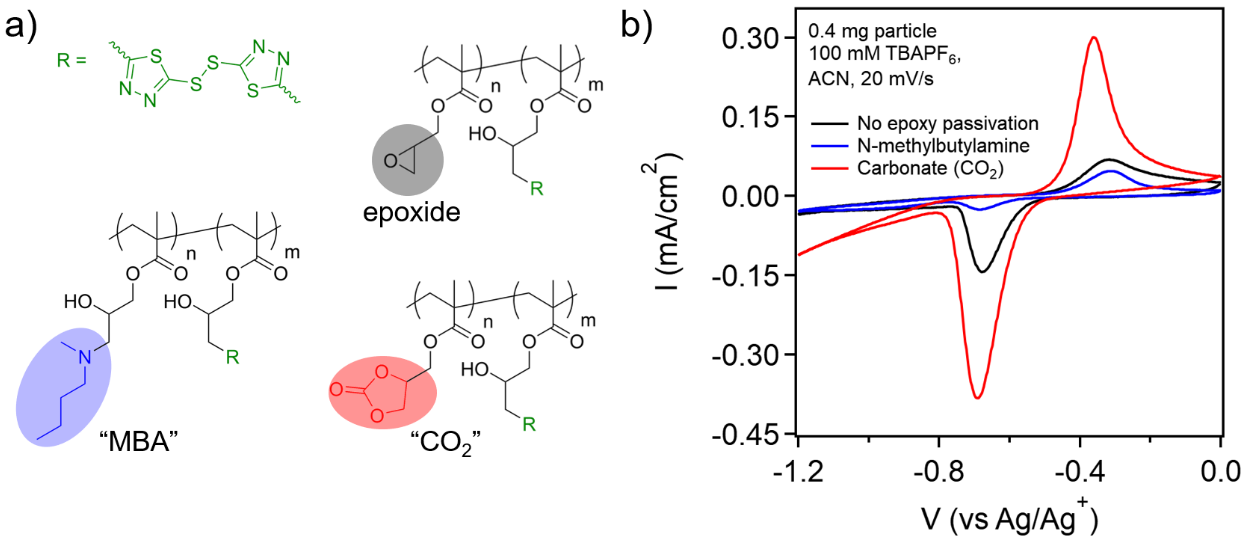

Figure 6.2. Impact of DS-RAP epoxide passivation. a) Epoxide pendant group motifs for DS-RAP. b) Cyclic voltammetry of cast DS-RAP with different side chain groups.

6.2.2 Polymerization of nano-sized PGMA particles for increased active surface area

Particle size has been noted as a key factor impacting the performance of redox active materials in batteries, with smaller particles performing better in terms of both capacity and efficiency, as the decreased characteristic length results in reduced charge trapping.[6] The effect of particle size on battery capacity has been observed in both inorganic and organic particles for electrode active material.[7] The general trend is that smaller particles decrease the diffusion length required for both the electronic charge to travel from the particle surface, as well as the balancing electrolyte ion, such as Li. Two particle sizes were investigated in the previous chapter, with dry sizes of ca. 800 and 1700 nm when dry, and 1000 and 1900 nm in high boiling point solvent (DMSO). The nearly 50% smaller particles resulted in a capacity increase of 101.2%, demonstrating the positive impact of decreased diffusion length and increased surface area (**Figure 5.4**). For this study, new "nano-sized" particles were synthesized with a diameter of 90 ± 5 nm (via SEM, **Figure 6.3**), further decreasing particle diameter by 95% vs the "larger" particles and 89% vs the "smaller" particles.

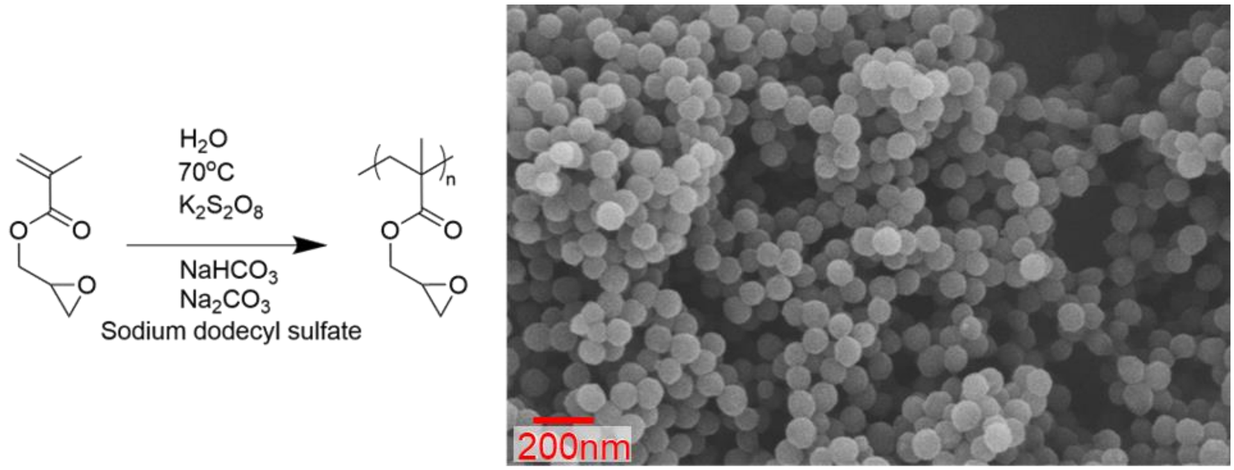

Figure 6.3. Synthetic scheme for and SEM images of monodispersed nano-sized PGMA particles.

6.2.3 Casting solvent selection dictates electrode particle-substrate interactions

As a final point of focus in this study, the impact of electrode preparation was examined. In the previous chapter, electrodes were prepared with a significant amount of conductive carbon black (CB) additive. The need for conductive additives in organic electrodes is well-documented, with active material to carbon ratios mirroring that of inorganic compositions, to carbon-rich blends with carbon outweighing active material. While the 1:1 blend of DS-RAP to CB is not uncommon compared to similar studies, it presents a limitation to the specific capacity of a theoretical battery full cell.[8] In addition, despite the high CB loading, the overall discharge capacity of the 1:1 blend was still relatively low. Looking back at the previously mentioned SEM images of the electrode (**Figure 5.13**), the CB can be seen surrounding the polymer particles. However, the amount of contact with the particle surface is relatively low, with the particles occupying voids within the CB, rather than making intimate contact, possibly the result of minor contraction when the casting solvent, ethanol, evaporates from the particles. In-post cycling images, small adhesion sites can be observed alongside a general deformation in particle shape, suggesting contact with the electrodes improved as a result of cyclic shifts in particle crosslinking as a result of disulfide reduction and oxidation. The observed improvement in performance with cycling corroborates this observation. For this study, rather than maintain a large percentage CB, efforts were made to improve the quality of the interface between a smaller amount of CB and the polymer particles. In theory, a more intimate mating of the two materials should result in greater interfacial area and therefore better charge conduction. In the initial investigation, ethanol was chosen as the solvent for electrode preparation. Ethanol is inexpensive, exhibits low environmental toxicity, and is a common solvent for organic systems. Despite all these benefits, ethanol may not be the ideal solvent for electrode preparation in this system. DLS of DS-RAP particles in ethanol show a relatively low degree of swelling, indicating the particles more likely to behave in a “hard sphere” manner, rather than soft, conformable microgels. Additionally, ethanol is unable to dissolve many common binders used in battery applications, most notably PVDF. By comparison, polar, high boiling point solvents such as DMSO, DMF, and NMP fulfill both these roles. DLS of DS-RAP in NMP showed appreciably more swelling (14.4% and 49.8% greater diameter and volume for the larger particle; 24.4% and 92.5% for the nano-sized particle). Once again turning to CV analysis, the impact of casting from NMP vs ethanol can be seen immediately. Particles cast from NMP display dramatically enhanced peak signal, suggesting dramatically enhanced contact with the electronically-conductive components of the electrode.

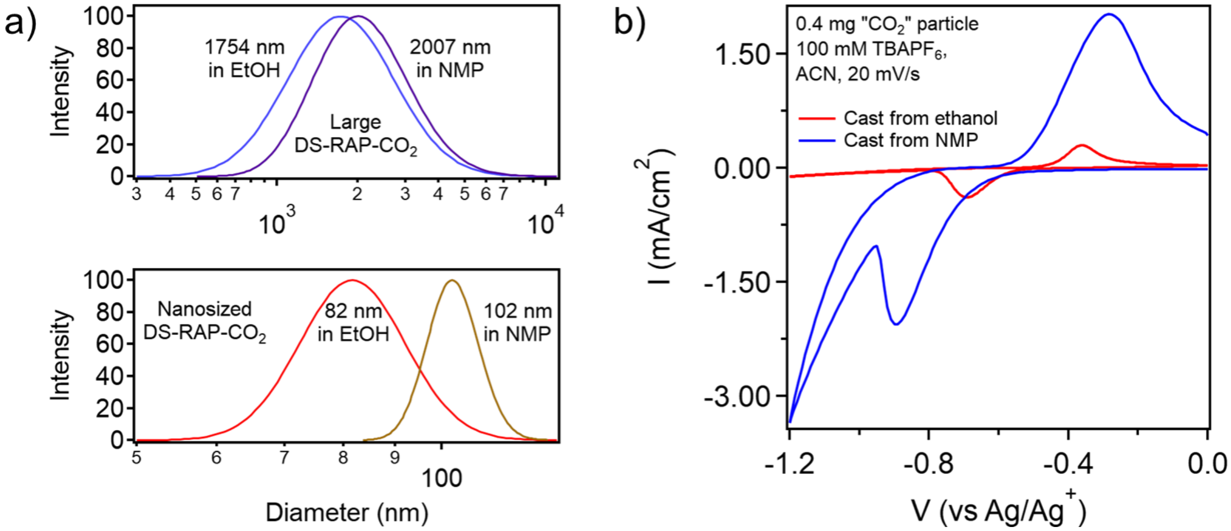

Figure 6.4. Impact of solvent selection on particle behavior. a) DLS of "CO$_2$" particles in ethanol vs DMF. b) CV of "CO$_2$" particles on carbon paper cast from ethanol or DMF solutions.

In addition, NMP is capable of dissolving PVDF, which helps maintain contact between the polymer particles and conductive carbon while the particles reversible swell with cycling. SEM images of both large (ca. 1700 nm) and nano-sized (ca. 90 nm) particles can be seen below (**Figure 6.5**). Using a smaller amount of carbon black (5 to 20% vs 50% by mass, 20% pictured here) with the addition of 5 mass% PVDF and using NMP as the casting solvent, a much more intimate coupling between particle and conductive carbon can be seen. The more irregular, pseudo-spherical nature of the particles indicates a more deformable particle body while swollen with solvent, and the addition of a binder material allows for maintenance of contact between the solids while the electrodes are dried. Conductive carbon is seen occupying the void space within particle packing, and irregularly coating exposed particle surfaces, but in a much more intimate manner than when casted from ethanol.

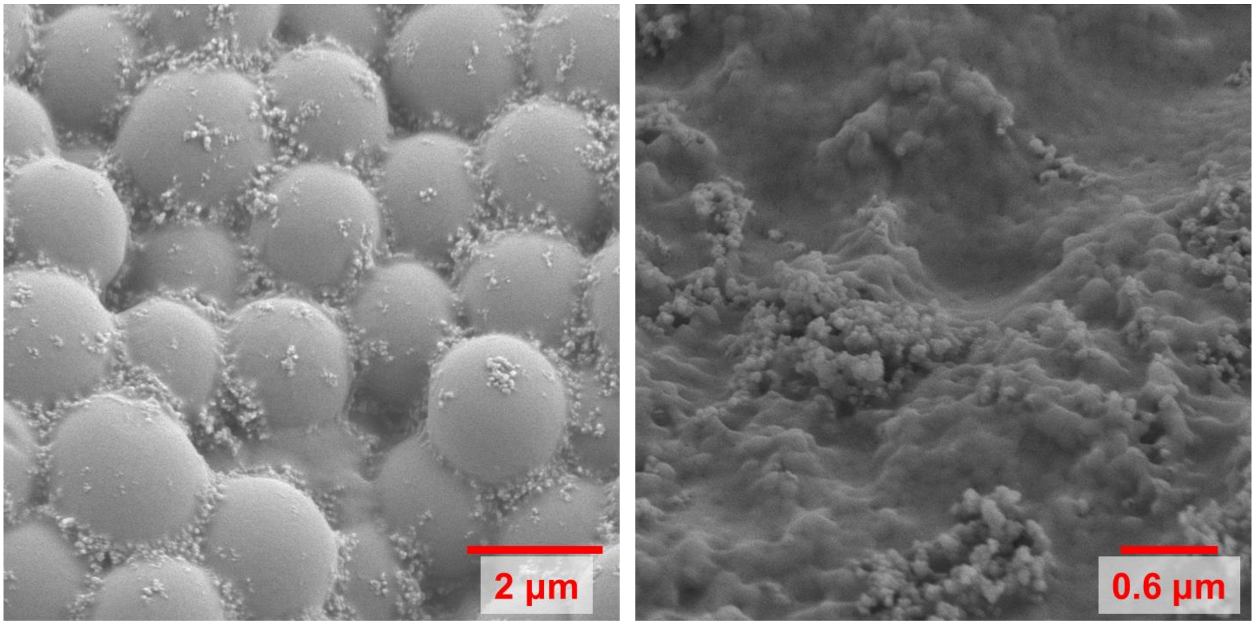

Figure 6.5. SEM images of “CO_2” particle electrodes with 75:20:5 active material/carbon black/PVDF mass ratios. Left - ca. 1700 nm particles. Right – ca. 90 nm particles.

6.2.4 Implementation of Li metal full-cell battery assemblies for cathode cycling studies

In the previous study, galvanostatic cycling experiments were performed using a three-probe configuration to characterize cathode half-cell performance against a non-aqueous Ag/Ag^+ reference electrode, allowing for investigation of multiple different solvents and electrolyte salts, including fully organic, Li, and Mg cations. While beyond-Li batteries continue to garner increasing interest, they are currently far from practical implementation due to issues with stability and manufacturing. Therefore, for this study, a focus is placed on application in Li-ion batteries. However, this narrowing of focus allows for one important benefit. By investigating only Li-ion electrolytes, the novel cathode materials can be tested using full cell battery assemblies. Li metal can be implemented as a proper anode, as opposed to a large capacitive counter electrode, as used in the previous chapter. For this study, a common full cell battery assembly was selected. Polished Li metal was selected as the anode. A porous separator commonly used in Li-ion batteries, Celgard

2325, allows for relatively unimpeded electrolyte diffusion. Tetraethylene glycol dimethyl ether, otherwise known as tetraglyme or G4, is a high boiling point short chain polyether capable of dissolving Li salts in high concentration. Lithium bis(trifluoromethanesulfonyl)imide (LiTFSI) was selected as the electrolyte salt due to its high solubility and stability in most Li metal-compatible solvents. Particles were still cast onto Sigracet GDL 39 AA carbon paper as a means of rapidly generating individual cathode samples. Modifying the cathode casting procedure to blade-coated foil electrodes would require a large amount of optimization outside the scope of this study and maintaining the same cathode substrate allowed for a fairer comparison to the results found in the previous study. The full cell battery was assembled using size 2032 coin cells. Coin cells, or button cells, allow for rapid assembly of full cell, half-cell, or symmetric cell batteries with a minimized distance between electrodes, and are an excellent demonstration of candidate battery materials in a practical arrangement. Methodology for assembly of coin cells for this study can be found in Chapter 2, section 4.

6.2.5 Galvanostatic cycling of Li metal full cells using improved DS-RAP cathodes

Using the full cell assembly described above, the impact of epoxide passivation chemistry was first examined using ca. 1700 nm particles blended with 5 mass% of both carbon black and PVDF. Examining the cycling results of the particles with either MBA or CO_2, a clear difference in capacity is observed (**Figure 6.6** and **6.11**).

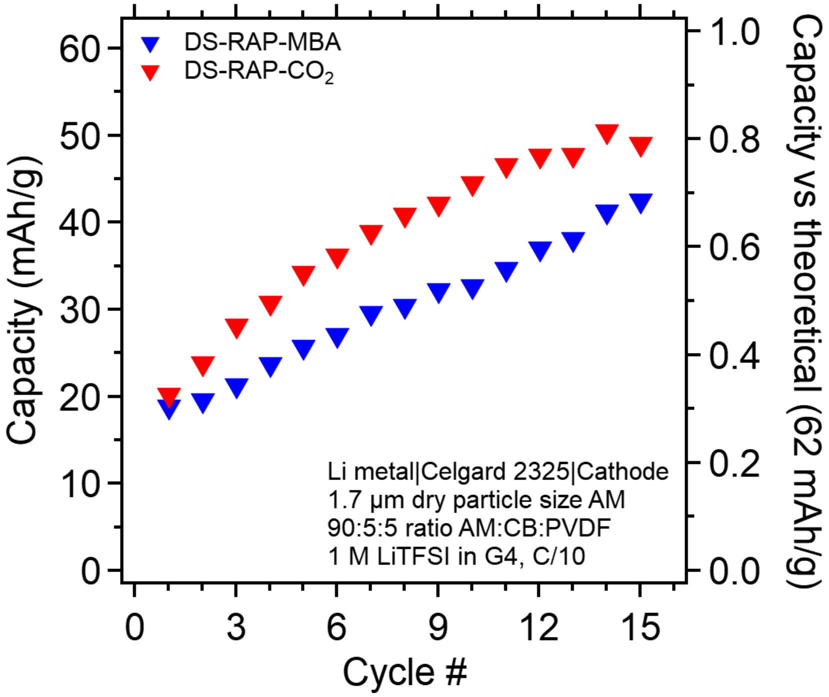

Figure 6.6. Impact of epoxide passivation chemistry on discharge capacity in Li metal full cell using DS-RAP cathode active material.

Over the first 15 cycles, both samples are still in the "conditioning" phases previously described, with increasing capacity over cycle number. However, the results show a marked increase in capacity for the particles functionalized with CO_2. At its highest, a discharge capacity of 50.5 mAh/g is achieved, exceeding 80% of the theoretical capacity for this material batch. In comparison, a maximum value of 42.6 mAh/g is obtained for the particles with MBA, less than 70% of theoretical, and 15.6% lower overall vs the more polar condition. These results provide strong evidence that the more polar pendant groups allow for increased electrochemical accessibility for DS-RAP particles of the same size and highlight the importance of tuning the properties of organic electrode materials outside the primary redox center.

Additionally, is it important to note that for both conditions, the discharge capacity vs theoretical dramatically outperforms the electrodes cast from ethanol, despite a large decrease in the amount of conductive carbon used in the preparation (5% vs 50% by mass). By selecting a more favorable processing solvent and blending the materials with a stable and flexible binder (PVDF), electrode performance can be drastically improved while using the same redox active material. With inorganic materials cast onto foil electrode, calendaring, the process of applying heated pressure via rollers to condense electrodes in the direction perpendicular to the substrate, is used to densify the electrode and improve over electrochemical accessibility. In order to evaluate the effect of this process on the DS-RAP electrodes, fully cast electrodes were compressed in a manual vertical hot press at 75 °C for 1 hour as a substitute procedure in lieu of calendaring. For hot pressed samples, the discharge capacity decreased for both passivation chemistries, suggesting the pressing of these polymer particles likely impacts the composite differently from hard inorganic cathode active materials (**Figure 6.7**).

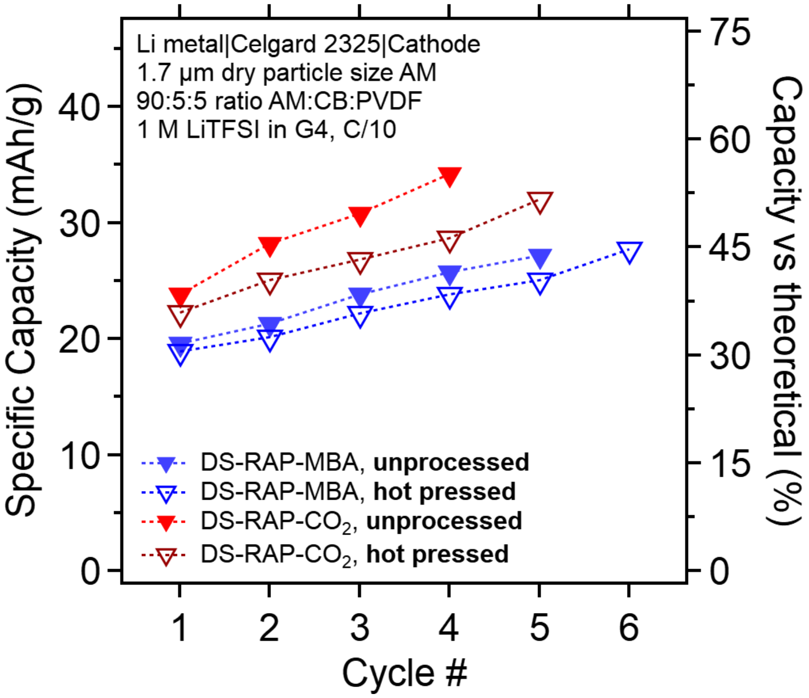

Figure 6.7. Galvanostatic cycling of "MBA" and "CO$_2$" particles with and without hot pressing.

With electrodes containing inorganic materials, densification occurs as a result of deformation of the polymer binder and decreasing porosity between hard particles as discussed earlier and illustrated with **Figure 6.1**. While some deformation of the active material occurs, the primary purpose is to minimize relatively large void spaces that exist within the composite matrix following casting. In contrast, organic materials are capable of high degree of swelling in solvent, resulting in dramatically different suspension and casting behavior. As seen in SEM images of DS-RAP particles cast from NMP, a large degree of inter-particle contact already exists as a result of the casting process with relatively little void space between neighboring particles. Examining electrodes following hot pressing at 75 °C for 1 hour shows the surface of the electrode mass has been compacted significantly into a nearly-flat plane. Organic polymer materials such as the PGMA in this study are significantly softer and more conformable than their organic counterparts, allowing for behaviors such as this, rather than simply fracturing under load. As such, it is important to consider differences such as these when eventually implementing organic materials such as these in practical application. Rather than improve cycling performance by closing gaps between neighboring particles, the surfaces of the cathode have been largely sealed, drastically impeding the diffusion of ionic species in the electrolyte and providing a bottleneck for effective charge transport.

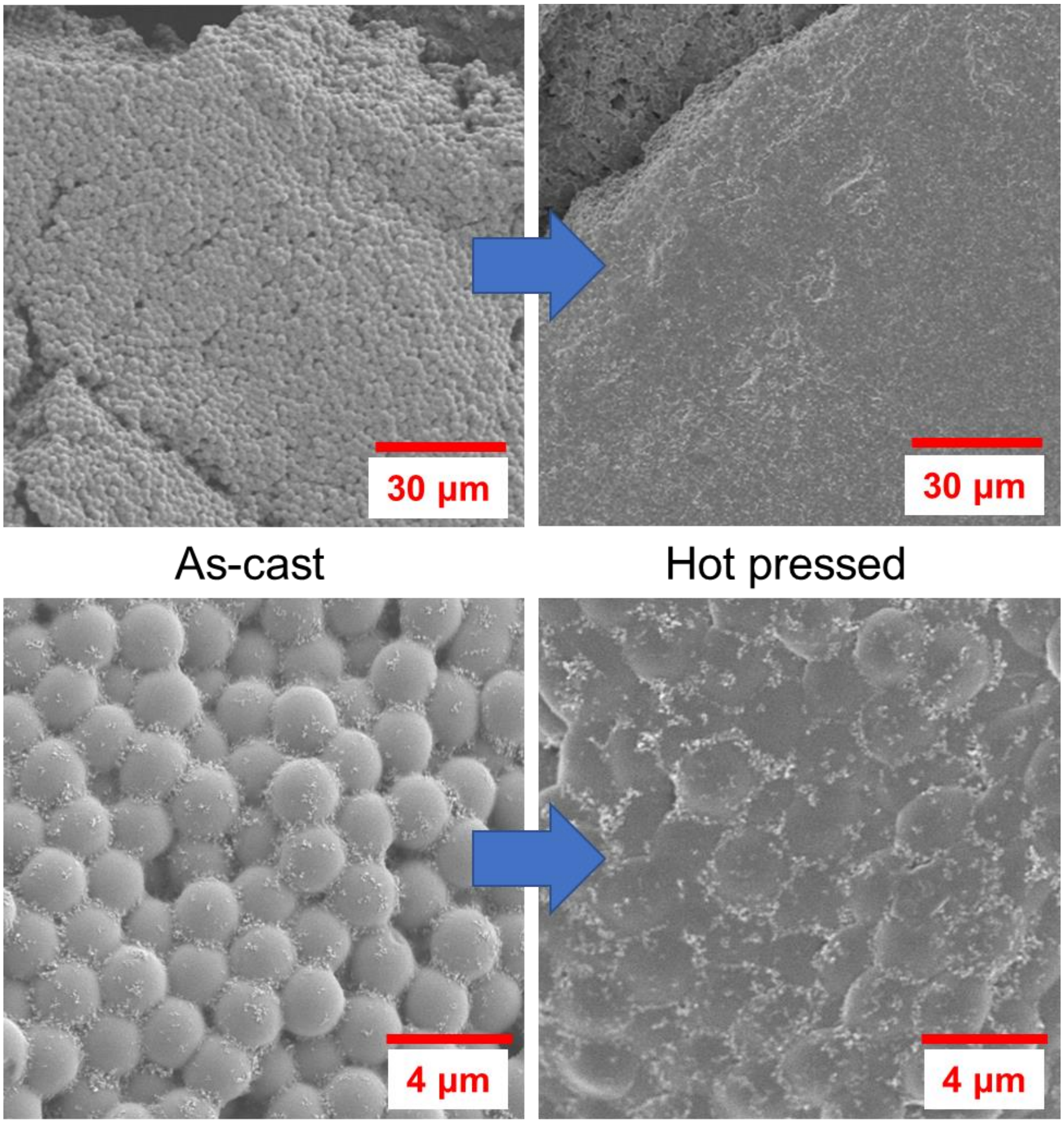

Figure 6.8. SEM images of DS-RAP particle electrodes cast from NMP before and after hot pressing. Electrodes consist of a 75:20:5 ratio of AM:CB:PVDF by mass.

Lastly, the impact of particle size was evaluated, comparing the discharge capacity and Coulombic efficiency of large (ca. 1700 nm) and nano-sized (ca. 90 nm) particles with different blend ratios of active material and carbon black (90:5 and 75:20 mass%/mass%, with 5 mass% PVDF held constant) (**Figure 6.9**).

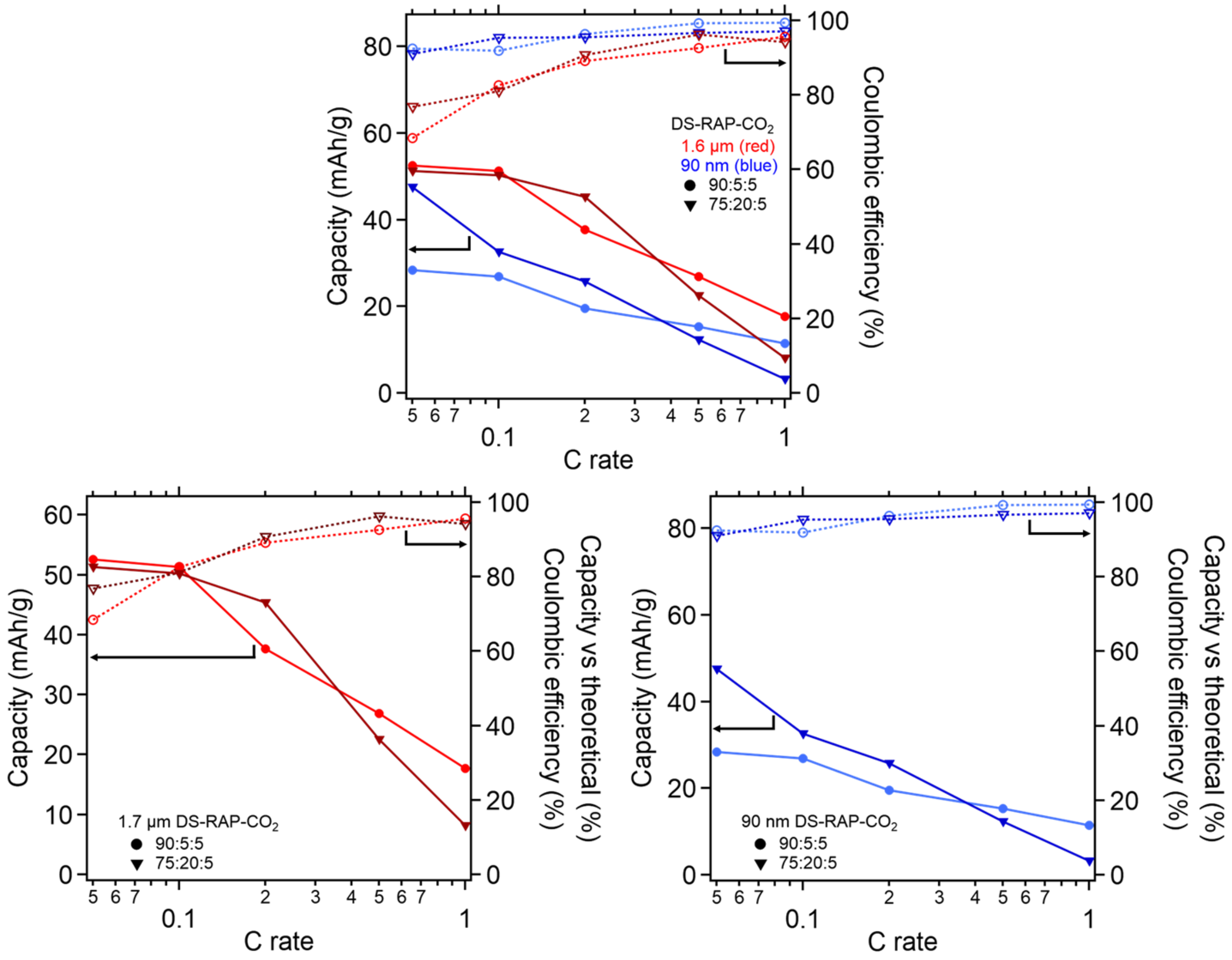

Figure 6.9. Galvanostatic cycling of differently sized “CO$_2$” particles with different blend ratios. Full cell consists of Li metal anode with Celgard 2325 separator and 1 M LiTFSI in G4 electrolyte.

Several key observations are immediately apparent. In comparing discharge capacity between the large and small particles, the larger particles are seen exhibiting a higher overall discharge capacity. In addition, their discharge capacity is significantly closer to the theoretical capacity of the material batch. Comparing both blends, increasing the amount of conductive carbon beyond 5% shows no real improvement in performance for both samples. Turning to Coulombic efficiency, however, the smaller particles show significantly improved efficiency at low charge rates. As the charge rate is increased, efficiency improves for both particle sizes, but the smaller particles maintain a higher percentage overall.

Interpreting these results relies on understanding the nature of the cathode preparation. In contrast to established understanding, decreasing the size of the active material particulate did not serve to improve electrode capacity. Despite this, it did significantly improve the overall Coulombic efficiency. An explanation for this can be found in examining the SEM images shown previously. By comparing the images of the large and small particle cathodes, it becomes apparent that the large particle cathode is much more homogenously distributed with regards to the active material and conductive additive. In contrast, the small particle blend is significantly more heterogeneous, with "islands" of carbon black interspersed among the sea of polymer particles. Despite the smaller particle's shorter characteristic diffusion length (radius), the majority of the particles in the greater bulk are spatially isolated from conductive regions of the electrode, resulting in a greater amount of "dead volume". However, the portion of the particles in contact with the conductive material are able to charge and discharge more efficiently owed to their decreased size, resulting in higher Coulombic efficiency. By comparison, the large particles may allow for more charge trapping, in which charged redox moieties in the depth of the particles are unable to discharge on the time scales of the cycling experiment, resulting in reduced efficiency. Going forward, more intensive blending of the nano-sized particle blend (ultrasonication, ball milling, spray homogenization) may result in additional improvements in discharge capacity while maintaining attractive efficiencies allowed by small particle size.

6.3 Conclusions and Outlook

In this chapter, it was demonstrated how leveraging numerous aspects concerning the design of active materials and preparation of electrodes for Li battery applications can improve performance, and how these considerations differ for organic active materials compared to common conventions historically adopted for use with inorganic cathode materials. By modifying chemistry unrelated to the redox center of the active material polymer (DS-RAP) to make it overall more polar, it was shown how a pathway to improved charge transport could increase performance of an otherwise sluggish and insulating redox active material. Additionally, in order to counter that known challenge, geometric considerations provided a path forward to improved performance. By reducing the particle size of the polymer active material, greater Coulombic efficiency was achieved at similar charge rates. To even greater effect, it was shown how careful consideration of components other than the redox active materials are critical to effect operation of an energy storage material such as the cathode of a Li-ion battery. By careful selection of solvent, binder, and conductive additive, a dramatic increase in performance was obtained relative to previous efforts. By simultaneously analyzing this performance data with structural analysis of the energy storage material (cathode composite), steps for additional improvement were also identified. Overall, this study provides multiple additional points of analysis for ongoing efforts in designing effective organic materials for energy storage applications.

6.4 Materials and Methods

Materials. Glycidyl methacrylate (GMA) containing inhibitor, 5-amino-1,3,4-thiadiazole-2-thiol, hydrogen peroxide solution (30% w/w) in aqueous solution containing inhibitor, polyvinylpyrrolidone (PVP) (average mol. wt 40,000), hexamethylenediamine, sodium dodecyl sulfate, and lithium bromide were purchased from Sigma-Aldrich. Sodium carbonate, anhydrous, ACS, 99.5% min was purchased from Alfa Aesar. All other reagents were purchased from Fisher Scientific. All reagents were used without further purification unless mentioned.

Synthesis of nano-sized PGMA particles. The recipe for nano-sized PGMA particles was adopted from a previously reported method. 212 mg sodium carbonate, 168 mg of sodium bicarbonate and 300 mg of sodium dodecyl sulfate were dissolved in 80 mL of DI water. The solution was stirred at 170 rpm using a stir bar. 10 mL of GMA monomer was added to the reaction vessel drop-wise. The solvent was purged for 30 min with filtered Ar gas. In the meantime, an initiator solution was prepared by dissolving 200 mg of potassium persulfate into 10 mL of DI water. After purging, the initiator solution was charged into the reaction vessel. The vessel was then heated to 30 °C and reaction carried out for 24 hrs. The resulting product was washed with methanol, centrifuged at 8000 rpm, and decanted a total of three times. The washed particles were then dried under vacuum oven at 50 °C for 2 days prior to functionalization with 1% HMDA as permanent crosslinker and ATDDS crosslinker as previously described.

Functionalization of carbonate pendants to PGMA by epoxide ring opening with CO_2. 200 mg of PGMA-ATDDS particulate (1.6 micron or 90 nm) was dispersed in 20 g of DMF via bath sonicator for 30 min. After sonication, 15 mg of lithium bromide was added to the dispersion. The reaction vessel was heated to 80 °C and sparged with CO_2 for two days. CO_2 gas flow was generated by storing dry ice in a sealed bottle connected to the reaction vessel, with sublimating dry ice providing sufficient pressure to sparge the reaction vessel. Dry ice was refilled every 8 hr to ensure a steady CO_2 flow into the reaction vessel. After functionalization, the product was washed according to the previously described methodology.

Fabrication of polymer particle active material cathodes. Using a paper punch, Sigracet GDL 39 AA carbon paper is cut into 0.5” round substrates. Substrates are placed on a flat Teflon sheet for casting. Cathode suspensions were prepared in NMP with 5 mg/mL PVDF to a total solids concentration of 100 mg/mL, with active material and carbon black ratios varied based on desired composition. Suspensions were homogenized using a bath sonicator. After casting onto the carbon paper substrates, samples were dried in a vacuum oven at 60 °C overnight before transferring into an argon glove box.

Assembly of coin cells. Li foil was polished and punched into 12 mm circles. Size 2032 coin cells were assembled according to the procedure in Chapter 2. A total of 90 μL of electrolyte (1M LiTFSI in G4) was used, applied in 3 separate aliquots of 30 μL, one atop each of the Li foil, Celgard 2325 separator, and cathode layers. Cells were crimped using an MTI Corporation MSK-110 crimper to a pressure of 600 psi (roughly 42 kg/cm^2). Coin cells were equilibrated overnight to fully develop any SEI layers, and were examined via EIS for shorting or other irregularities.

Galvanostatic Cycling. GC experiments were performed using a Neware CT-4008T-5V50mA 8-channel battery cycler. Coin cells were placed in 2032 cell holders with lead wires soldered to the terminals an insulated using fiberglass felt pockets to prevent sudden temperature fluctuations.

Condensation of cathode samples via hot pressing. Hot pressing was performed using a small vertical hot press of unknown make. Completed cathodes were placed between thin stainless-steel foils and placed into the press. Samples were pressed using the maximum obtainable pressure by the press. After the set pressing time, samples were allowed to cool before removing from the foil.

6.5 Appendix

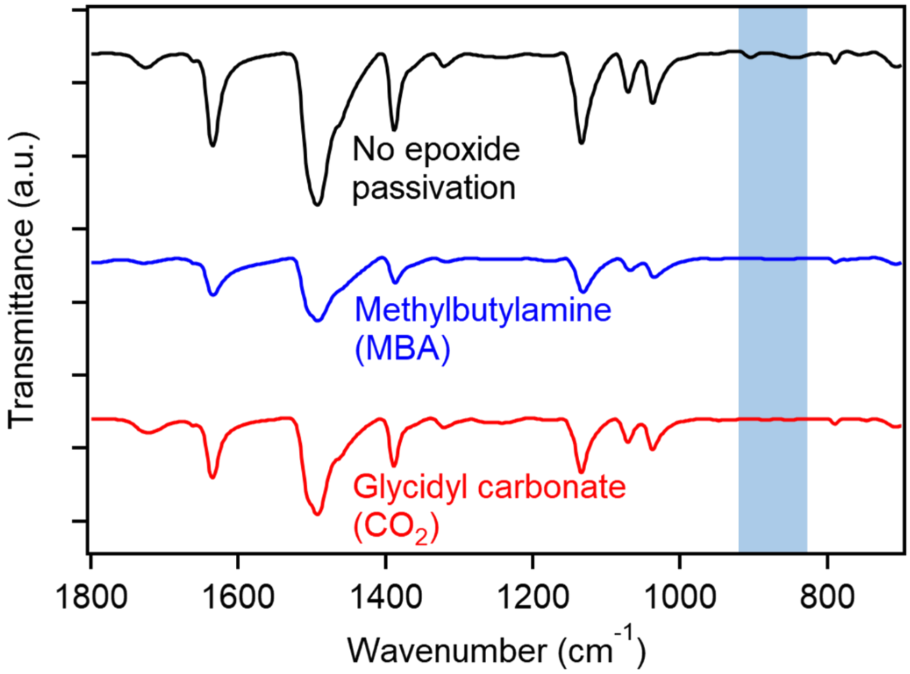

Figure 6.10. FTIR of PGMA-ATDDS particles with different epoxy passivation chemistries. The blue bar highlights the area of epoxide signal, showing signal depletion resulting from passivation with post-crosslinking synthetic procedures.

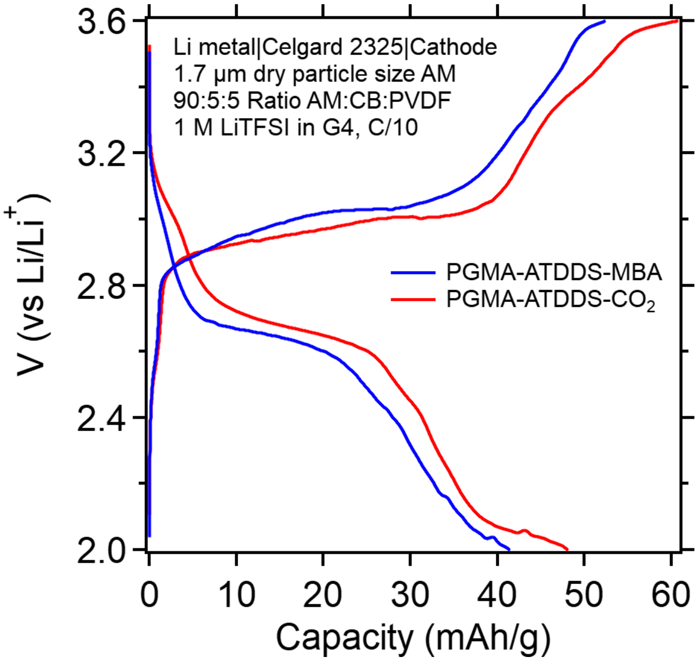

Figure 6.11. Representative charge-discharge curves for cathodes containing DS-RAP-MBA and DS-RAP-CO_2 active materials

6.6 Acknowledgements

I gratefully acknowledge financial support from the Joint Center for Energy Storage Research (JCESR), an Energy Innovation Hub funded by the U.S. Department of Energy, Office of Science, Basic Energy Sciences (BES). This work made use of the shared facilities at the University of Chicago Materials Research Science and Engineering Center, supported by National Science Foundation under award number DMR-2011854. Parts of this work were carried out at the Soft Matter Characterization Facility of the University of Chicago. I gratefully thank Hongyi Zhang for his close collaboration and skillful materials synthesis, and Priya Mirmira for her patience and guidance in the construction of Li metal coin cells.

6.7 References

(1) Hawley, W. B.; Li, J. Electrode Manufacturing for Lithium-Ion Batteries—Analysis of Current and next Generation Processing. *J. Energy Storage* **2019**, *25*, 100862.

(2) Lu, Y.; Chen, J. Prospects of Organic Electrode Materials for Practical Lithium Batteries. *Nat. Rev. Chem.* **2020**, *4* (3), 127–142.

(3) Grocke, G. L.; Zhang, H.; Kopfinger, S. S.; Patel, S. N.; Rowan, S. J. Synthesis and Characterization of Redox-Responsive Disulfide Cross-Linked Polymer Particles for Energy Storage Applications. *ACS Macro Lett.* **2021**, *10* (12), 1637–1642.

(4) Wheatle, B. K.; Keith, J. R.; Mogurampelly, S.; Lynd, N. A.; Ganesan, V. Influence of Dielectric Constant on Ionic Transport in Polyether-Based Electrolytes. *ACS Macro Lett.* **2017**, *6* (12), 1362–1367.

(5) Sakai, T.; Kihara, N.; Endo, T. Polymer Reaction of Epoxide and Carbon Dioxide. Incorporation of Carbon Dioxide into Epoxide Polymers. *Macromolecules* **1995**, *28* (13), 4701–4706.

(6) Zhang, J.; Qiao, J.; Sun, K.; Wang, Z. Balancing Particle Properties for Practical Lithium-Ion Batteries. *Particuology* **2022**, *61*, 18–29.

(7) Wang, Y.; Ding, Y.; Pan, L.; Shi, Y.; Yue, Z.; Shi, Y.; Yu, G. Understanding the Size-Dependent Sodium Storage Properties of Na2C6O6-Based Organic Electrodes for Sodium-Ion Batteries. *Nano Lett.* **2016**, *16* (5), 3329–3334.

(8) Zhu, Z.; Chen, J. Review—Advanced Carbon-Supported Organic Electrode Materials for Lithium (Sodium)-Ion Batteries. *J. Electrochem. Soc.* **2015**, *162* (14), A2393–A2405.

Chapter 7

Enhancing Performance of PEDOT-DMcT Hybrid Chemistry for Use in Li-Ion Battery Cathodes Through Synthesis of a Nanoparticle Morphology

Abstract: In addressing the relatively sluggish electrochemical kinetics associated with organosulfur disulfide redox chemistries, a great deal of work has gone into examining the electrocatalytic effect of conjugated polymers such as PEDOT, which has been shown to dramatically increase the rate of electron transfer when used as an electrode targeting the thiadiazole-based organosulfur, DMcT. Mostly recently, a study showcased the synthesis of a covalently-linked PEDOT-DMcT hybrid polymer material for use as a Li-ion battery cathode. However, it was found the particular thick-film morphology of the system limited its practical capacity to less than 20% of theoretical at a charging rate of 1 C. In this study, this challenge is addressed by synthesizing PEDOT-DMcT as a nano-scale particle, decreasing the characteristic charge carrier diffusion length, and making the material easily integrated into existing electrode preparation methodologies. Cycling of Li metal full cells containing PEDOT-DMcT particle cathodes showed improved performance, yielding 30 mAh/g at 1 C (34.8 % of theoretical) and 50 mAh/g at C/10 (59.8%), exceeding capacities obtained from cathodes constructed with similarly-sized DS-RAP particles. Cycling over multiple charging rates reveals PEDOT-DMcT is able to retain more capacity at higher rates as a result of the electrocatalytic effect and electronic conduction of the PEDOT backbone. Finally, electrodes containing PEDOT-DMcT are subjected to heated densification, leading to improved discharge capacities, showcasing their favorable response to conventional electrode preparation techniques. These results suggest that with proper optimization, PEDOT-DMcT and similar motifs may serve as attractive organic battery materials.

7.1 Introduction

As discussed throughout the previous chapters, all electrochemical systems conduct both ionically and electronically at some length scale. In the case of energy storage materials, namely batteries, improving electronic conduction within the electrodes is critical to good performance. This is traditionally accomplished using conductive additives, electronically linking the redox active material to the current collector, but also stands to be the limiting factor within the bulk of the redox active material itself. Electronically-insulating materials find themselves limited by the rate of self-exchange, where diffusion is the result of charge hopping between neighboring redox centers.[1] In the case of materials based on sulfurous redox centers, such as DS-RAP, this limitation can be dramatic. Reviewing the previous chapter's results, it can be seen that as charge rate of the DS-RAP-containing battery cell is increased, a fairly extensive decrease in overall capacity is observed.

An issue common to inorganic sulfur and organosulfur compounds is the kinetically sluggish nature of the pseudo-reversible redox process. Compared to commonly-studied molecules for organic energy storage such as TEMPO or viologen derivatives with heterogeneous charge transfer rate constants on the order of 10^{-1}, organic disulfide reduction has been shown to be on the order of 10^{-4} to 10^{-8}.[2-4] As a result, batteries featuring organosulfur compounds may be extremely limited in terms of charge rate. While fixation on an insoluble substrate has been shown to improve the reversibility of the redox couple by preventing reduced species from diffusing away from the electrode, it does not change the interaction with disulfides and the electrode themselves.[5] There have been efforts to improve performance in this regard by means of electrocatalysis, using additional molecular species to accelerate the charge transfer kinetics without being consumed. One such example is the use of conjugated polymers such as the commonly-studied poly(3,4-

ethylenedioxythiophene), or PEDOT, to improve both the rate of charge transfer and reversibility of the previously-mentioned 2,5-dimercapto-1,3,4-thiadiazole (DMcT) redox couple. First investigated by Oyama et al. by electrochemically polymerizing PEDOT on a glassy carbon electrode and comparing the relative electrochemical activity of DMcT on coated vs bare electrodes.[6] Subsequent computational studies elucidated the favorable thermodynamics of the system in which electron transfer from the HOMO of neutral PEDOT to the LUMO of oxidized forms of DMcT promotes DMcT reduction with simultaneous oxidation of PEDOT to a doped state.[7] Kinetic studies revealed the use of PEDOT as the electrode resulted in a 12,000x increase in redox reaction rate relative to a glassy carbon electrode.[8] Multiple works have focused on the improving battery performance of DMcT with PEDOT and analogous conjugated polymers. Initial investigations demonstrated the enhanced reactivity of DMcT solutions at a PEDOT electrode, and later by incorporating solid DMcT into PEDOT as a composite prior to cell assembly. While the electrocatalytic improved overall performance, diffusion of DMcT limited cycling lifetime of the material. More recently, the covalent attachment of DMcT to electropolymerized PEDOT-OTs films resulted in a hybrid material with impressive cycling stability, owed to the fixation of the DMcT moiety combined with electrocatalytic activity of the PEDOT-DMcT as well as conductivity of the PEDOT backbone.[9] Despite this, the electrodes suffered from low overall capacity, which was attributed to the thickness of the film resulting in diminished accessibility into the depth of the film.

In this chapter, it is endeavored to improve upon this electrocatalyzed system. As discussed previously, cathode materials based on PEDOT-DMcT have shown promise as a relatively fast organosulfur-based redox chemistry. However, whether it be poor stability due to diffusion of free DMcT from the electrode, or unexpectedly low performance resulting from too-thick electrodes, limitations in practicality seem to have stemmed from electrode design, rather than selection of chemistry. Taking lessons learned from the design and optimization of the DS-RAP particles for Li-ion cathode applications, it was sought out to synthesize nano-scale particles consisting of the PEDOT-DMcT chemistry, taking advantage of the spatial confinement of the disulfide moieties, electrocatalytic activity between the PEDOT and DMcT, and the electronic conductivity of PEDOT, while minimizing the limitations associated with large characteristic diffusion length observed in previous works. Compared to both electronically inert DS-RAP particles, as well as PEDOT-DMcT thick films previously reported, PEDOT-DMcT particles show greater capacity retention at high charge rates, demonstrating the benefits of enhanced electronic conduction along the polymer backbone coupled with the PEDOT-DMcT electrocatalytic effect on a material with small characteristic dimensions. In addition to increased accessibility, these nanoparticle materials can also be processed by conventional cathode fabrication techniques. Due to the dense and relatively insoluble and non-swelling nature of PEDOT, hot pressing techniques emulating inorganic cathode fabrication show additional improvement resulting from compaction of the electrode composite in contrast to DS-RAP where hot pressing resulted in reduced discharge capacity values.

7.2 Results and Discussion

7.2.1 Synthesis and characterization of PEDOT-DMcT nanoscale particles

Synthesis of the particles involved first functionalizing EDOT monomers with a sufficiently good leaving group in this case p-toluenesulfonate (OTs), following previously reported methods.[9] Using a modified recipe,[10] particles were polymerized from the functionalized monomer, and reacting the resulting particles with lithiated DMcT monomer, as shown in the scheme below (**Figure 7.1a**).

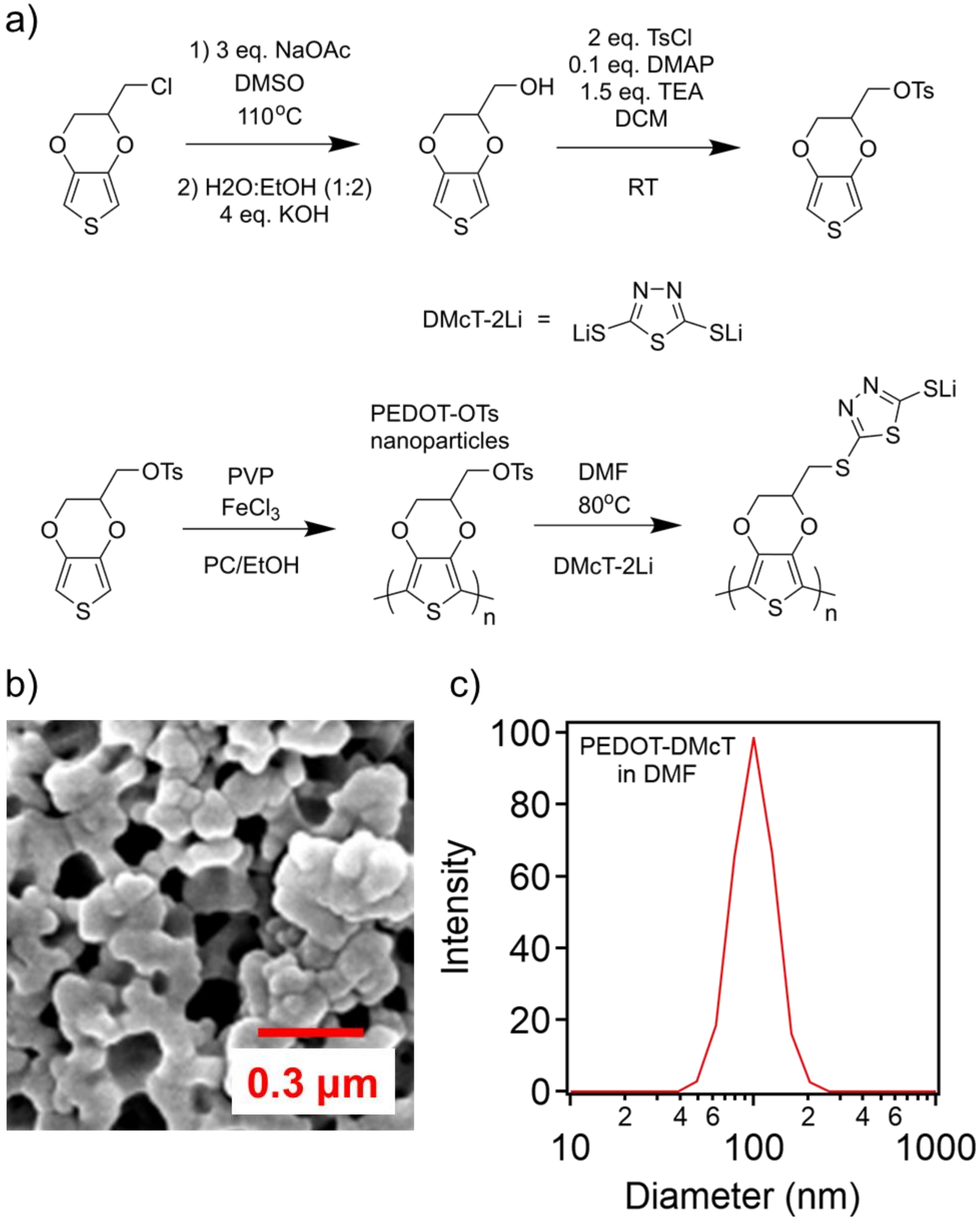

Figure 7.1. Synthesis of PEDOT-DMcT nanoparticles. a) Synthetic scheme for reaction of EDOT-Cl to EDOT-OTs, polymerization of EDOT-OTs to PEDOT-OTs, and functionalization of PEDOT-OTs with DMcT-2Li. b) SEM images of PEDOT-DMcT nanoparticles. c) DLS of PEDOT-DMcT nanoparticle suspension in DMF.

The results of synthesis are ca. 100 nm diameter PEDOT particles with reduced, lithiated DMcT pendant moieties (**Figure 7.1b and c**). Functionalization of DMcT was confirmed by TGA analysis (**Figure 7.2**), indicating mass loss for post-functionalized material from 120-200 °C, the anticipated thermal decomposition temperature range for the DMcT moiety.

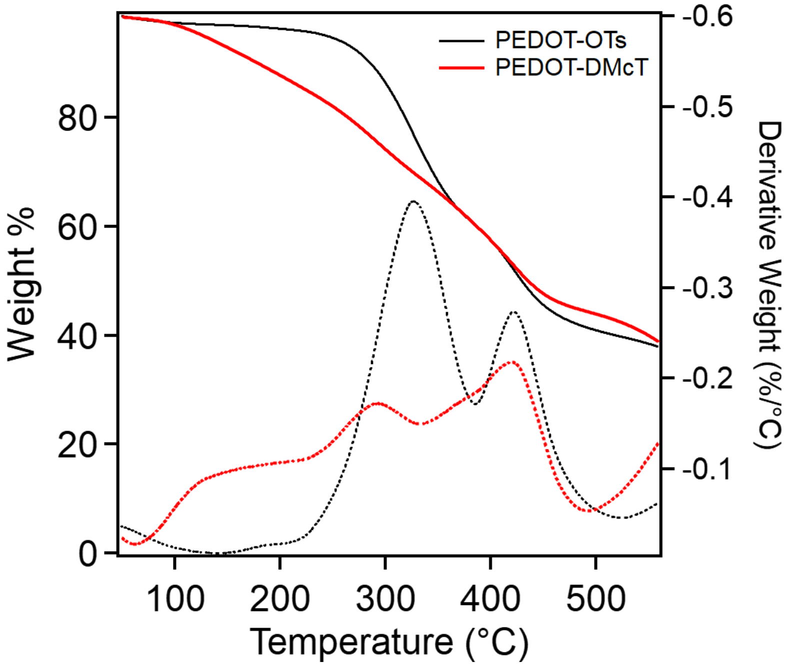

Figure 7.2. TGA analysis of PEDOT-OTs and PEDOT-DMcT particle powders.

7.2.2 Electrochemical characterization of PEDOT-DMcT nanoparticles using CV analysis

CV analysis of particles cast on carbon paper electrodes revealed a strong redox couple in the region anticipated for DMcT (**Figure 7.3**), indicating successful attachment of the moiety to the PEDOT backbone.

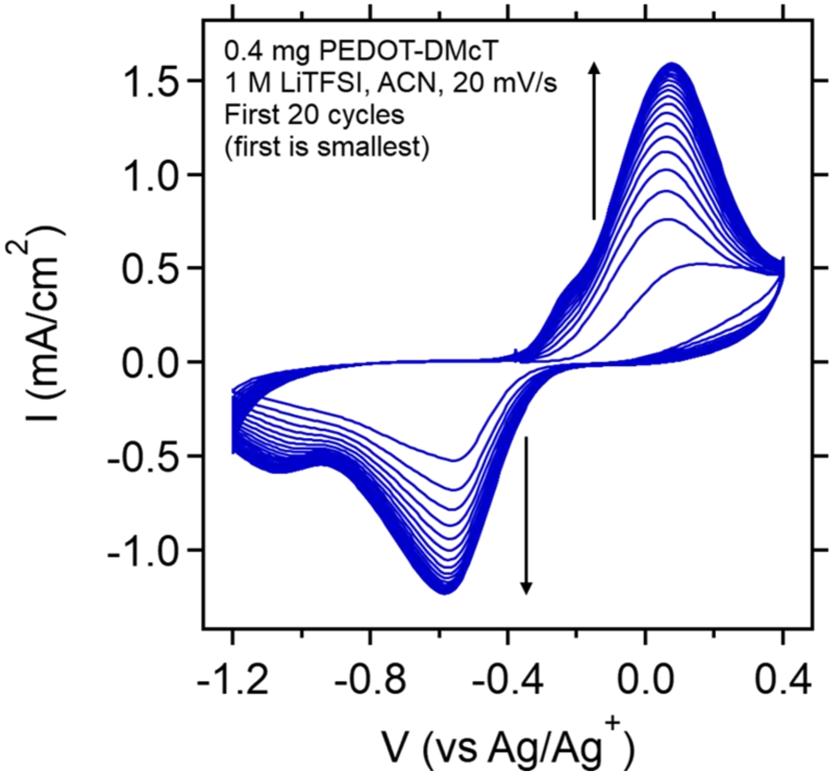

Figure 7.3. Cyclic voltammetry of PEDOT-DMcT particles cast on carbon paper electrode. Measurement is performed starting with positive sweep (oxidation, towards right). Multiple cycles are shown with arrows indicating evolution of curves with cycle number.

Additional peaks can be observed convoluted within this large process which correspond well to peaks observed in pure PEDOT particles at approximately -1 V during reduction and -0.3 V during oxidation (**Figure 7.4**). Additionally, overall peak intensity increased continually with repeated cycling. Based on these observations, it is assumed that oxidative electrochemical doping of the PEDOT backbone is occurring simultaneously with the oxidation of DMcT to the disulfide form.

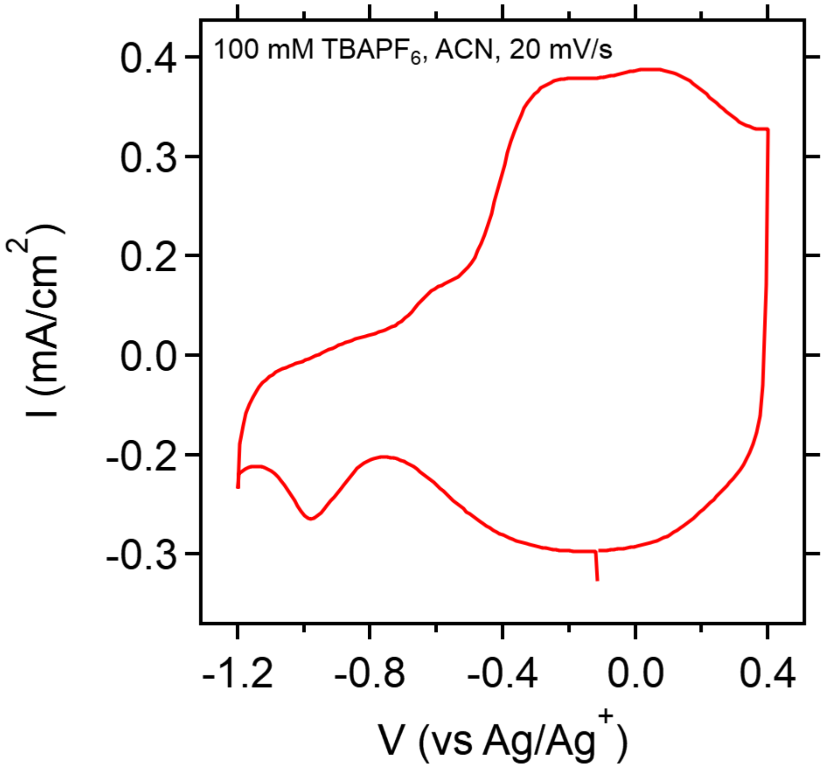

Figure 7.4. Cyclic voltammetry of PEDOT particles cast on carbon paper electrode. Measurement is performed starting with positive sweep (oxidation, towards right).

Despite the use of oxidative polymerization to synthesize the PEDOT-OTs particles, the subsequent processing steps, including washing via dialysis and functionalization with DMcT-2Li provide opportunities for the material to de-dope over time. Application of an oxidizing electrochemical stimulus allows re-introduction of the positive charge carriers, increasing electrochemical accessibility of the particle bulk. De-doping of PEDOT-OTs particles as a result of functionalization with DMcT is further supported by UV-Vis analysis (**Figure 7.5**). Examining spectra of particle suspensions before and after functionalization shows depletion in absorbance for wavelengths above 700 nm, a region of the spectra typically associated with the formation of positive charge carriers (polarons and bipolarons) along the PEDOT backbone.[11]

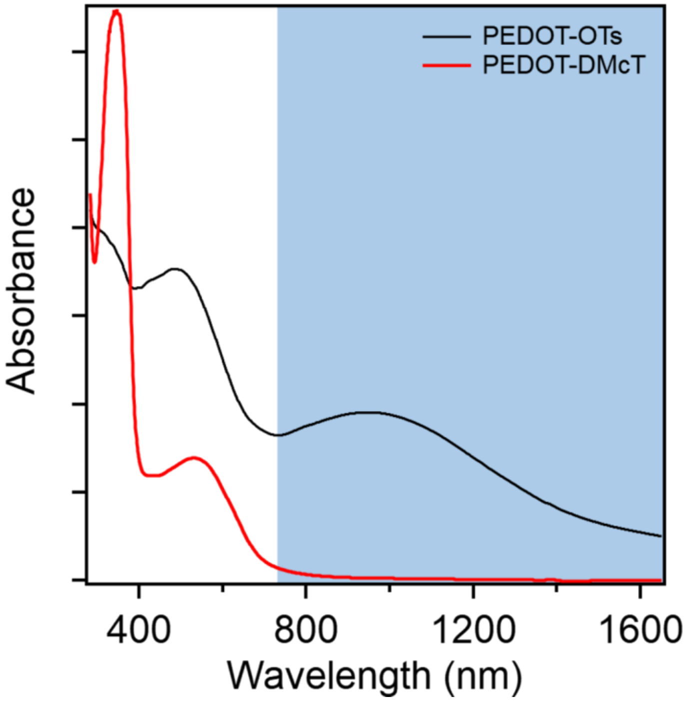

Figure 7.5. UV-Vis spectra for PEDOT-OTs and PEDOT-DMcT suspensions. The area highlighted in blue indicates the expected range for signature polaron (radical cation) and bipolaron (dication) peaks of doped PEDOT polymer.

7.2.3 Galvanostatic cycling of Li metal full cells with PEDOT-DMcT cathodes

PEDOT-DMcT nanoparticles were then cycled in a full cell configuration over a range of charge rates from C/100 to 1C before returning to slower rates (**Figure 7.6)**. Comparing the capacity values to previous works shows promising initial results. Without extensive electrode optimization, synthesizing PEDOT-DMcT as a nano-sized particle blended with additional CB allows for greater accessibility and therefore capacity, achieving ca. 30 mAh/g at 1C (34.8% of theoretical for capacity due to DMcT only, assuming the backbone charging occurred in the first cycle), in comparison to previously reported electrochemically-polymerized thick films, which only achieved 17 mAh/g (19.7% of theoretical). This is noteworthy as electrochemically-polymerized films are expected to exhibit much higher electronic conductivity, owed to the nature of the polymerization process. At C/10, a discharge capacity slightly over 50 mAh/g is achieved (59.8% of theoretical).

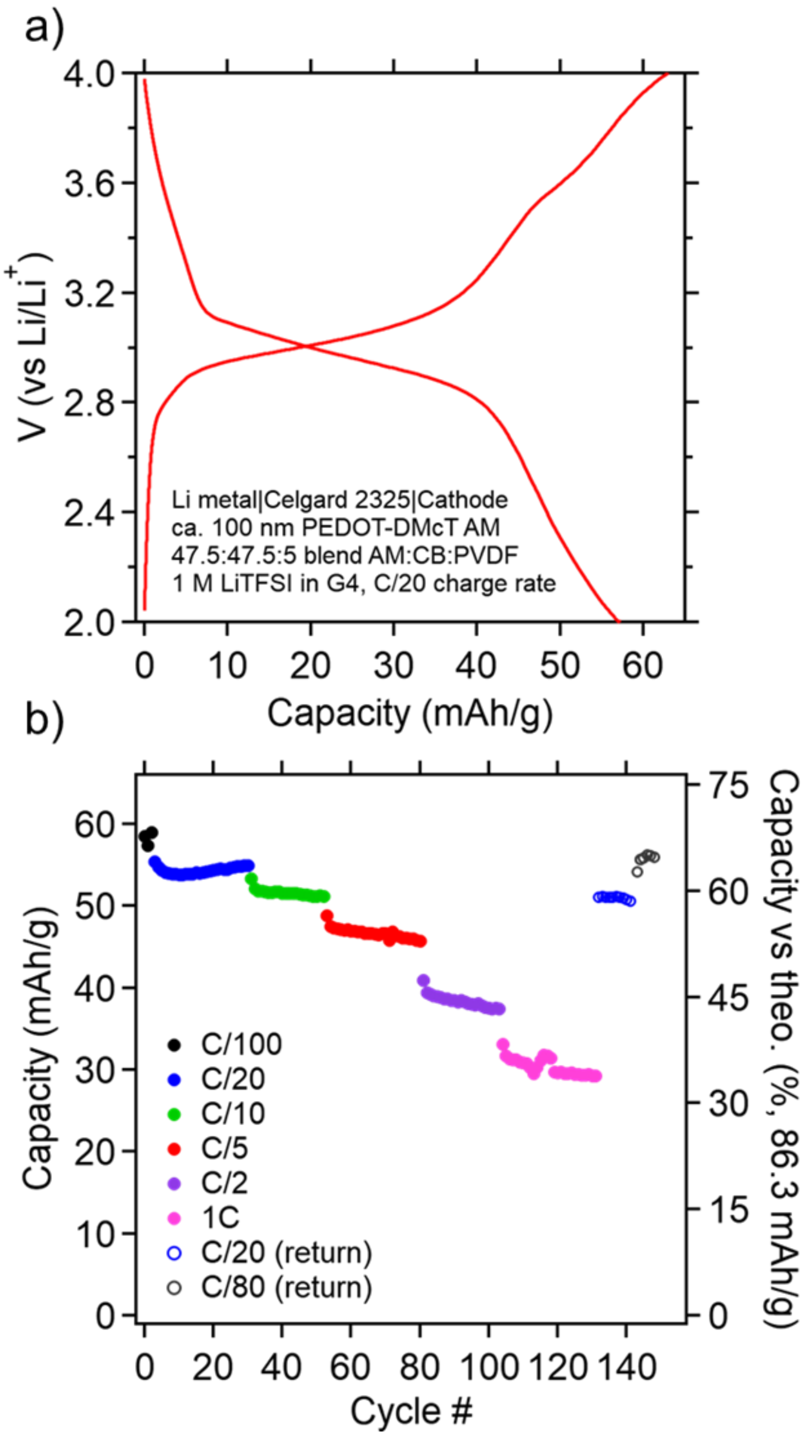

Figure 7.6. Galvanostatic cycling of Li metal cell with PEDOT-DMcT particle cathode. a) Representative charge-discharge curve of cathode with PEDOT-DMcT active material. b) Cycling data with charge rates from C/100 to 1C over 150 cycles.

7.2.4 Analysis of rate-dependent discharge capacity for disulfide-bearing polymer particles

With all battery materials, there is a negative correlation between charging rate and capacity. At faster charging rates, electrode charging or discharging is limited by the charge transfer rate of the material. As a result, heterogeneity in the state of charge occurs from the material interface into the bulk. Material near the surface becomes saturated or depleted of charge faster than the general body, and the potential limitations set by the charging procedure are reached prior to the electrode being fully charged or discharged. However, this effect is offset by materials with faster rates of charge transfer. Charge is able to diffuse into the bulk of the redox active material more homogeneously, reducing the accumulation of charge at the material interface. As a result, these materials are able to maintain higher capacities at fast charge rates.

The capacities of DS-RAP, both with and without polar carbonate pendant groups, as well as PEDOT-DMcT, were compared as a function of charge rate. Known as a modified Peukert plot, this method allows for determining resiliency of electrode capacity to increasing rate of charge transfer. By normalizing the data to the capacity at the lowest charge rate, the relative decrease in capacity over rate is easily visualized. Turning to the results, the impact of enhanced conductivity, both ionic and electronic can be seen (**Figure 7.7**).

First comparing unpassivated DS-RAP to that reacted to form polar carbonates, a sharp difference in capacity decrease can be observed. An overall shallower slope for DS-RAP-CO_2 suggests the additional polar character of the material enhances performance across the range of charging rates, resulting from enhanced mobility of the Li counterion into the particle polymer. Turning to the comparison between PEDOT-DMcT vs DS-RAP, an increase is once again observed resulting from enhanced conductivity, this time electronic. While the impact is less dramatic, PEDOT-DMcT maintains higher residual capacity throughout the range of the charge rates compared to the electronically-insulating PGMA-based particles. This phenomenon is made more impressive by the fact that PEDOT is a relatively poor ion conductor, demonstrating the importance of enhanced electronic conduction in enabling the material to offset otherwise performance-limiting characteristics.

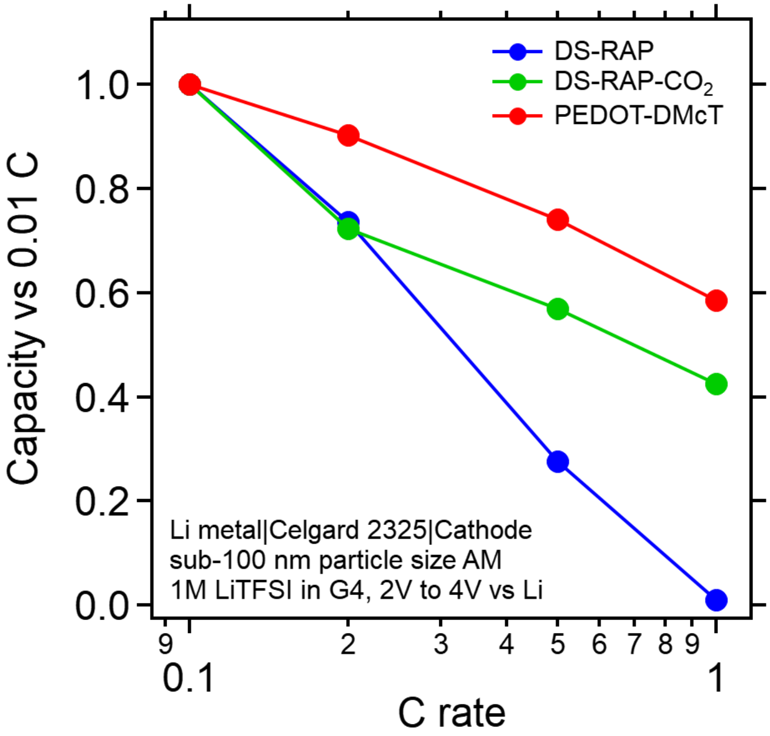

Figure 7.7. Modified Peukert plot of electrodes containing DS-RAP, DS-RAP-CO_2, or PEDOT-DMcT as the active material.

7.2.5 Improvement of PEDOT-DMcT discharge capacity via heated cathode densification

In an effort to improve the performance of the PEDOT-DMcT cathode, steps were once again taken to optimize electrode preparation. In comparison to particles bearing a PGMA backbone, which swell substantially in favorable solvents, PEDOT is quite resilient to swelling and dissolving, even without the presence of permanent crosslinkers. As such, cathodes cast with PEDOT-DMcT as the active material can be expected to behave more similarly to cathodes prepared with inorganic active materials. As outlined in the previous chapter, these composites consist of binder-coated dense materials separated by void spaces, and able to be densified by compaction in the presence of heat, improving electronic connectivity and overall performance. The impact of hot pressing was evaluated simply. Cathodes prepared with PEDOT-DMcT as the active material were treated using a benchtop hot press in place of a heated roller at different temperatures and for different times, followed by charge discharge cycling, the results of which can be seen in **Figure 7.8**.

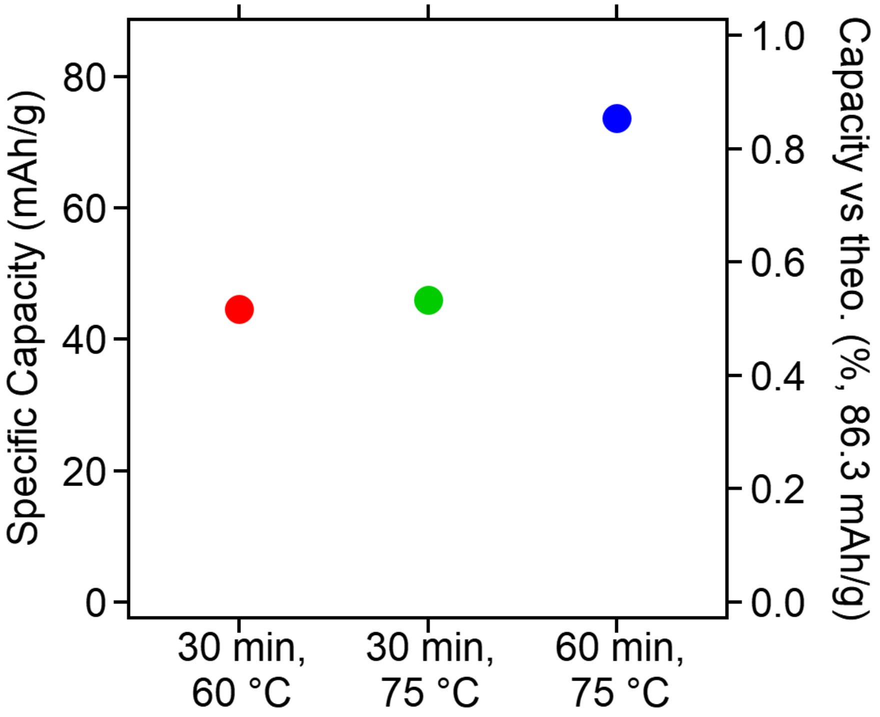

Figure 7.8. Discharge capacity of Li metal cell with hot-pressed PEDOT-DMcT cathodes. Cell consisted of Li metal separated by Celgard 2325 and a carbon paper cathode coated with a blend of 47.5:47.5:5 by mass PEDOT-DMcT/CB/PVDF with 1M LiTFSI in G4 as the electrolyte.

Pressure was not measured due to limitations of the instrument. For this initial investigation, a non-continuous approach was taken, sampling three conditions. The initial temperature chosen for this study was 60 °C, a low-end temperature used to calendar inorganic electrode compositions. A sample was pressed at 60 °C for 30 minutes as a baseline preparation. The next sample was prepared using a slightly elevated temperature of 75 °C, and a final sample was prepared at 75 °C for an extended time of 1 hour. As an important note, this batch of PEDOT-DMcT was found to exhibit lower capacity than that used in **Figure 7.4**. After pressing, samples were assembled into coin cells and cycled at 0.1 C.

Examining the discharge capacity of these samples, the positive influence of hot pressing can be seen. For samples pressed at 30 minutes, the increase in capacity for the sample pressed at 75 °C vs 60 °C is minimal. However, for the sample pressed at 75 °C for 1 hour, a substantial improvement is observed. The discharge capacity of the 75 °C / 60 min is 73.6 mAh/g or roughly 85% of the theoretical capacity, compared to 44.6 mAh/g, or 52% for the 60 °C / 30 min sample. This large increase in capacity suggests that PEDOT-DMcT particles stand to benefit from modern conventional techniques employed in fabrication of Li-ion battery cathodes using inorganic materials. With proper optimization, it may be possible to reach near the theoretical capacity of the PEDOT-DMcT chemistry. By modifying the polymer morphology and applying a minimal set of electrode optimizations, the performance of this material was dramatically improved from initial investigations, increasing the attractiveness of this chemistry for practical use as well as providing direction in the design of other organic chemistries for energy storage applications.

7.3 Conclusions and Outlook

In this chapter, an effort was made to improve the energy storage performance of disulfide-bearing insoluble particles by modifying the polymer backbone chemistry from PGMA, a non-interacting and insulating material, to PEDOT, an electronically-conductive polymer which has been shown to electrocatalyze the redox activity of the thiadiazole-based organosulfur molecule DMcT. Previous work on PEDOT-DMcT demonstrated the system’s electrocatalytic effect, but practicality for batteries was limited by issues with electrode design, including diffusion of DMcT or prohibitively large diffusion lengths. By transitioning to a nanoparticle morphology, it was possible to integrate the material into standard preparation techniques used in conventional Li-ion battery cathodes. Cycling performance in a Li metal full cell demonstrated capacities exceeding that of a previously reported electrochemically-polymerized film at similar charge rates. In addition, it was shown that PEDOT-DMcT particles maintain a higher percentage of overall capacity with increasing charge rate when compared to similarly-sized PGMA-based particles as a result of the enhanced charge transfer provided by their PEDOT backbone. Finally, a hot-pressing methodology imitating calendaring of conventional cathode materials resulted in increased overall capacity of the PEDOT-DMcT cathodes, indicating a favorable response to electrode compaction, suggesting further improvements in electrode preparation may lead to even higher obtainable capacities. Overall, this work provides one example of an approach for designing attractive organosulfur-based cathode materials for Li-ion batteries in a morphology suitable for integration into existing fabrication methodologies. With proper optimization, systems with enhanced electrochemical kinetics such as PEDOT-DMcT may yield simultaneous high capacities and fast charging frequently not associated with organic materials.

7.4 Materials and Methods

Materials. 2-Chloromethyl-2,3-dihydrothieno[3,4-b]-1,4-dioxine (95%), sodium acetate, iron(iii) chloride (reagent grade, 97%), and p-toluenesulfonyl chloride (ReagentPlus®, ≥99%) were purchased from Sigma-Aldrich. All reagents were used without further purification unless mentioned.

Synthesis of (2,3-Dihydrothieno[3,4-b][1,4]dioxin-2-yl) methyl 4methylbenzenesulfonate (EDOT-OTs) monomer. 2-(Chloromethyl)-2,3-dihydrothieno[3,4-b][1,4]dioxine (5 g) was dissolved in 68.5 mL DMSO with 3 eq. anhydrous sodium acetate (6.45, 78.6 mmol). The solution was purged with argon gas and heated at 110 °C overnight. The dark rose colored product was poured over 200 mL DI water and extracted four times with diethyl ether (100 mL). The organic layers were combined and dried over anhydrous magnesium sulfate. The dried solution was further purified by rotovap and vacuum dried overnight. The crude product was carried to the next step without purification. 4 eq. of potassium hydroxide were added to the crude product and dissolved in 225 mL 2:1 mixture (v:v) of water and ethanol. The mixture was stirred at room temperature overnight. The solution was acidified with concentrated HCl (6 M, 17.5 mL). The product was poured over 200 mL DI water and extracted four times with diethyl ether (100 mL). The reaction was monitored by TLC. The product was dissolved in 20 mL of DCM with 1.5 eq. of TEA and 0.1 eq of DMAP in an ice bath. 2 eq. p-toluenesulfonyl was dissolved in 80 mL DCM and added to the solution dropwise, after which the reaction was slowly warmed to RT overnight. The product was once again poured over water and extracted with diethylether as previously described. The EDOT-OTs was purified by flash chromatography with solvent changing from pure hexanes to pure DCM. A white solid product was collected by vacuum.

Synthesis of PEDOT-OTs particles. 2 g of EDOT-OTs was dissolved in 100 mL propylene carbonate and 300 mL ethanol. 2 g of PVP (40 KDa) was dissolved followed by 3.5 g of iron chloride. The reaction was carried out at 80 °C at 1200 rpm for 2 days. The product was placed in an 8 KDa dialysis membrane in 4 liters methanol for 3 days while changing methanol twice daily during the dialysis process.

Functionalization of PEDOT-OTs particles with DMcT-2Li to produce PEDOT-DMcT. 340 mg of PEDOT-OTs nanoparticles were dispersed in 0.5 M of DMcT-2Li/DMF and heated to 90

°C for 24 hrs. The resulting particles dispersion was concentrated via rotovap, followed by dialysis as described previously. The final product was washed and dried via vacuum.

Thermogravimetric analysis (TGA). TGA was performed using a TA Instruments Discovery at a rate of 10 °C/min. Samples were pre-dried in a vacuum oven overnight to remove residual water.

7.5 Acknowledgements

I gratefully acknowledge financial support from the Joint Center for Energy Storage Research (JCESR), an Energy Innovation Hub funded by the U.S. Department of Energy, Office of Science, Basic Energy Sciences (BES). This work made use of the shared facilities at the University of Chicago Materials Research Science and Engineering Center, supported by National Science Foundation under award number DMR-2011854. Parts of this work were carried out at the Soft Matter Characterization Facility of the University of Chicago. I gratefully thank Hongyi Zhang for his close collaboration and skillful materials synthesis, and Priya Mirmira for her patience and guidance in the construction of Li metal coin cells.

7.6 References

(1) Sato, K.; Ichinoi, R.; Mizukami, R.; Serikawa, T.; Sasaki, Y.; Lutkenhaus, J.; Nishide, H.; Oyaizu, K. Diffusion-Cooperative Model for Charge Transport by Redox-Active Nonconjugated Polymers. *J. Am. Chem. Soc.* **2018**, *140* (3), 1049–1056.

(2) Liu, M.; Visco, S. J.; De Jonghe, L. C. Electrode Kinetics of Organodisulfide Cathodes for Storage Batteries. *J. Electrochem. Soc.* 1990, *137* (3), 750–759.

(3) Antonello, S.; Daasbjerg, K.; Jensen, H.; Taddei, F.; Maran, F. Formation and Cleavage of Aromatic Disulfide Radical Anions. *J. Am. Chem. Soc.* **2003**, *125* (48), 14905–14916.

(4) Cook, S. K.; Horrocks, B. R. Heterogeneous Electron-Transfer Rates for the Reduction of Viologen Derivatives at Platinum and Bismuth Electrodes in Acetonitrile. *ChemElectroChem* **2017**, *4* (2), 320–331.

(5) Shadike, Z.; Tan, S.; Wang, Q. C.; Lin, R.; Hu, E.; Qu, D.; Yang, X. Q. Review on Organosulfur Materials for Rechargeable Lithium Batteries. *Mater. Horizons* **2021**, *8* (2), 471–500.

(6) Oyama, N.; Kiya, Y.; Hatozaki, O.; Morioka, S.; Abruña, H. D. Dramatic Acceleration of Organosulfur Redox Behavior by Poly(3,4-Ethylenedioxythiophene). *Electrochem. Solid-State Lett.* **2003**, *6* (12), A286.

(7) Kiya, Y.; Hatozaki, O.; Oyama, N.; Abruña, H. D. Kinetic Studies for the Electrocatalytic Reduction of Bis(2-Mercapto-1,3,4- Thiadiazoyl)-5,5′-Disulfide at a Poly(3,4-Ethylenedioxythiophene) Film-Modified Electrode via Rotating-Disk Electrode Voltammetry. *J. Phys. Chem. C* **2007**, *111* (35), 13129–13136.

(8) Kiya, Y.; Henderson, J. C.; Hutchison, G. R.; Abruña, H. D. Synthesis, Computational and Electrochemical Characterization of a Family of Functionalized Dimercaptothiophenes for Potential Use as High-Energy Cathode Materials for Lithium/Lithium-Ion Batteries. *J. Mater. Chem.* **2007**, *17* (41), 4366–4376.

(9) Rodríguez-Calero, G. G.; Conte, S.; Lowe, M. A.; Gao, J.; Kiya, Y.; Henderson, J. C.; Abruña, H. D. Synthesis and Characterization of Poly-3,4-Ethylenedioxythiophene/2,5-Dimercapto-1,3,4-Thiadiazole (PEDOT-DMcT) Hybrids. *Electrochim. Acta* **2015**, *167*, 55–60.

(10) He, J.; Su, J.; Wang, J.; Zhang, L. Synthesis of Water-Free PEDOT with Polyvinylpyrrolidone Stabilizer in Organic Dispersant System. *Org. Electron.* **2018**, *53*, 117–126.

(11) Massonnet, N.; Carella, A.; Jaudouin, O.; Rannou, P.; Laval, G.; Celle, C.; Simonato, J. P. Improvement of the Seebeck Coefficient of PEDOT:PSS by Chemical Reduction Combined with a Novel Method for Its Transfer Using Free-Standing Thin Films. *J. Mater. Chem. C* **2014**, *2* (7), 1278–1283.

Chapter 8

Stimulus-triggered release of surface-bound particles using reversible dynamic chemistries

Abstract: High molecular weight polymers have been demonstrated to be attractive candidates for flowable electrolytes in redox flow batteries, owed to their high upper concentration limit in organic solvents as well as their highly-tunable electrochemical behaviors. However, concern has been expressed over the possibility that these materials will accumulate over time on electrode surfaces, passivating them and diminishing flow battery performance. In addressing this future concern, this study showcases the design and characterization of a system for triggerable electrode regeneration by controllably de-crosslinking polymer particles at their interface with substrate surfaces. PGMA particles are functionalized with disulfide crosslinkers, capable of highly reversible cleavage to form thiolates under a reducing electrochemical stimulus or thiol radicals under application of UV photoexcitation. Under a convective flow, application of these stimuli is shown to weaken the adhesion of these particles to a substrate, resulting in dramatically enhanced removal, which is quantified over a variety of conditions. A fluorescent tagging scheme is used to study the nature of the electrochemical cleaning process, revealing only a small amount of crosslinkers nearest the electrode surface need to be broken in order to trigger particle release. Lastly, regeneration of a flow cell electrode is demonstrated by comparing the polarization profiles of pristine and fouled electrodes in targeting a ferrocene-bearing polymer particle fluid electrolyte, followed by electrode cleaning using a UV stimulus, resulting in near-complete recovery of electrode functionality. This investigation highlights the results of careful material design, incorporating responsive covalent chemistries into a modular polymer scaffold, imbuing important secondary functionalities for improved performance in conceptual energy storage materials.

8.1 Introduction

As populations transition from fossil fuels to renewable sources for grid-scale energy, the ability to store and balance intermittent generation becomes increasingly vital. One proposed system to meet this need is the redox flow battery (RFB), in which flowing electrolytes are used to decouple energy generation and storage by way of isolating electrolyte reservoirs from the cell stack. RFBs based on organic redox-active species are especially interesting due to the high abundance and inexpensive nature of the raw materials coupled with high tunability of the synthesized molecules, allowing for precise control over redox potential, solubility, and supramolecular structure, among other properties.[1-7] Of the possible organic molecular motifs, polymer RFBs are particularly promising for next generation technologies, as they can enable high performance batteries without the need for expensive, flux-inhibiting ion exchange membranes, with simpler size-exclusion membranes adequate for screening the high molecular weight active species.[8-14] This size-exclusion principle was demonstrated successfully in several soluble polymer systems, where the hydrodynamic radius of the solvated polymer species exceeded the threshold for crossover across commercially-available porous battery separators.[11,13]

While these polymers showed great resistance to crossover, they were limited in terms of the concentration of redox-active species attainable in solution. At moderate concentrations, the viscosity of polymers solutions becomes prohibitively high, negatively impacting the kinetics of the redox active species in solution, increasing energy losses due to pumping, and putting undo stress on mechanical components in the flow system, resulting in decreased performance and battery lifetime. As high concentration of active species is considered one of the key approaches to reducing performance-based cost of RFB systems, overcoming the challenges presented by high viscosity is critical for viability as a future technology.[15,16]

In response to the difficulties associated with high mass loading of soluble polymers, multiple efforts have turned to insoluble redox active colloids (RACs). RACs of a variety of size ranging from 10s to 1000s of nm can be synthesized simply using emulsion or dispersion polymerization techniques from a wide variety of polymer chemistries.[17-23] Functionalizing these particles during or after polymerization with a small degree of permanent crosslinking prevents dissolution in solvent, allowing for electrolytes with greatly reduced viscosity for the same or higher amount of mass loading. In addition to the rheological benefits resulting from the use of insoluble materials, the increased particle size of the RACs served to further improve the size exclusion phenomenon, improving crossover rejection and allowing for even more kinetically-beneficial membrane selection.

Despite the advantages granted by RACs, they are not without their own challenges. It is a well-established fact that particulates in flowing systems are susceptible to adhesion on fluid-exposed solid surfaces. This process, referred to as fouling, presents particular problems to RFBs, where particulates can obscure the separator membrane or coat electrodes. Given enough time, these particles can form inactive layers on the electrode surfaces that limits the ability of the battery to charge and discharge. Under the intense electrochemical conditions of the RFB, the material comprising these blocking layers can degrade and the passivation layer can become permanently adhered, resulting in the need for costly repairs and operational downtime.

In addressing this impending issue, numerous efforts are underway, leveraging opportunities for action at each step in the fouling process. Coatings and pretreatments for surfaces susceptible to fouling can help mitigate or prevent the process before it occurs, but such approaches can be complex and costly, and modulating the substrate surface stands to impact the material performance. On the other end of the process flow, many efforts have looked into regenerating surfaces once particulates have already accumulated and decomposed to a nonfunctional state. Besides the brute force approach of completely degrading the particulate using harsh chemical cleaning procedures, which also stand to damage the capital components of the RFB, several efforts have been made to design redox-active materials capable of being degraded in a controlled manner, with the degradation byproduct fit for recycling and eventual reuse. Work by Nguyen et al. demonstrated design of polymeric materials combining redox-active pendant groups to a polypeptide backbone, capable of being depolymerized using acidic conditions to amino acid small molecules potentially capable of later recycling back to macromolecular materials.[24] Going one step further, Qian et al. demonstrated proof of concept programmed degradation of redox-active polymers using an electrochemical stimulus, wherein homobenzylic ethers could be controllably cleaved by applying an oxidative potential.[25] This similarly allows for potential recapture of the degradation products, but both of these processes ultimately require separation of the degraded species from the greater system for further processing.

In this work, we present a system in which an adhered redox-active particle (RAP) is capable of controlled, programmed release from an electrode surface, but in which the greater structural integrity of the particle is maintained, allowing it to stay in service within the RFB for the remainder of its useful lifetime. This is accomplished through molecular design of the particle's structural components. The polymer comprising the particle scaffold is crosslinked via two different chemical species: permanent and reversible crosslinking agents. A minimal amount of permanent crosslinker is used to maintain the particle's structural integrity. In addition, a larger concentration of reversible crosslinks are used to impart change to the particle structure on demand. These reversible crosslinks are capable of cleaving under specific stimuli, resulting in a volumetric shift for the solvent-swollen polymer. This phenomenon can be localized to the regions of the particle in contact with the electrode surface, allowing for defouling while avoiding disrupting the greater particle structure.

The system designed for this study is comprised of poly(glycidyl methacrylate) (PGMA) particles minimally crosslinked with hexamethylenediamine (HMDA) and more densely with 2-amino-1,3,4-thiadiazole disulfide, yielding the redox-responsive "P2-SS" particles discussed in the previous studies. Disulfides were selected as the reversible crosslinker for this study for several reasons. Firstly, the cleavage of disulfides is highly reversible. In order to maintain a long lifetime of the RFB electrolyte, the chosen crosslinker must be able to cleave and reform multiple times with minimal irreversible degradation. Thiadiazole-based disulfides have gained particular interest as potential organosulfur redox centers for energy storage, an application that hinges on high material stability.[26] Secondly, disulfides are well-known to respond to multiple stimuli, providing flexibility in the control of programmed degradation. In this study, triggered defouling of disulfide-crosslinked particles is achieved using both a reducing electrochemical stimulus to form thiolate anions, as well as UV photoexcitation to form thiol radicals, resulting in de-crosslinking of the particle at the substrate surface, causing particle release (**Figure 8.1**). Particle defouling is studied using a custom flow system with model fouled electrodes produced by drop-casting particles onto a transparent 2D surface, allowing for characterization using conventional optical microscopy. Next, under the flow of supporting electrolyte, the adhered particles are subjected to different stimuli. The difference in number of particles before and after stimulus is quantified by software-aided particle counting. This analysis revealed a nearly four-fold increase in particle defouling is observed as a result of the application of cleaving stimulus vs convective flow alone. Additionally, a time-dependent study of particle removal reveals that for electrochemical defouling, particle removal requires a short initiation period, after which defouling occurs rapidly. These observations lead to a possible explanation for the defouling mechanism, in which a small amount of current is needed to sufficiently break the crosslinks nearest the point of electrode contact, after which the particles can be lifted without extensive charging into the particle body. This hypothesis is further investigated using confocal microscopy. A brominated fluorescent tag, 1-(bromomethyl)pyrene, is irreversibly covalently linked to thiolates when a reducing stimulus is applied to the particle surface in non-convective conditions. Subsequent fluorescent confocal microscopy of the reacted particles allows direct observation of the localized nature of the particle reduction to the electrode surface. In order to demonstrate proof-of-concept electrode defouling, ferrocene-bearing polymer particles were charged on electrodes in varying states of fouling. Electrodes with fouled surfaces resulted in significantly reduced charge transfer at given overpotentials. After application of a defouling stimulus, current density increased, approaching that of a pristine electrode. This system showcases the concept of how stimulus-responsive chemistries can be used to create multi-functional energy storage materials. Reversible covalent chemistries such as this can be integrated into polymer particles with charge storage capability for in-line cleaning as presented as well as numerous other potential systems.

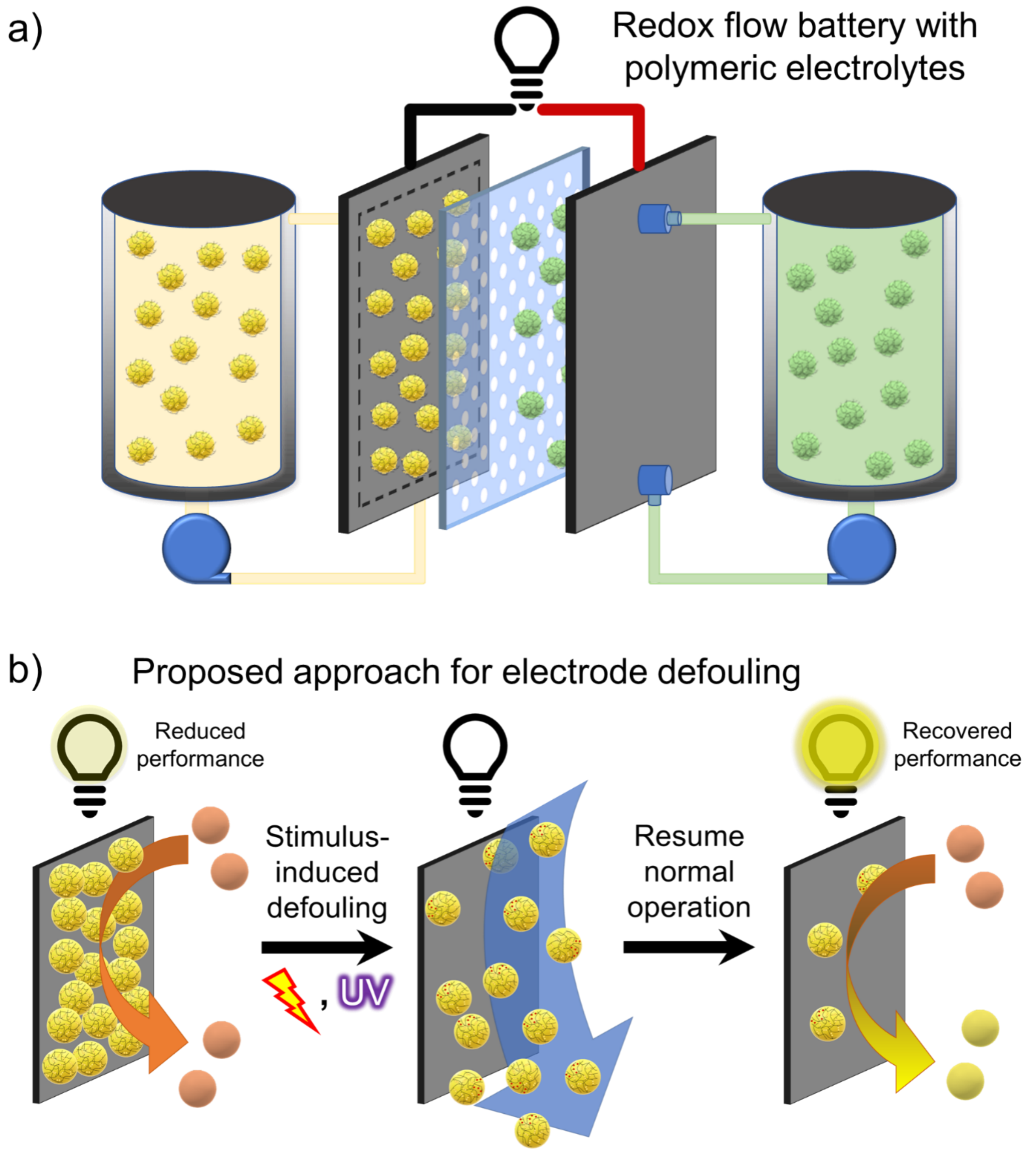

Figure 8.1. Concept schematic for stimulus-triggered defouling of redox flow battery electrodes. a) Redox flow batteries function by flowing electrolytes separated by a semi-permeable membrane over opposing electrode. These electrodes may become fouled over time. b) By applying a cleaning stimulus at the electrode surface, fouled electrolyte can be lifted with the aid of solvent flow, allowing increased access to the electrode and resulting improved battery performance.

8.2 Results and Discussion

8.2.1 Particle synthesis and characterization

Monodisperse PGMA particles of approximately 2198 ± 142 μm diameter in acetonitrile (ACN) were synthesized using dispersion polymerization followed by functionalization with 1 mol% of HMDA as permanent crosslinker to assure particle integrity. The particles were then functionalized with 2-amino-1,3,4-thiadiazole according to the procedure outlined in a recent work.[27] 2-amino-1,3,4-thiadiazole was selected for its mild reduction potential and relatively high electrochemical reversibility from a series of disulfides screened and by DFT simulation and verified by solution CV (**Figure 8.8**). Final particles consist of a lightly HMDA-crosslinked PGMA backbone and dense stimulus-responsive crosslinking with 1-SS-1, as shown in **Figure 8.2a**, verified via FT-IR and UV-Vis spectroscopy (**Figure 8.9 and 8.10**). The responsive nature of the disulfide bond allows for removal of unreacted crosslinkers as a final modification, wherein the particles are exposed to UV light in a DMSO suspension, resulting in disulfide cleavage and the subsequent diffusion of unbound thiol radical out of the particle and into bulk solution, leaving only bound moieties to reform into crosslinks. Diffusion of the unreacted small molecule is monitored via UV-Vis spectroscopy, as reported in previous work.[27] Due to the increase in dense disulfide crosslinking, the particles are reduced to ca. 1726 ± 106 μm in diameter. The particle size decrease is reversible with thorough disulfide cleavage and reformation (**Figure 8.2b**) and is demonstrated via chemical redox (**Figure 8.2c**). Control particles with only HMDA as a permanent crosslinker were synthesized to reach the same hydrodynamic radius as the disulfide functionalized particles (ca. 1726 ± 106 μm) in ACN.

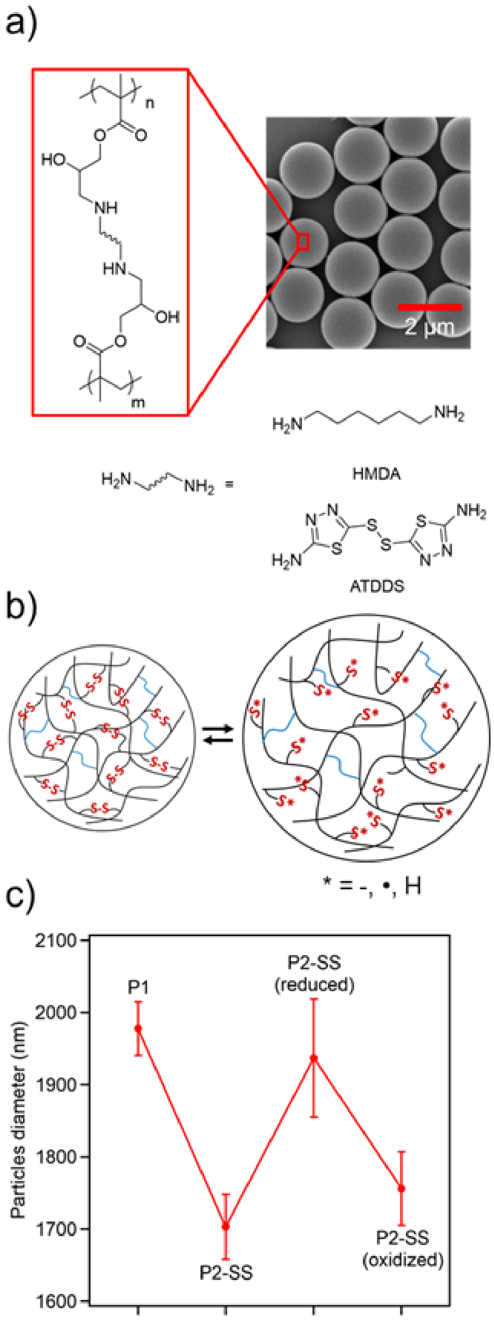

Figure 8.2. Scheme for particles bearing stimulus-responsive disulfide crosslinkers. a) Chemical structure and SEM image for "P2-SS" PGMA particles dual-crosslinked with HMDA and 1-SS-1. b) Scheme for mechanism of revisable particle size change with different cleaving stimuli. c) Reversible size change for P2-SS in suspension as result of chemical reduction and oxidation.

8.2.2 Stimulus-triggered controlled particle release from 2D surfaces

To create a model fouled surface, particles were adhered onto the substrate by drop-casting from sonicated particles dispersion (5mg/mL) with dry diameter of ca. 1.68 micron confirmed by scanning electron microscopy (**Figure 8.2a**). Demonstrating controlled stimulus-triggered release of particles from a flat surface was accomplished using a modular flow cell, a description of which can be seen in **Figure 8.11**. The flow cell allows for supporting electrolyte flow between interchangeable parallel plates while controlling for gap width using spacers of different thickness. Stimulus was applied to one plate acting as a substrate for drop-cast particles, either plain or ITO-coated glass slides, while simultaneously exposing the particle-bearing surface to the liquid shear flow. Any particles released, through the action of the disulfide crosslinkers breaking or otherwise, are washed away via solvent flow. After a set period of stimulus exposure, the cell is disassembled, and the substrate is collected.

To determine the change in number of particles during the experiment, substrates were imaged ex situ before and after exposure to stimulus in the flow cell (**Figure 8.3a-c**). Using an optical microscope, predefined spots were imaged at 10x and 50x magnification. Markers etched into the back (uncoated) side of the substrates, as well as any visible landmarks (specific particle arrangements, defects in the glass surface, etc.) were used to ensure exact alignment of the image field in before and after images (dashed line in **Figure 8.3b** illustrates concept, as particles and marker are not simultaneously visible). Landmarks were obtained and aligned, and then the image was focused to bring particles into view. ImageJ’s particle analysis tool was used to count the number of particles visible in the field of view (**Figure 8.3c**). The amount of particle release is then determined by the difference in particle number before and after exposure to stimulus in the flow cell.

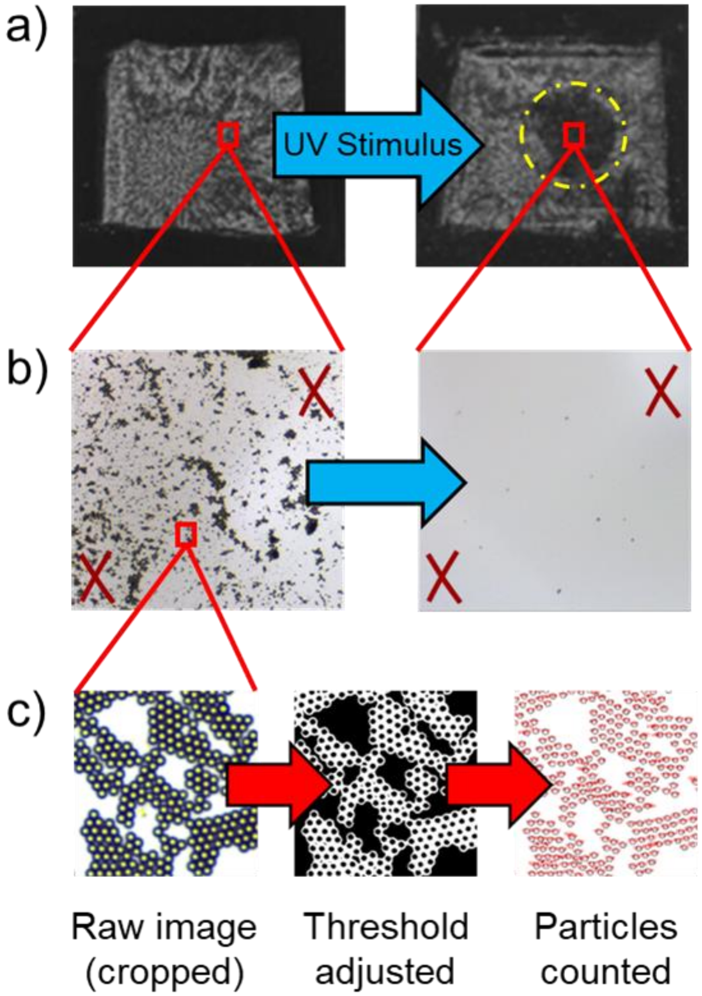

Figure 8.3. Process flow for quantitative determination of particle removal. a) Direct observation shows 2D substrates before and after particle removal. Yellow dashed circle indicates area exposed to UV stimulus via fiber optic source. b) Markers are used to find same spots before and after testing (Note – the markers are etched onto the back of the substrate, and therefor can't be simultaneously imaged with the particles). c) Software manipulation of 50x images resulting in particle counting (Images shown are small subset expanded to show detail).

In practical flow battery systems, it's not unreasonable to assume flow rate can be momentarily increased, using fluid sheer force to aid defouling. However, for this study, to ensure the majority of particle release was the result of stimulus and not purely the convective forces of fluid flow, a series of different flow rates were tested, up to the maximum nominal flow rate allowed by the equipment at hand. Calculations performed based on different flow rates of the selected solvent and cell geometry suggest flow through the cell in this study should be laminar, and fluid force should occur in the direction parallel to the substrate (**Figure 8.12, Table 8.1**). Particles were shown to remain mostly attached to the substrate surface up to a pump flow rate of 30 mL/min, with calculated particle removal around 10%. Rates approaching 40 mL/min began to show particle removal as a result of fluid convection only, with ca. 50% removal (**Figure 8.4a**) Based on these observations, the pump rate was held at 30 mL/min for the remainder of the study.

As mentioned previously, disulfides are known to reversibly cleave under the influence of a variety of stimuli. For this study, both electrochemical and UV stimuli were investigated for controlled particle release. Electrochemical stimulus was applied as a reducing voltage through the conductive surface of the ITO substrate. In order to apply an electrochemical stimulus, electrodes are attached to the ITO-coated glass slide and the opposing stainless steel current collector via alligator clips (**Figure S4b**). Due to the configuration of the flow cell, a potential is applied across the whole cell without using a reference electrode. A series of polarization losses that occur under normal operation of the flow battery, including polarization of the electrode and ohmic losses due to electrolyte resistance as two examples. Electrochemical impedance spectroscopy allows the user to probe these effects to a degree (example EIS data for the flow cell system used in this study can be found in the SI), but a complete deconvolution of the individual contributions can remain difficult. Additionally, the defouling concept employed in this study operates in such a way that in a practical setting, the redox potential required to cleave the crosslinker may not overlap with that required to charge the energy storage chemistry. As such, the opposite electrode may not undergo a faradaic process. In place, a capacitive process will occur, resulting in a cell potential larger than that necessary for the defouling redox process to occur. As a result of these realities, one must fix a cell potential higher than the disulfide reduction’s Nernst potential in order to initiate reductive cleavage of the particle crosslinkers. A 2 V total cell potential was used for this study. A 2 V total potential is a reasonable value achievable with many studied flow chemistries and does not pose a threat to the selected supporting electrolyte (100 mM $TBAPF_6$ in ACN). In this configuration, the particle-bearing ITO is set as the negative electrode, receiving an accumulation of negative charge (electrons) as the electrode polarizes to the necessary potential for 1-SS-1 reduction.

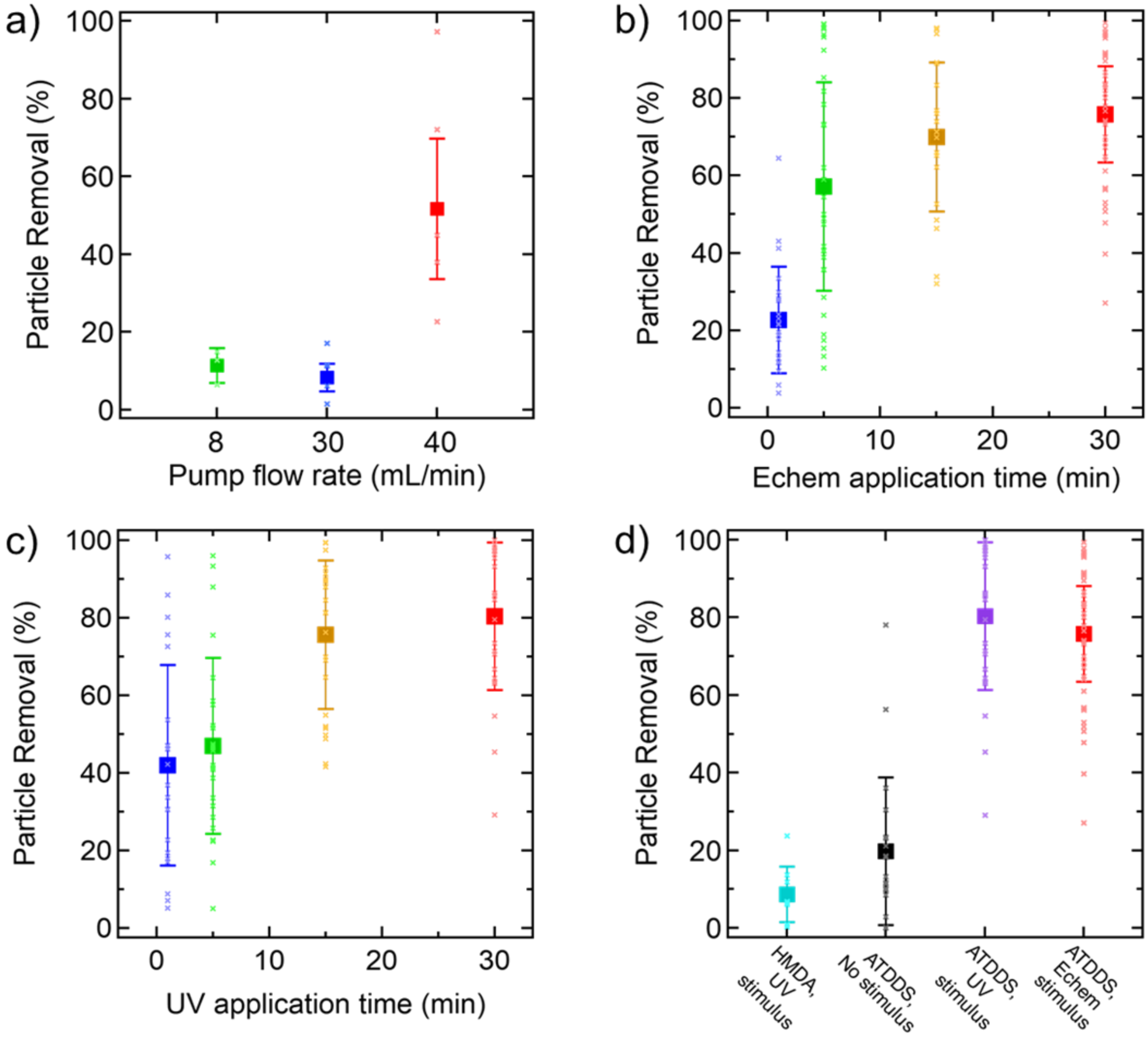

Figure 4. Particle removal from 2D substrates via controlled stimulus under sheer flow conditions. a) Experimental flow rate determination. b) Time-dependent particle removal with electrochemical stimulus and c) UV photoexcitation stimulus. d) Particle removal after 30 minutes, comparing control conditions to both stimulus sources.

The second stimulus investigated was photoexcitation by UV light. UV defouling was demonstrated with the same flow cell setup with electrochemical stimulus. UV stimulus was applied via a UV source at a wavelength of 320 nm to 500 nm through the back of the glass substrate using a hole in the center of the machined back panel, which also served to secure the location of the UV source fiber optic cable. 1-SS-1 is known to show UV absorption at 322 nm and use of the previously mentioned UV photo-annealing process has demonstrated the selected UV source provides adequate excitation to induce disulfide exchange within the P2-SS particles. Quartz glass microscope slides were selected for this portion of the study to ensure high UV transmittance in the wavelength range required for photoexcitation.

It is desirable to identify the approximate minimum stimulus time required to successfully remove the particles from their adhered substrate, as doing so not only reveals further insight into the defouling mechanism, but also allows for a more attractive, less energy-intensive cleaning process. As such, samples cast on ITO were exposed to a constant voltage for different periods of time (**Figure 8.4b).** During a short time period following polarization (≤1 minute), a relatively small number of particles are removed (ca. 23%), similar to that when P2-SS is exposed to convective flow only. After several minutes, more appreciable removal is observed (ca. 57, 70 and 76% at 5, 15, and 30 minutes, respectively) with increasing inter-sample consistency in the number of particles removed. This information suggests that a certain number of crosslinks must be broken for particle de-adhesion to occur, and the relatively sluggish kinetics of the disulfide redox couple leads to a small necessary initiation time for the defouling process. After this initiation process, particle removal occurs rapidly, and extended defouling time periods only result in a small degree of removal for more well-adhered particles. These results lend evidence for a likely hypothesis that only a small portion of the particle needs to be de-crosslinked to release the particle, this being the portion in direct contact with the electrode. In contrast, if the particle needed to be extensively de-crosslinked in order to free from the substrate surface, it would be expected that a longer time be required before substantial removal is observed. While the exact time required for substantial defouling will vary based on the practical electrode surface, this result is promising evidence for the electrochemical defouling process being relatively conservative in energy usage, needing only short applications of stimulus to clean electrode surfaces. A time-dependent analysis for UV defouling shows slightly different results **(Figure 8.4c**). A larger percentage of defouling occurs at the earliest time point (ca. 42% at 1 minute), attributed to the relatively instantaneous nature of the photo stimulus disulfide cleavage mechanism. However, at later time points (ca. 76 and 80% at 15 and 30 minutes, respectively), the amount of particle removal is roughly comparable to that of the electrochemical stimulus.

A set of negative control experiments were performed in which the samples were exposed to the fluid flow for 30 minutes, but not to either cleaving stimulus. Electrochemical stimulus experiments were performed with a constant cell potential at the open circuit value. UV experiments simply received no irradiation. Results from these conditions over numerous runs yielded only a small amount of removal (< 20%) (**Figure 8.4d**). By comparison, the application of a stimulus greatly enhanced the amount of particle release. As shown previously, electrochemical reduction and UV exposure showed ca. 76% and 80% particle removal, respectively, after 30 minutes of applied stimulus, a four-fold increase from fluid convection alone. In order to confirm the breaking of disulfide crosslinkers as a necessary component for this method of particle release, particles heavily crosslinked with HDMA only resulting in a similar solvated size to P2-SS were similarly drop-cast to substrates and subjected to the same procedure and stimuli. It was found that particles with only permanent crosslinkers demonstrated no substantial removal from surfaces with application of stimulus (ca. 8.7%, UV and electrochemical stimulus aggregate value), indicating that particle release is due to a mechanism involving reversible crosslinking, and not substantial destruction of the particle backbone or substrate surface (**Figure 8.4d**).

8.2.3 Examining surface-bound particle stimulus response via fluorescent tag imaging

Introducing a molecule capable of stably binding to the reduced thiolate allows for direct observation of where the particle is impacted by the reducing stimulus. 1-(bromomethyl)pyrene (BrMePyr) was selected as the tagging molecule for this study. It was anticipated that upon reduction of the disulfide bond, the resulting thiolates would displace the bromine group and form a more stable carbon-sulfur bond (**Figure 8.5a**). This process was investigated first via CV using small molecules in solution. An acetonitrile solution was prepared containing 1 mM ethylamino thiadiazole disulfide (2-SS-2) and 10 mM benzyl bromide (BnBr) as more soluble surrogates for particle-bound amino thiadiazole and BrMePyr, respectively, in addition to 100 mM TBAPF6 as supporting electrolyte. Sweeps were performed from 0 to -1.2V vs Ag/Ag+, causing reduction of the 2-SS-2 dimer to thiolate monomers, with a reduction peak potential around -1.13 V. In a solution absent of BnBr, an oxidation peak occurs around -0.20 V on the return sweep, indicating the re-oxidation of thiolates back to disulfides. However, in the presence of BnBr, there is a distinct lack of re-oxidation peak, suggesting that reaction with the brominated compound has sequestered the thiolates (**Figure 8.5b**).

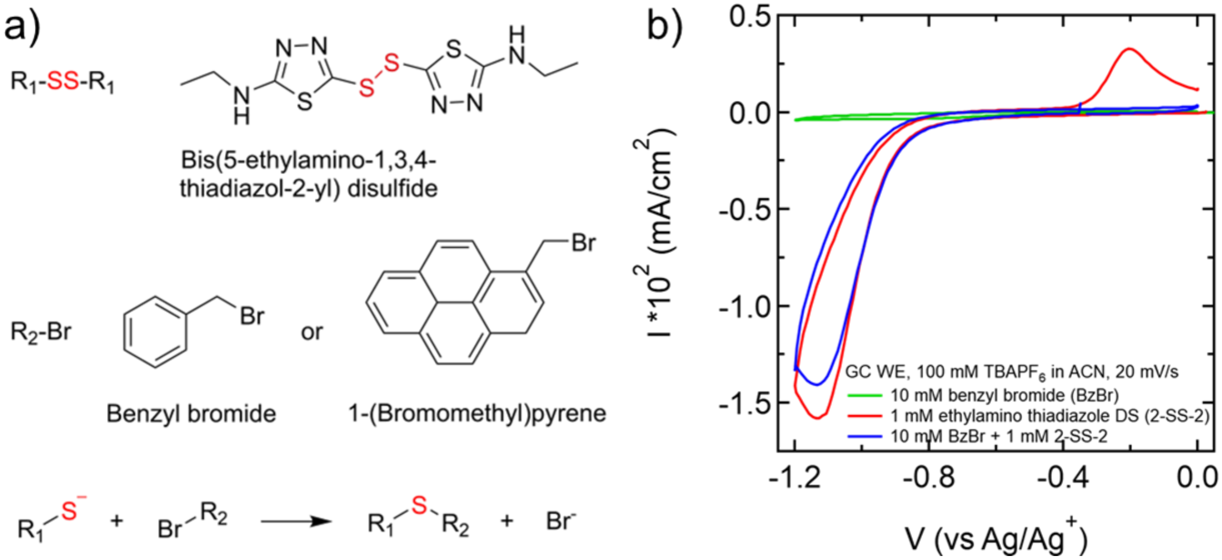

Figure 8.5. Approach for electrochemically reducing disulfides to thiolates and tagging with brominated compounds. a) Small molecules used for validation and tagging study and chemical scheme for thiolate tagging. b) Cyclic voltammetry showing sequestering of thiolates by reaction with brominated compounds resulting in lack of electrochemical reoxidation to disulfides.

Particle samples were prepared by casting P2-SS onto ITO-coated coverslips (SPI Supplies 06480-AB, #1.5 thickness, 15-30 ohms). The coverslips bearing particles were used as the working electrode in a 3-probe electrochemical cell. Electrodes were submerged in a DMSO solution 1 mM BrMePyr and 100 mM TBAPF$_6$. A constant potential of -1.0 V vs Ag/Ag$^+$ was applied to the working electrode for 5 minutes, after which the potential was removed and the system allowed to relax, as observed by open circuit potential. The ITO coverslip was removed from the solution and washed by soaking in clean DMSO, then clean acetone. Images were taken from a bottom-up view, taking progressive focal points further away from the substrate surface at 0.1 µm intervals, one layer of which is seen in the black and white image below (**Figure 8.6a**). A side-view projection of the reconstructed confocal image stacks allows for visualization of fluorescence in the direction perpendicular to the ITO substrate. The second image (blue color) shows fluorescence of the thiadiazole aromatic ring of 1-SS-1. The third image (green color) shows fluorescence resulting from 1-S-MePyr as a product of BrMePyr reacting with thiolate anions (**Figure 8.6b**). The dashed line represents the anticipated height of the particle.

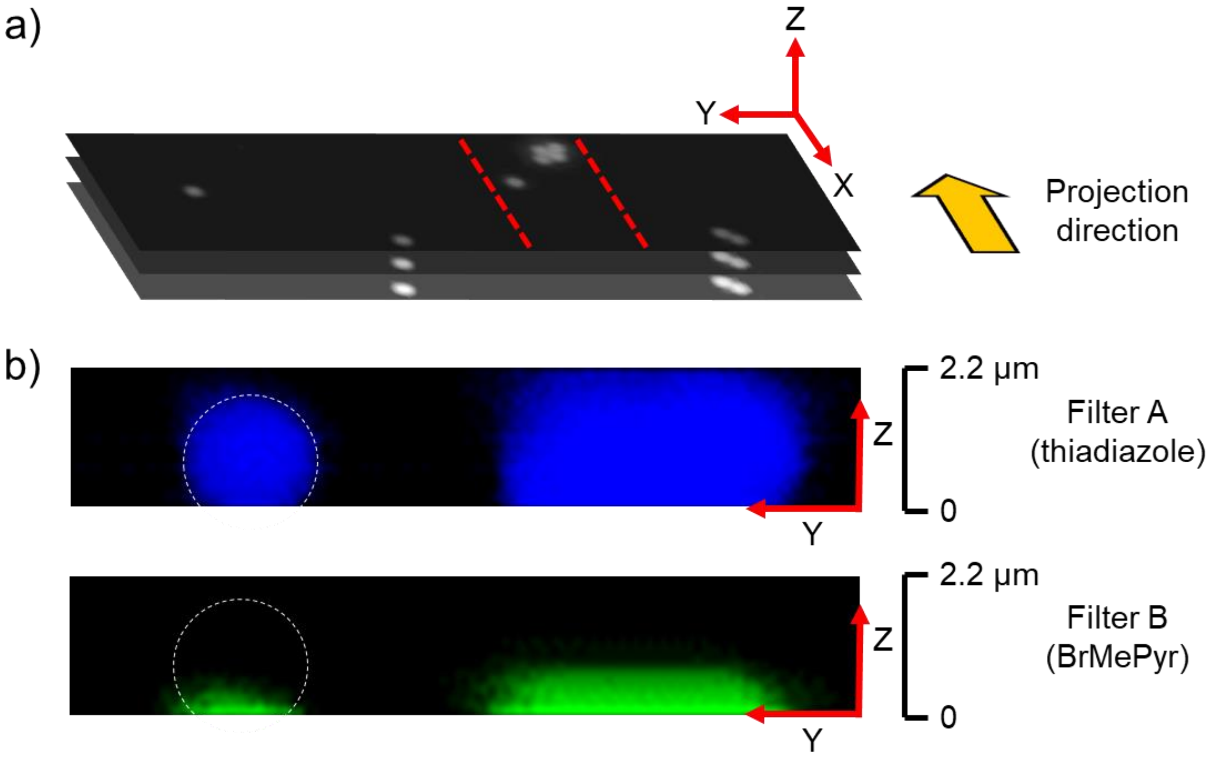

Figure 8.6. Confocal microscopy of P2-SS particles tagged with BrMePyr. a) Bottom-up view of isolated particle on ITO-coated cover slip. b) Side view of vertical projection of particles on substrate using different fluorescent filters.

Fluorescence from thiadiazole can be seen evenly distributed throughout the particle height, providing evidence for relatively homogeneous particle functionalization with 1-SS-1. By comparison, fluorescence from the 1-S-MePyr is most localized near the electrode surface. In the short time frame required for defouling as demonstrated by the flow cell studies, only disulfides in the portion of the particles nearest the electrode are allowed to reduce while the majority of the particle remains densely crosslinked. This phenomenon provides evidence for the theory that the defouling mechanism is mediated by de-crosslinking of the polymer at the electrode surface, exclusively in the case of electrochemical defouling.

8.2.4 Electrode performance regeneration via stimulus-induced surface defouling

To ultimately demonstrate the ability of the defouling mechanism explored in this study, a test was performed by probing the electrochemical accessibility of the flow cell working electrode to previously-reported[19] ferrocene-bearing particles (PVBC-Fc) (**Figure 8.13**) in the presence of varying degrees of “fouling” from drop-cast P2-SS particles. Accessibility of the electrode was probed using linear sweep voltammetry, measuring the amount of current delivered to PVBC-Fc particles at increasing polarization voltages. By using ITO as the working electrode and sweeping in the oxidizing (positive potential) direction, ferrocene was selected for as the dominant contributing factor to any current measured. As seen below in **Figure 8.7a**, ferrocene (Fc) was selected as a second redox center with substantial distance in redox potential from 1-SS-1. Ensuring adequate spacing between the “energy storage” and “defouling” electrochemical processes allows for materials with multiple functionalities to selectively target one functionality at a time. In the case of this system, future particles would feature both energy storage moieties as well as structurally-integral defouling chemistries. To determine the effect of particle removal, the oxidation of PVBC-Fc particles was first examined using a clean ITO electrode. Next, an electrode obscured with P2-SS particles was tested to determine losses in current due to electrode blockage. Finally, the same fouled electrode was put through the UV defouling procedure described earlier and tested again using linear sweep voltammetry.

When comparing the blank electrode to the fouled electrode, the impact of electrode fouling is made apparent. With the addition of the fouled layer, significant losses in current density were observed at moderate overpotentials. These results confirm that the layer was blocking access of many Fc-PVBC particles to the electrode, effectively passivating it (**Figure 8.6b**). After 30 min under UV irradiation at 30 mL/min of fluid flow, the same electrode was tested once more. Following defouling, a substantial increase in the current density was observed, indicating that much of the electrode's surface area that had been previously blocked was now accessible to the PVBC-Fc particles. The current densities achieved at high overpotentials nearly matched that of the pristine ITO electrode, indicating that nearly all the performance has been recovered through the stimulus-triggered defouling method.

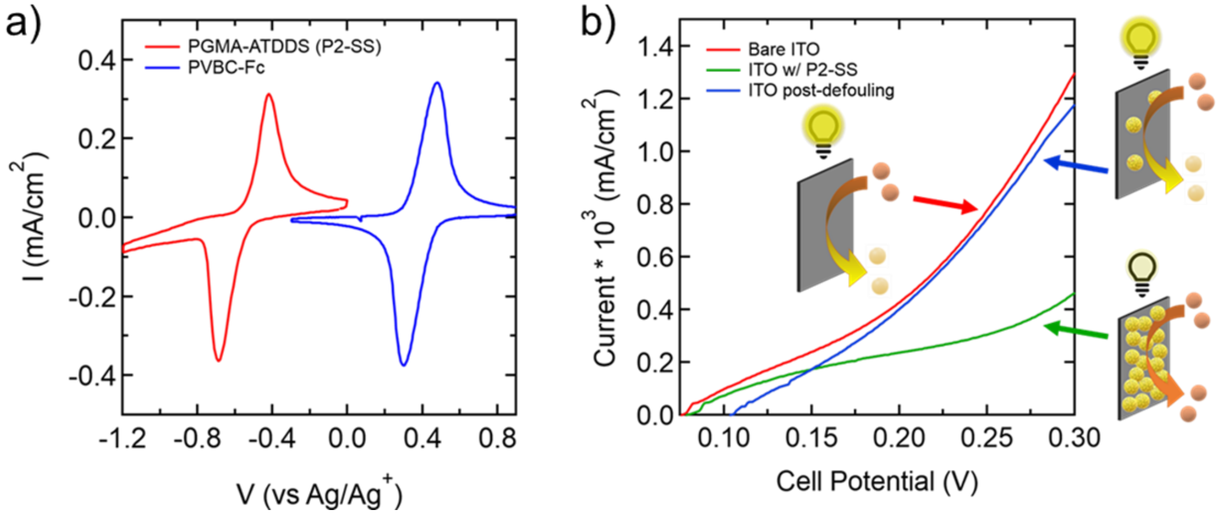

Figure 8.7. Examining the impact of fouling and defouling on electrode accessibility. a) CV of 1-SS-1 and ferrocene redox centers, demonstrating lack of activity overlap. b) Polarization curves for PVBC-Fc activity at ITO electrode surface, showing performance of a clean electrode and a fouled electrode before and after defouling.

8.3 Conclusions and Outlook

In summary, we have demonstrated a new strategy to realize stimulus-triggered release of surface-bound particles using reversible dynamic chemistries. Monodispersed PGMA microparticles were synthesized with a minimum amount of permanent crosslinkers to maintain structural integrity. The particles were subsequently crosslinked with reversible redox-active and stimulus-responsive bis(5-amino-1,3,4-thiadiazole-2-yl) disulfide crosslinkers. Model fouled surfaces were prepared by drop-casting particle dispersion onto transparent 2D substrates allowing characterization using an optical microscope. The particle defouling was studied in a custom flow cell under the flow of supporting electrolyte with either UV irradiation or electrochemical potential as stimuli for triggered defouling. By software-aided particle counting before and after exposure to fluid flow either with or without stimulus, a nearly 4-fold increase in removed particulate is observed with the application of stimulus. In a time-dependent study using electrochemical potential-induced defouling, a short initiation period was needed prior to rapid defouling. A proposed mechanism for particles defouling suggests that only a small amount of charge transfer is needed at the particle-electrode interface is sufficient to break contact between the electrode and particles. This hypothesis was verified by using a brominated pyrene fluorescent tag which irreversibly reacts with thiolate anions following disulfide reduction. Fluorescence confocal microscopy showed particle reduction is localized to the particle-electrode interface. To ultimately demonstrate the ability of the proposed defouling mechanism to regenerate performance of a flow battery electrode, ferrocene-bearing polymer particles were charged using a flow battery half-cell with the electrode in varying states of fouling. Sufficiently fouled electrodes showed diminished current density, which was restored to levels approaching a pristine electrode after a short period of exposure to UV stimulus. Overall, this work successfully demonstrates a modular redox active colloid platform which capable of controlled, programmed particle release from 2D surface through any one of multiple external stimuli. This design provides a promising route to resolve performance decrease resulting active material fouling anticipated in polymeric redox flow batteries without the need for dismantling and excessive downtime, as well as any one of numerous other applications.

8.4 Materials and Methods.

Materials. Glycidyl methacrylate (GMA) containing inhibitor, 5-amino-1,3,4-thiadiazole-2-thiol, hydrogen peroxide solution (30% w/w) in an aqueous solution containing inhibitor; polyvinylpyrrolidone (PVP) (average mol. wt. 40,000), hexamethylenediamine, tetrabutylammonium hexafluorophosphate, and acetonitrile were purchased from Sigma-Aldrich. All other reagents were purchased from Fisher Scientific. 1-(Bromomethyl)pyrene (BMP) was purchased Ambeed, Inc. All reagents were used without further purification unless mentioned.

Synthesis of PGMA (P1) particles. The P1 particles were synthesized by modified a reported study by Horák and coworkers.[28] The inhibitor in GMA monomer was removed by running through an alumina basic column. In a 250 mL round bottom flask, 2.1 g of PVP (40 KDa) was dissolved in 83 g of EtOH and 7.7g of water. The reaction vessel was heated to 70 C with a stir bar stirring at speed of 165 rpm and purged with argon gas for 20 min. 0.24 g of AIBN was dissolved in 12 g of purified GMA monomer. The monomer and initiator were charged drop-wise into the reaction vessel. The system was continued to purge with argon for 15 min. The product was washed with methanol and centrifuged for three times prior to drying in a vacuum oven.

Functionalization of P1 with 1-SS-1 to produce P2-SS. The P2-SS particles were synthesized following the same procedure previously reported by the same authors.[29] 0.5 g (~3.5 mmol of GMA repeating units) of P1 particles were dispersed in 25 mL of THF via bath sonication, followed by 1-SS-1 (4.65 g, 17.5 mmol) DMSO solution (100 mL). The reaction vessel was purged with argon gas and heated to 66 °C at 300 rpm for 6 days. Post functionalization, the particles were centrifuged at 4000 rpm for ten minutes, decanted, and washed with DMSO three times. The same process was repeated with methanol three times. The particles were then dispersed in DMSO and irradiated with a UV source as described in the previous work to remove mono-functionalized 1-

SS-1 from P2 to produce P2-SS. The particles were washed and centrifuged with 1:1 methanol and DMSO and dried under the vacuum at 55 °C overnight.

Synthesis of P1-HMDA control particles. 0.5 g (~3.5 mmol of GMA repeating units) of P1 particles were dispersed in 40 mL of EtOH via bath sonication. 200 mg (1.75 mmol) of HMDA in 10 mL of ethanol solution was charged to the reaction vessel. The reaction was carried out 50 °C with stirring for 2 days. The particles were washed with centrifuged, decanted, and washed methanol three times. The particles then dried under vacuum at 55 °C overnight.

Drop-casting particles onto a transparent 2D surface. Glass or ITO substrates were sonicated in acetone and methanol respectively for 5 minutes. The substrates were then blow-dried with nitrogen. 5 mg/mL of particles were dispersed in EtOH by bath sonication for 30 min prior to drop-casting. 20 microliter of particle dispersion was drop-casted onto the center of the substrate and allowed dry. Particles were imaged and counted before and after defouling experiments.

Synthesis of PVBC-Fc particles. The PVBC particles were synthesized following the reported procedure reported by Montoto and coworkers.[19] Polyvinylpyrrolidone (1.15 g, average mol. wt. 40,000) was dissolved in 95 mL of 200 proof EtOH with a magnetic stir bar stirring at 165 rpm. Inhibitors were removed from vinyl benzyl chloride and divinyl benzene monomer by passing through a basic alumina column separately. 0.1 g of AIBN was dissolved with 4.9 mL 4-vinyl benzyl chloride, 90%, and 0.1 mL of divinylbenzene, 80%. The monomer mixture with AIBN was charged into the reaction vessel. The reaction vessel was sealed and purged with filtered dry Ar for 30 min before being heated up to 70 °C. The reaction was carried for 12 hrs. The resulting particles were centrifuged, decanted, and washed with methanol three times prior to drying in a vacuum oven at 50 °C for 1 day.

1 g of dried PVBC particles were redispersed in 30 mL DMF and 30 mL THF solvent mixture using bath sonicator for one hour. 10 mL of (dimethylaminomethyl) ferrocene was added to the reaction vessel followed by 30 min purging with filtered Ar. The reaction vessel was heated to 50 °C and the reaction was carried out for 5 days. 12 g of ammonium hexafluorophosphate was dissolved in 30 mL of water and charged into the reaction vessel. The ion-exchange reaction was carried out for 1 day at RT with stirring. The resulting particles were centrifuged, decanted, and washed with THF three times and methanol three times prior to drying in a vacuum oven at 50 °C for 1 day.

Sample preparation for confocal microscope. P2-SS particles were dispersed in EtOH using a bath sonicator for 1 hour. 40 μL of dispersion was drop-cast onto ITO coverslips (# 1.5 thickness). The particles were dried in air and then mounted onto the custom-made electrode holder. The electrode holder was used as a working electrode and a Pt wire electrode (CH Instruments CHI115) was used as the counter electrode. The electrodes were then pre-soak in 100 mM $TBAPF_6$ in DMSO electrolyte to swell the particles. This pre-soaking step helps avoid uptake of fluorescence dye by absorption during particle swelling. In the electrochemical cell, 3 mL of DMSO electrolyte with 1 mM of BMP was added followed by the custom-made electrode holder. A non-aqueous Ag/Ag^+ reference electrode was used, comprised of an Ag wire immersed in 0.01 M $AgNO_3$ and 0.1 M $TBAPF_6$ in ACN. A constant voltage of -1 V was applied to the system for 5 min. After the reaction, the ITO was immersed in clean DMSO solution for 1 day to remove the unreacted BMP from the particles. The particle-bearing ITO substrate was then washed with acetone to remove residual DMSO prior to mounting onto a glass slide with 5 μL Vectashield antifade mounting medium.

Fluorescence confocal imaging. An Olympus "fixed cell" DSU spinning disk confocal was used for confocal fluorescence imaging. An inverted platform (model IX81) with 100x / 1.35 oil (UPlanApo) objective lens was used for imaging through slides with Z-galvo stage for Z-sectioning. The fluorescence of thiadiazole was be observed as blue emission using a 440/40 nm fluorescence filter and BMP was observed as green emission using a 525/30 nm fluorescence filter.

Electrode performance regeneration via stimulus-induced surface defouling.

For all experiments conducted, linear sweep voltammetry was conducted at 5 mV/s scan rate in a solution containing 100 mM $TBAPF_6$ and 10 mg/mL of Fc-PVBC particles.

UV defouling: Using the same cell as for previous defouling experiments, an aliquot of ACN containing 100 mM $TBAPF_6$ and 10 mg/mL Fc-PVBC particles was charged to the cell with a pristine ITO electrode. Linear sweep voltammetry (LSV) was then performed on the cell with ITO as the working electrode and stainless steel as the counter electrode.

To mimic a fouled electrode, 80 μL of a 10 mg/mL P2-SS EtOH dispersion was drop cast onto ITO and allowed to dry in open air. This process was repeated 8 times to ensure adequate coverage of the electrode surface area. Once dry, the 2-probe cell was assembled using the artificially-fouled ITO electrode as the working electrode and stainless steel as the counter electrode. The cell was then charged with a new aliquot of the same fluid electrolyte dispersion used for the pristine electrode. LSV was performed at the same conditions as the pristine electrode.

After performing LSV on the fouled electrode, the cell was run through a defouling procedure of 30 mL/min flow under UV irradiation for 30 min. After the defouling procedure, the cell was tested with the same LSV procedure.

8.5 Appendix

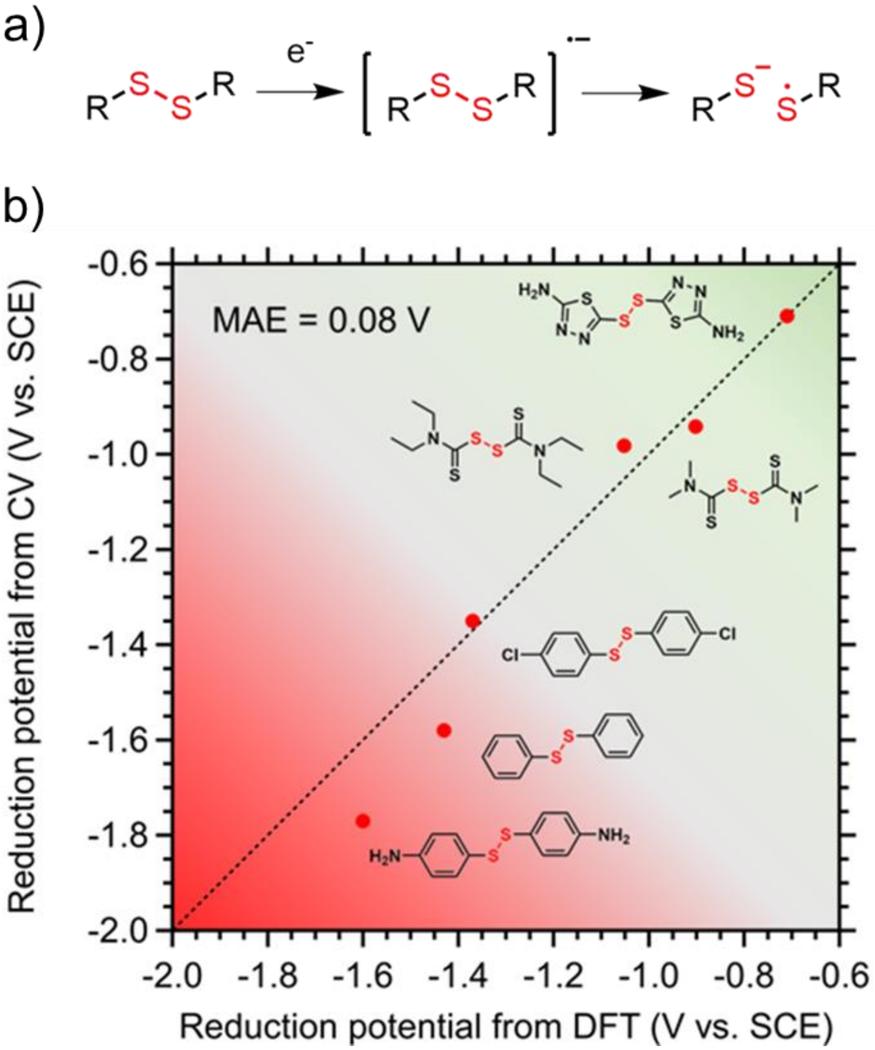

Figure 8.8. Methodology for selection of cleavable disulfide crosslinker. a) Schematic for disulfide reductive mesolytic cleavage reaction. b) Parity plot for comparison of disulfide mesolytic reduction potential from DFT vs CV experimental results.

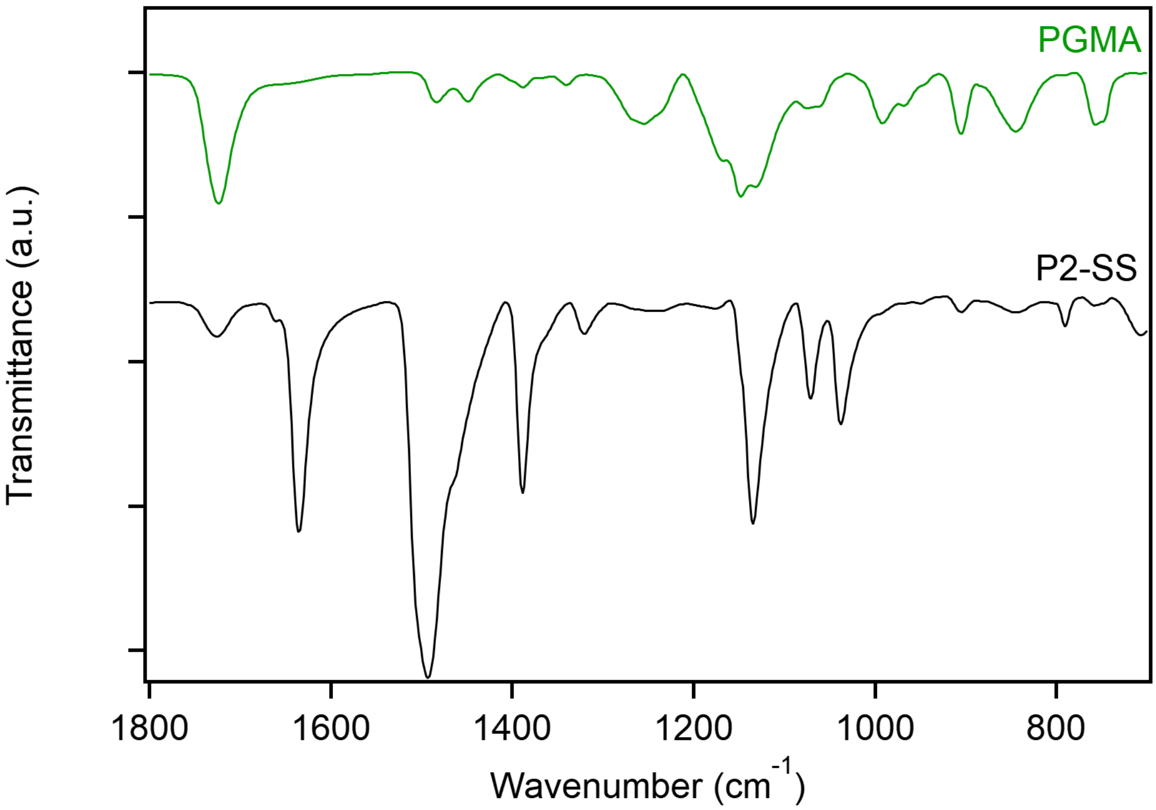

Figure 8.9. FT-IR spectra of PGMA and P2-SS.

Carbonyl peak at 1722 cm-1 was observed for particles at all functionalization states. Characteristic epoxy peaks at 846 cm-1 and 905 cm-1 indicate the symmetric and asymmetric stretching of the bonds. The decrease in epoxies peak in P2-SS and emerged peaks centered at 1668 cm-1 and 1508 cm-1 attributed to N-H bending confirm the amination of epoxide groups.

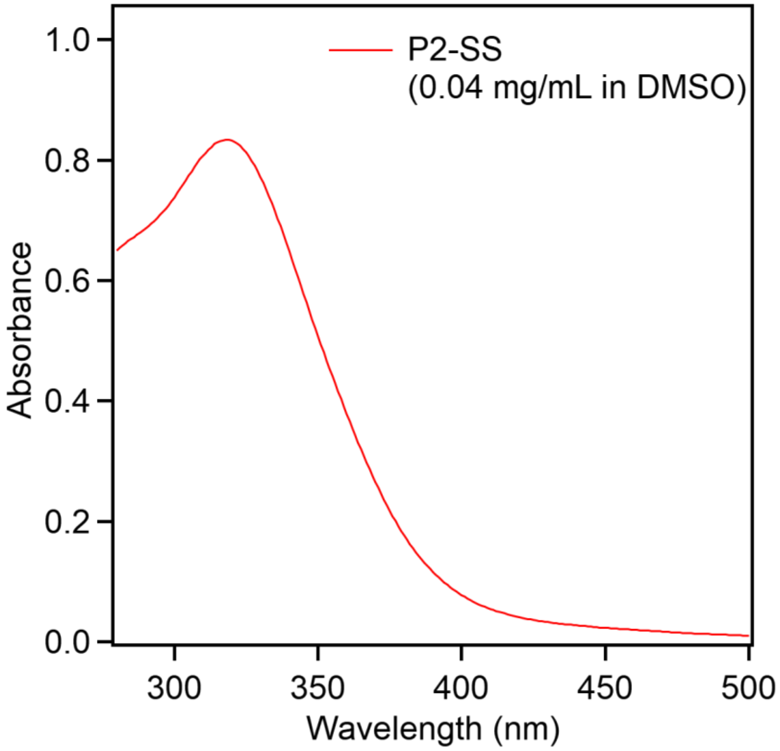

Figure 8.10. UV-Vis absorbance spectra for covalently-bound 1-SS-1 in P2-SS DMSO dispersion.

Backing plate and glass substrate

PTFE gasket (50 µm thick)

Positive electrode with flow channels

Flow cell body with connectors

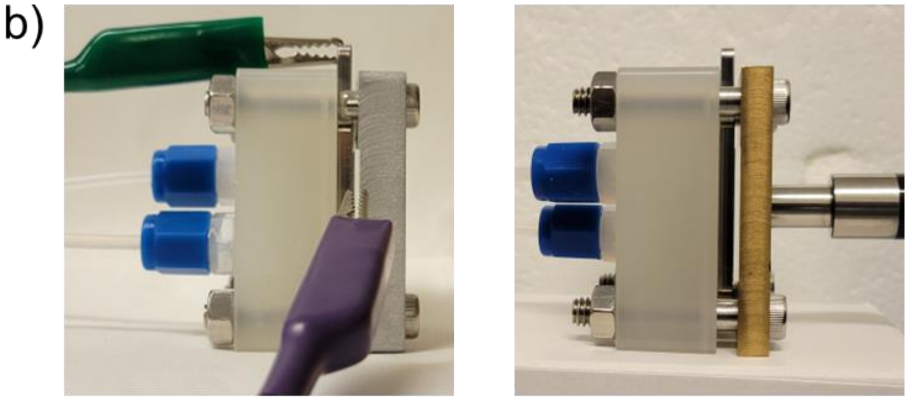

Electrochemical defouling setup

UV defouling setup

Figure 8.11. Design of modular half flow cell defouling apparatus. a) Assembly of flow cell with backing plate, glass or ITO substrate, PTFE gasket, positive electrode with flow channels and flow cell body with connectors. b) Installation of stimuli source, electrical leads, or UV fiber optic.

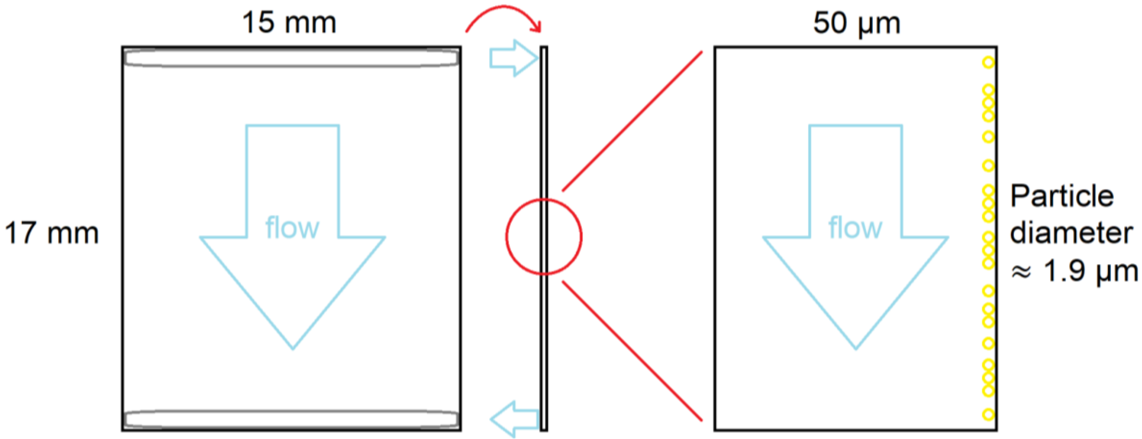

Figure 8.12. Geometry for flow through channel in defouling flow cell.

For Newtonian fluids flowing in a rectangular slit at a constant flow rate, Q, the shear rate at the wall, γ_w, is related to the flow rate as

$$\gamma_w = \frac{6Q}{wh^2}$$

where w and h are the width and the depth of the slit respectively For Newtonian fluids, the shear stress at the wall, τ_w, can be calculated by $\tau_w = \gamma_w * \mu$, where μ is the Newtonian viscosity of the fluid. Therefore, for a flow field with dimensions w =15 mm and h = 50 μm, flow rate ranging from 8 to 30 mL/min, and viscosity of fluid being 0.507 mPa s, the estimated shear rate and shear stress at the wall is

Table 8.1. Flow calculations for narrow channel flow field.

w	h	Q	γ_w	**Velocity (U)**	τ_w	**Re** [29]
[mm]	[μm]	[mL/min]	[s^{-1}]	[m/s]	[Pa]	[-]
15	50	8	21333	0.178	**10.816**	17.532
15	50	30	80000	0.667	**40.560**	65.746
2*	51.3*	1.8*	34200*	0.292*	17.338*	29.586*

The Reynolds number, or Re, is defined by the following equation.

$$Re = \frac{\rho U h}{\mu}$$

The Reynolds number is calculated as a means to determine the presence of laminar flow, where for Re values lower than the critical transition number of 2300, flow is laminar, and the shear rate and stress can be calculated by the methodology above.[30]

*The dimensions and flow rate here are the dimensions of microfluidic viscometer and the maximum flow rate it can achieve.[31]

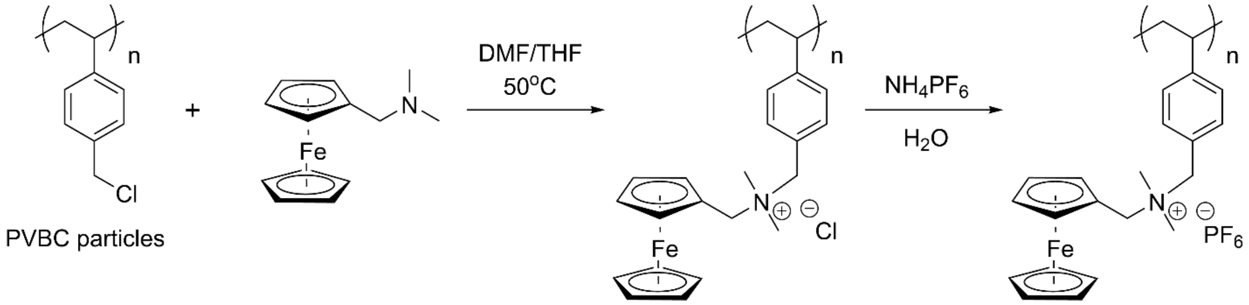

Figure 8.13. Synthetic scheme for PVBC-Fc particles for electrode regeneration experiment.

8.6 Acknowledgments

I gratefully acknowledge financial support from the Joint Center for Energy Storage Research (JCESR), an Energy Innovation Hub funded by the U.S. Department of Energy, Office of Science, Basic Energy Sciences (BES). This work made use of the shared facilities at the University of Chicago Materials Research Science and Engineering Center, supported by National Science Foundation under award number DMR-2011854. Parts of this work were carried out at the Soft Matter Characterization Facility of the University of Chicago. I gratefully thank Hongyi

Zhang for his close collaboration and skillful materials synthesis, and Sam Kopfinger for his close collaboration in the establishment of a functional flow cell system and related experiments.

8.7 References

(1) Wedege, K.; Draženić, E.; Konya, D.; Bentien, A. Organic Redox Species in Aqueous Flow Batteries: Redox Potentials, Chemical Stability and Solubility. *Sci. Reports 2016 61* **2016**, *6* (1), 1–13.

(2) Milshtein, J. D.; Barton, J. L.; Carney, T. J.; Kowalski, J. A.; Darling, R. M.; Brushett, F. R. Towards Low Resistance Nonaqueous Redox Flow Batteries. *J. Electrochem. Soc.* **2017**, *164* (12), A2487–A2499.

(3) Wei, X.; Pan, W.; Duan, W.; Hollas, A.; Yang, Z.; Li, B.; Nie, Z.; Liu, J.; Reed, D.; Wang, W.; et al. Materials and Systems for Organic Redox Flow Batteries: Status and Challenges. *ACS Energy Lett.* **2017**, *2* (9), 2187–2204.

(4) Ding, Y.; Zhang, C.; Zhang, L.; Zhou, Y.; Yu, G. Molecular Engineering of Organic Electroactive Materials for Redox Flow Batteries. *Chemical Society Reviews*. Royal Society of Chemistry January 7, 2018, pp 69–103.

(5) Singh, V.; Kim, S.; Kang, J.; Byon, H. R. Aqueous Organic Redox Flow Batteries. *Nano Res. 2019 129* **2019**, *12* (9), 1988–2001.

(6) Chai, J.; Lashgari, A.; Jiang, J. J. Electroactive Materials for Next-Generation Redox Flow Batteries: From Inorganic to Organic. *ACS Symp. Ser.* **2020**, *1364*, 1–47.

(7) Li, M.; Rhodes, Z.; Cabrera-Pardo, J. R.; Minteer, S. D. Recent Advancements in Rational Design of Non-Aqueous Organic Redox Flow Batteries. *Sustain. Energy Fuels* **2020**, *4* (9), 4370–4389.

(8) Janoschka, T.; Morgenstern, S.; Hiller, H.; Friebe, C.; Wolkersdörfer, K.; Häupler, B.; Hager, M. D.; Schubert, U. S. Synthesis and Characterization of TEMPO- and Viologen-Polymers for Water-Based Redox-Flow Batteries. *Polym. Chem.* **2015**, *6* (45), 7801–7811.

(9) Winsberg, J.; Hagemann, T.; Muench, S.; Friebe, C.; Häupler, B.; Janoschka, T.; Morgenstern, S.; Hager, M. D.; Schubert, U. S. Poly(Boron-Dipyrromethene)-A Redox-Active Polymer Class for Polymer Redox-Flow Batteries. *Chem. Mater.* **2016**, *28* (10), 3401–3405.

(10) Winsberg, J.; Janoschka, T.; Morgenstern, S.; Hagemann, T.; Muench, S.; Hauffman, G.; Gohy, J. F.; Hager, M. D.; Schubert, U. S. Poly(TEMPO)/Zinc Hybrid-Flow Battery: A Novel, "Green," High Voltage, and Safe Energy Storage System. *Adv. Mater.* **2016**, *28* (11), 2238–2243.

(11) Montoto, E. C.; Nagarjuna, G.; Moore, J. S.; Rodríguez-López, J. Redox Active Polymers for Non-Aqueous Redox Flow Batteries: Validation of the Size-Exclusion Approach. *J. Electrochem. Soc.* **2017**, *164* (7), A1688–A1694.

(12) Baran, M. J.; Braten, M. N.; Montoto, E. C.; Gossage, Z. T.; Ma, L.; Chénard, E.; Moore, J. S.; Rodríguez-López, J.; Helms, B. A. Designing Redox-Active Oligomers for Crossover-Free, Nonaqueous Redox-Flow Batteries with High Volumetric Energy Density. *Chem. Mater.* **2018**, *30* (11), 3861–3866.

(13) Hendriks, K. H.; Robinson, S. G.; Braten, M. N.; Sevov, C. S.; Helms, B. A.; Sigman, M. S.; Minteer, S. D.; Sanford, M. S. High-Performance Oligomeric Catholytes for Effective Macromolecular Separation in Nonaqueous Redox Flow Batteries. *ACS Cent. Sci.* **2018**, *4* (2), 189–196.

(14) Winsberg, J.; Benndorf, S.; Wild, A.; Hager, M. D.; Schubert, U. S. Synthesis and Characterization of a Phthalimide-Containing Redox-Active Polymer for High-Voltage Polymer-Based Redox-Flow Batteries. *Macromol. Chem. Phys.* **2018**, *219* (4), 1700267.

(15) Iyer, V. A.; Schuh, J. K.; Montoto, E. C.; Pavan Nemani, V.; Qian, S.; Nagarjuna, G.; Rodríguez-López, J.; Ewoldt, R. H.; Smith, K. C. Assessing the Impact of Electrolyte Conductivity and Viscosity on the Reactor Cost and Pressure Drop of Redox-Active Polymer Flow Batteries. *J. Power Sources* **2017**, *361*, 334–344.

(16) Barton, J. L.; Milshtein, J. D.; Hinricher, J. J.; Brushett, F. R. Quantifying the Impact of Viscosity on Mass-Transfer Coefficients in Redox Flow Batteries. *J. Power Sources* **2018**, *399*, 133–143.

(17) Zhao, Y.; Si, S.; Liao, C. A Single Flow Zinc//Polyaniline Suspension Rechargeable Battery. *J. Power Sources* **2013**, *241*, 449–453.

(18) Winsberg, J.; Muench, S.; Hagemann, T.; Morgenstern, S.; Janoschka, T.; Billing, M.; Schacher, F. H.; Hauffman, G.; Gohy, J. F.; Hoeppener, S.; et al. Polymer/Zinc Hybrid-Flow Battery Using Block Copolymer Micelles Featuring a TEMPO Corona as Catholyte. *Polym. Chem.* **2016**, *7* (9), 1711–1718.

(19) Montoto, E. C.; Nagarjuna, G.; Hui, J.; Burgess, M.; Sekerak, N. M.; Hernández-Burgos, K.; Wei, T. S.; Kneer, M.; Grolman, J.; Cheng, K. J.; et al. Redox Active Colloids as Discrete Energy Storage Carriers. *J. Am. Chem. Soc.* **2016**, *138* (40), 13230–13237.

(20) Hatakeyama-Sato, K.; Nagano, T.; Noguchi, S.; Sugai, Y.; Du, J.; Nishide, H.; Oyaizu, K. Hydrophilic Organic Redox-Active Polymer Nanoparticles for Higher Energy Density Flow Batteries. *ACS Appl. Polym. Mater.* **2019**, *1* (2), 188–196.

(21) Yan, W.; Wang, C.; Tian, J.; Zhu, G.; Ma, L.; Wang, Y.; Chen, R.; Hu, Y.; Wang, L.; Chen, T.; et al. All-Polymer Particulate Slurry Batteries. *Nat. Commun. 2019 101* **2019**, *10* (1), 1–11.

(22) Boujioui, F.; Zhuge, F.; Gohy, J. F. Redox Polymer–Based Nano-Objects via Polymerization-Induced Self-Assembly. *Macromol. Chem. Phys.* **2020**, *221* (1), 1900296.

(23) Kozhunova, E. Y.; Gvozdik, N. A.; Motyakin, M. V.; Vyshivannaya, O. V.; Stevenson, K. J.; Itkis, D. M.; Chertovich, A. V. Redox-Active Aqueous Microgels for Energy Storage Applications. *J. Phys. Chem. Lett.* **2020**, *11* (24), 1–5.

(24) Nguyen, T. P.; Easley, A. D.; Kang, N.; Khan, S.; Lim, S. M.; Rezenom, Y. H.; Wang, S.; Tran, D. K.; Fan, J.; Letteri, R. A.; et al. Polypeptide Organic Radical Batteries. *Nat. 2021 5937857* **2021**, *593* (7857), 61–66.

(25) Qian, H.; Counihan, M. J.; Doan, H. A.; Ibrahim, N. A.; Danis, A. S.; Setwipatanachai, W.; Purwanto, N. S.; Rodríguez-López, J.; Assary, R. S.; Moore, J. S. Mesolytic Cleavage of Homobenzylic Ethers for Programmable End-of-Life Function in Redoxmers. *J. Mater. Chem. A* **2022**, *10* (14), 7739–7753.

(26) Shadike, Z.; Tan, S.; Wang, Q.-C.; Lin, R.; Hu, E.; Qu, D.; Yang, X.-Q. Review on Organosulfur Materials for Rechargeable Lithium Batteries. *Mater. Horizons* **2021**.

(27) Grocke, G. L.; Zhang, H.; Kopfinger, S. S.; Patel, S. N.; Rowan, S. J. Synthesis and Characterization of Redox-Responsive Disulfide Cross-Linked Polymer Particles for Energy Storage Applications. *ACS Macro Lett.* **2021**, *10* (12), 1637–1642.

(28) Horák, D.; Shapoval, P. Reactive Poly(Glycidyl Methacrylate) Microspheres Prepared by Dispersion Polymerization. J. Polym. Sci., Part A: Polym. Chem. 2000, 38 (21), 855−3863.

(29) C. W. Macosko, RHEOLOGY: Principles, Measurements, and Applications (VCH Publishers, Inc., New York, 1994).

(30) R. H. Ewoldt, M. T. Johnston, and L. M. Caretta, “Experimental challenges of shear rheology: How to avoid bad data,” in Complex Fluids in Biological Systems, Springer Biological Engineering Series, edited by S. Spagnolie (Springer, 2015) pp. 207–241.

(31) Y. Wang et al., “Viscous flow properties and hydrodynamic diameter of phenothiazine-based redox-active molecules in different supporting salt environments,” Physics of Fluids, 32, 083108 (2020).

Chapter 9

Summary and Outlook

This work encompasses a broad collection of research topics pertaining to the design and characterization of redox-active polymer materials for energy applications. First, Chapter 3 discusses the design and fabrication of several custom instruments for the fabrication of functional polymer systems and their subsequent characterization. As the applications of redox-active polymers become more complex, there is an increasing need for precise control over their properties. The apparatuses described in Chapter 3 are designed to allow in-situ examination of electrochemical properties of polymeric materials under the application of heating, molecular doping, and electrochemical stimulus. Such approaches allow for a more granular and accurate understanding of these materials as a function of time and stimulus intensity and are critical for characterizing these materials to a sufficient degree for eventual practical application.

Chapter 4 discloses a multifaceted approach to characterizing the response of mixed conductivity in a family of commercially-available conjugated polyelectrolyte semiconducting polymers, poly[3-(potassium-*n*-alkanoate) thiophene-2,5-diyl] (P3K*n*T), to an environmental stimulus, relative humidity (RH). Through a combination of UV-Vis, electron paramagnetic resonance, and in-situ electrochemical impedance spectroscopies, it was demonstrated that increasing RH results in a concurrent increase in mixed conduction. This is the result of generation of both ionic and electronic charge carriers through a water-mediated self-doping process reliant on the liberation of potassium counterions following hydration. However, at high RH values, electronic conductivity was shown to decrease more than an order of magnitude from maximum values, despite this being the regime of highest electronic charge carrier concentrations. As such, a morphological analysis was employed to understand how RH influences the polymer microstructure in ways that impact electronic conduction. Dynamic vapor sorption coupled with in-situ ellipsometry revealed rapid water uptake in the regime of decreasing electronic conductivity. An in-situ humidified GIWAXS analysis showed that as water infiltrated the polymer thin film, not only did swelling occur within the crystalline domains of the material, but the overall ordering of the material bulk decreased with increasing water content. As efficient electronic conduction in conjugated polymers relies on both good local ordering within crystalline domains and sufficient electronic interconnectivity between neighboring domains, the rapid swelling and disordering of P3K*n*T with increasing water content explained the decreased performance at high RH. A comparison between different polymer species revealed that increasing both the side chain spacer length and polymer molecular weight resulted in increased resilience to the negative effects of increasing RH. Overall, P3K*n*T shows promise as an already commercially-available mixed conductor with relatively high values for both ionic and electronic conductivity. As research continues into complex devices requiring efficient mixed conduction, P3K*n*T may serve useful as laboratory model. In addition, the results from this study may provide guidance in the design of future materials, highlighting key considerations into maintaining performance across a variety of environmental conditions.

Chapters 5, 6, and 7 explored the design of a novel polymeric material for use as a secondary battery cathode active material. Bis(5-amino-l,3,4-thiadiazol-2-yl) disulfide (ATDDS) is an organosulfur molecule capable of a reversible 2-electron reduction process. By functionalizing this molecule to poly(glycidyl methacrylate) (PGMA) particles resulted in the synthesis of an insoluble material capable of facile blending with necessary additives and casting from suspension onto electrode substrates in approaches similar to conventional inorganic cathode materials. Fixation of the disulfide onto a polymer scaffold prevents diffusion of the reduced species after charging, resulting in improved electrochemical kinetics at the electrode surface. This phenomenon is important in the context that “shuttling”, or diffusion of reduced species across the battery separator, is a critical challenge in the design of Li-S batteries. Initial galvanostatic cycling of these materials yielded good stability over multiple cycles, showing promise for the concept as an energy storage material. However, the overall demonstrated capacity was detrimentally low.

In order to improve this metric, the synthetic and processing flexibilities of polymers were leveraged. The particles were first synthesized with a smaller diameter. By decreasing the characteristic diffusion length, charge is able to move both in and out of the particle more easily, improving material accessibility and preventing charge trapping. Next, improving the mobility of counterions into the polymer was addressed. After functionalization with ATDDS, a small amount of highly reactive PGMA epoxide pendant groups remain. In order to neutralize these moieties, a secondary chemistry is provided to drive the reaction to completion. In the interest of efficient ionic transport, the initial chemistry, an amine bearing insulating aliphatic chains, was substituted for a cyclic carbonate bearing similar structure to solvents frequently used in battery electrolytes. As a result, the particles bear increased polar character, making ion diffusion easier. Lastly, the processing of these particles into electrodes was addressed. In comparison to common inorganic cathode materials, polymers are able to undergo dramatic changes in characteristic in response to solvent swelling. By selecting for a stable, highly-swelling solvent, electrode morphology was visibly improved, leading to a highly-connected structure and relatively homogeneous blending with the conductive carbon and polymer binder additives. As a result of these modifications, cathodes containing the second-generation PGMA-ATDDS particles showed dramatically improved discharge capacities, utilizing significantly more of the theoretical capacity of the material, while requiring significantly less conductive additives.

The work done in Chapter 8 seeks to further improve the performance of these disulfide-based systems by addressing the sluggish electrochemical kinetics and insulating nature of organosulfur chemistries. By substituting the inert PGMA backbone for an electronically-conductive PEDOT conjugated backbone, it may be possible to enhance electronic charge transfer from the electrode-particle surface interface into the core of the particles, improving overall utilization of the active material. In addition, it has been shown that conjugated polymers such as PEDOT exhibit an electrocatalytic effect on the disulfide redox center, improving the rate of charge transfer, allowing for faster charge and discharge. Galvanostatic cycling of cathodes containing a PEDOT-based nanoparticle active material yielded just that. In addition to a relatively high discharge capacity, the PEDOT-based material retained much more capacity as a function of charge rate when compared to similarly-sized PGMA-based particles. The ability to transport electronic charge carriers more efficiently into the particles, coupled with the enhanced disulfide electrochemical kinetics, resulted in better performance at the higher rates. This is important in the context of modern battery applications, in which fast charging is critical to practical applications at any scale, from small devices to grid-scale energy storage.

While these initial results are promising, continued optimization of these systems may yield even better performance. Despite these materials being unable to achieve the same theoretical capacities as their inorganic counterparts by simple nature of their molecular structure, they have inherent benefits that cannot be ignored. Organosulfur compounds like ATDDS are already employed in countless applications, and relatively inexpensive commercial synthesis of these materials, coupled with a nearly limitless supply of raw base compounds, makes them highly attractive compared to minerals which must be extracted from deep below the surface of the earth. As more aspects of everyday life require access to reliable energy storage, sustainable organic chemistries such as organosulfurs will become a necessity.

Lastly, Chapter 8 considers an alternative use for the disulfide-crosslinked particle, still in the context of energy storage. In addressing energy storage at the grid-scale, one attractive technology is the redox flow battery, allowing for decoupled energy conversion and storage, making it highly flexible and scalable, with potential improvements in safety and economics vs traditional secondary batteries. Of the many possible selections for flow battery electrolytes, insoluble polymers offer many theoretical advantages, including high energy density without prohibitively high viscosity, and the ability to use inexpensive size-exclusion membranes. However, the deposition of these materials over time onto electrode surfaces, passivating them and diminishing performance, puts a practical limitation on battery lifetime. Designing an insoluble polymer material that allows for controlled electrode cleaning without the need for costly electrolyte or electrode replacement is therefore deemed critical.

The previous chapters demonstrated the capability of polymer particle-bound ATDDS to reversibly cleave to thiolates under the application of a reducing electrochemical stimulus. In addition, UV photoexcitation results in dynamic cleavage to form thiol radicals, which was used previously as a synthetic purification step. It was proposed that if these mechanisms could be employed in a controllable manner for particles adhered to a flow battery electrode surface, the resulting de-crosslinking would reduce the structural integrity of the interface, allowing the convective fluid flow to wash the particles away, improving accessibility of the electrode to the bulk electrolyte, regenerating performance. In order to test this hypothesis, custom flow half-cells were fabricated in order to expose PGMA-ATDDS particles drop-cast onto 2D electrodes to either an electrochemical reducing stimulus or a UV photo-stimulus, while also being subjected to the forces of electrolyte fluid flow. By taking before-and-after images of these electrodes using optical microscopy and quantifying the change in number of particles using software analysis, the effectiveness of this “cleaning” procedure was evaluated. It was found that both electrochemical reduction and UV photoexcitation stimuli were effective at enhancing particle removal from electrode surfaces exposed to flow. In addition, a control experiment using particles with only permanent crosslinkers showed the disulfide chemistry was critical to the mechanism. By irreversibly reacting the reduced thiolates with a fluorescent tag, it was also shown that the cleavage mechanism was localized to the particle-electrode interface at the time scales investigated in this study. As a final demonstration, the cleaning procedure was used in a flow cell containing an electrolyte suspension of ferrocene-bearing polymer particles. It was shown that in comparison to a pristine electrode, one fouled with PGMA-ATDDS particles exhibited greatly reduced charge transfer at the same applied potentials. By switching from the ferrocene-oxidizing potential to one capable of reducing ATDDS, particles were removed under the forces of the electrolyte flow. Switching back to the oxidizing potential, the electrode performance was greatly improved, nearly achieving the current values of a pristine electrode.

Being able to regenerate electrode surfaces in flow batteries without having to disassemble the system or employ harsh chemical cleaning agents makes them much more attractive for practical use. As in the demonstrated system with ferrocene, selecting for “storage” chemistries with redox potentials separated from that of the “cleavage” chemistry allows for control over when the particle charge storage mechanism and cleaning mechanism occur. Future work into integrating both molecules into a single particle will yield a fully-functional dual-responsive system with potential as a long-lifetime electrolyte for sustainable organic redox flow batteries.